PHASE ERROR MITIGATION TECHNIQUES IN ROBUST ANGLE- AND RANGE-BASED LOCALIZATION OF RESOURCE-CONSTRAINED DEVICES

Aleš Simončič

Doctoral Dissertation
Jožef Stefan International Postgraduate School
Ljubljana, Slovenia

Supervisor: Assoc. Prof. Dr. Tomaž Javornik, Jožef Stefan Institute and Jožef Stefan International Postgraduate School, Ljubljana, Slovenia
Co-Supervisor: Assoc. Prof. Dr. Andrej Hrovat, Jožef Stefan Institute and Jožef Stefan International Postgraduate School, Ljubljana, Slovenia

Evaluation Board:
Prof. Dr. Mihael Mohorčič, Chair, Jožef Stefan Institute and Jožef Stefan International Postgraduate School, Ljubljana, Slovenia
Prof. Dr. Andrej Žemva, Member, Faculty of Electrical Engineering, University of Ljubljana, Ljubljana, Slovenia
Prof. Dr. Philipp Svoboda, Member, Technische Universität Wien, Institut for Telecommunication, Wien, Austria

MEDNARODNA PODIPLOMSKA ŠOLA JOŽEFA STEFANA
JOŽEF STEFAN INTERNATIONAL POSTGRADUATE SCHOOL



Aleš Simončič

PHASE ERROR MITIGATION TECHNIQUES IN ROBUST ANGLE- AND RANGE-BASED LOCALIZATION OF RESOURCE-CONSTRAINED DEVICES

Doctoral Dissertation

TEHNIKE ZMANJŠEVANJA FAZNE NAPAKE PRI ROBUSTNI LOKALIZACIJI NA PODLAGI KOTA IN RAZDALJE ZA NAPRAVE Z OMEJENIMI VIRI

Doktorska disertacija

Supervisor: Assoc. Prof. Dr. Tomaž Javornik

Co-Supervisor: Assoc. Prof. Dr. Andrej Hrovat

Ljubljana, Slovenia, July 2026

To my family, and to Nika

Acknowledgments

I would like to express my sincere gratitude to my mentor, Assoc. Prof. Dr. Tomaž Javornik, and my co-mentor, Assoc. Prof. Dr. Andrej Hrovat, for your guidance and support throughout my doctoral studies. I am especially grateful for your availability and for always taking the time to discuss technical questions, provide constructive feedback, and offer advice whenever needed. I also appreciate your encouragement and support for additional training, including participation in summer schools and related educational programs, which enabled me to broaden my perspective and deepen my knowledge in areas relevant to this dissertation.

I also thank the members of the evaluation board, Prof. Dr. Mihael Mohorčič, Prof. Dr. Philipp Svoboda, Prof. Dr. Andrej Žemva, for agreeing to be members of the evaluation committee and for the time and effort dedicated to reviewing this dissertation.

I also acknowledge the financial support of the Slovenian Research and Innovation Agency (ARIS), which made this work possible.

I am grateful to my colleagues at the E6 department for providing a supportive and stimulating research environment. In particular, I would like to thank the colleagues with whom I shared an office for the daily discussions, collaboration, and mutual support that made the work both more productive and enjoyable.

Special thanks go to Dr. Teodora Kocevska, Dr. Grega Morano, Dr. Blaž Bertalanič, and Ana Jeknić. Your willingness to discuss technical challenges, share ideas, and collaborate closely had a major impact on this work. I sincerely appreciate your generosity, friendship, and everything I learned from you, not only related to work, over the years. If I could go back in time, I would gladly choose the same journey again, especially because of you.

Finally, I would like to thank my family and Nika for your encouragement, patience, understanding, and continuous support in every sense throughout this journey. / Na koncu se iskreno zahvaljujem svoji družini in Niki za spodbudo, potrpežljivost, razumevanje in podporo v vseh oblikah skozi celotno pot.

Abstract

As the number of location-aware applications grows, the demand for indoor localization systems is increasing. Motivated by the need for localization systems that enable accurate location estimation, robustness to multipath, simple deployment, and scalability, supported by low-cost devices, this dissertation focuses on two phase-based approaches within the measurement stage of localization: direction of arrival (DoA) estimation using single-radio-frequency (RF)-chain architectures, and distance estimation with the multi-carrier phase difference (MCPD) method. In both cases, the estimation parameter is derived from carrier-phase measurements, making both techniques sensitive to hardware non-idealities that are more pronounced in low-cost devices. The dissertation examines hardware-related mechanisms that distort phase measurements and introduce systematic bias, and develops mitigation approaches that enable accurate localization for resource-constrained devices.

The first part of the dissertation addresses DoA estimation using single-RF-chain architectures. The work initially examines phase errors introduced by the switched antenna array (SAA), which is required to obtain spatial samples for direction estimation. A complete SAA design workflow is presented, with an emphasis on minimizing phase distortions across switched antenna elements and RF paths to enable accurate DoA estimation without post-fabrication calibration, supporting simpler and lower-cost deployments. The dissertation then examines how asynchronization between devices, particularly sampling frequency offset (SFO) and carrier frequency offset (CFO), caused by non-ideal crystal oscillators, leads to phase-measurement errors in DoA estimation. It is shown that a conventional sequential spatial sweep across antenna elements induces a phase-error pattern that can be coupled with the DoA-dependent phase pattern, resulting in an estimation bias. An efficient mitigation approach based on antenna activation order is proposed to reshape the measured phase-error pattern across antenna elements and reduce bias.

The dissertation then transitions to MCPD ranging and analyzes how asynchronization between devices affects distance estimation. Specifically, the work first examines how SFO between devices alters sampling times, which, under the conventional linear frequency sweep, induces a linear phase-error trend across carriers that biases the distance estimate. An efficient bias-reduction approach based on carrier order is proposed to suppress this trend. In addition, the dissertation analyzes the impact of frequency-dependent CFO on distance estimation arising from phase-locked loop-based RF carrier generation, which can introduce a linear phase-error trend that biases distance estimates. To suppress this bias, timing diagram design strategies are developed using temporal differential correction and role-switching approaches.

The proposed asynchronization-mitigation approaches diverge from traditional estimation-and-correction and joint parameter-estimation approaches, which require additional measurements, longer observation windows, and greater computational load for effective phase-error mitigation. In contrast, the proposed mitigation approaches leverage switching-sequence and timing design to reduce systematic bias with negligible additional computational and measurement overhead.

Povzetek

Z naraščanjem števila aplikacij, ki zahtevajo zavedanje lokacije, narašča tudi potreba po lokalizaciji v notranjih prostorih. Zaradi zahtev po natančni oceni lokacije, robustnosti na večpotno razširjanje, enostavni namestitvi in razširljivosti z uporabo nizkocenovnih naprav se disertacija osredotoča na dva pristopa v merilni fazi lokalizacije: ocenjevanje smeri prihoda (ang. direction of arrival, DoA) z arhitekturami z eno radiofrekvenčno (ang. radio frequency, RF) signalno potjo ter ocenjevanje razdalje z metodo fazne razlike na več nosilnih frekvencah (ang. multi-carrier phase difference, MCPD). V obeh primerih je ocenjen parameter pridobljen iz meritev faze nosilca, zato sta obe tehniki občutljivi na neidealnosti strojne opreme, ki so pri nizkocenovnih napravah izrazitejše. Disertacija preučuje mehanizme v strojni opremi, ki popačijo fazne meritve in povzročijo sistematični prirastek ocene, ter razvije pristope za njegovo zmanjšanje, primerne za naprave z omejenimi viri.

Prvi del disertacije obravnava ocenjevanje DoA z arhitekturami z eno RF signalno potjo. Najprej analizira fazne napake, ki jih povzroča preklopno antensko polje (ang. switched antenna array, SAA), potrebno za pridobivanje prostorskih vzorcev za ocenjevanje smeri. Predstavljen je celovit postopek načrtovanja SAA, s poudarkom na zmanjševanju faznih nesimetrij med preklopnimi antenskimi elementi in RF potmi, ki omogoča natančno ocenjevanje DoA brez kalibracije polja ter s tem enostavnejšo in cenejšo postavitev sistema. Nato disertacija preučuje, kako neusklajenost med napravami, zlasti odmik vzorčnih frekvenc (ang. sampling frequency offset, SFO) in odmik nosilnih frekvenc (ang. carrier frequency offset, CFO), povzroča fazne napake pri ocenjevanju DoA. Pokazano je, da zaporedni prostorski prelet po antenskih elementih povzroči fazne napake, ki se lahko sklopijo s fazami zaradi DoA, kar povzroči sistematični prirastek oceni. Predlagan je učinkovit pristop zmanjšanja prirastka, ki temelji na vrstnem redu aktivacije anten, s katerim vplivamo na fazne napake posameznih anten.

Disertacija se nato preusmeri na določanje razdalje z metodo MCPD in analizira, kako neusklajenost med napravama vpliva na ocenjevanje razdalje. Najprej obravnava, kako SFO spremeni čase vzorčenja faze, kar pri linearnem frekvenčnem preletu povzroči linearen trend faznih napak in s tem prirastek oceni razdalje. Predlagan je učinkovit pristop zmanjšanja prirastka, ki temelji na uporabljenem vrstnem redu nosilcev in izniči linearen trend faznih napak. Poleg tega disertacija analizira vpliv frekvenčno odvisnega CFO na oceno razdalje, ki je posledica tvorjenja nosilcev na osnovi fazno sklenjene zanke. Tak vpliv lahko povzroči linearen trend fazne napake v odvisnosti od frekvence nosilcev in s tem prirastek oceni razdalje. Za zmanjšanje prirastka predlagamo načrtovanje časovnega diagrama z uporabo tehnik časovne diferencialne korekcije in pristopa zamenjave vlog.

Predlagani pristopi ublažitve vpliva neusklajenosti se razlikujejo od konvencionalnih pristopov ocenjevanja in popravljanja faznih napak ter skupnega ocenjevanja parametrov, ki za učinkovito zmanjšanje fazne napake zahtevata dodatne meritve, daljši opazovalni čas in večjo računsko obremenitev. Predlagani pristopi temeljijo na načrtovanju zaporedja preklapljanja in časovnega diagrama z zanemarljivo dodatno računsko zahtevnostjo in merilnim časom.

Contents

Abbreviations **xv**

1 Introduction **1**
1.1 Wireless Radio-based Localization . . . 1
1.2 Integrated Sensing and Communication . . . 3
1.3 Direction Estimation . . . 4
1.3.1 Direction Estimation with Single RF Chain . . . 4
1.4 Range Estimation . . . 5
1.4.1 Phase-Based Ranging . . . 5
1.5 Asynchronization Effect on Sensing Performance . . . 6
1.6 Motivation . . . 7
1.7 Aims and Objectives . . . 9
1.8 Hypotheses . . . 10
1.9 Scientific Contributions . . . 11
1.10 Dissertation Structure . . . 12

2 Design and Validation of a Switched Antenna Array for BLE Direction Finding **15**

3 Asynchronization-induced Phase Error in DoA Estimation **27**
3.1 Phase Error Mitigation via ASP Design . . . 28
3.2 Comprehensive ASP Design, Analysis, and Evaluation . . . 36

4 Frequency Switching Pattern Design for Robust MCPD Ranging **53**

5 Timing Diagram Design for Robust MCPD Ranging **77**

6 Conclusions and Future Work **99**
6.1 Summary of the Dissertation, Addressed Hypotheses, and Scientific Contributions . . . 99
6.2 Future Work . . . 101

References **103**

Bibliography **111**

Biography **115**

Abbreviations

5G	...	Fifth Generation Wireless Systems
6G	...	Sixth Generation Wireless Systems
AA	...	Antenna Array
AoA	...	Angle of Arrival
AoD	...	Angle of Departure
ASP	...	Antenna Switching Pattern
BLE	...	Bluetooth Low Energy
CFO	...	Carrier Frequency Offset
CFOSD	...	Carrier Frequency Offset Slope Difference
CFR	...	Channel Frequency Response
CIR	...	Channel Impulse Response
CTE	...	Constant Tone Extension
CW	...	Continuous Wave
DoA	...	Direction of Arrival
FSP	...	Frequency Switching Pattern
GNSS	...	Global Navigational Satellite System
IDFT	...	Inverse Discrete Fourier Transform
IFFT	...	Inverse Fast Fourier transform
IoT	...	Internet of Things
IQ	...	In-phase and Quadrature
ISAC	...	Integrated Sensing and Communication
LoS	...	Line of Sight
MCPD	...	Multi-Carrier Phase Difference
MUSIC	...	Multiple Signal Classification
PBR	...	Phase-Based Ranging
PLL	...	Phase-Locked Loop
RF	...	Radio Frequency
RP	...	Role Pattern
RSA	...	Role-switching Approach
RSSI	...	Received Signal Strength Indicator
RTT	...	Round-Trip Time
SAA	...	Switched Antenna Array
SFE	...	Sampling Frequency Error
SFO	...	Sampling Frequency Offset
SNR	...	Signal-to-Noise Ratio
SS	...	Sequential Sampling
SSW	...	Sequential Switching
STO	...	Sampling Time Offset
TDCA	...	Temporal Differential Correction Approach
TD	...	Timing Diagram
ToF	...	Time of Flight

UCA ... Uniform Circular Array
ULA ... Uniform Linear Array

Chapter 1

Introduction

The Internet of Things (IoT) connects a large number of low-cost, often battery-powered devices that sense, communicate, and interact with physical environments. The usefulness of sensed data and the effectiveness of action often depend on where devices and assets are located. As IoT deployments scale, the need for spatial context becomes more pronounced. Localization is the process of identifying where a device is in space. It is therefore a core enabling technology for applications that rely on location awareness, including industrial automation, asset tracking, physical access control, autonomous systems, smart buildings, safety and rescue operations, and wearable and consumer products [1–8]. From a technology perspective, location information can be obtained using different physical modalities, such as acoustics, visible light, inertial sensing, cameras, or radio frequency (RF) signals [2, 4, 8, 9]. Each technology leads to different trade-offs in achievable accuracy and resolution, as well as cost, infrastructure burden, robustness, privacy, and energy consumption [4, 8–13].

1.1 Wireless Radio-based Localization

RF-based localization is attractive for IoT deployments because it can reuse existing wireless infrastructure and communication waveforms, enabling localization on commodity radios with low hardware complexity and cost, and benefiting from established communication protocols for coordination and exchange of sensing-related information. Antenna design additionally enables control over spatial coverage and angular selectivity through configurable radiation characteristics. Compared with optical modalities, radio-based methods preserve privacy and remain effective under poor lighting and other visually challenging conditions [8, 12–14].

Radio waves propagate through space between wireless nodes, interacting with the environment through reflection, scattering, diffraction, and attenuation. As a result, the received signals carry signatures of the surrounding environment, including location-related information. This information can be extracted either from active signal exchanges with a wireless device carried by the target to be localized or, in device-free scenarios, from target-induced changes in the propagation channel. Localization methods exploit measurable signal attributes such as received signal strength, carrier phase, frequency, as well as timing information obtained from timestamped transmissions and receptions. Consequently, radio-based localization approaches are commonly categorized by the primary attribute they exploit, leading to power-based, time-based, phase-based, and hybrid methods that combine complementary measurements to improve robustness [1].

A location can be estimated directly by mapping observed signal attributes to position using a pre-learned model. A common example is fingerprinting, where a database

of signal attributes is collected through measurements or simulations in advance for a specific environment and stored for a discrete set of reference locations. During operation, the measured signal attributes are compared with the stored fingerprints, and the location is inferred from the closest match or from a weighted combination of the closest matches. Fingerprint accuracy depends strongly on the density and quality of reference locations and on how well the database captures temporal variability, while required memory and data acquisition effort scale with the number of stored locations. The need to collect environment-specific fingerprints and periodically update them as indoor environments change increases time and operational costs, which can limit scalability and degrade performance in dynamic deployments [8, 15]. Alternatively, a location can be estimated indirectly using model-based approaches that first estimate intermediate spatial quantities, most commonly direction and range, and then translate these estimates into a location estimate using standard geometric localization techniques [1]. Angle-based techniques estimate location by triangulation from direction estimates. Range-based techniques estimate location by (tri)lateration from distance estimates. Hybrid techniques combine angle and range estimates, which can reduce the required number of anchors and enable localization with a single anchor [3, 16–18]. Consequently, the quality of location estimates is fundamentally limited by the accuracy and robustness of the underlying angle and range estimates [19]. This dissertation focuses on the measurement stage of localization, specifically on the achievable performance of the intermediate spatial quantities of direction and range, while localization algorithms that use direction and range estimates to determine position are not analyzed.

Wireless localization can be categorized as active, also known as device-based, or passive, also known as device-free. In active localization, the target carries a device that participates in the localization process, for example a wireless tag that transmits, receives, or responds to known signals. In passive localization, the target does not require a dedicated device. Instead, the localization system infers the target's presence or location from changes in radio propagation caused by the target, such as shadowing, scattering, or reflection patterns observed at anchor nodes. This dissertation focuses on active localization for three practical reasons. First, active measurements are inherently associated with a target identity, simplifying multi-user operation, enhancing scalability, and reducing ambiguity in target association. Second, active links typically provide a more favorable link budget than passive localization, which relies on target reflections that can be weak and more sensitive to noise. Third, an established communication link enables (1) dynamic adaptation of measurement parameters to current channel conditions, such as channel or carrier selection, measurement duration, repetition, and beam direction, improving robustness to multipath, interference, and noise; (2) cooperative localization, where nodes exchange measurements or intermediate estimates and assist localization by acting as additional reference nodes; and (3) secure localization through authenticated exchanges and challenge-response procedures that reduce susceptibility to spoofing and replay attacks [20–22].

Outdoor localization is often well served by global navigation satellite systems (GNSS), but indoor environments require alternative solutions because satellite signals are strongly attenuated by roofs and walls, and indoor multipath propagation can further degrade accuracy. Additionally, GNSS receivers and antennas may be impractical for low-cost, low-power IoT devices [2, 3, 9, 10, 23]. As a result, indoor localization remains an active research and engineering challenge, requiring solutions that maintain accuracy in multipath-rich environments while meeting stringent IoT hardware and energy constraints.

1.2 Integrated Sensing and Communication

As demand for location awareness increases, wireless research and standardization are advancing toward integrated sensing and communications (ISAC), where sensing is no longer implemented as a completely separate system but is integrated with communication systems on shared hardware. ISAC aims to unify communication and sensing so that communication benefits from sensing-derived context, such as spatial awareness, link adaptation, and beam management, while sensing/localization benefit from communication signaling, scheduling, and infrastructure [24]. ISAC is widely discussed as an important component of beyond fifth and sixth generation wireless systems (5G and 6G) networks, motivated by the reuse of radio signals, spectrum resources, and transceiver platforms for both communication and sensing, which improves spectrum efficiency and reduces hardware duplication [25–28]. It is particularly relevant for IoT deployments, where scale, cost, and power constraints strongly favor reusing existing radio systems [5]. At the same time, ISAC introduces trade-offs in waveform design, transceiver architecture, and resource allocation because sensing and communication objectives are often not aligned [24, 29]. Communication design typically prioritizes throughput, latency, reliability, and energy efficiency through adaptive modulation, coding, and scheduling, while sensing prioritizes estimation accuracy and repeatability, often requiring deterministic and phase-stable waveforms, sufficient time–frequency diversity, and measurement patterns that support coherent integration. Bandwidth usage exemplifies misaligned objectives. Communication operates under regulated spectrum allocations and aims to maximize spectral efficiency, delivering as much throughput as possible within limited bandwidth. In contrast, sensing and localization benefit directly from larger effective bandwidth, as wider bandwidth improves time resolution and can increase robustness to multipath [25, 30, 31]. As a result, resource allocation and waveform choices optimal for communication systems can be suboptimal for sensing systems, and conversely, sensing-oriented systems can reduce spectral efficiency or increase overhead.

Trade-offs arising from the misalignment between sensing and communication objectives have led to a common classification of ISAC systems by design priority: communication-centric, radar-centric, or joint designs [24]. Communication-centric deployments are particularly attractive because sensing features can be added to widely deployed communication standards with minimal additional hardware modifications. However, communication-centric sensing is challenging because sensing performance requirements must be met with limited resources and standard constraints. A prominent example is Bluetooth Low Energy (BLE), where standardized (1) direction estimation enables angle-based localization and (2) channel sounding enables range-based localization. Both techniques are compatible with low-cost, battery-constrained, simple transceiver device architectures operating within standardized frequency bands [32]. Communication via BLE establishes the connection, exchanges sensing variables, and synchronizes the start of the sensing procedure. The communication procedure stops when the sensing procedure is performed. A similar trend is observed in Wi-Fi standardization, where IEEE 802.11 task group 802.11bf is considering sensing functionalities such as range, motion, and angle estimation, with the aim of extracting sensing information from communication waveforms and the corresponding channel frequency response (CFR) in realistic deployment environments [33–35].

1.3 Direction Estimation

Direction estimation is the process of determining the bearing of a signal source relative to a receiving node. Direction can be estimated using several measurement principles, depending on which signal parameters are observed. Power-based methods infer direction from received power variations measured with directional antennas, where the antenna radiation pattern is mechanically or electronically steered to scan azimuth and elevation and identify the direction that maximizes or minimizes received power. Frequency-based methods exploit Doppler shifts created by mechanical motion or electronically synthesized antenna rotation, where the Doppler signature depends on the direction of arrival (DoA). Time-based methods infer direction from relative delays, for example time-difference-of-arrival across spatially separated receiving nodes, or from delay differences across a sufficiently large sensor aperture. Phase-based methods infer direction from relative carrier-phase differences measured across spatially separated antenna elements, where the phase differences depend on propagation path-length differences associated with the DoA [36].

In indoor environments, multipath propagation and environmental dynamics can reduce the reliability of power-based and Doppler-based methods, while time-based direction estimation typically requires wide bandwidth and fast sampling clocks to achieve fine delay resolution. Phase-based DoA estimation using an antenna array (AA) is particularly attractive for indoor systems because narrowband radios can provide precise phase measurements, while the combination of spatial and frequency diversity improves robustness in multipath-rich environments. The spatial diversity needed to obtain DoA information is achieved by spatially separated antenna elements, which can be of the same or different types.

1.3.1 Direction Estimation with Single RF Chain

Practical realizations of phase-based DoA estimation with an AA depend on how the receiver samples the antenna elements. Simultaneous sampling across all antenna elements requires multiple RF chains, increasing cost and power consumption [37, 38]. Many low-cost and resource-constrained implementations therefore use a switched-antenna array (SAA) architecture, where a transceiver with a single RF chain is connected to one active antenna element at a time while the remaining elements are disconnected. The active element is then switched in time through an RF switch network to acquire phase samples across the array. The SAA architecture keeps hardware complexity and power consumption low while still enabling array-based direction estimation. It is for these practical reasons that the remainder of the dissertation on direction estimation focuses on phase-based DoA estimation using SAAs.

An example of standardized direction estimation with an SAA integrated into a communication protocol is the BLE Direction Finding feature, introduced in BLE version 5.1. This version specifies a link-layer protocol data unit that can include a Constant Tone Extension (CTE), during which a continuous wave (CW) is transmitted to support accurate direction estimation for low-cost IoT devices. BLE direction finding targets applications such as low-power indoor positioning and asset tracking, where direction estimates can be used directly for localization or can complement less reliable range measurements such as received signal strength indicator (RSSI) to improve robustness.

BLE direction finding supports two operation modes: angle of arrival (AoA) and angle of departure (AoD). In AoA, a transmitter sends a CW that is sampled at the receiver using a SAA. In AoD, the transmitter switches among multiple antenna elements while transmitting the CW, and the receiver estimates the direction using samples received with a single antenna element. The BLE standard defines when and how the CTE is sent and

partially specifies the in-phase and quadrature (IQ) sampling procedure. However, the standard does not specify the direction-estimation algorithms, the SAA design choices, or the antenna switching pattern (ASP), which defines the activation order of the available antenna elements as an ordered sequence of antenna element indices. As a result, real-world performance depends strongly on SAA design, switching strategy, and signal processing [39–42].

1.4 Range Estimation

Radio-based range estimation is the process of determining the distance between two wireless nodes, often an infrastructure node and a target device, using measurements derived from exchanged radio signals in the case of active localization. Range estimation can be implemented using several measurement principles, depending on available bandwidth, hardware capabilities, and protocol support.

Power-based methods that infer range from received power, such as RSSI, are widely used due to the widespread availability of the RSSI metric on most RF chipsets. However, methods that rely on path-loss models are strongly affected by multipath, shadowing, and device orientation, which cause large power fluctuations not correlated with distance. As a result, RSSI-based distance estimates are often unstable for fine-grained localization unless extensive environment-dependent calibration or fingerprinting is performed [2, 9, 43]. Time-based methods estimate range from signal propagation time, most commonly using the time of flight (ToF) method or its two-way variant, the round-trip time (RTT) method. These methods can achieve high estimation accuracy when sufficiently fine temporal resolution is available, typically through ultra-wideband signaling and high sampling clocks. However, this requires dedicated radios capable of ranging, a wider effective bandwidth, stricter regulatory constraints on transmit spectral density, and tighter timing requirements [3, 13, 23]. The RTT method does not require strict clock synchronization, but the measured round-trip time includes not only propagation time but also processing and scheduling delays, which impose practical accuracy limits on commodity radios [8]. Phase-based methods estimate range from carrier-phase measurements and are commonly referred to as phase-based ranging (PBR). Since carrier phase can be measured with high precision in narrowband radios, PBR enables accurate range estimation without requiring wideband waveforms or complex transceiver architectures [44, 45]. Frequency diversity also improves robustness in multipath-rich environments, which is beneficial for indoor localization. Given the practical suitability of PBR, the remainder of the dissertation on distance estimation focuses on this method.

1.4.1 Phase-Based Ranging

PBR is a distance estimation technique that relates the measured carrier phase to the propagation distance, as the phase of a wave evolves linearly with the distance it travels. In a single-frequency line-of-sight (LoS) scenario, the measured carrier phase is therefore directly related to the propagation distance, up to an unknown constant offset and modulo 2π. The inherent phase ambiguity limits the maximum unambiguous distance estimation range to the carrier wavelength, so practical implementations typically exploit frequency diversity by collecting phase measurements at multiple carrier frequencies in order to extend the maximum unambiguous distance interval. For uniformly spaced carriers with a frequency step Δf, the unambiguous distance interval extends to $c/\Delta f$, where c is the speed of light. In indoor environments, the measured phase is determined by the combined contributions of all multipath components, which can degrade estimation performance if

multipath is not properly taken into account. Frequency diversity also improves robustness in multipath-rich channels, since fades that strongly affect a narrow portion of the spectrum are unlikely to persist across the entire set of carrier frequencies. Therefore, increasing the total spanned bandwidth reduces the impact of deep fades on distance estimation. A practical limitation of using multiple carrier frequencies is that discontinuous transmissions on different carriers introduce random phase offsets due to phase-locked loop (PLL) re-locking, which corrupt the inter-frequency phase relationships caused by signal propagation and degrade distance estimation accuracy. These phase offsets can be suppressed by employing a two-way exchange between the ranging devices, commonly referred to as the initiator and the reflector [7, 46]. In this case, phase measurements are obtained at both devices and combined such that the per-frequency phase differences cancel the random PLL-induced phase offsets. This two-way PBR principle based on multiple carrier frequencies is commonly known as multi-carrier phase difference (MCPD) ranging.

Distance estimation from phase measurements across carrier frequencies can be performed using linear regression, where distance is estimated from the slope of the phase response versus frequency [47]. Although slope-based estimation is simple and computationally efficient, it can be biased in multipath channels because the measured phase is a superposition of all path components, causing the phase response to deviate from the ideal linear trend. Phase wrapping, outliers on deeply faded carriers, and frequency-dependent hardware distortions can further degrade the accuracy of the slope estimate. An alternative is to estimate distance using spectral analysis. IQ samples collected across carrier frequencies form a set of complex measurements representing the two-way CFR over the spanned bandwidth. Applying an inverse discrete Fourier transform (IDFT), typically implemented with an inverse fast Fourier transform (IFFT), yields an estimate of the two-way equivalent channel impulse response (CIR). The first dominant peak in the estimated CIR corresponds to the LoS component, and its delay relates to the propagation distance. Other high-resolution spectral estimation methods, such as Multiple Signal Classification (MUSIC), enable super-resolution delay estimation beyond the nominal IFFT bin width and provide good performance even in relatively low signal-to-noise ratio (SNR) conditions [48–52]. Besides model-based estimation methods, machine-learning-based approaches have also been proposed for distance estimation [44, 53].

Low energy consumption, low hardware complexity, and compatibility with existing narrowband standards make MCPD attractive for low-cost wireless systems [54–56]. BLE Channel Sounding feature is the standardized example of MCPD ranging, introduced in BLE version 6.0, released in September 2024. BLE Channel Sounding aims to provide secure and accurate fine ranging for low-cost IoT devices by standardizing a measurement procedure that can combine MCPD measurements with RTT estimation method to enhance resilience against relay attacks. The standard specifies how measurements are exchanged and reported but does not mandate a particular distance estimation algorithm, leaving the final distance estimation to the application layer.

1.5 Asynchronization Effect on Sensing Performance

In wireless sensing, synchronization refers to the degree to which spatially separated devices are aligned in time, frequency, and phase. Phase-coherent sensing estimation methods assume that sampling instants, carrier frequencies, and phase are aligned, either by using a shared reference clock or by relying on sufficiently accurate oscillators and stable timing relationships over the measurement interval. In practice, devices are often asynchronous, meaning each device uses an independent local oscillator and sampling clock, so the relative time, frequency and phase between devices are unknown to each other, differ across

devices, and can vary over time. Asynchronization is therefore the combined effect of time, frequency, and phase mismatch. The frequency mismatch is commonly expressed as carrier frequency offset (CFO). The time mismatch arises from both a clock offset and a clock drift, which manifest as a sampling-time offset (STO) and a sampling-frequency offset (SFO), respectively. Such mismatches can introduce deterministic phase drift that accumulates during sequential measurements, which can bias phase-based direction and ranging estimates.

While communication links typically tolerate larger residual synchronization errors through robust modulation, phase-based sensing can suffer large estimation errors even under moderate asynchronization [18, 43, 57]. Such sensitivity is especially problematic in ISAC designs, where sensing is added on top of an already functional communication technology whose synchronization requirements are typically less strict.

1.6 Motivation

Sensing is becoming a key capability in future wireless systems and standards. A rapid shift toward ISAC is now observed, driven by the **growing number of applications requiring location awareness** and the mutual benefits of communication and sensing. The ISAC trend is already evident in widely deployed wireless technologies, especially BLE and Wi-Fi, which are adding sensing and localization capabilities to established communication standards.

As the number of applications requiring location awareness increases, the demand for practical indoor localization systems continues to grow. Although accurate indoor localization systems exist, many solutions require complex, environment-specific installation procedures and depend on precise initial calibration. Maintaining high estimation accuracy often requires periodic recalibration because environmental changes, such as temperature and humidity variations, device aging, and physical changes in the environment, can affect hardware behavior and propagation conditions. The required installation effort and subsequent recalibrations limit scalability and increase operational costs. Large-scale deployments, therefore, require plug-and-play indoor localization and zero-touch provisioning to minimize deployment burden and maintenance effort for end users, while keeping total costs low to support scalability. **Achieving scalable, cost-effective deployments strongly motivates localization solutions implemented on low-cost, resource-constrained IoT devices and commodity transceivers deployed at scale.** However, IoT hardware constraints must be considered:

- limited energy and power resources,
- limited computational and memory resources,
- zero-touch operation, which requires avoiding costly calibration procedures,
- limited cost, often leading to the use of components with wide tolerances,
- limited size, space, and enclosure options, which constrain protective packaging solutions and increase exposure to environmental influences,
- limited wireless communication and sensing resources,
- limited interoperability across heterogeneous devices and physical-layer implementations.

It is therefore **necessary to understand how hardware non-idealities translate into estimation errors**, especially in systems based on low-cost components, where these non-idealities are **more pronounced and more susceptible to environmental conditions**. This understanding must then be **incorporated into system design and mitigation strategies** to improve robustness and maintain high accuracy without relying on calibration procedures.

Radio-based localization can be implemented in many ways as described above. For low-cost IoT indoor deployments, two phase-based approaches in the measurement stage of localization are especially promising: DoA estimation with SAA and MCPD ranging. Those approaches exploit spatial diversity across antenna elements and frequency diversity across multiple carrier frequencies, improving robustness to multipath while remaining compatible with narrowband, low-cost transceiver architectures. Both approaches rely on accurate phase measurements obtained from narrowband signals exchanged between devices, so **localization performance is fundamentally limited by the accuracy and stability of the measured phase used for DoA and range estimation**.

In DoA estimation with SAA, the antenna elements and RF-switch network constitute part of the receiver RF front end. As a result, RF path-length differences and coupling effects, including RF path coupling and mutual coupling between antenna elements, directly **distort the relative phases measured across the array**. Understanding how SAA RF non-idealities distort the measured phase and degrade DoA estimation is essential, because such effects can be **addressed during SAA design to reduce RF impairments** and to obtain DoA estimates that are less sensitive to phase-errors. Consequently, **costly and time-consuming calibration of produced SAAs can be reduced or eliminated** when the resulting performance already meets application requirements. DoA estimation performance also depends on SAA geometry and on signal-processing choices. One motivation of the dissertation is therefore to **quantify the DoA accuracy and precision achievable by a practical BLE direction-finding SAA receiver** under realistic indoor conditions, while avoiding calibration procedures.

Low-cost IoT devices also commonly use inexpensive crystal oscillators whose limited accuracy and stability, further affected by temperature variation, aging, and supply sensitivity, introduce CFO and sampling-clock mismatch [58–60]. CFO and timing mismatch are well-known issues in phase-coherent signal processing, and, as described above, even moderate impairments can produce phase errors that significantly affect estimation accuracy. DoA estimation with SAA relies on time-division multiplexing across antenna elements, while MCPD ranging relies on time-division multiplexing across carrier frequencies. **Phase measurements collected through sequential measurements procedure make both methods sensitive to timing and frequency mismatches** between devices, as additional phase progression accumulate between discontinuous measurement instants that is not attributable to the true DoA or range, and it therefore manifests as a phase error in the corresponding parameter estimate. **In SAA direction estimation, CFO and SFO distort phase progression across antenna samples and bias direction estimates** when sequential sampling (SS) is used, meaning antenna elements are activated sequentially in their spatial order, as typically done in practice [61–63]. **For MCPD ranging, clock drift and CFO, together with protocol timing and the use of a linear frequency sweep, introduce phase shifts that are correlated with distance-dependent phase terms, producing systematic bias in the distance estimate** [55, 64–66]. **An additional bias arises from the linear frequency dependence of CFO** in PLL-based RF frequency synthesis.

Two approaches have been reported to suppress the effect of phase errors induced by asynchronization on the estimation of the sensing-parameters. The first approach follows

the estimation-and-correction principle. In SAA-based DoA estimation, this is typically achieved by estimating the CFO from additional samples acquired on a reference antenna, then correcting the phase samples for the CFO-induced phase errors before DoA estimation [61–63]. In MCPD ranging, related work has proposed estimating the CFO or crystal-offset-related timing mismatch from additional samples acquired at a single frequency, followed by compensation of the measured phases [64–67]. The second approach relies on joint estimation of the sensing parameter and the nuisance parameter responsible for the phase error, for example, by jointly estimating DoA together with CFO [68–71]. Although both approaches reduce estimation bias, they require additional processing and are often associated with increased computational complexity, higher memory requirements, iterative or multidimensional optimization, and greater sensitivity to model mismatch. In addition, accurate estimation requires additional measurement time, which increases energy consumption and susceptibility to interference. An alternative approach was considered in [55], where timing diagram modifications were used to mitigate the CFO effect. However, this method relies on extra transmissions, which again increase the duration required for a single distance estimate.

The dissertation is motivated by the need for mitigation approaches that preserve phase-based sensing accuracy under realistic low-cost hardware non-idealities while remaining practical for IoT devices. Mitigation should reduce systematic bias without requiring additional RF chains, high sampling rate, heavy computation, or frequent calibration, and should remain effective under environmental variation that affects crystal oscillator performance. Mitigation must therefore remain effective at realistic CFO and timing-asynchronization levels because otherwise the resulting accuracy loss can limit practical usability in localization applications. If mitigation is sufficiently effective, the **oscillator requirements can be relaxed**, allowing the use of lower-grade crystal oscillators to reduce device cost while maintaining useful sensing performance.

1.7 Aims and Objectives

The aim of the dissertation is to **develop accurate DoA and distance estimation techniques for low-cost, resource-constrained wireless devices** that reuse communication-oriented radio architectures, consistent with the broader ISAC vision. Achieving high estimation accuracy requires **mitigating phase errors** introduced by inexpensive, non-ideal RF components to ensure robust sensing performance in real-world deployments. A second aim is to develop **robust estimation techniques that reduce or eliminate reliance on calibration procedures**, enabling practical deployments without costly and time-consuming per-device (re)calibrations and associated maintenance efforts.

To achieve the stated aims, the dissertation pursues several objectives. The overall objective is to examine how hardware non-idealities **distort phase measurements and introduce estimation bias in both SAA-based DoA estimation and MCPD ranging**. In the direction-estimation part of the dissertation, the first objective is to **assess the achievable DoA accuracy and precision** of practical single-RF-chain architectures that rely on antenna switching. This includes **designing an AA** suitable for single-RF-chain DoA estimation, with specifications that meet the requirements of the BLE direction-finding standard. A supporting objective is to **analyze which RF components and array effects contribute to phase distortion** and to incorporate that understanding into the AA design **to minimize phase distortion** and achieve the desired DoA estimation performance **without relying on costly and time-consuming array calibration**. The goal is to design a practical AA platform that is experimentally validated on low-cost hardware and is compatible with the BLE direction-finding standard.

The next objective is to **formalize and analytically derive the impact of oscillator-induced imperfections on phase-based estimation methods** that acquire phase samples sequentially in time, specifically across antenna elements in SAA-based direction estimation and across carrier frequencies in MCPD ranging. Based on the derived signal models that account for asynchronization, the objective is to **examine how CFO, SFO, and STO distort the measured phases and to identify the dominant bias mechanisms**. Building on this analysis, a subsequent objective is to **develop lightweight asynchronization mitigation approaches** that are feasible for low-cost embedded platforms in terms of computational complexity, memory footprint, measurement overhead, and energy consumption. The mitigation approaches aim to reduce the sensitivity to synchronization imperfections arising from oscillator performance variability, thereby reducing the need for recalibration and ensuring that estimation accuracy remains stable and robust over time. This work diverges from estimation-and-correction or joint parameter estimation approaches for asynchronization-induced phase shifts, which introduce computational complexity and increase measurement time. Instead, the goal is to reduce bias through ASP design strategies for DoA estimation with SAA, and through frequency switching pattern (FSP) and timing diagram (TD) designs for MCPD ranging.

The final objective is to **validate analytical models and mitigation approaches through numerical simulations and real-world experiments**. The simulations aim to quantify DoA and range accuracy under varying levels of timing asynchronization, CFO, frequency-dependent CFO, and noise. The experiments aim to validate the analytical predictions and simulation results by performing parameter sweeps of oscillator-related impairments in controlled measurement setups that isolate asynchronization effects on the estimated parameter and by using representative embedded platforms. This enables direct validation of the effectiveness of mitigation approaches.

1.8 Hypotheses

This dissertation is structured around a set of hypotheses that reflect the technical questions addressed in the included papers. The hypotheses formalize the main claims about achievable sensing performance under hardware non-idealities that introduce phase errors, dominant bias mechanisms caused by CFO and timing asynchronization, and mitigation through optimized antenna-switching, frequency-switching, and TD design strategies. The corresponding statements are as follows:

H1 **A practical BLE direction-finding compatible SAA for single-RF-chain systems enables sub-degree DoA estimation accuracy suitable for indoor localization on low-cost IoT hardware without requiring array calibration.**

H2 **In SAA-based DoA estimation and MCPD ranging, sequential phase sampling across antenna elements or carrier frequencies, in the presence of CFO and timing asynchronization, induces phase shifts that can correlate with propagation-induced phase shifts, resulting in systematic estimation bias.** The dominant bias terms can be identified through analytical analysis of the derived signal models.

H3 **In SAA-based DoA estimation, bias caused by CFO, SFO, and sequential phase sampling across antenna elements can be efficiently mitigated by optimally switching between antenna elements**, which decouples asynchronization-induced phase terms from DoA-dependent phase terms.

H4 In MCPD ranging, bias caused by CFO, timing asynchronization, and linear frequency sweep can be efficiently mitigated by optimally choosing the order in which carrier frequencies are used during the MCPD procedure, using an FSP that decouples asynchronization-induced phase terms from propagation-induced phase terms.

H5 A linearly frequency-dependent CFO introduces systematic bias in MCPD ranging with the standard TD, which can be efficiently mitigated through appropriate TD design.

The hypotheses are tested through analytical derivations, simulation studies, and controlled experiments.

1.9 Scientific Contributions

The dissertation contributes to phase-based approaches in the measurement stage of localization with commodity transceivers by combining practical hardware development, analytical bias analysis based on the signal model, and lightweight mitigation strategies that maintain sensing performance under low-cost oscillator behavior. Figure 1.1 summarizes how the papers included in the dissertation relate to the scientific contributions and to the two measurement stages of localization addressed: DoA estimation with SAA and distance estimation with MCPD ranging. The main scientific contributions of the dissertation are:

SC1 Design workflow and experimental evaluation of a practical BLE direction-finding compatible SAA platform, with quantified real-world DoA performance in indoor and outdoor environments.

SC2 ASP design for robust DoA estimation with SAA under asynchronization. This contribution consists of four parts:

- **SC2.1** Formulation of DoA estimation bias caused by asynchronization when SS is used.
- **SC2.2** Introduction of a mitigation approach that suppresses SS-induced estimation error under asynchronization by rearranging the antenna activation order within the ASP.
- **SC2.3** Design and formulation of optimized ASPs.
- **SC2.4** Evaluation of optimized ASPs through numerical simulations under different asynchronization and noise levels, and experimental validation using controlled CFO sweeps.

SC3 FSP design for robust MCPD ranging under asynchronization. This contribution consists of four parts:

- **SC3.1** Derivation of an MCPD ranging signal model that incorporates oscillator-related impairments and analytical identification of dominant bias mechanisms under asynchronization.
- **SC3.2** Introduction of a mitigation approach that suppresses linear-frequency-sweep-induced estimation error under asynchronization by rearranging the carrier-frequency order in the FSP.
- **SC3.3** Design and formulation of a set of novel FSPs.

SC3.4 Evaluation of the proposed FSPs through numerical simulations under different asynchronization and noise levels, and experimental validation using controlled CFO sweeps.

SC4 TD optimization to mitigate frequency-dependent CFO bias in MCPD ranging. This contribution consists of three parts:

SC4.1 Identification and modeling of frequency-dependent CFO as a systematic bias mechanism in MCPD ranging.

SC4.2 Design and formulation of TDs that suppress frequency-dependent CFO effects on distance estimation.

SC4.3 Evaluation of proposed TDs effectiveness through simulations under different asynchronization and noise levels, and experimental validation using controlled CFO sweeps.

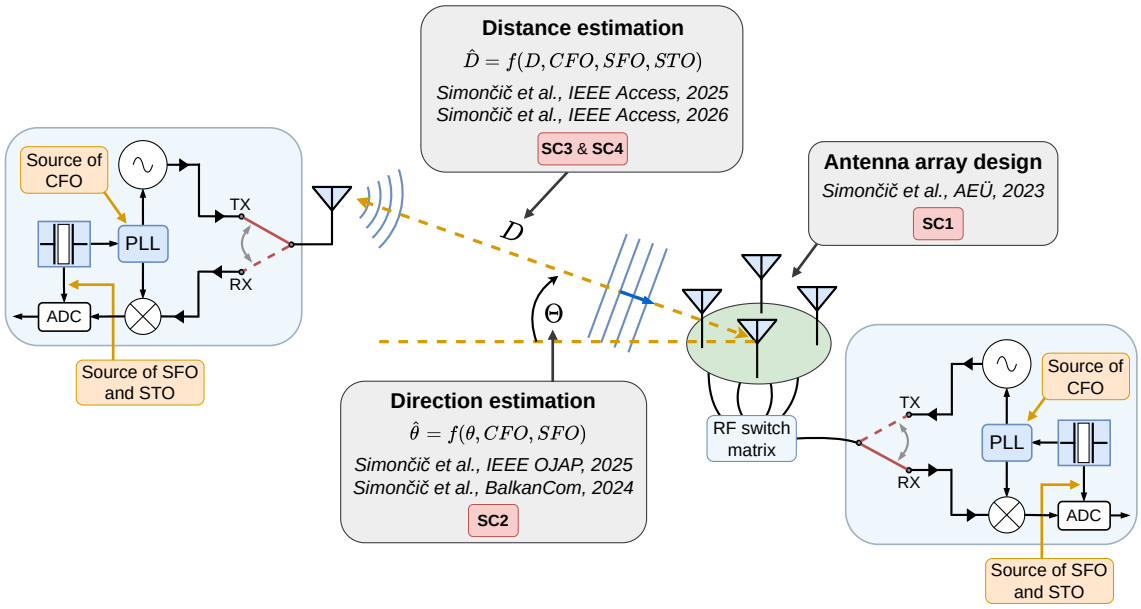


Figure 1.1: Conceptual visualization of DoA estimation using SAA and MCPD ranging, including the transceiver architecture and the source of asynchronization between devices. Papers included in the dissertation and related scientific contributions are mapped to the corresponding functional elements of the system.

1.10 Dissertation Structure

The dissertation begins with an introduction and motivation that place indoor localization in the broader context of IoT deployments and radio-based sensing. Direction and distance estimation are then introduced as the two main technical topics of the dissertation. The introductory chapter also outlines the motivation, research objectives, hypotheses, and main scientific contributions.

The main body of the dissertation consists of four chapters that include five published papers, of which four are peer-reviewed journal articles and one is a peer-reviewed conference paper. Each paper is presented as a self-contained section. Before each paper, a short preface provides the required background and clarifies which hypotheses and scientific

contributions are addressed. The dissertation first focuses on phase errors that translate into DoA errors in SAA receivers, and then on phase errors that translate into distance estimation errors in MCPD ranging.

Chapter 2 focuses on BLE direction-finding hardware and presents the design and performance evaluation of a SAA receiver suitable for single-RF-chain systems. The chapter covers antenna array design choices, RF switch network implementation aspects, and the impact of RF non-idealities on phase measurements, as well as DoA estimation performance evaluation in controlled and real propagation environments. The main material corresponds to the paper titled *Direction of arrival estimation for BLE: Antenna array design and evaluation* [72].

Chapter 3 addresses the sensitivity of DoA estimation with SAA to asynchronization and introduces ASP design as a lightweight mitigation approach suitable for low-cost IoT devices. The chapter includes two papers, each presented in its own section: *Optimizing Switching Pattern to Reduce CFO Effects in Single RF Chain Direction Finding Systems* [73] and *Experimental Evaluation of Enhanced Antenna Switching for CFO Mitigation in DoA Estimation* [74]. The first paper introduces ASP design as a mitigation approach to asynchronization-induced estimation bias and provides initial simulation-based validation. The second paper extends the analysis and ASP variants, and provides extensive validation through simulations and experiments.

Chapter 4 shifts from direction estimation to PBR, focusing on asynchronization effects in MCPD distance estimation and on mitigating these effects through FSP design. The main material for this chapter is the paper *Optimizing Frequency Switching Pattern to Reduce Asynchronization Effect in MCPD Ranging Systems* [75].

Chapter 5 continues the discussion of PBR by considering frequency-dependent CFO as a source of distance estimation bias and developing TD optimization to mitigate this bias. In this chapter the paper included is *Mitigating Frequency Dependent Carrier Frequency Offset in Multi-carrier Phase Difference Ranging through Timing Diagram Design* [76].

The dissertation concludes in Chapter 6 with a discussion of the validated hypotheses and the main scientific contributions, and an outlook on future research directions toward robust phase-based sensing.

Figure 1.2 summarizes the conceptual structure of the dissertation in terms of the research questions addressed, the corresponding objectives and hypotheses, and the resulting scientific contributions.

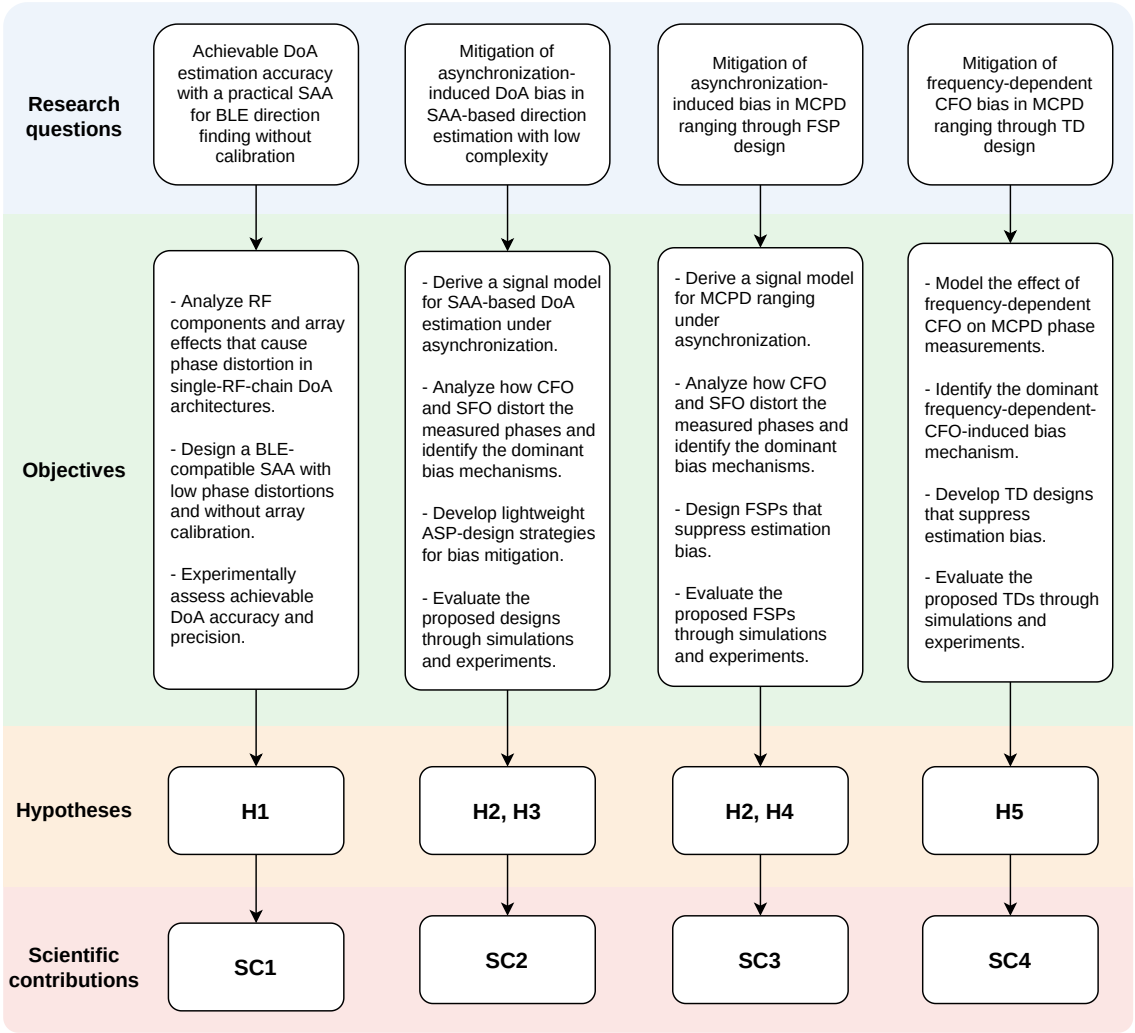


Figure 1.2: Conceptual structure of the dissertation and the relation between the research questions, objectives, hypotheses, and scientific contributions.

Chapter 2

Design and Validation of a Switched Antenna Array for BLE Direction Finding

Publication included in this chapter:

A. Simončič, T. Javornik, A. Sešek, and A. Hrovat, "Direction of arrival estimation for BLE: Antenna array design and evaluation," *AEU - International Journal of Electronics and Communications*, vol. 168, p. 154 722, Aug. 1, 2023, ISSN: 1434-8411. DOI: 10.1016/j.aeue.2023.154722

In phase-based DoA estimation, a CW impinges on the AA, and the receiver estimates the DoA from phase differences measured across spatially separated antenna elements. These phase differences arise from direction-dependent propagation path-length differences. The estimation algorithm then compares the measured phase differences with the array phase response determined by the array geometry. Accurate BLE direction-finding with single-RF-chain receivers therefore requires an SAA that preserves inter-element phase differences and does not introduce additional phase-difference distortion across antenna elements. Any element-dependent phase offsets unrelated to DoA can bias the estimate, and if such distortions are not sufficiently minimized, per-path calibration after AA manufacturing becomes necessary, which is costly, time-consuming, and sensitive to environmental variation, such as humidity-driven changes in effective substrate permittivity. The BLE direction-finding standard specifies the IQ sampling procedure but does not define the design of SAA, nor the DoA estimator, so both are left to the implementer and both strongly influence achievable accuracy and precision. This chapter focuses on SAA design choices that minimize calibration needs by reducing phase distortion differences at the hardware level in single-RF-chain architectures compatible with the BLE direction-finding standard.

Phase shifts introduced by the SAA are unavoidable because the RF path from each antenna element phase center to the radio RF front end, through the switching network, imposes an electrical length that causes a phase shift. The critical requirement is phase-shift equality across switched paths, or differences equal to integer multiples of 2π, so that the DoA-dependent phase differences across antenna elements are not distorted. A practical implication is the use of the same antenna type with matched phase response and a similar electromagnetic environment around each antenna element, so that antenna coupling and edge effects do not create element-dependent radiation pattern and phase distortions. Periodic array geometries, such as a uniform circular array (UCA), reduce element-to-element variability because each element has an equivalent electromagnetic neighborhood. In a

uniform linear array (ULA), passive elements at the ends can approximate periodicity for the active subset, at the cost of increased array size.

Another potential source of phase distortion is RF path coupling within the switching network and its interconnections. The topology and layout of the switching network are determined by the available RF switch components and their properties, including the number of RF ports per device, which sets the number of switching stages, and the physical placement and orientation of RF ports, which limit routing symmetry across switched paths. Additionally, different phase responses of RF switches can introduce path-dependent phase distortion, which motivates the use of the same components and implementations across switched paths so that each path experiences comparable phase impairments. Achieving matched phase distortion across all switched paths is therefore challenging, so RF-routing asymmetries and coupling effects must be minimized through careful RF design in order to keep DoA bias below the required level without relying on calibration.

The remainder of this chapter presents the included paper, which covers the BLE direction-finding context, the SAA design workflow, and its evaluation through real-world experiments. This includes array geometry selection, simulation-driven optimization of array parameters, switching network design, high-frequency RF path design, antenna selection and tuning, simulation of radiation pattern distortions caused by the proximity of antenna elements to the AA edge and to adjacent antenna elements, and validation through outdoor and indoor measurements, including channel diversity analysis to mitigate the multipath effect on DoA estimation. Together, these elements constitute scientific contribution **SC1**. By demonstrating that a practical SAA can achieve the target DoA estimation accuracy when the array geometry is appropriately selected and phase-distortion differences across the switched RF paths are minimized, the included paper addresses hypothesis **H1**.

Int. J. Electron. Commun. (AEÜ) 168 (2023) 154722

Contents lists available at ScienceDirect

Int. J. Electron. Commun. (AEÜ)

journal homepage: www.elsevier.com/locate/aeue

Regular paper

Direction of arrival estimation for BLE: Antenna array design and evaluation ☆

Aleš Simončič [a,b,*], Tomaž Javornik [a,b], Aleksander Sešek [c], Andrej Hrovat [a,b]

[a] Jožef Stefan Institute, Jamova cesta 39, Ljubljana, SI-1000, Slovenia
[b] Jožef Stefan International Postgraduate School, Jamova cesta 39, Ljubljana, SI-1000, Slovenia
[c] Faculty of Electrical Engineering, Laboratory for Integrated Circuits Design, Tržaška 25, Ljubljana, SI-1000, Slovenia

ARTICLE INFO

Keywords:
Antenna array
RF switch
Direction of Arrival
Bluetooth Low Energy
Phase difference
MUSIC

ABSTRACT

The use of smart antenna arrays in wireless communication systems is becoming increasingly popular, as they improve the performance of the radio link and allow the integration of communication and sensing functions. In this paper, we present the design and performance evaluation of a uniform circular antenna array (UCAA) with 12 monopole antennas and RF switches to select the active antenna for the signal direction of arrival (DoA) estimation. The antenna configuration was optimized through simulations for a different number of antennas and antenna array radius. The frequency tuning of the antennas considered the coupling of the active antenna with adjacent antennas. The performance of the antenna array was evaluated by (1) simulations that examined the proximity of the antenna to the edge of the antenna array and the influence of adjacent antennas on the performance of the active antenna, and (2) measurements in outdoor and indoor environments. The results of the simulations show that antenna coupling can cause nulls in the radiation pattern, which affects the DoA estimation by reducing the signal-to-noise ratio. In a semi-controlled environment, we achieved a DoA estimation error of less than 1 degree by using the Bluetooth Low Energy (BLE) Angle of Arrival feature.

1. Introduction

In the last decades, the trends in the development and design of wireless communication systems are heading toward the usage of multiple smart antenna arrays at the base station and mobile terminal as well. The usage of antenna arrays with appropriate steering results in an improved range of the communication system, lower time dispersion of the received signal, and increase signal-to-noise (SNR) and signal-to-interference ratio (SIR) [1]. Another important antenna array functionality is the radio signal direction of arrival (DoA) estimation. DoA is commonly applied to steer the main beam of the antenna array toward the user to improve the radio link, or as an interference mitigation technique by steering the antenna nulls toward interfering signals [2].

However, DoA estimation is not only applied to communications, but it is widely used in navigation, localization, military application, radio astronomy, weather monitoring, autonomous vehicles, security, surveillance, tracking wildlife, industrial automation, sports analytics, etc. The DoA accuracy, resolution and update rate depends on the application requirements, from high-precision military and professional systems to less demanding requirements for general public use.

The Bluetooth Low Energy (BLE) wireless technology, from version 5.1, specifies a new link-layer protocol data unit (PDU) that can be used to determine the direction of a transmitter [3]. Depending on the configuration, the PDU may contain additional data known as Constant Tone Extension (CTE), which consists of binary 1 symbols whose length is predefined according to system requirements and can vary from 16–160 μs. Since the signal is not modulated during this period, an efficient implementation of DoA algorithms based on measured phase differences from spatially separated antennas can be applied. Integrated circuits that support BLE-compatible wireless peripherals are typically designed to be cost-effective, often resulting in the implementation of a single radio frequency signal chain. When reception of a signal with multiple antennas is required, as is the case with DoA estimation, an additional antenna selection circuit with RF switches must be implemented. The resulting design for DoA estimation is still able to maintain its low complexity, low cost and low power consumption.

BLE 5.1 opens up the possibility of integrating DoA capabilities into BLE-equipped devices for potential localization applications. However, such a device must be equipped with an antenna array. Therefore, the aim of this work was to develop, design, and evaluate a low-cost antenna array system for DoA estimation that utilizes only one RF

☆ This document is the results of the research supported by ARRS, Slovenia [grant numbers J2-2507, J2-3048, P2-0016, J2-4461, and PR-12348].
* Corresponding author at: Jožef Stefan Institute, Jamova cesta 39, Ljubljana, SI-1000, Slovenia.
E-mail address: ales.simoncic@ijs.si (A. Simončič).
URL: https://e6.ijs.si/people/ales-simoncic (A. Simončič).

https://doi.org/10.1016/j.aeue.2023.154722
Received 27 February 2023; Accepted 13 May 2023
Available online 18 May 2023
1434-8411/© 2023 The Author(s). Published by Elsevier GmbH. This is an open access article under the CC BY-NC-ND license (http://creativecommons.org/licenses/by-nc-nd/4.0/).

signal chain which is compatible with BLE technology. Although the method was validated using BLE technology, it can be applied to any communication technology operating in the 2.4 GHz band that provides the functionality of controlling antenna switches and transmitting continuous wave tones.

The main contributions of this work are (1) design workflow of the uniform circular antenna array (UCAA) for the DoA estimation with sub-degree accuracy, (2) implementation of RF switch matrix and the RF part of the design, (3) the analysis of antenna array non-idealities, such as the proximity of the antenna to the antenna array edge and the influence of the nearby antennas to the antenna performance and (4) the DoA estimation performance evaluation in real propagation environments.

The organization of this paper is as follows. After the introduction, an overview of the related work is given in Section 2. Section 3 presents the advantages of the selected antenna array configuration, followed by the description of the printed circuit board (PCB) design, antenna selection and frequency tuning. Next, the influence of parasitic antennas is investigated through simulations in Section 4 which includes also the description of the applied DoA algorithm and the evaluation of the system. The paper concludes with a summary and discussion.

2. Related work

The optimal locations of the antennas in the antenna array must be determined for the best performance of the desired application. In practice, three types of antenna arrays are commonly used: uniform linear arrays (ULA), uniform rectangular arrays (URA) and uniform circular arrays (UCA) [4]. In mentioned configurations, the antennas are uniformly arranged in a straight line, a two-dimensional grid, and a circle, respectively. In the works listed below, the authors have used various techniques to find such an optimal configuration of the antenna array.

In main beam steering applications, the radiation pattern depends on the position of the antennas and their weighting (phase delay and signal attenuation at each antenna). In [5], the authors used two algorithms to optimize the radiation pattern, namely Multiverse Optimiser (MVO) and Modified MVO (MMVO), to determine the antenna positions and signal amplitudes of the UCA array. Similarly, in [6], the authors used the Artificial Bee Colony (ABC) algorithm to optimize the phases and switch-on time of the time-modulated UCA array and in [7], they used an efficient variant of the differential evolution (DE) algorithm, namely sub-populated differential evolution (subDE) for the null synthesis of the time-modulated UCA array.

A combination of the induced electromotive force (EMF) method and a genetic algorithm was used in [8] to optimize the excitation of each antenna. Using the EMF method, they calculated and compared the mutual coupling impedances at different distances between the two dipoles. A vector analyzer was used to generate a signal that was delayed and attenuated for each antenna in the four-dipole antenna array. Finally, the optimized radiation patterns from the simulations were compared with the measured radiation patterns.

The authors in [9] proposed a UCAA design in which the distance of the antennas from the center of the antenna array (R) can be changed dynamically during signal reception. Using the designed antenna array, they determined the DoA of the signal using the MUSIC algorithm. They showed that even a small change in the carrier frequency of the signal can result in a significant decrease in the resolution and accuracy of the algorithm, while the dimensions of the antenna array remain unchanged. By dynamically varying the distance R in response to the change in carrier frequency, they ensured the optimal spacing of the antennas.

Another approach to optimizing antenna arrays is a simulation, which allows engineers to test and evaluate the performance of an antenna array before it is built. By simulating the behavior of an antenna array, engineers can identify potential problems and optimize the design to improve performance by exploring a wide range of design options and evaluating the tradeoffs between them, saving time and manufacturing costs compared to designing real hardware for each development iteration. In [10], the authors used the Altair FEKO software to analyze how the different number of antennas affects the radiation pattern of a single antenna in UCA configuration and consequently the DoA estimation using a neural network. The training data generated using Altair FEKO software included voltage vectors at the antenna ports due to an incident plane wave impinging from different azimuth angles. The authors in [11] designed a switched-mode UCAA. In HFSS software, they analyzed the effect of GND splits between two adjacent antenna elements on directivity, bandwidth, and gain. In [12], the authors simulated the antenna array ULA in the Matlab simulation environment. They investigated how the key parameters (number of antennas, antenna spacing (D), number of incident signals, and number of data samples) affect the calculated MUSIC spectrum. By increasing the number of antennas and the distance between them, higher accuracy and resolution can be achieved. This work has been the basis of our antenna array design workflow. From the simulation results, the optimal key parameters, such as the number of antennas and the distance between them, can be derived.

3. The design of antenna array

An antenna array was designed to measure the phase differences caused by different propagation times of a signal to the antennas for DoA estimation. First, the configuration of the antennas was selected. Then, the model of the antenna array was simulated to determine the optimal number of antennas and their physical spacing. Based on the simulation results, the antenna array PCB with a suitable RF switch matrix was designed to be compatible with radios that have only one radio frequency signal chain, which is achieved by switching an active antenna. Finally, the antennas were tuned to the selected frequency band.

3.1. Antenna array configuration

The antenna array configuration impacts its performance and the design of the switching system. The UCA configuration was selected, due to its capability to determine both the azimuth and elevation angle, while the ULA antenna array is capable to determine only the azimuth. When calculating the elevation angle, each solution is limited to one of the subspaces defined by the plane of the antenna array. Due to the circular symmetry, the UCA configuration has additional advantages compared to ULA, namely (1) the design and implementation of the RF links between antennas and switches is less complex, resulting in a design with lower phase difference errors, and (2) the effect of adjacent parasitic antennas on the active antenna is the same for all antennas. The latter is not the case for the ULA configuration, so the phase centers of the antennas may vary, resulting in a phase difference and thus an error in the DoA calculation. Fig. 1 shows the schematics of the designed UCA antenna array.

The optimal number of antennas and radius of the antenna array were determined by simulations in the Matlab[1] environment, simulating the signal impinging on the antenna array and estimating its DoA using the MUSIC algorithm [13]. The result of the algorithm is a spectrum that contains a peak at an angle corresponding to DoA due to the orthogonality of the steering vector and the noise subspace. The algorithm key performance indicators are its ability to simultaneously detect the number and direction of multiple signals, high accuracy, low sensitivity to noise, high resolution, and the ability to update the estimate of DoA in real time using high-speed technologies such

[1] https://www.mathworks.com/products/matlab.html.

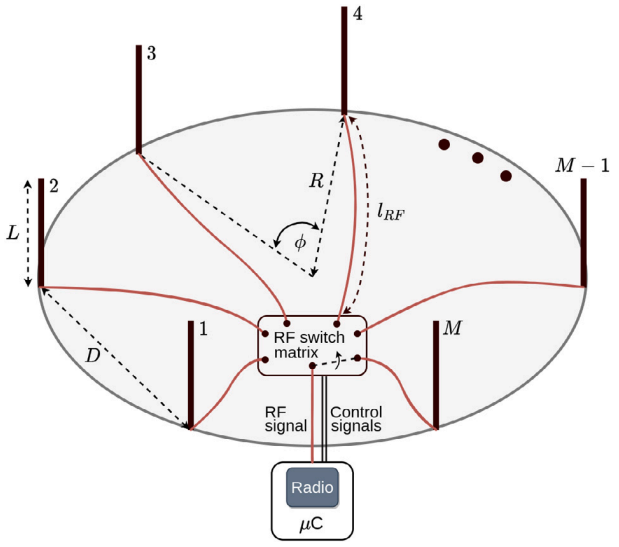


Fig. 1. The designed UCA antenna array schematics.

as a digital signal processing unit (DSP) and a floating point unit (FPU) [13–15].

The spectrum of the MUSIC algorithm was compared for a different number of antennas and different antenna array radii. To determine the influence of each parameter on calculated MUSIC spectrum, we analyzed them separately by varying one parameter and fixing the value of another. A signal of 10 IQ samples was generated for each antenna, to which the Additive White Gaussian Noise (AWGN) was added with the signal-to-noise ratio (SNR) being 10 dB.

Fig. 2 shows the results of the calculated MUSIC spectrum for a range of $[-180°, 180°]$ azimuth angles for different antenna array radii with a fixed number of antennas (12) and two transmitters with azimuth directions of $-30°$ and $30°$, where r_{max} denotes the maximum radius of the antenna array corresponding to a distance between antennas of $\lambda/2$. It can be seen from the graph that with the enlarging radius the resolution of the DoA estimation is increasing. Very similar results are obtained with a different number of antennas. The distance between the antennas is proportional to the radius of the antenna array. The maximum distance is limited by the periodic properties of the trigonometric functions in the steering vector and is $\lambda/2$. If a larger distance is used, multiple solutions are acquired. The condition can be interpreted as a spatial interpretation of the temporal signal sampling, where the Nyquist condition must be satisfied for a complete reconstruction of the signal. Therefore, the highest resolution is achieved when the antennas are separated by $\lambda/2$. With a larger distance between the antennas, the mutual interference of the antennas and the influence of multipath signal propagation are also reduced. On the other hand, a larger distance increases the dimensions of the PCB and thus the price and practicality.

Fig. 3 shows the results for a different number of antennas with two transmitters at azimuth of $-20°$ and $20°$. The radius corresponds to the distance between the antennas set to $\lambda/2$. At first glance, the results show that increasing the number of antennas improves angular resolution. A more detailed analysis showed that this depends on the direction of the transmitters, the distance between them, noise, and the number of collected IQ samples. In some cases, higher resolution can be achieved with fewer antennas because noise is added in the simulation, making the simulation nondeterministic and possibly biasing a particular solution, as seen in Fig. 3 for 12 and 14 antennas.

To determine the optimal number of antennas, we compared the calculated spectrums for different directions of the transmitter over the entire 360° azimuth range in a step of 1°. The computed spectrum was

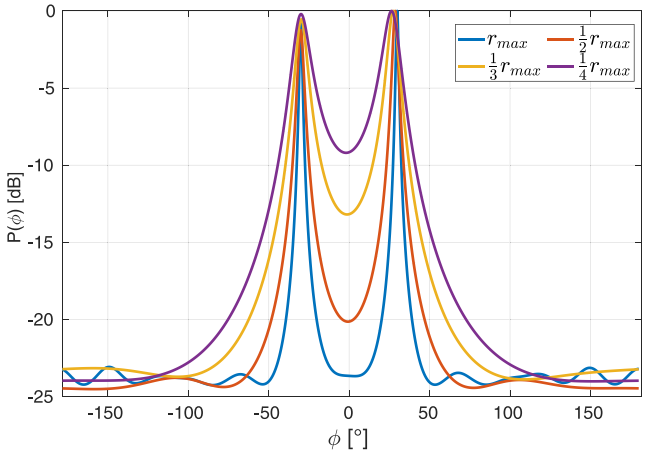


Fig. 2. Calculated MUSIC spectrums with two transmitters for different antenna array radii. r_{max} is the maximum radius of the antenna array at which the antennas are separated by $\lambda/2$.

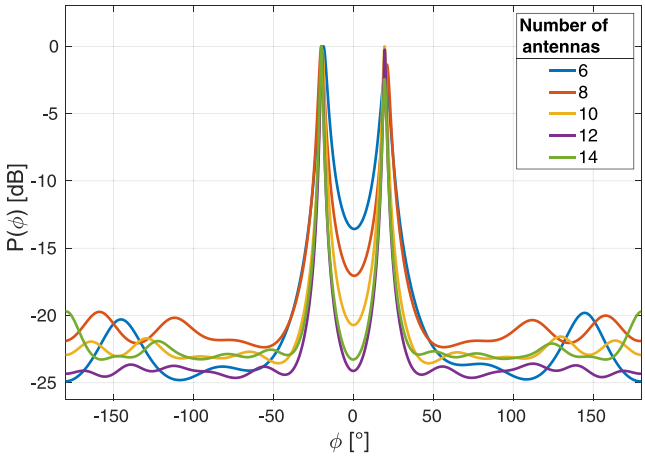


Fig. 3. Calculated MUSIC spectrums with two transmitters for a different number of antennas. The antennas were $\lambda/2$ apart.

the input to the objective function, which rewards correct estimate, a high dynamic range between the noise floor and peak value, and a narrow peak at an angle corresponding to the DoA. The cost values obtained from the objective function were added for all transmitter directions. The simulation was run several times with different seed values for noise generation to reduce a possible bias of the result in favor of a certain number of antennas. The results of the calculated cost values show that better performance is achieved with an increasing number of antennas, as can be seen in Fig. 4. The simulation was also performed using two transmitters with different angular spacings, from 10° to 180°, giving similar results.

A simulation, similar to the cost function calculation, was also performed for the calculation of the root mean square error (RMSE) of the DoA estimation for different directions of the transmitter over the entire 360° azimuth range in a step of 1°. The results, shown in Fig. 5, indicate that the RMSE decreases as the number of antennas increases. Although there is no significant difference between the errors for $8-14$ antennas with 10 IQ samples, the errors increase with a smaller number of IQ samples. In localization applications, for a given DoA error, the position error of the tag increases with the distance between the tag and the anchor. For example, if the distance between the anchor and the tag is known to the positioning system and is 15 m, the position estimate error would be approximately 0.5 m for a DoA error of 2°. In this case, the number of antennas would need to be 12 or more to

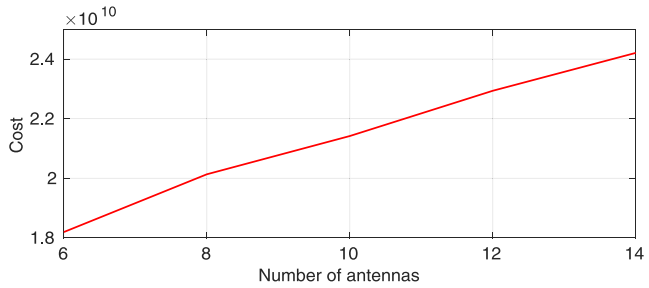


Fig. 4. Calculated cost values for a single transmitter with DoA over the entire azimuth range in the step of 1° for a different number of antennas. The simulation was repeated 50 times with different seed values for random number generation.

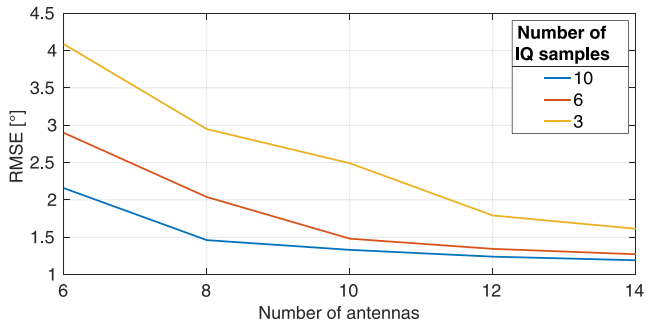


Fig. 5. Calculated RMSE values for a single transmitter with DoA over the entire azimuth range in the step of 1° for different number of antennas. The simulation was repeated 50 times with different seed values for random number generation.

achieve a position estimate error of less than 0.5 m with at least 3 IQ samples per antenna.

In addition to the azimuth angle also the effect of the elevation angle on DoA estimation was analyzed. Fig. 6 shows MUSIC spectrums for signals with fixed azimuth angle (0°) and different elevation angles impinging on the antenna array with 12 antennas. $\theta = 0°$ corresponds to the zenith direction (the elevation angle corresponds to an angle equal to $90° - \theta$). The MUSIC spectrum was calculated only by iterating the azimuth directions with a fixed θ angle of 90°. It can be seen that with the decreasing θ angle, the noise floor of the MUSIC spectrum increases. At θ angles of approximately 45° and less, the true value of DoA can no longer be determined. The results show that the correct azimuth angle can be determined when the θ angle is greater than approximately 45°. The findings are particularly useful in applying solutions to low-cost devices with insufficient computational power to simultaneously iterate azimuth and elevation angles.

To achieve the highest possible resolution and accuracy with a circuit size still acceptable for stationary use applications, we chose an antenna array with 12 antennas and an antenna spacing of $\lambda/2$. The antennas are positioned 115 mm from the center of the antenna array. To ensure sufficient grounding for monopole antennas, an additional area around the antennas with a radius of $\lambda/4$ is added according to [16] for the smallest but still acceptable ground size. As described later in Section 3.3, the antennas were frequency tuned by adjusting their length, considering also the reduced ground size. It should be noted that the minimum ground size of $\lambda/4$ extends only in the direction of the PCB edge and is larger in other directions. The diameter of the PCB is therefore 292 mm.

The active antenna (low insertion loss between the antenna and RF output of the antenna array) is determined by the control signals provided to the RF switches that route the RF signal through the transmission paths. Since the designed antenna array has 12 antennas, the RF switch matrix must be designed to route each of the 12 inputs to an output. This can be achieved in various ways, depending on the

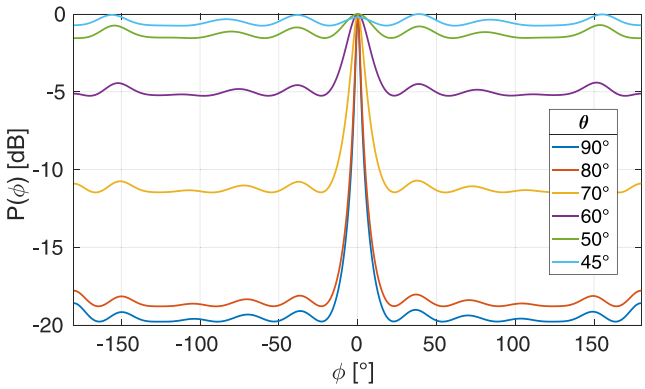


Fig. 6. Calculated MUSIC spectrums iterating azimuth angles between $[-180°, 180°]$ of 6 signals with different elevation angles.

number of inputs and outputs of the selected switches. However, to ensure that all 12 paths have the same phase delay, the RF signal must pass through the same number and type of RF switches for each path. In the selection of a suitable switch, the following characteristics were preferred:

- the switching speed is <1 μs due to the length of the switching sections in the CTE of BLE,
- low insertion loss (<1 dB for the entire BLE frequency band) and
- high isolation (RFC to RF1,2,3,4) > 30 dB.

In addition, the switch must be absorbing, which means that the received signal is terminated at the inactive antennas with the matched load impedance to prevent an open transmission line from resonating. The two-level switch matrix was designed with SKY13575-639LF SP4T RF switches from Skyworks[2] to obtain the desired number of different RF paths. The control signals for switches are provided to the PCB via the GPIO header.

3.2. PCB design

When designing the PCB we paid special attention to the precise positioning of the RF components on the PCB, the overall symmetry and the design of the high-frequency lines (HF). To avoid introducing additional phase differences by the hardware, the HF lines from the transceiver to the antennas must be the same length or may differ by multiple wavelengths. HF lines are designed as microstrip lines with standard 50 Ω impedance. Although a grounded coplanar waveguide (GCPW) provides better isolation to adjacent conductors due to the lower dispersion of electric field lines, a microstrip line provides lower losses because a greater portion of the electric field is in the air rather than in the laminate. The relatively large dimensions of the PCB allow larger spacing between the HF lines, which ensures adequate isolation. The impedance of the microstrip line is mainly influenced by the thickness and dielectric constant of the laminate. Both of these data were obtained from the PCB manufacturers, and the most suitable PCB stack up was chosen where the width of the HF line is close to the width of the selected DC voltage blocking capacitors to minimize impedance jumps and thus reflections. The FR4 laminate was chosen due to acceptable performance in the 2.4 GHz frequency band, and the moderate price compared to special HF laminates (e.g., Rogers). Using the KiCad[3] calculator and approximate values for the dielectric constant and loss tangent at 2.4 GHz, we calculated the signal attenuation of the

[2] https://www.skyworksinc.com/-/media/SkyWorks/Documents/Products/2201-2300/SKY13575_639LF_203270D.pdf.

[3] https://www.kicad.org/.

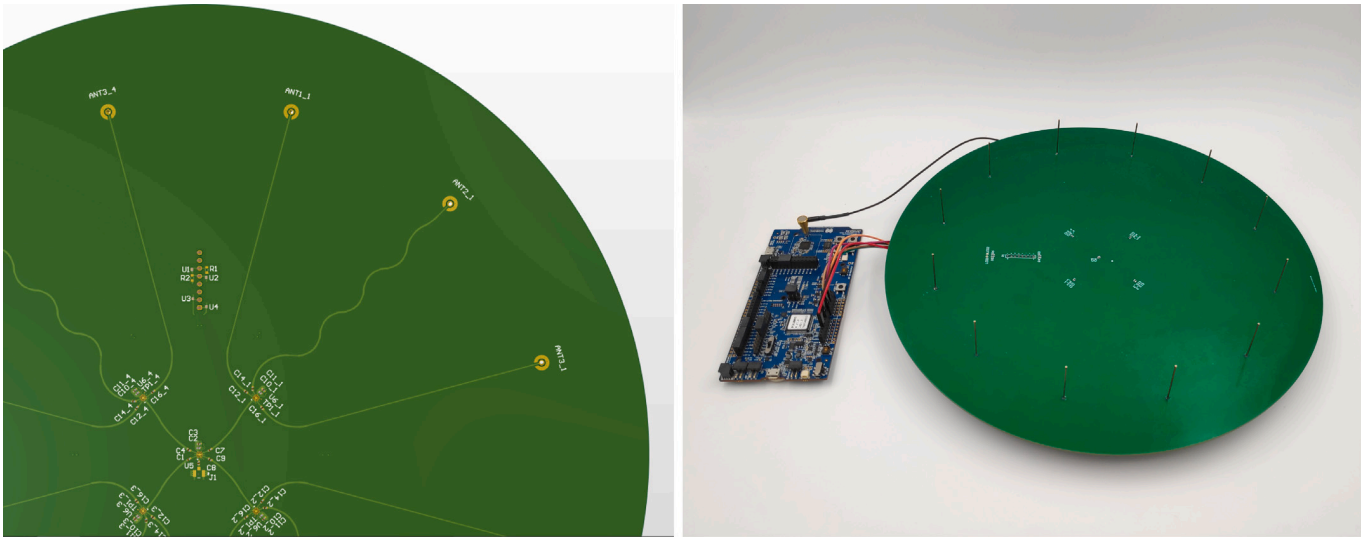


Fig. 7. Zoomed bottom side of the designed PCB with visible HF lines (left) and the antenna array connected to the nRF5340 Development Kit (right).

entire HF line to each antenna caused by resistive and dielectric losses to be approximately 1 dB.

Fig. 7 shows the zoomed bottom side of the PCB with visible HF lines (left) and the antenna array connected to the nRF5340 Development Kit (right).

3.3. Antenna type and frequency tuning

To achieve the 360° coverage for the DoA estimation, we chose non-directional antennas. In addition, the use of directional antennas in multipath scenarios may result in an incorrect DoA estimation if the DoA of an indirect ray coincides with the directivity of the antenna, and thus a higher power of an indirect ray is received compared to a direct ray. This increases the influence of multipath signal propagation on the DoA estimation. Large number of directional antennas in a conformal array structure could provide the desired coverage area for DoA estimation. However, the design is more suitable for higher frequencies allowing for more antennas to be implemented in a smaller area. Since the accuracy of DoA estimation depends on the number of available antennas, directional antennas reduce the number of available antennas for a given DoA. The RF switch matrix for a large number of antennas becomes too complex for low-cost devices with a single RF signal chain. In addition, the processing time for data with a large number of antennas is not negligible. On the other hand, the disadvantage of using omnidirectional antennas is the higher mutual coupling between the antennas.

Most BLE transceivers utilize single-ended signals, thus we opted for monopole antennas. Although monopole antennas can only radiate above the ground plane, in our case this is not a limitation since the DoA estimation performed with UCAA is limited to one of the subspaces defined by the plane of the antenna array. As mentioned in the 3.1 section, the ground plane does not extend equally in all directions around the antennas, so some directivity of the antennas is expected. The monopole antennas were made of 1 mm diameter copper wire wide enough to be mechanically stable and provide adequate bandwidth [17]. The antennas were soldered vertically to the PCB. The length of the antenna stub on the bottom side of the PCB is 3 mm.

Antennas' lengths were determined iteratively by measuring parameter S11 with a network analyzer at different antenna lengths. To account for adjacent antennas coupling with the active antenna, we conducted these measurements on a selected antenna placed between two other antennas of the same length. The core of the coaxial cable from the vector analyzer was soldered to the pad of the blocking

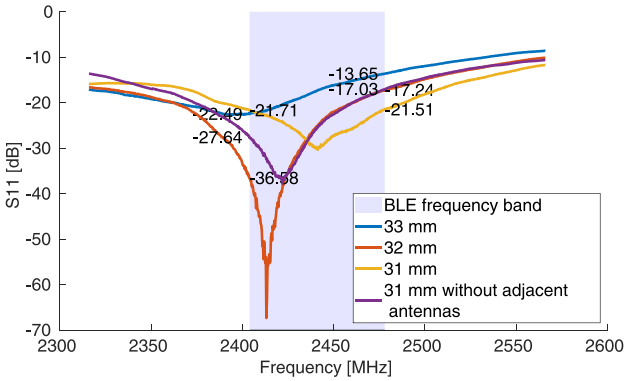


Fig. 8. Reflection coefficient as a function of frequency at different lengths of the antennas. (For interpretation of the references to color in this figure legend, the reader is referred to the web version of this article.)

capacitor between the antenna and the RF switch so that the path between them and the antenna were included in the measurement. In addition, to determine the direct influence of the adjacent antennas, we removed them and performed the measurement for a single antenna.

The results for different antenna lengths shown in Fig. 8 reveal that the optimal antenna length is 31 mm for the BLE frequency band highlighted in blue. At this length, the reflectivity was less than −21 dB for the entire frequency band. In the measured frequency range from 2316 MHz to 2566 MHz, the maximum value of the reflection coefficient is −11.73 dB. The purple curve shows the measurement at the optimal length without adjacent antennas. A shift of the minimum to lower frequencies can be observed, which means that the influence of adjacent antennas electrically shortens the measured antenna.

4. Performance evaluation

The performance of the antenna array was evaluated through simulations and measurements in a semi-controlled environments.

4.1. Simulations

To study the effect of non-idealities of the antenna array on the radiation pattern of the active antenna (proximity to the edge of the antenna array and influence of adjacent parasitic antennas), we

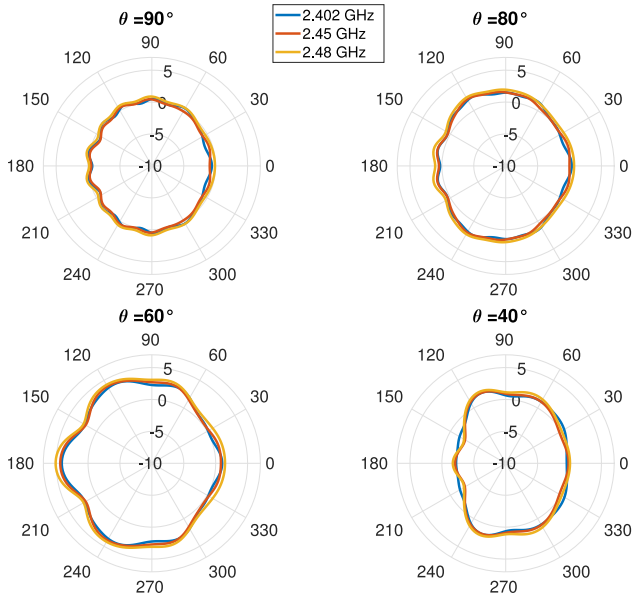


Fig. 9. Radiation patterns of single antenna at the edge of the PCB.

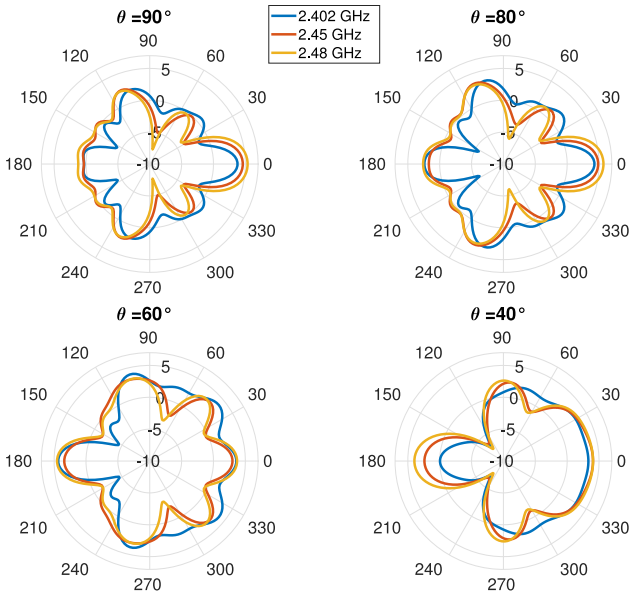


Fig. 10. Radiation patterns of a single active antenna with other antennas acting as parasites.

modeled and simulated the geometry of the antenna array in the XFdtd[4] software environment.

First, we tested how the proximity to the edge of the antenna array affects the radiation pattern of a single antenna without parasitic antennas. Fig. 9 shows the radiation patterns at four θ angles (the elevation angle corresponds to an angle equal to $90° - \theta$) and at three different frequencies corresponding to the edge and center frequency of the BLE band. The azimuth angle $\phi = 0°$ corresponds to a halfline with the origin at the center of the antenna array passing through the point of the measured antenna, and the $\theta = 0°$ corresponds to the zenith direction. With θ angle close to 90°, the radiation pattern is omnidirectional, as required when selecting monopole antennas. As the θ angle decreases, the gain in the $\phi = 180°$ direction first increases to approximately 5 dBi and then decreases below 0 dBi.

Fig. 10 shows the radiation patterns of the antenna array geometry with all antennas, one of which has been excited and the others acting as parasites. Compared to the simulation with a single antenna, the radiation patterns are more directed in the $\phi = 0°$ direction (radial direction outward the antenna array), and nulls are formed. As the θ angle decreases, the main and back lobe become more prominent, with the main lobe having a wider beamwidth. A stronger frequency dependence is also observed, with nulls at higher frequencies occurring toward the center of the antenna array, while at lower frequencies they tend to occur toward the outside the antenna array. This is due to the different phase shifts of the EM waves caused by the different spacing of the parasitic antennas with respect to the wavelength and the frequency dependence of the parasitic antennas' reactance.

A direct comparison of the two simulations shows that the nulls are due to the influence of the adjacent parasitic antennas. When DoA coincides with the direction of the null, the influence of noise on the DoA estimation increases due to the lower SNR. In the UCA configuration, each antenna has a different orientation of the radiation pattern shown in Fig. 10. Consequently, there is no DoA that could cause a null response for all antennas. The effect of nulls on the DoA estimation can be reduced by increasing the number of antennas as the number of antennas without a null response increases. Compared to the ULA configuration, which is also frequently used for direction finding, the effect of nulls is larger because the null response of all antennas is possible if DoA coincides with a null in the radiation pattern of the antennas.

4.2. Measurements

The performance of the antenna array was tested by measurements in two environments, namely (1) in an unpopulated outdoor environment with no obstacles in close proximity and no transmitters present at 2.4 GHz, and (2) in an empty office measuring 5 × 6.5 m. The designed antenna array was connected to the nRF5340 DK, which served as the BLE receiver. The nRF52833 DK was used as a BLE transmitter sending periodic advertisement packets with CTE attached and transmitting with 8 dBm of power. DoA was estimated at the receiver with the MUSIC algorithm using IQ samples from CTE. An angular resolution of 1° was chosen for the algorithm. Also, the algorithm for phase correction due to a mismatch of the carrier frequencies of the receiver and transmitter was implemented. To ensure a sufficient number of estimates for all 37 BLE data channels, 500 DoA estimates were collected for each angle.

In outdoor environment the transmitter and receiver were placed on stands 119 cm above the ground and 3.5 m apart. During measurements, the transmitter was stationary and the receiver was rotated to obtain the DoA estimates for angles from 0° to 360° in increments of 15°.

In indoor environment the transmitter and receiver were placed on stands 119 cm above the floor and 1.8 m apart. The receiver remained stationary while the transmitter was positioned to achieve the desired distance and measurement angle as shown in Fig. 12. To study the impact of receiver positioning on DoA estimation, we conducted three different measurement scenarios within the office.

In scenario 1, the receiver was placed in the center of the office and the transmitter was placed around the receiver to obtain the DoA estimates for angles from 0° to 360° in increments of 30°.

In scenario 2 the receiver was placed next to and in the middle of the wall. Measurements were made for angles 0°, 15°, 30°, and 60°, where 0° represents the angle at which the transmitter was positioned perpendicular to the wall (same setup as shown in Fig. 12 with the roles of transmitter and receiver reversed).

For measurement scenario 3 the receiver was placed in the corner of the office and the measurements were made for angles 0°, 15°, 30°,

[4] https://www.remcom.com/xfdtd-3d-em-simulation-software/.

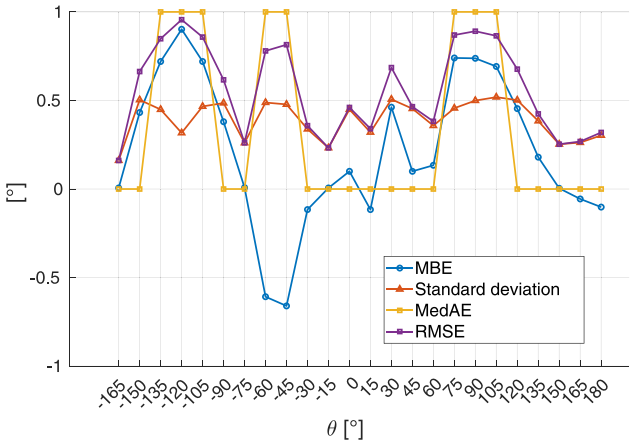


Fig. 11. Measurement results with the UCAA and the MUSIC algorithm in outdoor environment for azimuth angles from 0° to 360° in increments of 15°. (For interpretation of the references to color in this figure legend, the reader is referred to the web version of this article.)

and 45°, where 0° corresponded to the position of the transmitter at an angle of 45° to both walls. With these scenarios, we wanted to test how different receiver positions affect the DoA estimation, assuming that the multipath effect would be larger in scenarios 2 and 3 than in scenario 1.

Fig. 11 shows the results of the measurements in the outdoor environment. For each angle, the mean bias error (MBE), represented by the blue curve, does not exceed 1°. The average standard deviation (orange curve) is approximately 0.4° while RMSE, represented by the purple color, has similar values to the absolute values of the MBE. The DoA estimates for individual BLE channels also varied by less than 1°.

Fig. 13(a) shows the results of indoor measurements for scenario 1. Analysis of the MBE and standard deviation curves reveals substantial estimate errors for angles −150°, −90°, 30°, and 150°. A more detailed analysis was performed for these angles based on measurement results for each BLE frequency channel separately, as shown in Fig. 13(b), where the 0° angle is also shown as a reference without notable differences in the estimates across the different channels. From the data presented, it appears that the measurement error, evident in the spikes on the graph, is limited to a small number of adjacent frequency channels. To ensure that the errors were not due to interference from other devices operating in the same frequency band, several measurements were repeated and it was found that the results were consistently similar. To enhance the robustness of our analysis, we made additional measurements by positioning the transmitter at angles ±15° from those angles that showed notable differences in the estimates across the different channels. We also made measurements with slightly reduced distances between measurement units. The results obtained from these measurements do not show notable differences in the estimates across the different channels.

From the comprehensive results, it can be concluded that the observed errors were caused by strong multipath interference on some frequency channels for particular positions of transmitter and receiver within the office. Since the errors were limited to a small number of adjacent channels, it is possible to obtain an accurate estimate of the DoA by estimating the DoA on several widely separated channels and discarding possible outliers caused by multipath propagation.

It is noteworthy that the mean of the absolute MBE values of all angles without notable differences in estimates across the different channels (namely −120°, −60°, −30°, 0°, 60°, 90°, 120°, and 180°) is 0.45°, with the MBE of only one angle slightly exceeding the error threshold of 1°. The mean standard deviation of estimates for the same angles is 2.12°, which is larger than that observed in the outdoor



Fig. 12. Measurement setup with the UCAA and the MUSIC algorithm in the indoor environment with receiver placed in the center of the office.

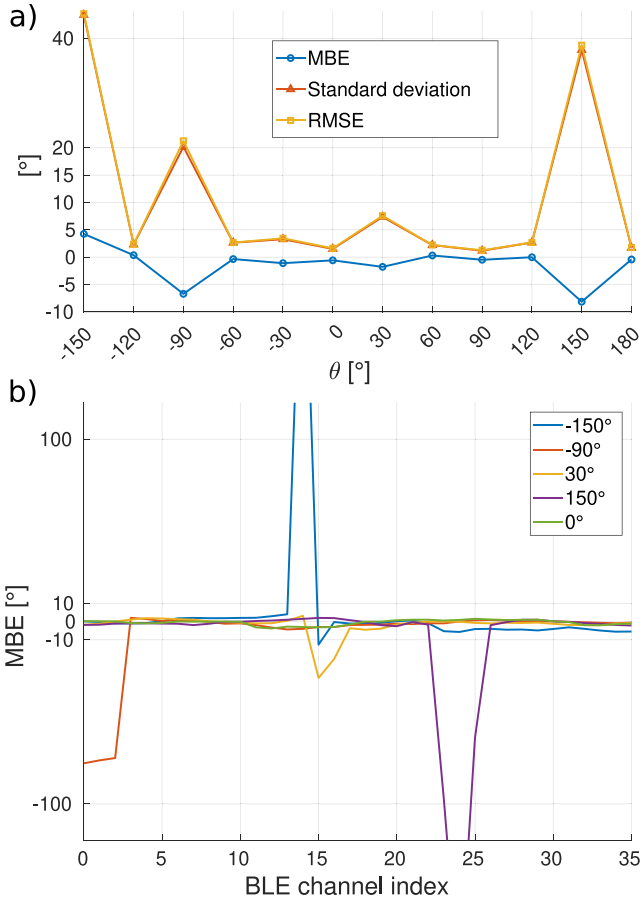


Fig. 13. Measurement results with the UCAA and MUSIC algorithm in a closed room. (a) Calculated MBE and standard deviation for different angles. (b) MBE of estimates for separate frequency channels.

environment. Conversely, the mean standard deviation of the estimates for separate channels is 0.30°, indicating that the spread of the estimates for separate channels is of the same order of magnitude as for the outdoor measurements. While the spread of estimates is larger across all frequency channels, separate channels provide data with low spread, whose combined mean is close to the true value. Consequently, the technique of channel hopping is critical to reducing the influence of multipath propagation on the DoA estimation.

Scenarios 2 and 3 have notable estimation errors on more adjacent channels compared to scenario 1, as can be seen in Fig. 14(a) and (b). In addition, the mean of the absolute MBE values of all angles without

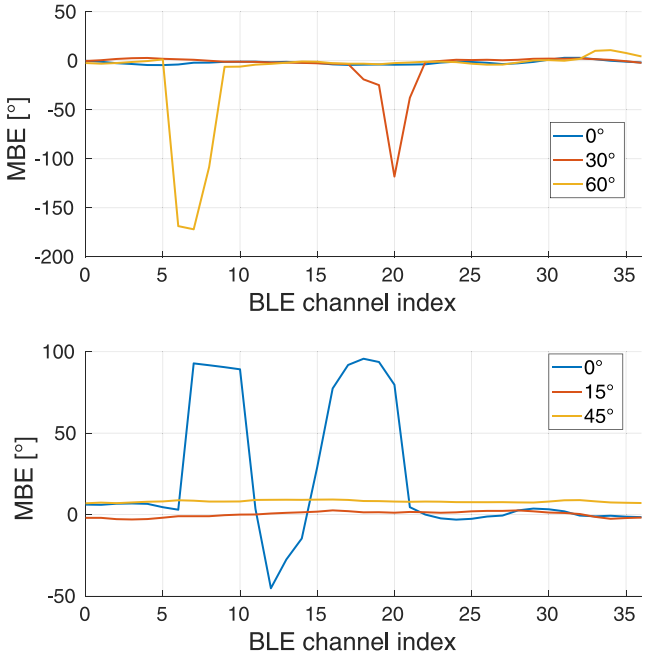


Fig. 14. Measurement results with the UCAA and MUSIC algorithm in a closed room. (a) Calculated MBE of separate frequency channels of measurement scenario 2. (b) Calculated MBE of separate frequency channels of measurement scenario 3.

notable differences in the estimates across the different channels are also larger for scenarios 2 and 3, resulting in mean errors of 1.45° and 3.97° with mean standard deviations of 1.58° and 1.69° for scenarios 2 and 3, respectively. However, the mean standard deviation of estimates on separate channels for these angles is 0.36° and 0.37°, similar to scenario 1.

Calibration of antenna arrays is a common practice because it is difficult to predict all the factors that affect the phase delay of the signal during PCB design. In this study, our goal was to avoid the lengthy procedures of calibrating each manufactured antenna array, therefore, we performed measurements without prior calibration and analyzed the performance we can achieve with the uncalibrated antenna array. Based on the measurement results, we decided that calibration was not necessary for the following two reasons: (1) the average error was smaller than the selected resolution of the algorithm (1°) and (2) performing the calibration and calculating the phase correction would most likely cause a larger error than estimating DoA without calibration due to the difficulties in making such precise angular measurements.

5. Conclusion and discussion

In this paper, the design process of a UCAA for DoA estimation was described and the usage of the UCA configuration was entitled. The number of antennas and their radii were determined by simulation, using MUSIC DoA estimation algorithm. The details of the PCB design were presented. We also discussed the use of monopole antennas, their advantages, and the frequency tuning process. The antenna array performance was evaluated through simulations to determine the effects of non-idealities on the radiation pattern and measurements in a semi-controlled environment. The results show that the designed antenna array is capable of achieving DoA estimation accuracy of less than 1° in simple environments with BLE. However, in environments with multipath propagation, less accurate DoA estimation can be expected on some adjacent frequency channels. The number of channels with less accurate estimates is expected to increase as the strength of non-line-of-sight (NLoS) paths increases relative to line-of-sight (LoS) paths. However, when the number of channels with inaccurate estimates is small, the true DoA can be estimated by comparing multiple estimates from different frequency channels, discarding the outliers. Simulations have shown that antenna coupling causes nulls in the radiation pattern that can affect the accuracy of the DoA estimation.

The designed antenna array is limited to the vertical polarization of the signal. The polarization mismatch between the transmitter and receiver reduces the SNR and the accuracy of DoA estimation. Therefore, in future work, we will consider using circularly polarized antennas or use similar approach as in [18], where an antenna array with tilted antennas was designed that is capable of determining the signal DoA with different polarizations (vertical, horizontal, 30°, 45° and 60°). An additional direction of future work is also the use of circularly polarized antennas in conformal array structures that enables the estimation of larger elevation angles, which is one of the drawbacks of existing designs. However, the structure needs additional optimization to be used for low-cost and computationally limited devices.

Due to its size, the designed antenna array is more suitable for stationary use. Given the popularity of mobile devices, it would be useful to develop a system for estimating signal DoA using a smaller antenna array. The performance of such a system should first be analyzed through simulations to find the optimal antenna configuration. Depending on the requirements of different applications, it would be useful to analyze the performance of other high-resolution algorithms (PDDA, ESPRIT [19]).

Declaration of competing interest

The authors declare that they have no known competing financial interests or personal relationships that could have appeared to influence the work reported in this paper.

Data availability

Data will be made available on request.

References

[1] Owoola EO, Xia K, Ogunjo S, Mukase S, Mohamed A. Advanced marine predator algorithm for circular antenna array pattern synthesis. Sensors 2022;22(15):5779.
[2] Goldsmith A. Wireless communications. Cambridge University Press; 2005.
[3] SIG B. Bluetooth core specification, V 5.1. Tech. rep. 5.1, Bluetooth SIG; 2019.
[4] Balanis CA, Ioannides PI. Introduction to smart antennas. Morgan & Claypool Publishers; 2007.
[5] Taser AE, Guney K, Kurt E. Circular antenna array synthesis using multiverse optimizer. Int J Antennas Propag 2020;2020:1–10.
[6] Yang J, Li WT, Shi XW, Ren Z. Artificial bee colony algorithm for time-modulated circular antenna array synthesis. In: 2012 international conference on microwave and millimeter wave technology (ICMMT), Vol. 3. 2012, p. 1–4.
[7] Guney K, Basbug S. Null synthesis of time-modulated circular antenna arrays using an improved differential evolution algorithm. IEEE Antennas Wirel Propag Lett 2013;12:817–20.
[8] Abdul Malek N, Seager RD, Flint JA, Zainal Abidin Z. Analysis, optimization, and hardware implementation of dipole antenna array for wireless applications. Int J Antennas Propag 2022;2022:e1741454.
[9] Park CJ, Pearce CN, Ackie A, Vassallo F, Duncan KJ. Dynamically reconfigurable direction-finding antenna array for unmanned arial systems. In: 2021 IEEE 21st annual wireless and microwave technology conference (WAMICON). 2021, p. 1–5.
[10] Friedrichs GR, Elmansouri MA, Filipovic DS. On the use of machine learning for direction finding with circular monopole antenna arrays. In: 2021 international applied computational electromagnetics society symposium (ACES). 2021, p. 1–3.
[11] Sharawi MS, Aloi DN. Design of an 8-element switched mode circular antenna array for vehicular direction finding. In: WAMICON 2011 conference proceedings. 2011, p. 1–4.
[12] Mohanna M, Rabeh ML, Zieur EM, Hekala S. Optimization of music algorithm for angle of arrival estimation in wireless communications. NRIAG J Astron Geophys 2013;2(1):116–24.
[13] Schmidt R. Multiple emitter location and signal parameter estimation. IEEE Trans Antennas and Propagation 1986;34(3):276–80.
[14] Tang H. DOA estimation based on music algorithm. 2014.
[15] Introduction into theory of direction finding. https://cdn.rohde-schwarz.com/us/campaigns_2/a_d/Introduction-Into-Theory-of-Direction-Finding.pdf.

[16] Bach C. ANTENNA BASICS – basic antenna design considerations for enocean based products. 2019, URL https://www.enocean.com/wp-content/uploads/application-notes/AN102_ANTENNA_DESIGN_2019.pdf.
[17] Balanis CA. Antenna theory: analysis and design. John Wiley & Sons; 2015.
[18] Mueller R, Lutz S, Lorch R. A novel circular direction finding antenna array for unknown polarizations. In: 2013 7th European conference on antennas and propagation (EuCAP). 2013, p. 1514–8.
[19] Sesma Santos V, Egorov V. Improved accuracy for indoor positioning with bluetooth 5.1: from theory to measurements. Student paper, 2020.



Aleš Simončič received his B.Sc. and M.Sc. degrees in electrical engineering from the University of Ljubljana in 2019 and 2022, respectively. His master's thesis was focused on angle of arrival estimation using BLE technology and antenna arrays.

He is currently working as a young researcher at the Department of Communication Systems at the Jožef Stefan Institute, Ljubljana, and is pursuing his Ph.D. in Information and Communication Technologies at the Jožef Stefan International Postgraduate School.

His research interests are in the area of radio communication systems. In particular. protocols, antennas and arrays, direction of arrival estimation methods, embedded systems, and radio environment characterization.



Tomaž Javornik (Member, IEEE) received his B.Sc., M.Sc., and Ph.D. degrees in electrical engineering from the University of Ljubljana, Ljubljana, Slovenia, in 1987, 1990, and 1993, respectively. He is a Scientific Counsellor with the Communication Systems Department, Jozef Stefan Institute, Ljubljana, Slovenia, and an Assistant Professor with the Jozef Stefan International Postgraduate School, Ljubljana. He participated in several COST and Framework Programme projects. He has coauthored more than 100 refereed journal and conference papers and several books and book chapters in the field of mobile and wireless communications. He holds two international patents.

His research experience is in the field of telecommunications, focusing on the development and performance analysis of fixed and mobile systems, radio-channel measurements, modeling and simulations and in indoor localization.

Dr. Javornik serves as a TPC Member or a reviewer for several IEEE conferences and journals.



Aleksander Sešek (Member, IEEE) received his B.Sc. and Ph.D. in electrical engineering from the University of Ljubljana, Ljubljana, Slovenia, in 2003 and 2008, respectively. He is an Assistant Professor at Faculty for Electrical Engineering, University of Ljubljana, teaching courses of analogue integrated circuits, telecommunication electronics and integrated circuits at high frequencies.

His research experiences are in the field of integrated electronics, sensor fabrication and their integration and in the high frequency integrated circuits and elements. He is involved in a several domestic and international industrial and research projects.

Dr. Sešek is author or co-author of many international papers, conference contributions and serves as reviewer of several international journals and conferences.



Andrej Hrovat (Member, IEEE) received his B.Sc. and M.Sc. degrees in electrical engineering from the University of Ljubljana in 2004 and 2008 and finished his Ph.D. at the Jozef Stefan International Postgraduate School in 2011. He is with the Department of Communication Systems at the Jožef Stefan Institute since 2004, at present holding the position of a senior research fellow.

His research and working experience are in the field of telecommunications, focusing on development and performance analysis for fixed and mobile systems, including terrestrial, stratospheric, and satellite systems, and radio-channel modeling for fixed and mobile narrowband and broadband radio communication systems. He works on several projects connected with professional mobile communication systems, 2/3/4G, WiFi and WiMAX technologies, satellite and sensor networks, including several COST actions, Framework Program projects, H2020 projects, European Space Agency (ESA) projects, and numerous national research and application projects.

Dr. Hrovat is the author or co-author of more than 100 peer-reviewed journal and conference papers, serves as a journal editorial board member and guest editor, reviewer for several international impact-factor journals, and is a TCP member for various international conferences and workshops.

Chapter 3

Asynchronization-induced Phase Error in DoA Estimation

Beyond the phase distortions introduced by the RF implementation of the SAA discussed in the previous chapter, single-RF-chain DoA estimation is also affected by phase errors caused by asynchronous operation between the transmitter and receiver. In a multi-RF-chain receiver, the signal is sampled simultaneously at all antenna elements. If AA-induced phase distortions are neglected, the measured inter-element phase differences reflect only the array phase response due to signal propagation. With a single-RF-chain receiver, simultaneous sampling is not possible, so the receiver must sequentially switch between antenna elements to acquire phase samples on selected elements. The measured phase differences therefore depends not only on the DoA, but also on the time at which each antenna element samples the CW.

When the impinging signal frequency f is known and the receiver is perfectly synchronized with the transmitter, sequential sampling with single-RF-chain receiver can emulate simultaneous sampling by scheduling antenna switching so that the time separation between two samples at consecutive antenna elements equals the signal period $T = 1/f$. This follows the equivalent-time sampling principle, where each antenna element samples the CW signal at the same phase instant across switching events, ensuring that the resulting inter-element phase differences remain only DoA-dependent.

In practical radios, both the sampling clock and the RF carrier frequency are ultimately referenced to a crystal oscillator frequency. Because perfect frequency generation is not achievable, the oscillator frequency deviates from its nominal value, and this deviation varies with operating conditions. Lower-cost oscillators typically have greater frequency tolerance and drift. For this reason, the transmitter and receiver oscillators are not perfectly synchronized, so CFO and SFO are present. As a result, the downconverted signal frequency differs from the expected value by the CFO, while the actual sampling instants deviate from the intended ones as the sampling frequency differs from its nominal value by the sampling frequency error (SFE). Together, CFO and SFO introduce an asynchronization-induced frequency error in the sampled signal, producing a phase error that evolves over time. In sequential antenna sampling, this phase error appears as additional phase shifts added to the ideal phase shifts acquired at the antenna elements caused by propagation path-length differences. As a result, the phase shifts across antenna elements are no longer solely a function of the DoA, which can introduce DoA estimation bias.

A common mitigation approach for phase error in related literature is to estimate and correct the asynchronization-induced phase errors by acquiring multiple samples on a single antenna element. Sampling a single element avoids the introduction of additional DoA-

dependent phase difference while allowing the estimation of the measured phase deviation over time from the nominal phase progression. The estimated phase errors are used to correct acquired phase samples across antenna elements prior to DoA estimation. However, accurate estimation typically requires a relatively large number of samples collected over a wide time window, increasing measurement overhead and energy consumption, reducing the estimation refresh rate, and adding computational load to already resource-constrained devices. Another approach for mitigating asynchronization-induced phase error is joint estimation of the sensing parameter and the nuisance parameter responsible for the phase error. However, joint estimation is less suitable for low-cost IoT devices, as it increases computational complexity, requires more memory, involves iterative or multidimensional optimization, and is more sensitive to model mismatch.

The next two sections present two papers that propose an alternative to the estimation-correction and joint parameter estimation approaches. The proposed approach reduces the impact of asynchronization-induced phase error on DoA estimation by optimizing ASP. The ASP optimization mitigation approach is inherently less sensitive to phase error and does not require additional computation to estimate phase errors. The first paper introduces the ASP design as a mitigation approach and provides initial simulation-based validation. The second paper broadens the analysis, considers additional ASP variants, and provides extensive validation through simulations and experiments.

3.1 Phase Error Mitigation via ASP Design

Publication included in this section:

A. Simončič, G. Morano, A. Švigelj, A. Hrovat, and T. Javornik, "Optimizing Switching Pattern to Reduce CFO Effects in Single RF Chain Direction Finding Systems," in *2024 7th International Balkan Conference on Communications and Networking (BalkanCom)*, Jun. 2024, pp. 113–118. DOI: 10.1109/BalkanCom61808.2024.10557208

In SAA-based DoA estimation, the signal cannot be sampled simultaneously at all antenna elements, so the receiver must define the sequence in which the antenna elements are activated, specifying which antenna element is active at each sampling instant. The activation order of antenna elements is determined by the ASP, represented as an ordered sequence of antenna element indices that indicates the order in which the antenna elements are activated. Because the antenna elements are sampled sequentially, CFO introduces additional phase shifts that can cause estimation bias. Rather than mitigating the resulting phase error through explicit estimation and correction for phase errors, or through joint parameter estimation as commonly considered in the literature, the approach proposed in the paper presented reduces CFO sensitivity by leveraging ASP design, presenting the scientific contribution **SC2.2**. ASP design allows control over the time instants at which individual antenna elements sample the signal and, consequently, over the magnitude of phase errors across the antenna elements.

The key observation is that CFO introduces a phase rotation that increases linearly with time, so each consecutively activated antenna element experiences a constant phase error increment relative to the previously activated element. The ASP therefore determines how the asynchronization-induced phase errors increments are mapped onto the spatial samples. A commonly used ASP in related literature is a geometric sweep, where antenna elements are activated sequentially in spatial order. For a ULA, this sequential geometric sweep produces a CFO-induced phase error pattern across antenna elements

that increases linearly with the element index. Because the DoA-dependent phase pattern also varies linearly with the antenna index, sequential geometric sampling produces phase errors correlated with phase shifts due to DoA and biases the estimate. A similar bias mechanism is observed for UCA and other array configurations.

ASP optimization can be interpreted as assigning the phase errors associated with all individual sampling instants to antenna elements so that the resulting phase-error pattern across the antenna elements is as dissimilar as possible to the DoA-dependent phase patterns within the considered angular range. The objective of ASP design is therefore to make the phase-error pattern across antenna elements appear more noise-like to the estimator and to prevent it from interpreting asynchronization-induced phase errors as a valid spatial phase response.

The paper presented in this section formulates the relationship between CFO, the sampling instants on antenna elements, and the resulting phase distortion. It further shows how the induced phase distortions can correlate with DoA-dependent phase terms and bias the estimate, thereby supporting hypothesis **H2** and contribution **SC2.1**. The paper derives a heuristic ASP design approach that decouples asynchronization-induced phase shifts from DoA-dependent phase shifts, delivering contribution **SC2.3**. The heuristic approach is further refined by introducing a phase-based center-of-gravity metric R, which weights antenna element position vectors by the CFO-induced phase errors and, together with brute-force search, identifies ASPs that minimize the distance between R and the geometric array center R_g, thereby narrowing the set of optimal candidate ASPs. The proposed ASP mitigation approach is validated through simulation-based evaluation for ULA and UCA, where DoA-estimation performance is assessed and compared under various CFO values, partially supporting **SC2.4**. The results show greatly reduced estimation error, approaching zero for both array configurations, confirming the effectiveness of the proposed ASP design-based mitigation and thereby addressing hypothesis **H3**.

2024 7th International Balkan Conference on Communications and Networking (BalkanCom)

Optimizing Switching Pattern to Reduce CFO Effects in Single RF Chain Direction Finding Systems

Aleš Simončič*†, Grega Morano*†, Aleš Švigelj*†, Andrej Hrovat*†, Tomaž Javornik*†
*Department of Communication Systems, Jožef Stefan Institute, Ljubljana, Slovenia
†Jožef Stefan International Postgraduate School (IPS), Ljubljana, Slovenia.
Emails: {ales.simoncic, grega.morano, ales.svigelj, andrej.hrovat, tomaz.javornik}@ijs.si

2024 7th International Balkan Conference on Communications and Networking (BalkanCom) | 979-8-3503-6595-5/24/$31.00 ©2024 IEEE | DOI: 10.1109/BalkanCom61808.2024.10557208

***Abstract*—Single RF chain multi-antenna wireless communication systems are increasingly favored for Direction of Arrival (DoA) estimation due to their low cost, efficiency and simplicity. However, non-simultaneous signal sampling and slight carrier frequency differences, known as carrier frequency offset (CFO), lead to phase errors that degrade DoA accuracy. In this paper, we propose an Antenna Switching Pattern (ASP) design method to minimize CFO-induced phase errors. The CFO errors are represented as phase weights and by calculating the center of gravity from these weights, we derive the candidates for optimal ASP. We performed a comparative analysis with conventional round-robin ASP, evaluating the DoA estimation error. MATLAB simulations using MUSIC algorithm with uniform linear and circular antenna arrays show significantly reduced DoA errors and reveal a CFO upper bound, making the method applicable in scenarios with coarse CFO estimation and correction.**

***Index Terms*—antenna switching pattern (ASP), Carrier Frequency Offset (CFO), Direction of Arrival (DoA), Internet of Things (IoT), MUSIC, single RF chain, uniform circular array (UCA) , uniform linear array (ULA)**

I. Introduction

Localization of wireless devices in the Internet of Things (IoT) has become an increasingly important function as it helps to improve the efficiency of a network, enables context-aware decisions and enhances security in IoT networks. The unknown location of a device can be determined either by estimating the distance or/and the angle to neighboring devices with known location. The angle to the neighboring device determines the direction of arrival (DoA), which can be estimated by measuring the phase angle of the incoming signal at multiple antennas. Due to mass production, IoT devices are inexpensive and usually only use a single radio frequency (RF) chain. To realize multiple antennas, an RF switch is used to connect RF chain to the antenna arrays of different types (uniform linear array (ULA), uniform circular array (UCA), etc.) with various number of elements. Since only one antenna element can be active at a time, it is important to define a predetermined sequence of antenna indices that specifies the order in which the elements sample the signal. This is generally referred to as the antenna switching pattern (ASP) [1]. Another outcome of the low-cost requirements of IoT devices is the use of low-accuracy crystal oscillators for system's clock and RF generation, resulting in a carrier frequency offset (CFO) between the transmitter and the receiver. The frequency mismatch, together with the non-simultaneous phase sampling, leads to a phase error that degrades the accuracy of the DoA estimation [2].

The use of wireless system with a single RF chain has the following disadvantages: (1) sequential sampling is M times longer to acquire samples on all antenna elements compared to simultaneous sampling, where M is the total number of antenna elements, and (2) the occurrence of an additional phase error of the signal between samples compared to simultaneous sampling. The phase error increases linearly with time, meaning the signal sample at the first element has a smaller phase error than the signal of the last element. Neglecting the CFO effect on the phase shift can lead to significant errors in DoA estimation.

The main contribution of this paper is the proposal of a novel method to determine an optimal antenna switching pattern that combats the CFO effect in DoA estimation. The structure of this paper is as follows. After the introduction, the survey of previous work is given in Section II, and the signal model is presented in Section III. Section IV presents a method for determining the candidates for optimized ASP. Subsequently, the proposed method is validated with simulations in MATLAB in Section V. The paper concludes with a summary and discussion.

II. Related work

The Bluetooth Low Energy (BLE) standard has introduced the Angle of Arrival/Departure (AoA/AoD) functionality in version 5.1 assuming a single RF signal chain. According to the BLE specification [1], the deviation of the carrier frequency must be limited to ± 150 kHz, including the allowed maximum crystal's drift of ± 50 kHz, with a maximum allowed drift rate of 400 Hz/μs. Even though the specified maximum frequency deviation can be relatively high, the absolute CFO frequencies in the real world are rarely greater than 30 kHz with typical values of 15 kHz [2].

The error in DoA estimation due to CFO can be mitigated by CFO estimation and subsequent correction of the phase samples to neutralize its influence on the phase measurements.

This research was funded by the Slovenian Research And Innovation Agency (ARIS) grant no. J2-4461, J2-3048, P2-0016, and PR-12348.

Authorized licensed use limited to: Institute Jozef Stefan. Downloaded on November 20,2024 at 13:04:22 UTC from IEEE Xplore. Restrictions apply.

For example, the BLE specification defines a preamble period in which up to 8 phase samples can be collected on a reference antenna element, which are later used for CFO estimation. Various algorithms for CFO estimation have been proposed, such as Fast Fourier Transform (FFT), Moose algorithm, MUltiple SIgnal Classification (MUSIC), etc. [2]–[4]. When selecting a CFO estimation algorithm, a trade-off between accuracy and computational complexity must be considered. For resource-constrained embedded devices, excessive computational complexity of CFO estimation is not desirable as high-resolution algorithms for DoA estimation such as MUSIC already consume significant resources and additional complexity may exceed the capabilities of the device. Conversely, simpler CFO algorithms may not provide the required accuracy for certain applications.

The ASP commonly used in previous works is the round-robin (RR) ASP. In RR ASP, the antenna indices increase sequentially and then return to antenna one from the last antenna. The first row of Table I illustrates RR ASP for four antenna elements. Some studies have investigated alternative ASPs by manipulating the number of samples for the reference antenna element. This adjustment is made because the accuracy of the CFO estimate depends on the number of samples and the sampling times. An example of such an ASP is the return-to-first (RTF) ASP, where assigning more samples for the reference antenna element improves the accuracy of the CFO estimate at the expense of fewer samples for the DoA estimate [4]. The second row of Table I illustrates RTF ASP for four antenna elements.

The possibility of using mirror ASP (the concatenation of two ASPs in which all antenna elements first sample with arbitrary ASP and then in reverse order of the first ASP) is mentioned in [2], [4], but it was not analyzed further. The third row of Table I illustrates the mirror ASP. The mirror ASP and RTF ASP double the time for DoA estimation.

TABLE I
COMMONLY USED ASP SCHEMES FOR 4-ELEMENT ANTENNA ARRAY.

	Switching sequence									
RR	1	2	3	4 ;	1	2	3	4 ;	1	...
RTF	1	2	1	2	1	3	1	4 ;	1	...
Mirror	1	2	3	4	4	3	2	1 ;	1	...

In a study [5], the researchers tried to determine the most effective time to switch between antenna elements and find the optimal number of samples to collect with a single element before switching to a new one. However, the ASP used for the elements remained constant and followed an RR sequence.

III. SIGNAL MODEL AND PROBLEM FORMULATION

The most straightforward approach for direction finding is the reception of an unmodulated, i.e. continuous wave (CW) signal. A system model including a transmitter and receiver with a single RF chain and M-element antenna array is shown in Fig. 1. The transmitted CW signal with carrier frequency f_c can be expressed as

$$s_{Tx}(t) = \Re\{a\, e^{\jmath(2\pi f_c t)+\Phi_{Tx}}\}, \tag{1}$$

where a, and f_c are the amplitude and the frequency of the transmitted signal, respectively. Without loss of generality, we can assume that the phase of the transmitted signal is zero $\Phi_{Tx} = 0$. When a radio signal propagates between the transmitter and receiver it is attenuated by channel attenuation h and delayed, which is represented as the phase shift of a CW signal $2\pi f_c \frac{d}{c}$, where c is the speed of light and d is the distance between the devices.

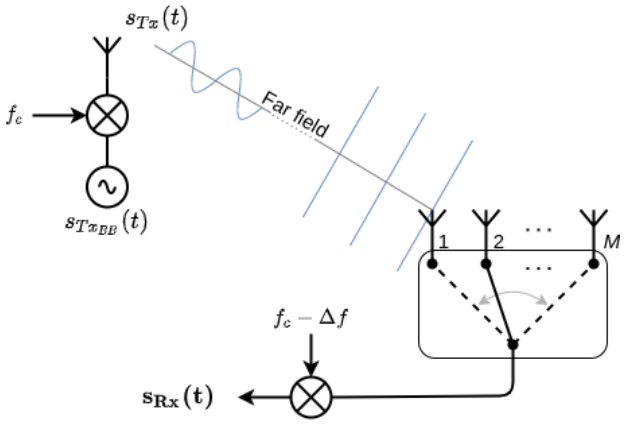


Fig. 1. A system with a transmitter and a receiver with a single RF chain.

At the receiver, the received CW signal is down-converted using the receiver carrier frequency, which is generally slightly different from that of the transmitter $f_c - \Delta f$. The Δf is called the carrier frequency offset (CFO) and can also include the frequency shift due to the movement of the receiver or the transmitter, i.e. Doppler frequency shift. The down-converted signal can be expressed as:

$$s_{Rx}(t) = \Re\{a\, h\, e^{\jmath(2\pi f_c(t-d/c))}\, e^{-\jmath(2\pi(f_c-\Delta f)t+\Phi)}\}$$
$$s_{Rx}(t) = \Re\{a\, h\, e^{-\jmath 2\pi f_c d/c}\, e^{-\jmath\Phi}\, e^{\jmath 2\pi\Delta f t}\},$$

where the value Φ denotes the phase of the receiver carrier frequency. In the case of the receiver with M-element antenna, the received signal can be given in a vector form:

$$\mathbf{s}_{Rx}(t) = \Re\{a\, e^{\jmath 2\pi\Delta f t} e^{-\jmath\Phi} \begin{bmatrix} h_1\, e^{-\jmath 2\pi f_c \frac{d_1}{c}} \\ h_2\, e^{-\jmath 2\pi f_c \frac{d_2}{c}} \\ \vdots \\ h_M\, e^{-\jmath 2\pi f_c \frac{d_M}{c}} \end{bmatrix}\}. \tag{2}$$

When the signal propagates from the transmitter to the receiver, each antenna element at Rx experiences a different phase shift of the signal due to the different path lengths of the signal propagation, which is represented by different distances between transmitter and receiver d_i in eq. 2. We

Authorized licensed use limited to: Institute Jozef Stefan. Downloaded on November 20,2024 at 13:04:22 UTC from IEEE Xplore. Restrictions apply.

assume the plain radio waves, i.e. receiver is in the far-field of the transmitter, consequently, the channel attenuation is equal at all elements $h_i = h$. The reference point of the antenna array at a distance d_0 from the transmitter can be defined, and the eq. 2 can be rewritten to

$$\mathbf{s}_{Rx}(t) = \Re\{a\ h\ \ e^{\jmath 2\pi \Delta f t}\ e^{-\jmath \Phi}\ e^{-\jmath 2\pi f_c \frac{d_0}{c}} \begin{bmatrix} e^{-\jmath \mathbf{k} \mathbf{r_1}} \\ e^{-\jmath \mathbf{k} \mathbf{r_2}} \\ \vdots \\ e^{-\jmath \mathbf{k} \mathbf{r_M}} \end{bmatrix}\}, \quad (3)$$

where $\left[e^{-\jmath \mathbf{k} \mathbf{r_1}}, e^{-\jmath \mathbf{k} \mathbf{r_2}}, \dots e^{-\jmath \mathbf{k} \mathbf{r_M}}\right]^T$ is an antenna array steering vector $\mathbf{A}(\theta)$, and denotes the phase shift of the received signal at each element from antenna reference point. $\mathbf{r_i}$ is the vector from antenna reference point to the i^{th} element, and $\mathbf{k} = \mathbf{j}\frac{2\pi}{\lambda}$ is wave number, where λ is a continuous signal wavelength, and $\mathbf{j}$ is a unit vector in the direction of plain wave propagation. If the signal is sampled at all antenna elements simultaneously, the DoA can be calculated using the steering vector and the measured phases of the received CW signal [6].

However, in the case of a single RF chain system, only one antenna element samples the signal at a time, and the other elements are sampled at the sampling frequency $(1/T_s)$, consequently the additional phase shift in the steering vector has to be considered,

$$\mathbf{A}(\theta) = \begin{bmatrix} e^{-\jmath \mathbf{k} \mathbf{r_1}}\ e^{\jmath 2\pi \Delta f (\mathbf{A}_{st}[1]-1) T_s} \\ e^{-\jmath \mathbf{k} \mathbf{r_2}}\ e^{\jmath 2\pi \Delta f (\mathbf{A}_{st}[2]-1) T_s} \\ \vdots \\ e^{-\jmath \mathbf{k} \mathbf{r_M}}\ e^{\jmath 2\pi \Delta f (\mathbf{A}_{st}[M]-1) T_s} \end{bmatrix}, \quad (4)$$

where $\mathbf{A}_{st}$ is a vector of integers, where each integer corresponds to the switch on time of a specific element in the switching sequence, with the index of the array indicating the corresponding antenna element. $\mathbf{A}_{st}$ thus specifies the additional phase shift due to CFO into steering vector $\mathbf{A}(\theta)$.

In the most general RR ASP, the additional phase shift due to the CFO between two consecutively sampled antenna elements is $2\pi\,\Delta f\,T_s$. The largest phase shift due to the CFO $(2\pi\,\Delta f(M-1)\,T_s)$ occurs at the last, M^{th} element. A linear increase of phase due to CFO appears for the elements in between $(\Delta\Phi_i = i\ 2\pi\Delta f T_s)$. The difference in the additional phase progression between the last and the first element depends on Δf, T_s, and the number of elements M. The effect of the phase shift due to CFO in the DoA estimation can be interpreted as a displacement of the element from the original position closer to the source in the case of $\Delta f < 0$ and further from the source in the case of $\Delta f > 0$, as shown in Fig. 2. It is shown that the DoA estimate is incorrect due to the displacement of the elements. Depending on the DoA of the source, the virtual position of the element lies on a circle with a radius $R = (i-1)\ \Delta f\ T_s\ \lambda$ around the real position of the elements.

If the large phase shifts due to the CFO are concentrated on one side of the antenna array, which is particularly noticeable in RR ASP, the signal appears to come more from that direction. At a low CFO, the DoA estimate error is small, while a large CFO results in high errors.

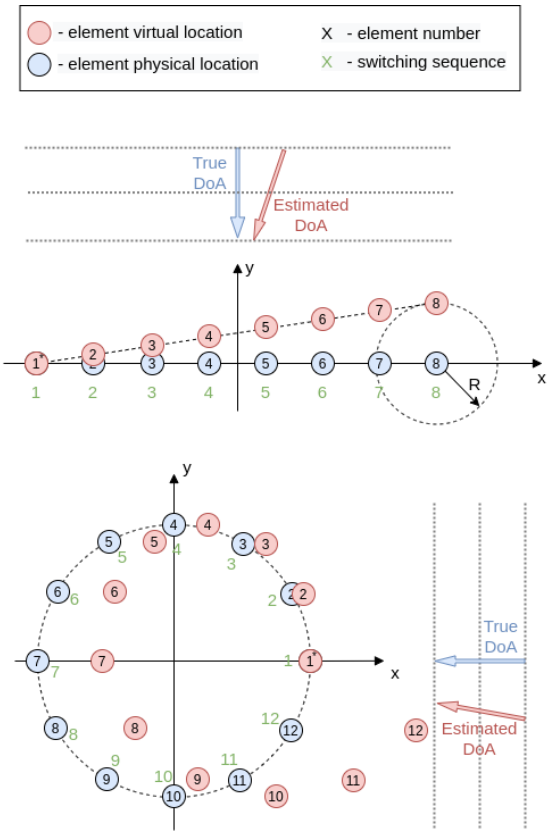


Fig. 2. Virtual antenna elements positions that are shifted relative to the physical positions due to the CFO phase progression when using RR ASP. '*' indicates that the virtual and physical locations of the antenna element overlap.

To investigate the impact of the CFO on DoA estimation, we conducted a MATLAB simulation in which we calculated the mean absolute error (MAE), maximum absolute error (MAX AE) and root mean square error (RMSE) of the DoA estimates. The calculations were performed for a 12-element UCA and an 8-element ULA over different angle intervals, specifically $[-179°, 180°]$ for UCA and $[15°, 165°]$ for ULA, with a step of $1°$ and T_s of $16\,\mu$s. The DoA was estimated using the MUSIC algorithm with 6 samples per antenna element without additional noise. The results shown in Table II reveal that the MAE for CFOs above 0.5 kHz is already greater than $1°$.

IV. Antenna Switching Pattern Optimization Method

Systematic error of the DoA estimation introduced by CFO can be minimized with uniform distribution of the phase error across the antenna array by manipulating the ASP. The basic idea of the proposed method is that the two antenna elements, whose physical locations are mirrored over the center of the antenna array, are assigned the sampling time that corresponds to similar values of the phase shift due to the CFO. In this

Authorized licensed use limited to: Institute Jozef Stefan. Downloaded on November 20,2024 at 13:04:22 UTC from IEEE Xplore. Restrictions apply.

TABLE II
DOA ESTIMATION ERRORS FOR DIFFERENT CFOS WITH RR ASP FOR ULA WITH 8 ANTENNA ELEMENTS AND UCA WITH 12 ANTENNA ELEMENTS

CFO [kHz]	DoA estimation error	ULA (8 elements)	UCA (12 elements)
0.1	MAE	0.29°	0.23°
	MAX AE	0.73°	0.37°
	RMSE	0.13°	0.11°
0.5	MAE	1.44°	1.17°
	MAX AE	4.09°	2.00°
	RMSE	0.66°	0.56°
1	MAE	2.93°	2.36°
	MAX AE	11.31°	4.00°
	RMSE	1.53°	1.12°
2	MAE	11.33°	4.90°
	MAX AE	155.08°	7.25°
	RMSE	28.86°	2.13°
3	MAE	17.92°	20.99°
	MAX AE	151.11°	179.78°
	RMSE	36.07°	42.78°

way, the similar values of phase shifts act as a counterweight to each other, which prevents the accumulation of large phase shifts in one part of the antenna array. In addition, we try to distribute the elements with the large phase shift uniformly across the antenna arrays so that the reduced accumulation of large $\Delta\Phi_i$s applies to all possible DoA. This heuristic idea is illustrated in Fig. 3 and explained in the following steps:

1) Assign a sampling time M to an arbitrary element, due to the circular symmetry of the UCA. For example, element 1 is selected resulting in $\mathbf{A}_{st} = [8, \cdot, \cdot, \cdot, \cdot, \cdot, \cdot, \cdot]$, where $\cdot$ denotes the elements without assigned switch on time. This element will gave the largest phase shift of $(M-1)2\pi\Delta f T_s$.
2) Next, select the element, whose physical position is opposite to the center of the antenna array. The second largest phase shift acts as a counterweight on the first element. In the example in Fig. 3 this is element 5 with the sampling time $M-1$, which results in $\mathbf{A}_{st} = [8, \cdot, \cdot, \cdot, 7, \cdot, \cdot, \cdot]$.
3) Assign a sampling time $M-2$ to one of the elements located on the line orthogonal to the line connecting the previously assigned elements. In show-case example element 3 is selected, thus $\mathbf{A}_{st} = [8, \cdot, \cdot, 6, \cdot, 7, \cdot, \cdot]$.
4) For the sampling interval $M-3$ the procedure described in step (2) is applied, resulting in $\mathbf{A}_{st} = [8, \cdot, \cdot, 6, \cdot, 7, \cdot, 5, \cdot]$.
5) Find an unassigned element whose neighbors have the smallest value of $\mathbf{A}_{st}$, i.e. the smallest phase shift due to the CFO. In show-case example $a_2 = 14, a_4 = 13, a_6 = 12, a_8 = 13$. Thus element 6 is selected next, resulting in $\mathbf{A}_{st} = [8, \cdot, \cdot, 6, \cdot, 7, 4, 5, \cdot]$.
6) For the sampling interval $M-5$, the procedure described in step (2) is used, which results in $\mathbf{A}_{st} = [8, 3, 6, \cdot, 7, 4, 5, \cdot]$.
7) For the sampling interval $M-6$, the procedure described in step (5) is used, which results in $\mathbf{A}_{st} = [8, 3, 6, 2, 7, 4, 5, \cdot]$.
8) Assign the position $M-7$ to the remaining element, resulting in $\mathbf{A}_{st} = [8, 3, 6, 2, 7, 4, 5, 1]$.

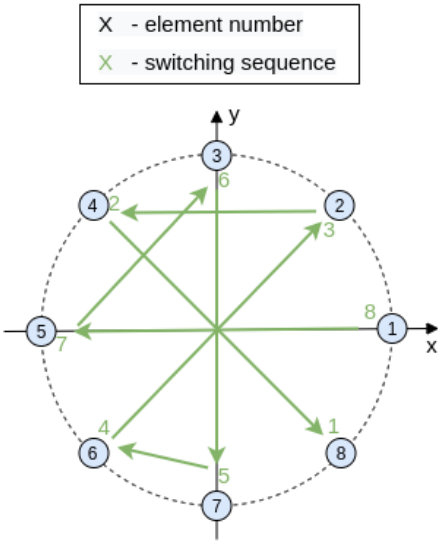


Fig. 3. Optimized ASP for UCA with 8 elements.

The heuristic example works well in the case of 8 element antenna array. However, if a different number of elements is used, there are several options for choosing a particular element without a clear reason for that decision, and the process is no longer straightforward. Therefore, we have modeled the problem of determining the optimized ASP as the center of gravity problem, where $\Phi_i = (\mathbf{A}_{st}[i]-1)2\pi\Delta f T_s$ represents the phase weights at the i-th element position. Additionally, the distances of the elements from the origin of the coordinate system are normalized, thereby considering only the angular positioning of the elements. The position of i-th element with normalized distance is denoted as $\mathbf{r_{in}}$. The modeled phased-based center of gravity $\mathbf{R}$ is given by:

$$\mathbf{R} = \frac{\sum_{i=1}^{M} \Phi_i \cdot \mathbf{r_{in}}}{\sum_{i=1}^{M} \Phi_i} = \frac{2\sum_{i=1}^{M} (\mathbf{A}_{st}[i]-1) \cdot \mathbf{r_{in}}}{M(M-1)}. \quad (5)$$

The optimal solution is obtained when the phase-based center of gravity R is closest to the center of antenna array gravity R_g with weight equal to unity at all antenna elements positions

$$\min_j \left|\mathbf{R}_g - \mathbf{R}_j\right| = \\ = \min_j \left| \frac{\sum_{i=1}^{M} \mathbf{r_{in}}}{M} - \frac{2\sum_{i=1}^{M} (\mathbf{A}_{st}[i]-1) \cdot \mathbf{r_{in}}}{M(M-1)} \right| \quad (6)$$

where the index $\mathbf{R}_j$ denotes the j^{th} realization of ASP. To find optimal ASP, brute force approach is applied.

V. SIMULATION RESULTS AND DISCUSSION

To validate the proposed method, we conduct MATLAB simulations for 8-element ULA and 12-element UCA. In both

Authorized licensed use limited to: Institute Jozef Stefan. Downloaded on November 20,2024 at 13:04:22 UTC from IEEE Xplore. Restrictions apply.

scenarios, the distance between antenna elements is set to $\lambda/2$, and samples are collected with each element. The sampling period T_s is 16 μs. The DoA estimation is performed using the MUSIC algorithm with an angular resolution of 0.001° for the whole applicable range of angles. Initial simulations for ULA and UCA were performed with a CFO of 1 kHz, followed by further simulations with higher CFO values to evaluate the performance of the methods for the high-frequency limit.

A. Uniform Linear Array

The proposed method yields 2303 ASP candidates with the same minimum difference between the phase-based center of gravity and antenna array center of gravity. Fig. 4 shows the absolute error (AE) of the estimated DoA with all possible ASP candidates compared to the common RR ASP (shown with a thicker blue line). Large errors of the DoAs around 0° and 180°, also known as end-fire directions, are typical for the ULA geometry [7]. Therefore, only the range between 15° and 170° is shown for comparison, as unpredictably high errors can occur outside this range.

From all possible candidates, we can select the optimal one by calculating the MAE over all angles and finally selecting the one with the smallest error. In this case, 4 candidates have the smallest MAE of 0.00019° compared to RR ASP with an MAE of 3.13°.

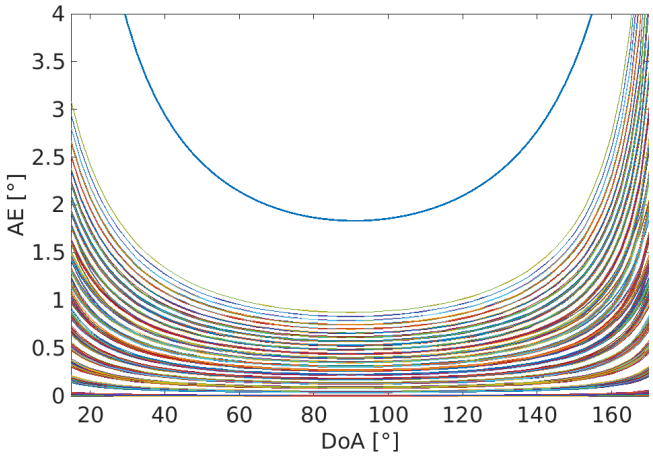


Fig. 4. Absolute error of DoA estimation with all ASP candidates, for ULA with 8 elements and CFO of 1 kHz. The RR ASP is drawn with a thick blue line.

Next, we examined the CFO bound of the ASP candidates by changing the CFO from 1 kHz to 5 kHz in steps of 1 kHz. The AEs of the estimated DoA follow similar trend as shown in Fig. 4, but with larger errors as the CFO value increases. Out of the 4 remaining ASP candidates, the sequence with the lowest MAE for all CFOs tested turns out to be $[2, 4, 5, 6, 8, 7, 1, 3]$. This ASP is therefore the optimal ASP for ULA with 8 elements, based on center of gravity solutions and the calculated MAEs at different CFO frequencies. The MAE, MAX AE, and RMSE values for optimal ASP, are summarized in Table III.

TABLE III
DoA estimation errors for 8-element ULA and ASP $[2, 4, 5, 6, 8, 7, 1, 3]$.

CFO [kHz]	MAE	MAX AE	RMSE
1	0.00019°	0.001°	0.00040°
2	0.0029°	0.009°	0.0015°
3	0.0084°	0.0029°	0.0049°
4	0.0164°	0.0055°	0.0093°
5	37.1°	133.93°	41.43°

To explain the upper CFO limit, we look at the MUSIC pseudo spectrum at CFO 5 kHz and sampling period $T_s = 16\mu$s for RR ASP and optimized ASP. We observed more peaks in the pseudo spectrum at some DoA angles for the optimized ASP, while the RR ASP only provides one sharp peak of the MUSIC algorithm pseudo spectrum. In the case of RR ASP and ULA, the phase increase due to CFO is correlated with the phase increase due to DoA, which means that the phase difference between two antenna elements separated by $(i\,\lambda/2)$ due to the DoA is $i\pi \sin\theta$, where θ is the angle between the plane radio wave and the ULA, and the phase increase due to CFO is $(i\,2\pi\Delta f T_s)$. This results in a single peak of the MUSIC pseudo spectrum, but wrong DoA angle. The AE of the DoA estimate increases with the CFO value and T_s. The MAE of the specified range of DoAs for the RR ASP with 5 kHz CFO and $T_s = 16\mu$s is 28.45°. This value is not accurate enough for most applications, especially considering that noise was excluded from the simulated data.

In the case of an optimized ASP, an increase in phase due to CFO along the elements is not linear and thus does not correspond to any DoA. The MUSIC algorithm treats this as noise which increases with CFO frequency leading to the observation of a high-frequency limit. Since the phase errors at the antenna elements are constant for certain CFO, T_s, and ASP, this systematic error favors an incorrect DoA estimate. When the phase errors are small, the MUSIC algorithm treats them as small noise, and the result is a single sharp peak corresponding to the true DoA. However, as the CFO frequency increases, the DoA of the systematic phase errors has a larger impact, so another peak is observed, up to the point where the peak of the false DoA is larger than the true DoA, which is observed at 5 kHz CFO in our optimized ASP. The value of false DoA then changes for different ranges of CFO values above the high frequency limit. In contrast, for the noise sources, we can assume an independent Gaussian distribution over all antenna elements, so that no particular DoA is favored when multiple samples are acquired on all antenna elements, as the phase errors caused by the noise tend to cancel out. The more samples that are acquired, the lower the influence of the noise sources on DoA. This does not apply to the effect of the CFO on DoA estimation, as more samples do not reduce the influence of systematic errors. If the ASP were randomly selected for each sampling cycle on the antenna elements, this would be similar to the true noise scenario and would likely provide better results than the RR ASP when multiple samples are acquired.

Authorized licensed use limited to: Institute Jozef Stefan. Downloaded on November 20,2024 at 13:04:22 UTC from IEEE Xplore. Restrictions apply.

B. Uniform circular array - UCA

The method proposed in this study is computationally complex and time consuming, as the computational cost increases with $M!$. For a larger number of antenna elements, the last few antenna elements in the ASP can be selected manually using the proposed method described in Section IV, leveraging the symmetry of the UCA. The sequence of the remaining elements can be determined using the proposed center of gravity search algorithm. In the case study, we used a 12-element UCA and manually determined the sequence of the first 4 elements $M-(M-3)$ in the ASP to be the elements that lie on either the x-axis or the y-axis (similar to elements 1, 5, 3, and 7 in Fig. 3).

The proposed center of gravity search algorithm yields 25 optimal ASP candidates. The AEs of the ASP candidates compared to the RR ASP (marked with a thicker blue line), over the entire angular range $[-179°, 180°]$, are shown in Fig. 5. The AEs of all optimized ASP candidates are significantly lower than the AEs of RR ASP. By calculating the MAE across all angles, we found two ASPs with the lowest DoA estimation error: $[2, 8, 11, 5, 6, 12, 3, 9, 10, 4, 7, 1]$ and $[2, 8, 11, 5, 3, 9, 6, 12, 10, 4, 7, 1]$. They reduce the MAE of the RR ASP from 2.36° to 0.0017°.

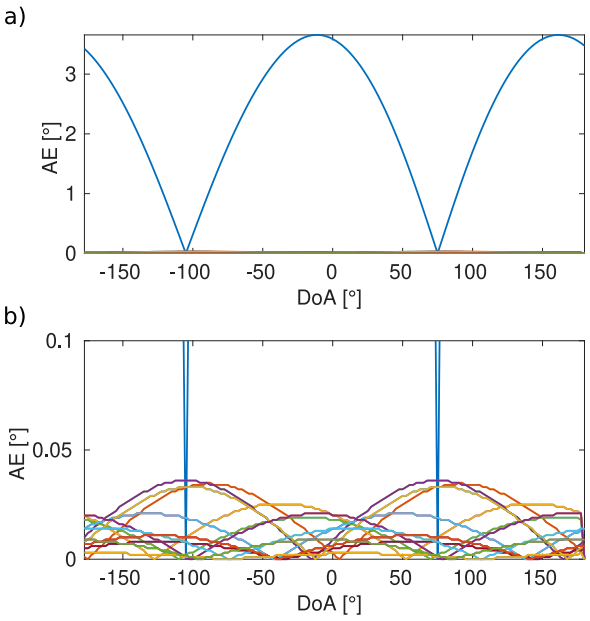


Fig. 5. a) AEs for different DoAs and SPs for UCA with 12 elements when CFO equals 1 kHz. b) Zoomed in version of graph a). The RR ASP is drawn as a reference with a thick blue line.

In addition, Fig. 5 displays the operational characteristics of UCA. Each ASP exhibits two DoAs where the AE approaches 0°. This phenomena can be explained by the fact that an antenna array is divided into two halves by the line from the center of the antenna array to the transmitter. If the sum of the phase shifts on each half is not equal, a bias in the DoA estimate is expected. Therefore, it is possible to construct an ASP that produces an AE close to 0° at an arbitrary angle, but this does not guarantee a relatively small AE at other DoAs.

Similar to ULA, there is a high CFO limit around 3 kHz at which more peaks in the MUSIC spectrum occur and the estimated DoA are no longer correct. For UCA, the ideal phase progressions due to DoA do not correlate with the CFO phase progressions like in the ULA case, so approximately the same high-frequency limit is observed for RR and optimized ASP. For CFO above 1 kHz, only one ASP from the candidates with the smallest MAE remains, namely $[2, 8, 11, 5, 6, 12, 3, 9, 10, 4, 7, 1]$, which is declared as the optimal ASP for UCA with 12 elements. The MAE, MAX AE, and RMSE values for optimized ASP for set of CFOs are summarized in Table IV.

TABLE IV
DoA estimation errors for different CFOs with 12-element UCA and ASP $[2, 8, 11, 5, 6, 12, 3, 9, 10, 4, 7, 1]$.

CFO [kHz]	MAE	MAX AE	RMSE
1	0.00017°	0.003°	0.00095°
2	0.00179°	0.00270°	0.0081°
3	59.05°	114.82°	52.29°

VI. Conclusion

Carrier frequency mismatches between receiver and transmitter significantly affect the accuracy of DoA estimation in single-chain RF systems. Usually, only a limited number of samples are available for DoA estimation, and a portion of these samples is used for CFO estimation and calibration. With our proposed method of ASP design, the CFO effects are greatly reduced by strategically selecting the sequence of elements in the ASP. Although the presented method has an upper CFO frequency limit, it can be used in addition to the usual CFO estimation and calibration algorithms, since the CFO estimation errors can still reach into the kHz range, especially when the SNR is low. The proposed method does not introduce any computational complexity for a device and can achieve an absolute DoA error close to 0° for CFOs that are below the high frequency threshold.

References

[1] B. SIG, "Bluetooth Core Specification, V 5.1," Tech. Rep. 5.1, Bluetooth SIG, 2019.
[2] S. Cloudt, "Bluetooth Low Energy Direction Finding on Embedded Hardware by Mitigating Carrier Frequency Offset and Multipath Fading,"
[3] G. Morano, A. Simončič, T. Kocevska, T. Javornik, and A. Hrovat, *Angle of Arrival Estimation Using IEEE 802.15.4 TSCH Protocol*. Sept. 2023. Pages: 7.
[4] L. Yao, "Bluetooth Direction Finding," 2018.
[5] P. Avital, G. Chardon, and J. Picheral, "Design of switching sequences for sine parameters estimation on switched antenna arrays," *Signal Processing*, vol. 188, p. 108244, Nov. 2021.
[6] Z. Chen, G. Gokeda, and Y. Yu, *Introduction to Direction-of-arrival Estimation*. Artech House, 2010. Google-Books-ID: IsZQmAEACAAJ.
[7] S. Shirvani-Moghaddam and F. Akbari, "A novel ULA-based geometry for improving AOA estimation," *EURASIP Journal on Advances in Signal Processing*, vol. 2011, p. 39, Aug. 2011.

Authorized licensed use limited to: Institute Jozef Stefan. Downloaded on November 20,2024 at 13:04:22 UTC from IEEE Xplore. Restrictions apply.

3.2 Comprehensive ASP Design, Analysis, and Evaluation

Publication included in this section:

A. Simončič, K. Guan, G. Morano, A. Švigelj, A. Hrovat, T. Kocevska, and T. Javornik, "Experimental Evaluation of Enhanced Antenna Switching for CFO Mitigation in DoA Estimation," *IEEE Open Journal of Antennas and Propagation*, vol. 6, no. 4, pp. 1022–1036, Aug. 2025, ISSN: 2637-6431. DOI: 10.1109/OJAP.2025.3558671

This section builds on the ASP-based CFO mitigation approach for DoA estimation introduced in the previous section by providing a deeper analysis and expanding validation through simulations and outdoor experiments. The core idea remains that, in single-RF-chain architectures with SAA, CFO causes time-dependent phase rotations of the sampled signal, which are mapped onto spatial samples by the antenna switching order. A properly designed ASP reshapes this mapping so that the resulting phase-error pattern across antenna elements is less correlated with DoA-dependent phase patterns, thereby reducing bias in DoA estimation.

The presented paper extends the analytical biasing analysis of commonly used ASP in related literature, SS, where a geometric sweep is performed by sequentially activating antenna elements in spatial order, further supporting hypothesis **H2**. In addition to the previously considered ASP design method, the paper introduces an antenna switching method based on concatenating an arbitrary ASP with its reverse order, referred to as Mirror-SP, thereby further supporting **SC2.3**. The underlying principle is that a given ASP introduces a systematic CFO-induced estimation error, while applying the same ASP in reverse order produces an estimation error of opposite sign, equivalent to the effect of a negative CFO under the original order. The systematic bias is mitigated by combining two sequences with complementary error behavior.

The evaluation of the proposed ASPs is extended in three directions compared to the previous section. First, the impact of additive Gaussian noise on distance estimation with different ASPs is analyzed, with performance characterized across different SNRs. Second, DoA bias behavior is examined across a wider range of CFO values, and the CFO bounds within which the proposed ASPs maintain high accuracy are identified and analyzed. Third, the study includes experimental validation through outdoor measurements designed to minimize multipath influence and isolate the asynchronization effect on DoA estimation. All evaluations are performed for ULA and UCA configurations across multiple DoAs, and the proposed ASPs are compared with SS ASP. Through this extended simulation and experimental analysis, the paper further supports **SC2.4**. The results demonstrate that the proposed ASP designs mitigate asynchronization-induced bias across different CFO and noise conditions within the identified CFO bounds, thereby further supporting hypothesis **H3**.

To extend the optimal operating range of the proposed ASPs beyond the identified CFO bounds, the included paper proposes a coarse CFO estimation and correction step. The motivation is that coarse correction of CFO-induced phase errors enables operation within the high estimation accuracy region of the proposed ASPs, provided the residual CFO is within the identified bounds. Compared with fine correction, coarse correction reduces computational requirements and is more suitable for resource-constrained devices.

IEEE Open Journal of Antennas and Propagation IEEE OPEN JOURNAL OF ANTENNAS AND PROPAGATION, VOL. 6, NO. 4, AUGUST 2025 1022

Received 3 March 2025; revised 26 March 2025; accepted 4 April 2025. Date of publication 7 April 2025; date of current version 12 August 2025.

Digital Object Identifier 10.1109/OJAP.2025.3558671

Experimental Evaluation of Enhanced Antenna Switching for CFO Mitigation in DoA Estimation

ALEŠ SIMONČIČ [1,2] (Student Member, IEEE), KE GUAN [1,3] (Senior Member, IEEE), GREGA MORANO [1,2] (Graduate Student Member, IEEE), ALEŠ ŠVIGELJ [1,2] (Senior Member, IEEE), ANDREJ HROVAT [1,2] (Senior Member, IEEE), TEODORA KOCEVSKA [1] (Member, IEEE), AND TOMAŽ JAVORNIK [1,2] (Member, IEEE)

[1]Department of Communication Systems, Jožef Stefan Institute, 1000 Ljubljana, Slovenia
[2]Jožef Stefan International Postgraduate School, 1000 Ljubljana, Slovenia
[3]State Key Laboratory of Advanced Rail Autonomous Operation and the School of Electronic and Information Engineering, Beijing Jiaotong University, 100044 Beijing, China

CORRESPONDING AUTHOR: A. SIMONČIČ (e-mail: ales.simoncic@ijs.si)

This work was supported by the Slovenian Research and Innovation Agency (ARIS) under Grant PR-12348, Grant J2-4461, Grant J2-3048, and Grant P2-0016.

ABSTRACT Direction-of-arrival (DoA) estimation in the Internet of Things (IoT) and embedded devices is typically performed using single-RF chain systems and antenna switching using time-division multiplexing. The accuracy of the DoA estimation is reduced due to the additional phase shifts between the samples on the antenna elements caused by the carrier frequency offset (CFO). We propose to use optimized antenna switching patterns (ASPs) to mitigate the effect of CFO on accuracy in DoA estimation using a multiple signal classification (MUSIC) algorithm. We evaluated two switching methods referred to as *EvenCFO-SP* and *Mirror-SP* with simulations and confirmed the validity with measurements. Performance is analyzed and compared with a standard sequential sampling (SS) method. Uniform linear and circular array configurations are considered to evaluate the impact of the noise and the CFO value on estimation accuracy. The results show that the optimized ASPs outperform the SS method, with lower performance gain at small signal-to-noise ratios. The ASP sensitivity to the CFO value is studied, and the frequency bounds within which the optimized ASPs maintain high estimation accuracy are identified. A coarse CFO correction, effective for frequency estimation errors within the kHz range, extends the frequency bounds. Compared to a fine calibration, this reduces computational requirements, making it a viable option for embedded and IoT devices with limited hardware resources.

INDEX TERMS Antenna switching pattern (ASP), carrier frequency offset (CFO), direction-of-arrival (DoA), Internet of Things (IoT), MUSIC, noise, single-RF chain, switched array, uniform circular array (UCA), uniform linear array (ULA).

I. INTRODUCTION

LOCALIZATION functionality within Internet of Things (IoT) devices is increasingly important for emerging industries, precision agriculture, autonomous transportation, environmental monitoring, asset tracking, disaster response, wearable technology, smart homes, and more [1]. Accurate location information considerably extends the benefits of IoT systems [2]. Among localization methods, the estimation of the direction of arrival (DoA) is favored in practice due to its high precision without the need for precise time synchronization between devices [3], [4]. However, the computational and power limitations of devices within massive IoT networks present challenges in achieving a precise DoA estimation, creating a need for solutions that meet strict accuracy requirements while considering limited resources.

Various IoT communication standards have integrated DoA estimation functionality. High-accuracy indoor positioning is enabled in Bluetooth Low Energy (BLE) with its angle-of-arrival (AoA) / angle-of-departure (AoD) functionality [5]. Accurate localization in dense IoT networks in industrial environments is possible with DoA estimation within the 6TiSCH standard [6].

© 2025 The Authors. This work is licensed under a Creative Commons Attribution 4.0 License.
For more information, see https://creativecommons.org/licenses/by/4.0/

1023 IEEE OPEN JOURNAL OF ANTENNAS AND PROPAGATION, VOL. 6, NO. 4, AUGUST 2025 IEEE Open Journal of Antennas and Propagation

Single-RF chain systems are common in IoT devices due to cost constraints, where samples for DoA estimation are acquired by switching antenna elements using time-division multiplexing [7]. The accuracy of DoA estimation is reduced by the presence of carrier frequency offset (CFO) and antenna switching, which introduce additional phase shifts at the antenna elements. The CFO is caused mainly by the low-cost design with low-accuracy crystal oscillators and is additionally affected by temperature variations, component aging, and power stability fluctuations.

Estimation and correction methods are conventionally used to address the CFO effect on DoA estimation. Fine estimation leads to an unacceptably high computational overhead for resource-constrained IoT and embedded devices, affecting real-time responsiveness. Therefore, more computationally efficient methods are required. This study proposes to exploit the signal sampling order of antenna elements referred to as the antenna switching pattern (ASP). ASP is represented as an ordered sequence of antenna element indices that determines the sampling order of the signal across the antenna elements.

Sequential sampling (SS) is typically used with switching based on round-robin (RR), where antenna elements are activated sequentially in their spatial order, looping back to the first antenna element after completing a full cycle. In this work, we propose to optimize the ASP for reducing the systematic error in DoA estimation with the multiple signal classification (MUSIC) algorithm by considering the phase shifts at the antenna elements as counter-weighed weights and compensating the systematic error using the reverse order ASP configuration. The main contributions of the paper are summarized as follows:

- Formulation of the ASP optimization for mitigating the CFO impact on DoA estimation and ASP design;
- Performance evaluation of the optimized ASPs for uniform linear arrays (ULAs) and uniform circular arrays (UCAs) compared to a baseline SS approach;
- Analysis of the impact of noise and CFO on the effectiveness of the optimized ASPs;
- Experimental validation of DoA estimation with optimized antenna switching for CFO mitigation using measurements.

The remainder of the paper is organized as follows. After the introduction, the related work is summarized in Section II. Section III formalizes the antenna switching pattern optimization. The ASP performance evaluation with simulations is discussed in Section IV. Section V describes the experimental validation. Finally, the findings and future directions are summarized in Section VI.

II. RELATED WORK

Phase correction after CFO estimation is a conventional technique to reduce DoA estimation errors. A single antenna has to be used to obtain the samples because phase shifts exist for multiple antenna elements due to the different propagation lengths of the signal. For example, in the standardized direction estimation in BLE, a preamble with constant tone extension provides eight IQ samples acquired with a reference antenna. The CFO can be estimated with algorithms such as linear regression, the fast Fourier transform (FFT), the Moose algorithm, and MUSIC, which differ in the trade-off between accuracy and computational complexity [6], [8], [9]. High-precision algorithms such as MUSIC are accurate, computationally intensive, and may exceed the device's capabilities. Simpler and computationally lighter methods, such as linear regression, cannot provide the precision required for high-resolution DoA applications. Maximizing the samples over a long period, as in the return-to-first ASP, where the switching is based on returning to a reference antenna after sampling, results in more accurate CFO estimation while increasing the transmission time, power consumption, and likelihood of interference. Using samples for CFO estimation from sample slots longer than the acquisition time is another approach suggested for improving accuracy [6]. The accuracy of DoA estimation can be improved by exploiting the ASP. In [10], authors analyzed how the number of samples acquired on each antenna element before switching and the different ASPs affect the Cramér-Rao bound (CRB) for the estimation of sinusoidal parameters and the estimation of DoA. Through an exhaustive search, they identified the ASP that provided the lowest CRB and introduced a *Mirrored Rotation* ASP and showed that these two ASPs improve the performance over SS ASP.

Techniques developed for Doppler shift mitigation in frequency-modulated continuous wave (FMCW) radar systems can be adapted and applied to combat the CFO effect on DoA estimation accuracy due to the similarity of the problem. One of the main issues is the additional phase shift between antenna switching times correlated to the phase shifts caused by DoA impinging on the ULA for moving targets. An ASP was designed for the ULA configuration and a simple mathematical operation was applied on the first three antenna elements of the ASP to remove the effect of velocity on DoA estimation [11]. To eliminate phase shifts caused by motion without velocity estimation and correction, a double-time switching scheme based on reference samples equal to the number of antenna elements was proposed, where reference values are first acquired from a single antenna element, then the antenna elements are switched in sequential pattern, and the acquired phases are subtracted from the references [12]. Another approach without estimation-calibration procedure was proposed in [13] that introduces two ASPs where the sign of velocity-induced phase shifts alternates between the indices in the ASP, which produces high-frequency, windowed, sinusoidal-like phase shifts that minimally affect slope estimation and effectively reduce ghost targets. Switching performed in a single frequency modulation period considering randomized ASP was studied to evaluate how the different random realizations of ASP affect the resolution and sidelobe levels based on the analysis of the ambiguity function showing

that lowest sidelobes and resolution can be achieved with a random permutation of antenna element indexes varied for each modulation cycle [14].

Optimizing the ASP was applied in channel-sounding applications for extending the Doppler frequency estimation range for switched arrays with SS ASP, since a trade-off exists between an accurate AoA/AoD estimation, where more antenna elements result in better performance, and the range of Doppler frequency estimation, which is inversely proportional to the number of antenna elements. A simulated annealing algorithm was used for ASP optimization based on the Fisher information matrix, with the drawback that simulated annealing may converge to local minima instead of finding the global optimum [15]. For a realistic antenna array, the optimal ASP was found using a simulated annealing algorithm, and the effect of ASP on the ambiguity function was studied [16]. ASP optimization based on the objective function derived from the space-alternating generalized expectation maximization (SAGE) algorithm has been evaluated, showing that different ASPs not only extend the Doppler frequency estimation range, but also affect the side lobes of the objective function and consequently the robustness to noise [17]. To extend the study, a model of the MIMO channel sounding system based on the concept of bispatiotemporal apertures and using side-lobe level as a figure of merit to noise immunity was proposed [18].

III. ANTENNA SWITCHING PATTERN OPTIMIZATION

The impact of the CFO on the phase shifts at the antenna elements and the error in the DoA estimation are investigated using the signal model. Subsequently, the switching patterns are optimized to combat the influence of the CFO-induced phase shifts on the DoA estimation.

A. SIGNAL MODEL AND PROBLEM FORMULATION

Single-RF chain system model is studied with a M-element antenna array at the receiver and single antenna element at the transmitter considering a transmitted continuous wave (CW) signal $s_{Tx}(t)$, received signal $\mathbf{s}_{Rx}(t)$, and the CFO (Δf) effect as shown in Fig. 1. The transmitted signal is attenuated, delayed, and at the receiver down-converted with a receiver carrier frequency that is different from the transmitter carrier frequency f_c due to the CFO effect, i.e., the combined effect of carrier mismatch and a Doppler frequency shift due to the motion of the receiver or transmitter. The received signal is given by

$$\mathbf{s}_{Rx}(t) = \Re\{\, e^{\jmath 2\pi\cdot\Delta f\cdot t} e^{-\jmath\Phi}\cdot\mathbf{H}\}, \tag{1}$$

where the transmitted signal has unit amplitude, and Φ is the initial phase of the receiver's carrier signal. Here, $\mathbf{H}$ represents the channel gain vector, with each element $H_i = a_i\, e^{-\jmath 2\pi f_c \frac{d_i}{c}}$, where a_i and d_i denote the attenuation and distance between the transmitter and the i-th antenna element, respectively, for $i = 1, \ldots, M$, and c represents the speed of light.

Taking the point O as a reference, which is a distance d_0 away from the transmitter, the received signal at the antenna elements is expressed as

$$\mathbf{s}_{Rx}(t) = \Re\{a\; e^{\jmath 2\pi\,\Delta f t}\; e^{-\jmath\Phi}\; e^{-\jmath 2\pi f_c \frac{d_0}{c}}\mathbf{A}(\theta)\}, \tag{2}$$

where $\mathbf{A}(\theta) = [e^{-\jmath\mathbf{kr_1}}, e^{-\jmath\mathbf{kr_2}}, \ldots e^{-\jmath\mathbf{kr_M}}]^T$ is the antenna array steering vector denoting the phase shift due to DoA of the received signal at each element with respect to the antenna array reference point O, $\mathbf{r_i}$ is the vector from O to the i^{th} element, $\mathbf{k} = \mathbf{j}\frac{2\pi}{\lambda}$ is the wavenumber, λ is the wavelength of a CW signal, $\mathbf{j}$ is a unit vector in the direction of plane wave propagation, and a is the attenuation, which we assume to be the same for all antenna elements.

In single-RF chain systems, where only one antenna element samples the signal at a time, the sampling times for each antenna element must be specified. Assuming that each antenna element samples the signal once per cycle over N identical cycles and that $\mathbf{A}_{st}$ is a vector, where the value at the index i represents the i-th antenna element switch on index ranging from 1 to M, then the phase shifts due to DoA and CFO Δf at i-th antenna element are

$$\Delta\phi_i[n] \;= e^{-\jmath\mathbf{kr_i}}\; e^{\jmath 2\pi\,\Delta f(\mathbf{A}_{st}[i]-1+n\cdot M)T_s}, \tag{3}$$

where T_s is the sampling time and n is the index of the cycle in which the samples are taken raging from 0 to N.

The modified steering vector $\mathbf{A}'(\theta, \Delta f)$, accounting for phase shifts due to CFO Δf, which also represents the sampled phase differences on antenna elements, is then defined as

$$\mathbf{A}'(\theta, \Delta f)[n] = \begin{bmatrix} e^{-\jmath\mathbf{kr_1}}\; e^{\jmath 2\pi\,\Delta f(\mathbf{A}_{st}[1]-1+n\cdot M)T_s} \\ e^{-\jmath\mathbf{kr_2}}\; e^{\jmath 2\pi\,\Delta f(\mathbf{A}_{st}[2]-1+n\cdot M)T_s} \\ \vdots \\ e^{-\jmath\mathbf{kr_M}}\; e^{\jmath 2\pi\,\Delta f(\mathbf{A}_{st}[M]-1+n\cdot M)T_s} \end{bmatrix}. \tag{4}$$

For the SS ASP the $\mathbf{A}'(\theta, \Delta f)$ is

$$\mathbf{A}'(\theta, \Delta f)[n] = \begin{bmatrix} e^{-\jmath\mathbf{kr_1}}\; e^{\jmath 2\pi\,\Delta f\cdot(n\cdot M)}\; T_s \\ e^{-\jmath\mathbf{kr_2}}\; e^{\jmath 2\pi\,\Delta f\cdot(1+n\cdot M)}\; T_s \\ e^{-\jmath\mathbf{kr_3}}\; e^{\jmath 2\pi\,\Delta f\cdot(2+n\cdot M)}\; T_s \\ \vdots \\ e^{-\jmath\mathbf{kr_M}}\; e^{\jmath 2\pi\,\Delta f\cdot(M-1+n\cdot M)}\; T_s \end{bmatrix}, \tag{5}$$

Equation (4) highlights that the phase shifts at each antenna element are influenced not only by the DoA but also by the CFO, introducing errors in the DoA estimation if the CFO contribution is not addressed. The findings from paper [19] show the significant impact of neglecting CFO with SS ASP on DoA estimation with MUSIC algorithm: for example, with a sampling period of 16 μs and a CFO of 0.5 kHz, the mean absolute error across a specified DoA range exceeds 1°, demonstrating the sensitivity of DoA accuracy to even modest CFO values. The accuracy of DoA estimation is closely related to the chosen sampling period. For the validation of the proposed concepts by simulations and measurements, the sampling period of 16 μs is selected due to the hardware limitations used.

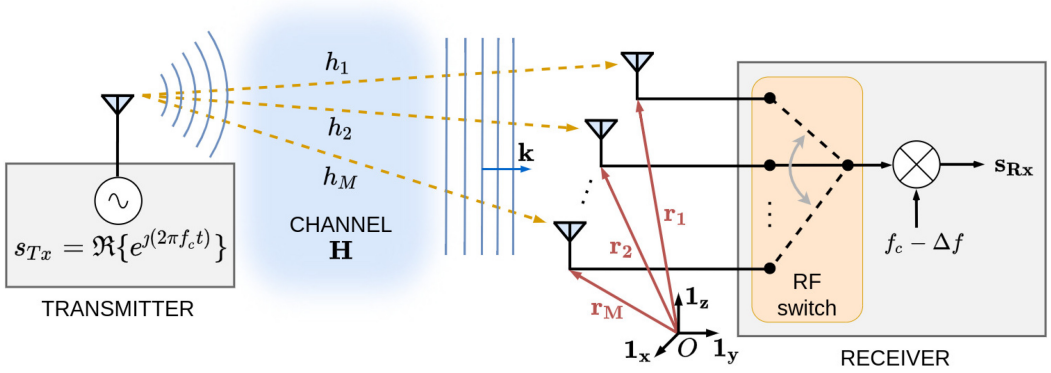


FIGURE 1. A system with a transmitter and a receiver with a single-RF chain.

B. ANTENNA SWITCHING PATTERN OPTIMIZATION METHODS

The ASP optimization techniques in this study involve two distinct approaches: spatially distributing phase progressions due to CFO associated with the antenna elements evenly around the center of the antenna array so that they contribute as noise rather than serving as a source of systematic error in DoA estimation, and using a reverse order ASP configuration to cancel out systematic error.

The evenly distributed CFO phase progressions are applied for ASP optimization in the method referred to as *EvenCFO-SP* [19]. The main design principle is to structure the ASP to result in CFO-induced phase shifts similar to additive noise, which, if sufficiently small, can be treated by the MUSIC algorithm as part of the noise subspace. The design is based on a heuristic idea in which the spatial weights are evenly distributed and counter-weighted to lower the systematic error when the CFO-induced phase shifts on the antenna elements are considered weights. The weights are spatially distributed by leveraging the order in the ASP. To find the optimal ASP based on the center of gravity calculation, an exhaustive search for the minimum cost function is performed. Optimal ASP for 8-element ULA was found to be [2, 4, 5, 6, 8, 7, 1, 3] and for 12-element UCA [2, 8, 11, 5, 6, 12, 3, 9, 10, 4, 7, 1].

The concatenation of the arbitrary order of the antenna element indices and its reverse is used in the ASP, referred to as *Mirror-SP*. The underlying principle of this method is that a particular ASP introduces a systematic error, which can be mitigated by the same ASP with the elements arranged in reverse order. This method is expected to be effective because applying an ASP in the reversed order produces error behavior equivalent to that induced by a negative CFO with the original ASP. At least two samples per antenna element are required, and the same number of samples per antenna element is needed in the reversed and the original sequence to avoid the reintroduction of systematic error. A separate or joint approach can be used to apply the reversed order ASP to the DoA estimation. In the separate approach, the DoA is first estimated separately with the arbitrary ASP in the original and reverse order. Then, the final DoA is calculated as the mean of the individual estimates. The joint approach applies the MUSIC algorithm for DoA estimation to the total samples acquired with concatenated ASPs of arbitrary ASP and its reverse order. In this study, the latter approach is considered, where the ASP is a concatenated sequence of the *SS* in original and reverse order, as shown in Figure 2, which illustrates the process of signal sampling with different ASPs during a sampling cycle, demonstrated on the example of the UCA with 12 antenna elements.

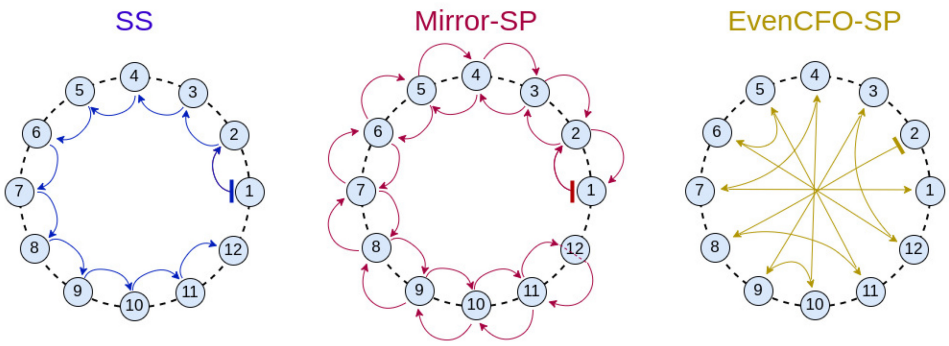
IV. EVALUATION OF DOA ESTIMATION ERRORS

We evaluated the performance improvement of DoA estimation using the MUSIC algorithm with the optimized ASPs compared to the *SS* ASP under different conditions through simulations in a MATLAB environment, focusing on two antenna array configurations: an 8-element ULA and a 12-element UCA. The DoA was estimated as the angle at which the pseudospectrum of the MUSIC algorithm reaches its maximum value. In particular, we analyzed the effects of different noise levels assuming a fixed CFO on the DoA estimation error across a range of DoA angles and investigated how different CFO values affect the DoA estimation error for a fixed DoA angle without noise. For *EvenCFO-SP*, we chose the ASPs listed in Section III-B.

A. NOISE IMPACT ON DOA ESTIMATION ERROR

The impact of different noise levels on *EvenCFO-SP* and *Mirror-SP* compared to *SS* ASP is analyzed.

The signal was generated for different DoAs over a range of signal-to-noise ratios (SNRs), with a fixed CFO of 1 kHz. DoA was estimated using the MUSIC algorithm with an angular resolution of 0.01° to calculate the pseudospectrum. To reduce the bias error due to the specific random sequence and to obtain statistically reliable results, a noise signal was generated 200 times for each SNR and the root mean squared error (RMSE) of the DoA estimates was calculated. For a ULA, the DoA ranged from 30° to 150°, where 90° corresponds to the direction perpendicular to the array axis, and for UCA it ranged from −180° to 180°. In both cases,



ASP method	ASP
SS	1, 2, 3, 4, 5, 6, 7, 8, 9, 10, 11, 12
Mirror-SP	1, 2, 3, 4, 5, 6, 7, 8, 9, 10, 11, 12, 12, 11, 10, 9, 8, 7, 6, 5, 4, 3, 2, 1
EvenCFO-SP	2, 8, 11, 5, 6, 12, 3, 9, 10, 4, 7, 1

FIGURE 2. Visualization of ASP methods for UCA with 12 elements.

the DoA step was 2°, the ASP was repeated sufficient times to acquire 6 IQ samples per antenna element, the carrier frequency was set to 2405 MHz, and the sampling period was 16 μs.

1) ULA EVALUATION

The RMSEs for the considered DoA range for ULA configuration and different SNRs is shown in Fig. 3. The case with 30 dB SNR serves as a reference where the noise minimises the DoA estimation error. For SNRs above 0 dB, the minimal RMSE occurs at the DoA of 90° and it increases when deviating from it, which is consistent with the ULA theory stating that the errors increase towards the end-fire directions of array [20]. As expected, the RMSEs increase with decreasing SNR. For SNRs above 0 dB, noticeably better performance is seen for *Mirror-SP* and *EvenCFO-SP* in comparison to *SS*. As the SNR decreases, the performance gain difference between the optimized ASPs and *SS* ASP is smaller, as can be seen in Table 1, showing the mean RMSE across the whole DoA range for all ASPs.

The performance gains of *Mirror-SP* and *EvenCFO-SP* compared to *SS* at an SNR of 30 dB are 2.282° and 2.287°, respectively. This decreases to 1.122° and 1.254°, respectively, for SNR of 1 dB. The SNR of 0 dB is a threshold at which noise starts to dominate over the phase shifts caused by CFO and DoA for all ASPs, and the noise effect becomes even more evident below 0 dB, leading to high RMSEs, which can be observed as a steep increase in RMSE values that are more prominent towards the end-fire directions of the array, where the system is more affected by noise. For SNRs of 1 dB and above, the *EvenCFO-SP* slightly outperforms the *Mirror-SP*, but the differences are small. Only for SNRs of 1 dB and 2 dB is the difference greater than 0.1°. This difference increases with decreasing SNR, and at high SNRs there is no significant difference.

TABLE 1. Mean RMSE of DoA estimates for 8-element ULA across the DoA range from 30° to 150° for different SNRs.

SNR	*SS*	*Mirror-SP*	*EvenCFO-SP*
30 dB	2.334°	0.052°	0.047°
20 dB	2.341°	0.165°	0.149°
10 dB	2.388°	0.524°	0.476°
6 dB	2.466°	0.845°	0.774°
3 dB	2.607°	1.247°	1.153°
2 dB	2.691°	1.441°	1.336°
1 dB	2.820°	1.698°	1.566°
0 dB	5.375°	6.945°	7.124°

2) UCA EVALUATION

RMSEs for the different DoAs, SNRs, and selected ASPs using 12-element UCA are shown in Fig. 4, and the results are summarized in Table 2.

For high SNRs, when the DoA estimation is negligibly affected by noise, the RMSE curve of the *SS* ASP has two minima approaching zero, which can be demonstrated with the results for SNR equal to 30 dB where the minima approach zero for DoAs around -105° and 75°. The RMSE curve peaks at approximately 3.66° between the minima. Fundamentally, DoA estimation algorithms compare the observed phase shifts on antenna elements with those of a set of candidate angles and look for the best match. For example, in the context of maximum likelihood estimation (MLE), one can write:

$$\hat{\theta} = \arg\min_{\phi} \sum_{i=1}^{M} \left| A_i'(\theta, \Delta f) \; - A_i(\phi) \right|^2, \tag{6}$$

where $A_i'(\theta, \Delta f)$ is the observed phase shift at the i-th antenna element, incorporating both DoA and CFO contributions, and $A_i(\phi)$ is the phase shift of a candidate

1027 IEEE OPEN JOURNAL OF ANTENNAS AND PROPAGATION, VOL. 6, NO. 4, AUGUST 2025 IEEE Open Journal of Antennas and Propagation

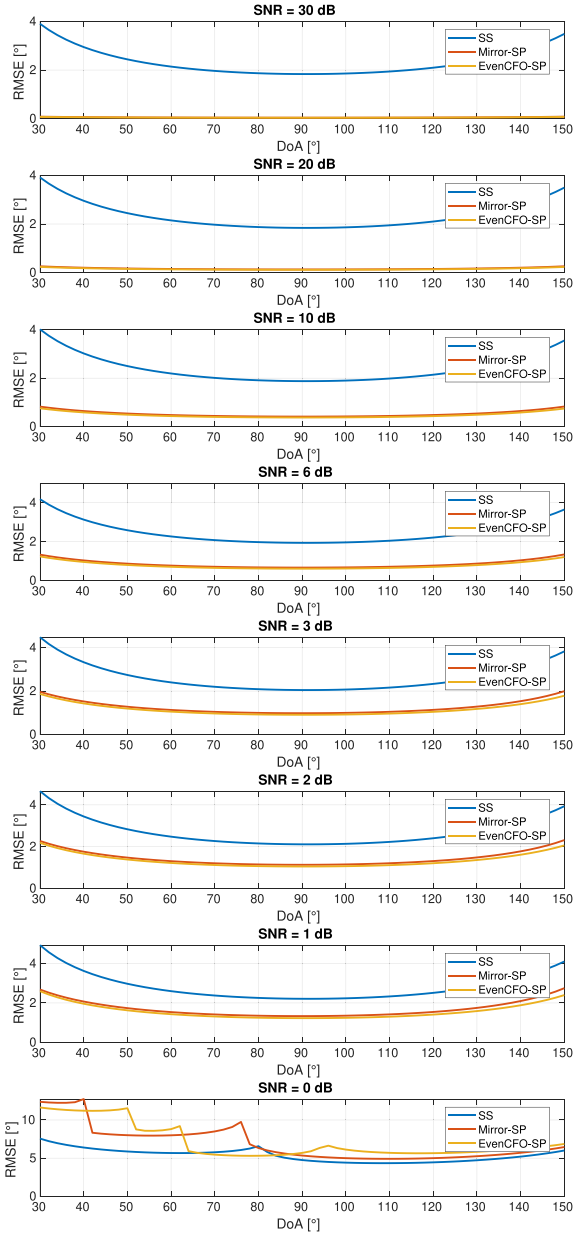


FIGURE 3. RMSE of DoA estimates for various DoAs, SNRs, and selected ASPs for the 8-element ULA, given a CFO of 1 kHz.

angle ϕ. The CFO distorts the ideal phase shifts determined by the DoA, which can make the observed phase shifts more similar to the phase shifts of an angle other than the true DoA. For UCA with a spacing of $\lambda/2$ between the antenna elements, the phase shifts due to DoA at the antenna elements are:

$$A_i(\theta) = \exp\Big(-j\tfrac{2\pi R}{\lambda}\cos\big(\theta - \tfrac{2\pi\,(i-1)}{M}\big)\Big), \tag{7}$$

where R is the radius of the array, and $i \in 1,,M$ is the antenna element index. The extent to which, for a given antenna element, the phase shift of neighboring angles of the true DoA is more similar to the observed phase shift compared to the ideal phase shift of the true DoA depends on the position of the cosine function at which the antenna element operates (which is determined by the true DoA) and on the magnitude of the additional CFO phase shift (which is determined by the ASP). This results in individual antenna elements favoring neighboring angles over the true DoA to varying degrees, and the overall estimation error depends on how all antenna elements collectively exhibit these preferences. For high SNRs, the minima in Fig. 4 of *SS* ASP occur when the phase shifts due to DoA and CFO best match the ideal phase shifts of true DoA, while maxima arise when the measured phase shifts best match the phase shifts of an angle farthest from the true DoA. By exploiting how the antenna elements sample the signal with different ASP configurations, we can control the amount of CFO-induced phase shifts at each antenna element to better match the ideal phase shifts of the true DoA. For example, by selecting *EvenCFO-SP*, the estimation error is zero for all DoAs as can be seen in Fig. 4 for 30 dB SNR and which is also the case for *Mirror-SP*. This shows the advantage of using optimized ASPs for accurate DoA estimation, especially for DoAs between the minima of the *SS* ASP curve.

TABLE 2. Mean RMSE of DoA estimates for 12-element UCA across the DoA range from -180° to 180° for different SNRs.

SNR	*SS*	*Mirror-SP*	*EvenCFO-SP*
30 dB	2.354°	0.056°	0.056°
20 dB	2.353°	0.177°	0.177°
10 dB	2.396°	0.566°	0.566°
6 dB	2.480°	0.910°	0.910°
3 dB	2.622°	1.319°	1.316°
2 dB	2.699°	1.503°	1.497°
1 dB	2.800°	1.726°	2.010°
0 dB	3.835°	3.068°	2.912°
-1 dB	10.405°	13.723°	10.007°

The *Mirror-SP* and *EvenCFO-SP* show a comparable performance down to an SNR of 1 dB, achieving similar mean RMSE values. In contrast, *EvenCFO-SP* shows slightly better performance in the case of the ULA. At an SNR of 1 dB, the *EvenCFO-SP* already exhibits some significant rectangle-shaped peak errors, whereas this is not the case for the other two ASPs. This indicates a low SNR threshold for *EvenCFO-SP* and that the estimation for some DoAs is more susceptible to noise. At an SNR of 0 dB, all ASPs exhibit multiple rectangle-shaped peak errors for DoAs more susceptible to noise, indicating that the influence of noise is significant for all ASPs, and at -1 dB the errors appear more random due to even higher noise level. Compared to *SS*, the *Mirror-SP* and *EvenCFO-SP* exhibit 1.196° to 1.830° lower mean RMSE for SNRs of 2 dB to 10 dB and above 2° for higher SNRs, as can be seen in Table 2.

B. CFO IMPACT ON DOA ESTIMATION ERROR

The noise impact on DoA estimation at a fixed value of CFO is analyzed in Section IV-A, while in this subsection,

we analyze the impact of different values of CFO on DoA estimation accuracy. We limit our analysis to DoAs of 90° and 60° for the ULA test case and −10°, 30° and 75° for UCA. In this respect, the analysis was carried out in the CFO range between −50 kHz and +50 kHz without adding Gaussian noise to the signal. The DoA was estimated using the MUSIC algorithm, and the absolute error (AE) was calculated for each CFO value.

1) ULA EVALUATION

The AEs for the different CFOs, ASPs, and DoAs when ULA is used, are shown in Fig. 5. The blue curve shows the AEs for the *SS* ASP. By comparing the *SS* curves for DoAs of 90° and 60°, it is evident that the curve for 90° is symmetric around the zero CFO line, while the symmetry does not exist for 60°. This can be explained by considering the scenario with two antenna elements, where the DoA denoted as θ is estimated based on the phase shift denoted as $\Delta\Phi$ between the antenna elements, according to the relationship

$$\theta = \arccos\left(\frac{\Delta\Phi\,\lambda}{2\pi d}\right), \tag{8}$$

where d is the distance between antenna elements. $\Delta\Phi$ is the sum of $\Delta\Phi_{DoA}$, which is the phase shift due to the different travel distances depending on DoA, and the $\Delta\Phi_{CFO} = 2\pi\,\Delta f\,T_s$, which is the phase shift due to CFO Δf. This sum indicates that the $\Delta\Phi_{DoA}$ component establishes the operating point of the arccos function, which can then be shifted to the left or right depending on the sign of the $\Delta\Phi_{CFO}$ component, as illustrated in Fig. 6 when d is $\lambda/2$. For a DoA of 90°, $\Delta\Phi_{DoA}$ is zero, resulting in an operating point at $(0, 90°)$. The function arccos is approximately linear and symmetric when its argument is close to zero, so the value of the function for a positive CFO is equal to its negative counterpart. This explains the symmetry and approximately linear behavior of the AE curve of *SS* for low CFO values.

However, the arccos function exhibits non-linearity for non-zero arguments, resulting in different AEs for DoAs that deviate from 90° when a positive CFO is compared to its negative counterpart. The further the DoA deviates from 90°, the greater the asymmetry and slope of the curve, resulting in larger AEs caused by the CFO.

Comparison of AE curves for *SS* for DoAs of 60° and 90° in Fig. 5 shows a steeper slope near 0 Hz CFO for DoA of 60°, leading to larger AEs. The CFO frequency at which the AE of the *SS* ASP reaches its maximum is determined when the argument of the arccos function is 1. If d is $\lambda/2$, this frequency is calculated as $\Delta f = \frac{\pm 1 - \cos(\theta)}{2T_s}$. It is also worth noting that the ASP with the reversed elements of the *SS* sequence produces a curve that mirrors the *SS* ASP curve around zero CFO line.

Mirror-SP and *EvenCFO-SP* are represented by the red and yellow curves, respectively. For small absolute values of CFO, the AEs for both ASPs and both considered DoAs are 0°, demonstrating the proposed CFO-independent DoA estimation approach, which is the aim of this paper.

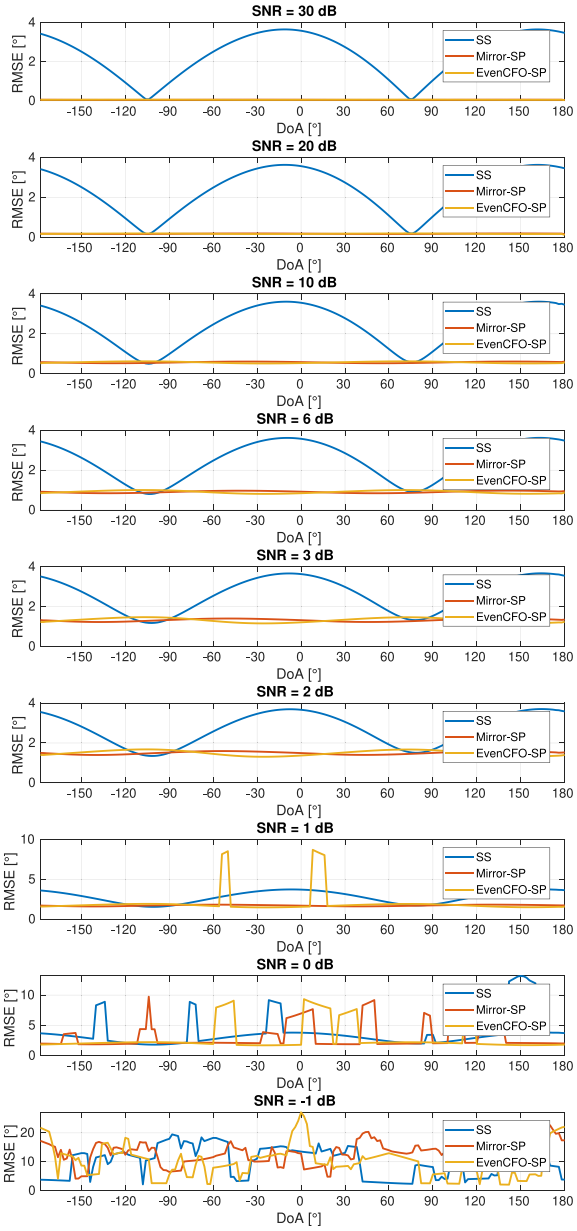


FIGURE 4. RMSE of DoA estimates for various DoAs, SNRs, and selected ASPs for a UCA with 12 elements, given a CFO of 1 kHz.

At ±3900 Hz, the AE of *Mirror-SP* jumps instantaneously, indicating the low and high frequency bounds of the CFO, beyond which the proposed approach is no longer effective. Empirical analysis based on our observations have shown that these bounds are independent of DoA, the configuration of the antenna elements and the number of samples per antenna element, and for the MUSIC algorithm are equal to $\pm 1/(2\,T_s\,M)$. Beyond these bounds, an ambiguity between two peaks in the MUSIC pseudospectrum is observed, leading to DoA estimation errors similar to those when

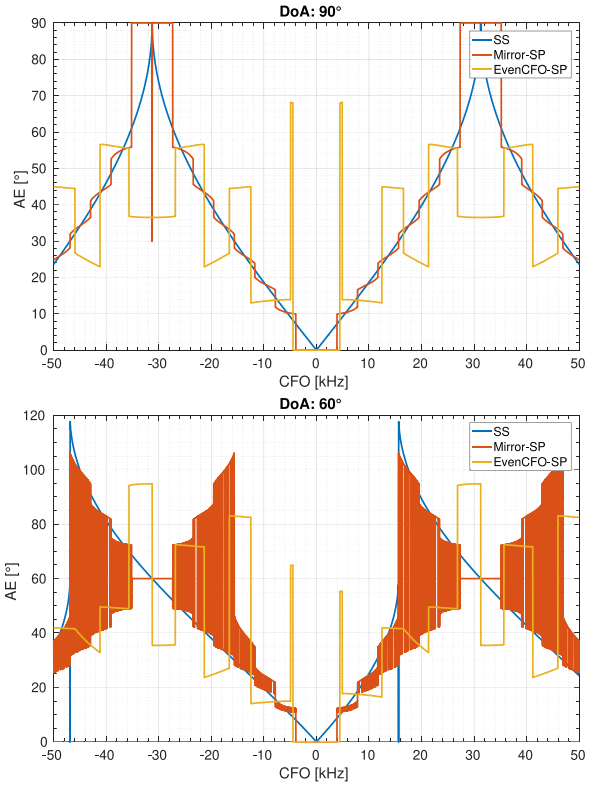


FIGURE 5. AEs of different CFOs at fixed DoA for 8-element ULA with no added noise.

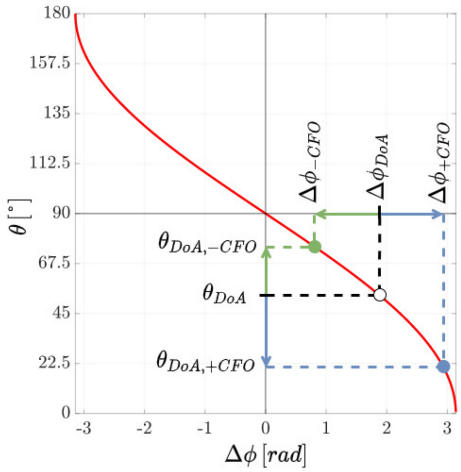


FIGURE 6. CFO effect on DoA estimation.

using *SS* ASP and ASP with reverse order elements of *SS*. This effect is shown in Fig. 7, where two MUSIC pseudospectra are depicted: one with CFO within the identified frequency bounds, demonstrating the optimal performance of *Mirror-SP*, and another with CFO exceeding these bounds, demonstrating the two-peak ambiguity problem, where none of the peaks have the position at the correct

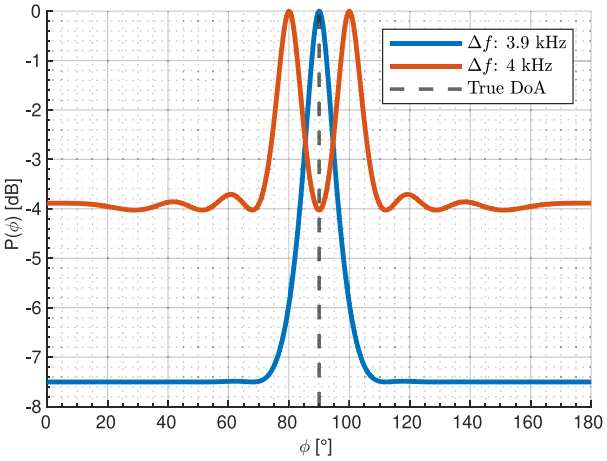


FIGURE 7. MUSIC pseudospectra for ULA and the DoA of 90° showing the impact of CFO on the pseudospectrum when *Mirror-SP* is used for CFO below (3.9 kHz) and above (4 kHz) the frequency bound.

angle. If the *SS* ASP or its reverse order counterpart are individually employed for DoA estimation under CFO conditions, both produce a single dominant peak in the MUSIC pseudospectrum: the *SS* ASP yields a peak that is shifted relative to the true DoA due to the CFO, while its reverse order counterpart yields a peak that is shifted equivalently to the scenario of using *SS* ASP with a negative CFO. Since *Mirror-SP* is a concatenation of these two ASPs, the resulting pseudospectrum of *Mirror-SP* also contains two peaks at approximately the same positions as those of the individual ASPs, although not exactly the same due to the mutual influence of the peaks. Due to numerical errors inherent in the computational process, there are small differences in amplitude between these peaks. Since the DoA is determined by finding the angle corresponding to the highest peak, these small numerical fluctuations lead to frequent instantaneous jumps in AE beyond the CFO frequency bounds, whose envelopes approximately follow the AE curves of the *SS* ASP and its mirrored version around the zero CFO line corresponding to *SS* ASP with reversed order of the elements. Within the CFO bounds, *Mirror-SP* performs optimally because the two peaks in the MUSIC pseudospectrum remain closely spaced and due to the limited resolution of the MUSIC algorithm, they are effectively merged into a single peak centered at their mean position, which coincides with the correct DoA.

Similar to *Mirror-SP*, the CFO bounds for *EvenCFO-SP* are observed at ±4450 Hz, which are slightly higher than those of *Mirror-SP* and are also independent of DoA, antenna elements configuration, and the number of samples per antenna element. Beyond these bounds, the errors are high but change less frequently than for *Mirror-SP*. The effect of different CFOs manifest as distinct patterns of peaks in the MUSIC pseudospectrum. When the CFO is close to zero, a single dominant peak corresponding to the correct DoA estimate is observed. As the CFO increases, a

secondary peak emerges that increases in size. As long as this secondary peak is lower than the primary peak, the correct DoA estimate is maintained. However, if the CFO continues to increase, the secondary peak exceeds the primary peak in magnitude and becomes the dominant peak. This transition leads to a sudden jump in the estimation error, marking the CFO bounds. As the CFO continues to increase, yet another peak appears, repeating the pattern of a new peak gradually strengthening until it dominates the pseudospectrum causing a sudden jump in the estimation error. This behavior explains the observed jumps in the AE curve, with relatively stable regions in between.

Although it may initially seem advantageous to use *SS* ASP, given that *EvenCFO-SP* has limited CFO bounds where the AE increases significantly, the AEs of *SS* ASP at CFO bounds of *EvenCFO-SP* are already 8.23° for a DoA of 90° and are even larger for DoAs that deviate from 90°. For a DoA of 60° the errors are 10.03° and 9.1°. These errors are insufficient for most applications. The significant jump in error can also be seen as an advantage when estimating DoA from several consecutive estimates, as outliers can be easily detected.

It is worth noting that CFO bounds of optimized ASPs may vary with the choice of DoA search algorithm. We observed differences when using MUSIC, MLE and angle-FFT, as the algorithms may react differently to CFO-induced phase distortions. The CFO bounds presented here are specific to the MUSIC algorithm and may change for other algorithms. Although a detailed analysis is beyond the scope of this paper, this remains an interesting direction for future research.

The AE of *SS* ASP, and consequently the performance improvement of the proposed methods within CFO bounds, can be calculated using (8) as follows:

$$AE = |\arccos(cos\theta + 2 \cdot \Delta f \cdot Ts) - \theta|. \tag{9}$$

In linear region of arccos and for angles close to 90° the relation approximates to

$$AE \approx 2 \cdot |\Delta f| \cdot Ts. \tag{10}$$

2) UCA EVALUATION

For the UCA analysis, we chose DoAs of −10°, 30°, and 75° to capture a range of AE behaviors associated with the *SS* ASP, which is DoA dependent and has two minima with a peak in between, as shown in Fig. 4. For a DoA of -10° (which roughly corresponds to the maximum of *SS* ASP in Fig. 4), the optimized ASPs should provide the largest performance gain, while no gain is expected at 75° (which corresponds to the minimum of *SS* ASP in Fig. 4). The DoA of 30° represents a medium-case scenario with moderate improvement potential. Fig. 8 shows the AEs for different CFOs for the aforementioned DoAs.

The results for DoAs of −10° and 30° show that for small absolute CFO values (close to 0 Hz) the AEs of the *SS* ASP increase approximately linearly, whereby the AEs for a DoA of −10° are larger than those for 30°, which is consistent with the positions of the maxima from the results in Fig. 4. In contrast, both *Mirror-SP* and *EvenCFO-SP* have zero AEs, demonstrating their effectiveness in eliminating the CFO effect in DoA estimation within their CFO bounds. At higher absolute values of CFO, all three ASPs show significant jumps in DoA estimation errors. For *Mirror-SP*, the CFO frequency bounds occur at ±2600 Hz, which is lower than in the ULA case due to the larger number of antenna elements used. In contrast, the CFO bounds for *EvenCFO-SP* are slightly higher than those for *Mirror-SP* and are DoA dependent, with not necessarily equal positive and negative bound. Across all angles, none of the ASPs exhibit symmetry about the zero CFO line.

For a DoA of 75°, all three ASPs have 0° AEs within their CFO bounds, with the absolute bounds of *SS* ASP being the highest and those of *Mirror-SP* the lowest. Notably, the error-free estimates within the CFO bounds of *SS* ASP for this DoA coincide with the positions of the minima in Fig. 4.

For *EvenCFO-SP*, the effect of CFO on the MUSIC pseudospectrum within and beyond the CFO bounds approximately follows the patterns observed in the ULA case. For *Mirror-SP*, the behavior in UCA differs from ULA, especially beyond the CFO bounds, where the AE curve does not show frequent jumps as observed in the ULA case due to the two-peak ambiguity. Although two dominant peaks are still seen in the MUSIC pseudospectrum beyond the CFO bounds, they have unequal magnitudes, resulting in more stable AE regions where the AE curve does not change much with respect to CFO changes. At sufficiently high CFO values, the MUSIC pseudospectrum no longer resembles the two-peak structure anymore, but rather the pseudospectra of *EvenCFO-SP*. Similarly, *SS* ASP shows sharp transitions in AE curve, as the phase shifts due to DoA and CFO are not correlated in contrast to the ULA case.

V. EXPERIMENTAL VALIDATION

The experimental validation involves a comparison of *SS*, *EvenCFO-SP* and *Mirror-SP* using an 8-element ULA and a 12-element UCA [21]. For a fixed angle, different CFOs were systematically introduced at the receiver (RX), and the AEs of the DoA estimates were analyzed to compare the performance of the selected ASPs and identify the frequency bounds. The results are presented both without and with CFO calibration.

A. MEASUREMENT SETUP

Measurements were performed outdoors in a small park without close obstacles to minimize the multipath effect, which is not the focus of this paper. The transmitter (TX) was positioned at a fixed location with a transmit power of approximately 14 dBm at the output of the transceiver, and the RX was placed on a rotating stand, allowing it to rotate around the center of the antenna array. This setup enabled the estimation of DoA at multiple angles relative to the TX. For the ULA configuration, the measurement was performed

1031 IEEE OPEN JOURNAL OF ANTENNAS AND PROPAGATION, VOL. 6, NO. 4, AUGUST 2025 IEEE Open Journal of Antennas and Propagation

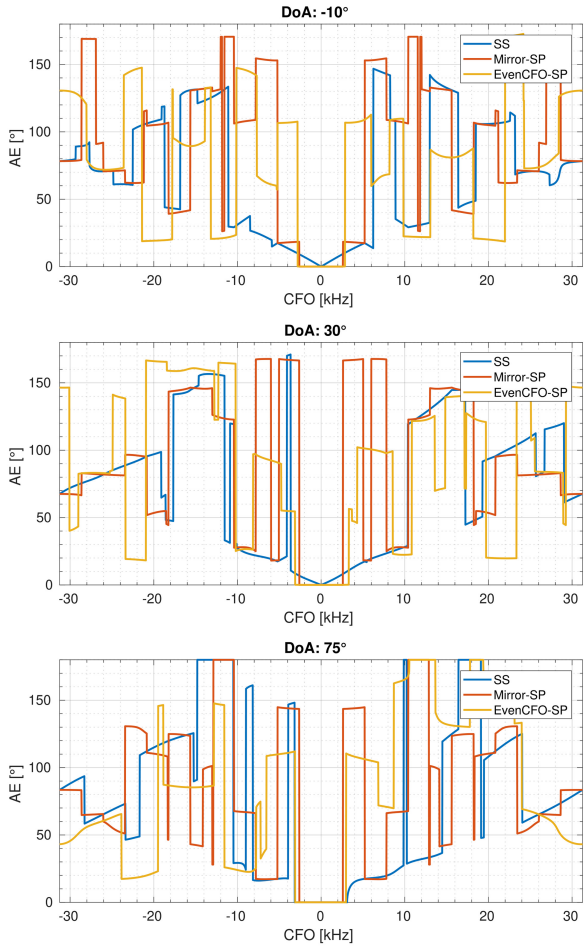


FIGURE 8. AEs of different CFOs at fixed DoA for 12-element UCA with no added noise.

at a DoA of 90°, while for the UCA the measurements were performed at −30°, 30°, and 90°. The angles for the UCA were chosen as multiples of 30° to facilitate the measurement procedure, particularly the exact positioning of the RX, and to approximately match the simulation setup.

The TX and RX were positioned 2.5 m apart to satisfy the far-field condition of the antenna arrays and mounted at the same height, approximately 1.5 m above the ground. Both antenna arrays have an antenna element spacing of 6 cm. The operating frequency was set to 2405 MHz. The initial results indicated that the activity of the nearby WiFi access points is lowest in this frequency band, resulting in reduced interference. For measurements with ULA, we used transceivers with low-cost microcontrollers [22] and an IEEE 802.15.4-compliant radio AT86RF215 with a Phase Measurement Unit (PMU) for register-based phase monitoring of the received signal [23]. We used OpenMote-B boards based on the same radio for the UCA case. To extend the single-RF signal chain of the radio, the devices incorporate a 12 or 8 channel RF switch [24]. The sampling



FIGURE 9. Measurement setup.

period was 16 μs, matching the simulation setup. The measurement setup is shown in Fig. 9.

We considered a similar implementation of the sampling and switching scheme as in [6], where the first 8 IQ samples are acquired at the reference antenna for the coarse CFO calibration, followed by sampling the signal with *SS*, *EvenCFO-SP*, and *Mirror-SP* in this order. This sampling scheme ensures that coarse calibration is performed on the same reference samples for all ASP methods, allowing for unbiased comparison unaffected by different CFO estimation results. The problem arises if CFO has a high drift. Then the CFO estimate may only be accurate for the *SS* ASP, as it follows the reference samples and may be obsolete for the other two ASPs. We assumed the CFO drift is small enough to mitigate this issue. For DoA estimation, we acquired 10 IQ samples on each antenna element in the case of ULA and 6 IQ samples in the case of UCA, which is the maximum possible considering the limitation of 90 sample slots available and maintain an even number of samples, as *Mirror-SP* performs best with even sample counts.

The measurements were performed with the RX operating at a frequency offset from the center frequency ranging from -20.196 kHz to 20.196 kHz in steps of 396 Hz, which is the minimum carrier frequency step supported by the radio. Based on prior measurements, we assumed that the CFO of the devices would be within this range. At each RX frequency offset, 50 DoA estimates were obtained using the MUSIC algorithm for the ULA case and 100 for the UCA case. Since the measurements for UCA had a lower SNR, we doubled the number of DoA estimates. The AE was then calculated as the median of these 50/100 measurements minus the true angle.

Since the expected differences in performance between the selected ASPs are on the scale of several degrees, even small inaccuracies in angular positioning during the measurements could lead to significant deviations that would strongly influence the interpretation of the results. Therefore,

the measurements were first processed by applying the MLE algorithm to calculate the exact DoA and CFO for each angle set when the frequency offset at the RX was set to 0 Hz, using all collected IQ samples for a given ASP. However, these estimates showed slight variations between ASPs due to additional factors such as hardware imperfections, CFO drift, etc. To address this differences, the average of the estimated DoAs of all ASPs was taken as the calibrated angle, which was subsequently used as the true reference angle for the measurement setup.

B. ULA EXPERIMENTAL EVALUATION

The AE as a function of the frequency offset at the RX for the ULA case without CFO calibration is shown in Fig. 10(a). The *SS* ASP is used as a reference, as it is expected that the AE reaches its minimum at the frequency offset that compensates for the real CFO of the devices due to hardware imperfections. For our TX-RX pair, this occurs at a value slightly above 5 kHz, and is referred to as the compensated CFO point (CCFOP). For this reason, the curves in Fig. 10(a) are shifted for the real CFO value compared to the simulation results in Fig. 5. The results demonstrate a linear trend in AE growth as the frequency offset deviates from the CCFOP, aligning with the simulation findings presented in Section IV-B. There is also a good alignment between simulation and measurement results for the optimized ASPs.

We empirically define a flat region as a region within the positions of a rapid jump in the AE that resembles a step-like transition corresponding to CFO bounds. For *EvenCFO-SP* the mean and standard deviation of AEs within the flat region are 0.14° and 0.07°, respectively, while for *Mirror-SP* they are 0.47° and 0.28°. The slightly higher AEs observed for *Mirror-SP* can be attributed to its greater sensitivity to noise, as shown with simulations in Section IV-A, as well as to the imperfect process of true angle calibration. For comparison, the mean and standard deviation of the AEs for the *SS* ASP within the flat region of *EvenCFO-SP* are 4.32° and 2.60°, while within the flat region of *Mirror-SP* they are 3.81° and 2.15°, respectively.

The flat region of *EvenCFO-SP* has a width of $BW_{CFO} =$ 8.316 kHz, while the width of *Mirror-SP* is $BW_{CFO} =$ 7.524 kHz, which agrees with the simulation results where the *EvenCFO-SP* region is 2×4450 Hz$=$ 8900 Hz wide and the *Mirror-SP* region is 2×3900 Hz$=$ 7800 Hz wide, especially considering that the minimum frequency step is 396 Hz and that additional simulations with noise have shown that BW_{CFO} decreases as the noise level increases. The measured results show a difference between the center frequencies of the flat regions for *EvenCFO-SP* and *Mirror-SP*, which should be the same according to the simulation results in Section IV-B. This deviation indicates a drift in actual CFO between the measurements for *EvenCFO-SP* and *Mirror-SP*.

A disadvantage of *EvenCFO-SP* is that significant errors can occur if the CFO values are outside the flat region. In

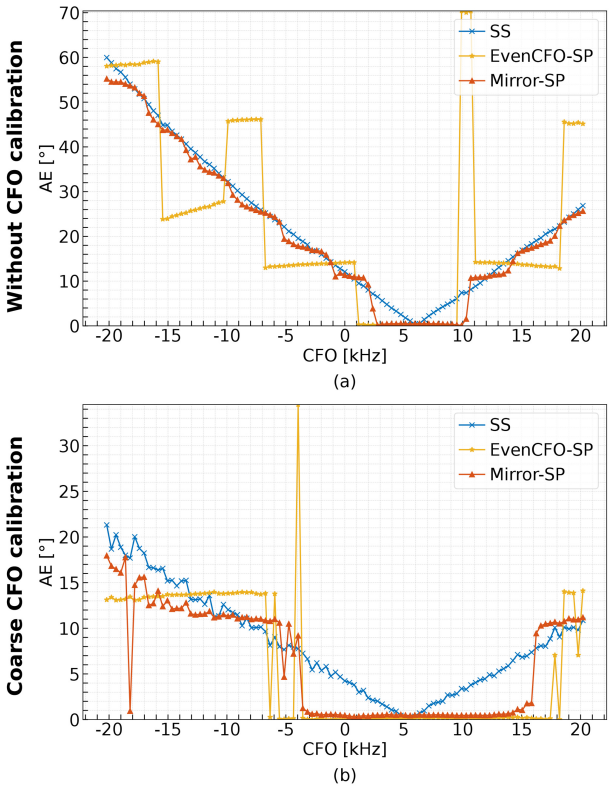


FIGURE 10. AEs for ULA for DoA of 90° considering different frequencies offset at RX without and with coarse CFO calibration.

contrast, *Mirror-SP* shows error behavior similar to that of *SS* ASP in such cases. To ensure optimal performance of optimized ASPs, it is crucial that the CFO is within the frequency bounds ($|\Delta f| < BW_{CFO}/2$). Since these bounds may be too low for some IoT devices, optimized ASPs combined with a coarse CFO estimation and calibration offer a computationally efficient alternative. This approach only requires sufficient accuracy of the CFO calibration to ensure that the corrected CFO remains within the frequency bounds of the specific ASP. To implement this approach, coarse CFO estimation and calibration was performed on 8 reference samples sampled with antenna 1, which was chosen arbitrarily. Since the signal is sampled at 1/8 of the baseband frequency, the CFO remains the only frequency component in the sampled signal. The CFO was estimated using a Fourier transform with a zero padding of length 256, followed by a parabolic interpolation considering the first neighborhood samples as described in [6]. DoA estimation was then performed on the corrected phase samples as described above. The results are shown in Fig. 10(b). If the CFO calibration were perfect, all ASPs would have an error of 0° across all Rx frequency offsets. However, due to the limited number of samples available, limited CFO estimation resolution, hardware imperfections such as sampling time inaccuracies and the relatively short observation period used for the CFO estimation, errors are to be expected.

1033 IEEE OPEN JOURNAL OF ANTENNAS AND PROPAGATION, VOL. 6, NO. 4, AUGUST 2025 IEEE Open Journal of Antennas and Propagation

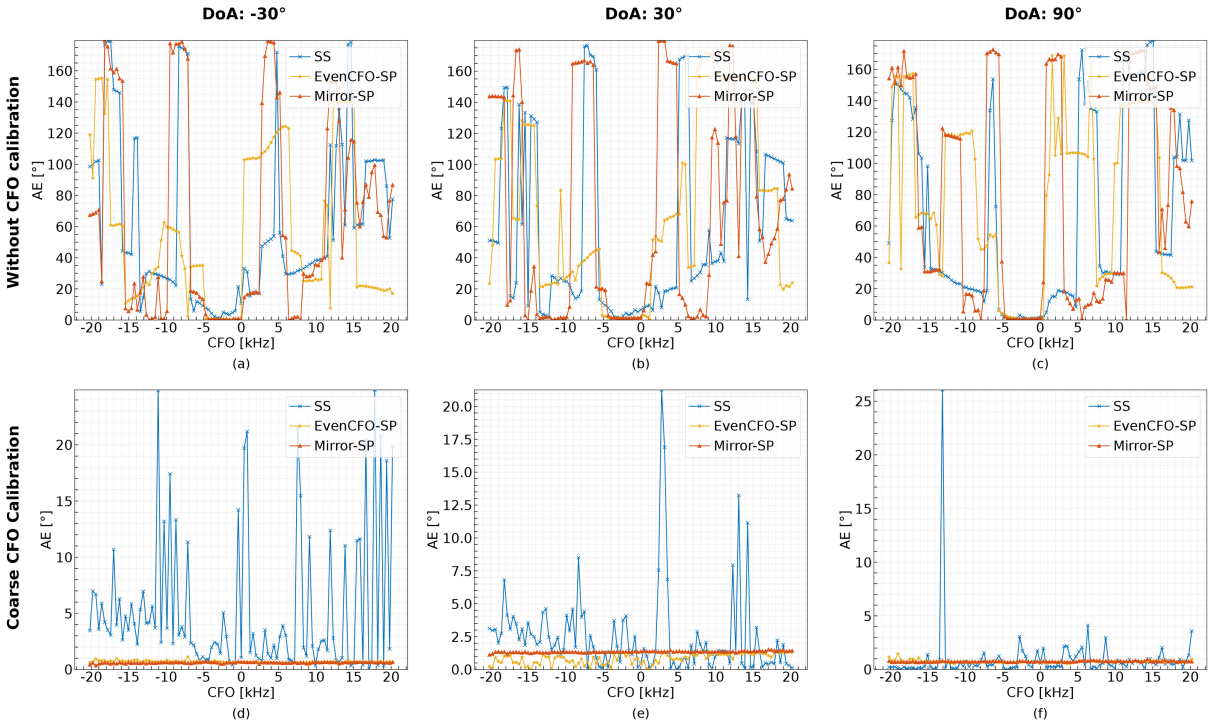


FIGURE 11. AEs for UCA for DoAs of -30°, 30°, and 90° considering different frequencies offset at RX without and with coarse CFO calibration.

The results show that with coarse CFO calibration, the flat regions around the CCFOP point of *EvenCFO-SP* and *Mirror-SP* are larger than in the case without CFO calibration, indicating that the CFO calibration was partially successful. For regions outside the flat regions of *EvenCFO-SP* and *Mirror-SP*, similar conclusions can be drawn as from the results without CFO calibration. With more accurate CFO estimation, the wider flat regions of *EvenCFO-SP* and *Mirror-SP* are expected. The mean value and standard deviation of AEs of *EvenCFO-SP* within its flat region are 0.10° and 0.07°, respectively, while for *Mirror-SP*, they are 0.60° and 0.30°. For comparison, the calculated mean and standard deviation of the AEs for the *SS* ASP within the flat region of *EvenCFO-SP* are 4.01° and 2.36° and within the flat region of *Mirror-SP* they are 3.68° and 2.12°.

TABLE 3. Comparison of ASPs in DoA estimation metrics for UCA without CFO calibration.

ASP	Metric	-30°	30°	90°
EvenCFO-SP	Mean	0.79°	1.35°	1.59°
	Std	0.32°	0.64°	1.57°
	BW_{CFO}	4752 Hz	6336 Hz	5940 Hz
SS*	Mean	6.07°	5.58°	1.71°
	Std	5.09°	3.10°	1.58°
Mirror-SP	Mean	0.51°	1.59°	1.03°
	Std	0.27°	0.44°	0.37°
	BW_{CFO}	4356 Hz	4356 Hz	4752 Hz
SS**	Mean	5.94°	4.20°	1.19°
	Std	5.28°	2.22°	0.78°

* SS within the *EvenCFO-SP* flat region
** SS within the *Mirror-SP* flat region

C. UCA EXPERIMENTAL EVALUATION

AEs for UCA at different RX frequency offsets without CFO calibration are shown in Fig. 11(a)-(c). Due to the use of different transceiver devices for the UCA measurements, the CCFOP differs from the ULA case and is approximately -2.3 kHz. Although the measurements with UCA have higher noise compared to the ULA measurements, the flat regions where *EvenCFO-SP* and *Mirror-SP* perform optimally are clearly visible.

Mean values and standard deviations (Std) of AEs within the flat regions of the optimized ASPs are listed in Table 3. These values are compared with those of the *SS* whose samples are within the same flat regions of the corresponding optimized ASP. As predicted by the simulations, the performance gain of the optimized ASPs compared to *SS* is highest at a DoA of -30°, with the difference in mean value between *SS* and *EvenCFO-SP* being 5.28° and the difference between *SS* and *Mirror-SP* being 5.43°. The performance gain is lower for a DoA of 30°, with differences in mean value of 4.23° for *SS* versus *EvenCFO-SP* and 2.61° for *SS* versus *Mirror-SP*. The smallest performance gain occurs at a DoA of 90°, where the mean values for *SS*, *EvenCFO-SP* and *Mirror-SP* are almost identical. Due to the high noise

TABLE 4. Comparison of ASPs in DoA estimation metrics for UCA with coarse CFO calibration.

ASP	Metric	-30°	30°	90°
EvenCFO-SP	Mean	0.70°	0.84°	0.75°
	Std	0.08°	0.39°	0.12°
Mirror-SP	Mean	0.61°	1.35°	0.76°
	Std	0.05°	0.06°	0.05°
SS	Mean	5.31°	2.50°	0.96°
	Std	6.22°	3.27°	2.60°

level, a direct comparison between *EvenCFO-SP* and *Mirror-SP* is difficult; however, the measurements indicate similar performance for both. The measured BW_{CFO} are slightly lower than the simulated values, which is also observed for the ULA case. The higher measured BW_{CFO} of *EvenCFO-SP* compared to that of *Mirror-SP*, agrees with the simulations.

AEs for UCA at different RX frequency offsets with coarse CFO calibration, as previously described for the case of ULA, are shown in Fig. 11(d)-(f). In this case, the coarse CFO calibration proved to be sufficiently accurate for all DoAs, so that the flat regions of the optimized ASP extend over the entire RX frequency offsets. The CFO estimates achieved higher accuracy compared to the ULA case due to lower sampling time inaccuracies in the hardware used for the measurements with the UCA. The AEs of the *SS* ASP are more scattered as they depend on the efficiency of the CFO calibration compared to the AEs of the optimized ASP. The standard deviations of the ASPs are listed in Table 4 showing that the scatter of the *SS* AEs is highest for DoA of -30°, lowest at 90° and in between at 30°, which is consistent with the AEs of *SS* as a function of CFO within the flat regions of the optimized ASPs, as shown in Section IV-B. For a DoA of 90°, the mean value of the AEs of *SS* is comparable to the optimized ASPs. For DoA of -30°, the difference in the mean value between *SS* and *EvenCFO-SP* is 4.61° and the difference between *SS* and *Mirror-SP* is 4.70°. For DoA of 30°, these differences are 1.66° and 1.15° for *EvenCFO-SP* and *Mirror-SP*, respectively.

VI. CONCLUSION

In this study, we addressed the challenge of minimizing the effect of CFO on DoA estimation without increasing computational complexity. Compared to the standard *SS* approach, we demonstrated the performance improvements of two optimized ASPs, *EvenCFO-SP* and *Mirror-SP*. The three ASPs were evaluated under two antenna array configurations: the ULA and UCA. Through simulations, we analyzed the impact of noise on DoA estimation accuracy for all three ASPs at various angles. The results indicate that the performance gain of the optimized ASPs decreases with decreasing SNR. Additional simulations examined how varying CFO levels influence the AE of the optimized ASPs, revealing that each has specific CFO bounds within which it performs optimally. The results of the experimental validation are consistent with the simulations, affirming that when a coarse CFO correction is applied, the CFO bounds for optimal performance can be extended. This correction can be implemented with lower computational cost, achieving accuracy within the kHz range, compared to fine CFO estimation. Consequently, optimized ASPs are well suited for embedded or IoT devices with limited computational resources. This approach also allows fewer IQ samples to be allocated to CFO estimation, increasing the number of samples available for DoA estimation, which improves localization accuracy. The advantage of the optimized ASP approaches used in this study is that they avoid the computationally impractical exhaustive ASP search required by previous methods to find the optimal ASP, as they are independent of the number of antenna elements, with *Mirror-SP* using any ASP as a basis and *EvenCFO-SP* employing a heuristic strategy. Although the focus of this paper is on the performance gain by using optimized ASP for DoA optimization with the MUSIC algorithm, we have observed a similar performance gain also for the angle-FFT algorithm and parametric algorithms such as maximum likelihood estimation (MLE), provided that the search parameter is restricted to DoA and the CFO is assumed to be zero. Furthermore, we anticipate that similar conclusions can be applied to other subspace-based DoA estimation algorithms such as Estimation of Signal Parameters via Rotational Invariant Techniques (ESPRIT) and Root-MUSIC. In future work, we plan to extend antenna switching optimization by considering different switching schemes in the sampling cycles, modify *Mirror-SP* to use different base switching schemes, and investigate how the optimized ASPs effectively mitigate the CFO effect in DoA estimation with algorithms other than MUSIC.

REFERENCES

[1] Y. Li et al., "Toward location-enabled IoT (LE-IoT): IoT positioning techniques, error sources, and error mitigation," *IEEE Internet Things J.*, vol. 8, no. 6, pp. 4035–4062, Mar. 2021. [Online]. Available: https://ieeexplore.ieee.org/document/9184896

[2] F. Zafari, A. Gkelias, and K. K. Leung, "A survey of indoor localization systems and technologies," *IEEE Commun. Surveys Tuts.*, vol. 21, no. 3, pp. 2568–2599, 3rd Quart., 2019. [Online]. Available: https://ieeexplore.ieee.org/document/8692423

[3] N. Paulino and L. M. Pessoa, "Self-localization via circular Bluetooth 5.1 antenna array receiver," *IEEE Access*, vol. 11, pp. 365–395, 2023. [Online]. Available: https://ieeexplore.ieee.org/document/10003199

[4] Y. Yuan, C. Liu, L. Zhou, Z. Xu, Z. Liu, and K. Ma, "Improving AOA accuracy in BLE-based Localization with a hierarchical estimation framework and phase correction mechanism," *IEEE Trans. Instrum. Meas.*, vol. 73, pp. 1–10, 2024. [Online]. Available: https://ieeexplore.ieee.org/document/10643481

[5] "Bluetooth core specification, V.5.1," Bluetooth, SIG, Kirkland, WA, USA, Rep. 5.1, 2019. Accessed: Nov. 18, 2024. [Online]. Available: https://www.bluetooth.com/specifications/specs/core-specification-5-1/

[6] G. Morano, A. Simončič, T. Kocevska, T. Javornik, and A. Hrovat, "Angle of arrival estimation using IEEE 802.15.4 TSCH protocol," in *Proc. IEEE 34th Annu. Int. Symp. Pers., Indoor Mobile Radio Commun. (PIMRC)*, 2023, pp. 1–7. [Online]. Available: https://ieeexplore.ieee.org/document/10293886/

[7] D. Xiao, S. Hu, K. Kang, and H. Qian, "An improved AoA estimation algorithm for BLE system in the presence of phase noise," *IEEE Trans. Consum. Electron.*, vol. 69, no. 3, pp. 400–407, Aug. 2023. [Online]. Available: https://ieeexplore.ieee.org/document/10064356

[8] S. Cloudt, "Bluetooth low energy direction finding on embedded hardware by mitigating carrier frequency offset and multipath fading," M.S. thesis, Math. Comput. Sci., Eindhoven Univ. Technol., Eindhoven, The Netherlands, 2021.

[9] L. Yao, "Bluetooth direction finding," M.S. thesis, Delft Univ. Technol., Delft, The Netherlands, 2018. [Online]. Available: https://repository.tudelft.nl/islandora/object/uuid

[10] P. Avital, G. Chardon, and J. Picheral, "Design of switching sequences for sine parameters estimation on switched antenna arrays," *Signal Process.*, vol. 188, Nov. 2021, Art. no. 108244. [Online]. Available: https://www.sciencedirect.com/science/article/pii/S0165168421002814

[11] L. Yi, T. Guo, M. Guo, and Y. Fu, "Motion compensation for SAA FMCW radar based on specific switching scheme," *Appl. Sci.*, vol. 9, p. 3441, Aug. 2019.

[12] L. Yi, K. Yang, M. Guo, and Y. Fu, "Elimination of motion-induced phase based on double-time switching scheme for SAA FMCW radar," *Electronics*, vol. 8, p. 786, Jul. 2019.

[13] P. Feil, "Optimizing switching sequence in the case of switched antenna arrays," U.S. Patent 182 174 A1, Jul. 2012. [Online]. Available: https://patents.google.com/patent/US20120182174A1/en

[14] C. Hu, Y. Liu, H. Meng, and X. Wang, "Randomized switched antenna array FMCW radar for automotive applications," *IEEE Trans. Veh. Technol.*, vol. 63, no. 8, pp. 3624–3641, Oct. 2014. [Online]. Available: https://ieeexplore.ieee.org/document/6750120

[15] A. Al-Ameri, J. Park, J. Sanchez, X. Cai, and F. Tufvesson, "A hybrid antenna switching scheme for dynamic channel sounding," in *Proc. IEEE 97th Veh. Technol. Conf. (VTC-Spring)*, Jun. 2023, pp. 1–6. [Online]. Available: https://ieeexplore.ieee.org/document/10199525

[16] R. Wang, O. Renaudin, C. U. Bas, S. Sangodoyin, and A. F. Molisch, "On channel sounding with switched arrays in fast time-varying channels," *IEEE Trans. Wireless Commun.*, vol. 18, no. 8, pp. 3843–3855, Aug. 2019. [Online]. Available: https://ieeexplore.ieee.org/document/8728188

[17] T. Pedersen et al., "Joint estimation of Doppler frequency and directions in channel sounding using switched Tx and Rx arrays," in *Proc. IEEE Global Telecommun. Conf.*, vol. 4, Nov. 2004, pp. 2354–2360. [Online]. Available: https://ieeexplore.ieee.org/document/1378429/authors#authors

[18] T. Pedersen, C. Pedersen, X. Yin, and B. H. Fleury, "Optimization of spatiotemporal apertures in channel sounding," *IEEE Trans. Signal Process.*, vol. 56, no. 10, pp. 4810–4824, Oct. 2008. [Online]. Available: https://ieeexplore.ieee.org/abstract/document/4579719

[19] A. Simončič, G. Morano, A. Švigelj, A. Hrovat, and T. Javornik, "Optimizing switching pattern to reduce CFO effects in single RF chain direction finding systems," in *Proc. 7th Int. Balkan Conf. Commun. Netw. (BalkanCom)*, Jun. 2024, pp. 113–118. [Online]. Available: https://ieeexplore.ieee.org/document/10557208

[20] S. Shirvani-Moghaddam and F. Akbari, "A novel ULA-based geometry for improving AOA estimation," *EURASIP J. Adv. Signal Process.*, vol. 2011, no. 1, p. 39, Aug. 2011. [Online]. Available: https://doi.org/10.1186/1687-6180-2011-39

[21] A. Simončič, T. Javornik, A. Sešek, and A. Hrovat, "Direction of arrival estimation for BLE: Antenna array design and evaluation," *AEU Int. J. Electron. Commun.*, vol. 168, Aug. 2023, Art. no. 154722. [Online]. Available: https://www.sciencedirect.com/science/article/pii/S1434841123001966

[22] *VESNA Platform*, Dept. Commun. Syst., Jožef Stefan Inst., Ljubljana, Slovenia, 2013. Accessed: Nov. 14, 2024. [Online]. Available: https://log-a-tec.eu/hw-vesna.html

[23] "AT86RF215 datasheet," Data Sheet, Atmel Corp., San Jose, CA, USA, 2016. Accessed: Nov. 14, 2024. [Online]. Available: https://www.microchip.com/en-us/product/at86rf215

[24] G. Morano, A. Simončič, T. Kocevska, T. Javornik, and A. Hrovat, "Distance- and angle-based hybrid Localization integrated in the IEEE 802.15.4 TSCH communication protocol," *Sensors*, vol. 24, p. 3925, Jun. 2024.



ALEŠ SIMONČIČ (Student Member, IEEE) received the B.Sc. and M.Sc. degrees in electrical engineering from the University of Ljubljana in 2019 and 2022, respectively. He is currently pursuing the Ph.D. degree in information and communication technologies with the Jožef Stefan International Postgraduate School. His master's thesis focused on the estimation of the angle of arrival using BLE technology and antenna arrays. He is currently working as a Young Researcher with the Department of Communication Systems, Jožef Stefan Institute, Ljubljana. His research interests are in radio communication systems, particularly protocols, antennas and arrays, direction of arrival estimation methods, embedded systems, and radio environment characterization.



KE GUAN (Senior Member, IEEE) received the B.E. and Ph.D. degree from Beijing Jiaotong University in 2006 and 2014, respectively.

He is a Full Professor with the State Key Laboratory of Advanced Rail Autonomous Operation and the School of Electronics and Information Engineering, Beijing Jiaotong University. He is with the Department of Communication Systems, Jožef Stefan Institute, Ljubljana, Slovenia. He is the Pole Leader of EURNEX (European Railway Research Network of Excellence). He has authored/coauthored two books and one book chapter, more than 200 journal and conference papers, and four patents. His current research interests include measurements and modeling of wireless propagation channels, high-speed railway communications, vehicle-to-x channel characterization, and indoor channel characterization for high-speed short-range systems, including future terahertz communication systems. In 2015, he has been awarded a Humboldt Research Fellowship for Postdoctoral Researchers. He was the recipient of a 2014 International Union of Radio Science Young Scientist Award. His papers received ten Best Paper Awards, including IEEE Vehicular Technology Society Neal Shepherd Memorial Best Propagation Paper Award in 2019 and 2022. He is an Editor of *IEEE Vehicular Technology Magazine*, IEEE ACCESS, *IET Microwave, Antenna and Propagation*, and *Physical Communication*, and a Guest Editor of the IEEE TRANSACTIONS ON VEHICULAR TECHNOLOGY and *IEEE Communication Magazine*. He serves as the Publicity Chair in PIMRC 2016, the Publicity Co-Chair in ITST 2018, the Track Co-Chair in EuCNC, the International Liaison of EUSIPCO 2019, the Session Convener of EuCAP 2015–2022, and a TPC Member for many IEEE conferences, such as Globecom, ICC, and VTC. He has been a delegate in 3GPP and a member of the IC1004 and CA15104 initiatives.



GREGA MORANO (Graduate Student Member, IEEE) received the M.Sc. degree in electrical engineering from the University of Ljubljana in 2021. He is currently pursuing the Ph.D. degree in information and communication technologies with the Jožef Stefan International Postgraduate School.

He is a Research Assistant with the Department of Communication Systems, Jožef Stefan Institute, Ljubljana. His research interests include IoT communication protocols, integrated sensing and communication, wireless sensor networks, and wireless experimental testbeds.



ALEŠ ŠVIGELJ (Senior Member, IEEE) received the B.Sc., M.Sc., and Ph.D. degrees in electrical engineering from the University of Ljubljana, Ljubljana, Slovenia, in 1997, 2000, and 2003 respectively.

He is a Senior Research Fellow with the Department of Communication Systems, Jožef Stefan Institute and a Full Professor with the Jožef Stefan Postgraduate School. He has extensive research in modeling, simulation, and design of advanced telecommunications elements, systems, and services. He has also participated as a coordinator in several national and international projects, including COST Projects. He co-authored several books/book chapters and more than 100 peer-reviewed journal and conference papers. His current work focuses on advanced networking technologies for wireless systems.



ANDREJ HROVAT (Senior Member, IEEE) received the B.Sc. and M.Sc. degrees in electrical engineering from the University of Ljubljana in 2004 and 2008, respectively, and the Ph.D. degree from the Jozef Stefan International Postgraduate School in 2011.

He has been with the Department of Communication Systems, Jožef Stefan Institute since 2004, where he is currently a Senior Research Fellow. He is the author or a co-author of more than 120 peer-reviewed journal and conference papers. He works on several projects connected with professional mobile communication systems, 2G-5G, WiFi and IoT technologies, satellite and sensor networks, including several COST actions, Framework Program projects, H2020 projects, European Space Agency projects, and numerous national research and application projects. His research and working experience are in telecommunications, focusing on development and performance analysis for fixed and mobile systems, including terrestrial, stratospheric, and satellite systems, and radio-channel modeling for fixed and mobile narrowband and broadband radio communication systems. He serves as a journal editorial board member and a guest editor, is a reviewer for several international impact-factor journals, and is a TCP member for various international conferences and workshops.



TEODORA KOCEVSKA (Member, IEEE) received the B.Sc. and M.Sc. degrees in electrical engineering from the Ss. Cyril and Methodius University, Skopje, North Macedonia, in 2017 and 2018, respectively, and the Ph.D. degree from the Jožef Stefan International Postgraduate School, Ljubljana, Slovenia, in 2023.

She has been with the Department of Communication Systems, Jožef Stefan Institute since 2019, where she is currently a Research Assistant. Her research experience is in telecommunications, focusing on radio channels, integrated communications and sensing, radio environment characterization, environmentally aware communications, and the application of machine learning in telecommunications.



TOMAŽ JAVORNIK (Member, IEEE) received the B.Sc., M.Sc., and Ph.D. degrees in electrical engineering from the University of Ljubljana, Ljubljana, Slovenia, in 1987, 1990, and 1993, respectively. He is a Scientific Counsellor with the Communication Systems Department, Jozef Stefan Institute, Ljubljana, and an Assistant Professor with the Jozef Stefan International Postgraduate School, Ljubljana. He participated in several COST and Framework Programme projects. He has co-authored more than 100 refereed journal and conference papers and several books and book chapters in mobile and wireless communications. He holds two international patents. His research experience is in telecommunications, focusing on the development and performance analysis of fixed and mobile systems, radio-channel measurements, modeling and simulations, and indoor localization. He serves as a TPC member or a reviewer for several IEEE conferences and journals.

Chapter 4

Frequency Switching Pattern Design for Robust MCPD Ranging

Publication included in this chapter:

A. Simončič, G. Morano, A. Hrovat, and T. Javornik, "Optimizing Frequency Switching Pattern to Reduce Asynchronization Effect in MCPD Ranging Systems," *IEEE Access*, vol. 13, pp. 169 791–169 811, 2025, ISSN: 2169-3536. DOI: 10.1109/ACCESS.2025.3614753

The dissertation initially focused on phase-based DoA estimation with a single-RF-chain receiver, motivated by its suitability for resource-constrained devices. Robust DoA estimation in rich multipath environments benefits from the use of frequency diversity. This motivates the consideration of phase-based estimation approaches that inherently exploit frequency diversity. In this context, MCPD ranging is particularly suitable because it is compatible with simple radio architectures and, by design, uses multiple carrier frequencies. MCPD ranging can therefore serve as an alternative to phase-based DoA estimation or as a complementary technique to improve localization accuracy.

In MCPD ranging, distance is inferred from carrier-phase measurements that are acquired sequentially over time while switching across multiple carrier frequencies. An FSP specifies the order in which the available carrier frequencies are applied during the MCPD procedure and is represented as an ordered sequence of carrier-frequency indices corresponding to the carrier sequence used throughout the MCPD procedure. In conventional MCPD implementations, a linear frequency sweep is performed by applying carrier frequencies in ascending order with uniform frequency steps, referred to as the sequential switching (SSW) FSP. The disadvantage of using the SSW FSP arises under asynchronous conditions. As noted in the previous chapter, low-cost devices typically use lower-grade oscillators with greater frequency tolerance and drift. As a result, the transmitter and receiver are not perfectly synchronized, leading to timing and frequency asynchrony between the devices.

In MCPD ranging, STO is suppressed by the two-way exchange and is therefore not a source of ranging bias. However, for accurate distance estimation, the time difference between the phase sample acquired at the reflector and the corresponding phase sample acquired at the initiator, denoted as ΔT_o, must remain constant across carrier frequencies. When an SFO difference exists between the devices, the sampling instants at the initiator and reflector deviate from their intended values, causing ΔT_o to vary linearly over the MCPD carrier sweep, assuming constant SFO. The deviation of ΔT_o from its nominal value introduces an additional phase progression in the acquired samples at each carrier

frequency. For the SSW FSP, the resulting phase errors exhibit a linear trend across carrier frequencies and are correlated with the distance-induced phase shifts, thereby introducing systematic ranging bias.

Instead of estimating and compensating for asynchronization-induced phase errors or performing joint parameter estimation, as is commonly done in related literature at the cost of measurement overhead and increased computational load, the paper presented in this chapter develops a lightweight mitigation approach based on FSP design, thereby providing contribution **SC3.2**. This approach does not introduce measurement overhead or additional computational load and is therefore suitable for resource-constrained devices. The key observation is that asynchronization induces phase errors that increase linearly with time and map into structured phase distortions across the carrier frequencies. By rearranging the carrier-frequency order in the FSP, the mapping of phase errors onto carrier frequencies is reshaped. The goal of FSP optimization is to decouple the asynchronization-induced phase distortions from the distance-induced phase shifts across carrier frequencies. In particular, the phase-error pattern across carrier frequencies should exhibit a zero linear trend to mitigate systematic bias. The principle of FSP optimization is conceptually analogous to the ASP optimization discussed for SAA-based DoA estimation. The problem can be viewed as having a set of available phase errors at the sampling instants of the MCPD procedure and assigning these phase errors to carrier frequencies so that the resulting linear trend across carriers is suppressed.

The presented paper derives a signal model for MCPD ranging that accounts for CFO and timing mismatches, and provides an analytical characterization of the effect of asynchronization on phase measurements, including the bias mechanism introduced by the SSW FSP, thereby addressing hypothesis **H2** and establishing contribution **SC3.1**. Building on this analysis, the paper proposes rearranging carrier frequencies in the FSP and introduces a set of structured FSPs that suppress the linear phase-error trend across the carrier frequencies, along with an analysis and evaluation of randomly generated FSPs, thereby providing contribution **SC3.3**. The effectiveness of bias mitigation is validated through numerical simulations across SFO mismatch conditions, numbers of carriers, and SNR values, as well as through experimental evaluation in which the proposed FSPs are compared with the SSW FSP and an estimation-and-correction approach, providing contribution **SC3.4**. The results demonstrate the effectiveness of the proposed FSPs in mitigating estimation bias, thereby addressing hypothesis **H4**.

IEEE Access
Multidisciplinary ⋮ Rapid Review ⋮ Open Access Journal

Received 28 August 2025, accepted 20 September 2025, date of publication 26 September 2025, date of current version 2 October 2025.

Digital Object Identifier 10.1109/ACCESS.2025.3614753

RESEARCH ARTICLE

Optimizing Frequency Switching Pattern to Reduce Asynchronization Effect in MCPD Ranging Systems

ALEŠ SIMONČIČ, (Student Member, IEEE), GREGA MORANO, (Member, IEEE), ANDREJ HROVAT, (Senior Member, IEEE), AND TOMAŽ JAVORNIK, (Member, IEEE)
Department of Communication Systems, Jožef Stefan Institute, 1000 Ljubljana, Slovenia
Jožef Stefan International Postgraduate School, 1000 Ljubljana, Slovenia

Corresponding author: Aleš Simončič (ales.simoncic@ijs.si)

This work was supported by Slovenian Research and Innovation Agency (ARIS) under Grant J2-4461, Grant P2-0016, and Grant PR-12348.

ABSTRACT Accurate distance estimation in two-way multi-carrier phase difference (MCPD) ranging systems is degraded by carrier frequency offset (CFO) and timing discrepancies caused by asynchronized clocks between nodes. In previous work, carrier frequencies were typically utilized in ascending order during the MCPD process, a method referred to as sequential switching (*SS*) frequency switching pattern (FSP). Under asynchronous conditions, the *SS* FSP induces a linear phase trend across the frequency spectrum, resulting in systematic biasing. Existing works address this problem by estimating and compensating for the phase shifts caused by the asynchronization, but introduce additional computational complexity, latency, and power consumption. In this paper, we present a new signal model accounting for the relevant hardware imperfections, characterizing the effects of asynchronization on the phase measurements, and highlighting the limitations of the *SS* FSP. Building on this analysis, we propose rearranging carrier frequencies in the FSP and introduce a set of novel FSPs that eliminate the linear phase trend across the frequency spectrum and reduce the estimation error without requiring estimation or correction procedure. The results of the simulation study show that the proposed FSPs outperform the *SS* FSP under different oscillator mismatches achieving sub-centimeter systematic error at high signal-to-noise ratios (SNR), with performance gain decreasing with decreasing SNR and performance variability occurring with different numbers of carriers. Real-world experimental validation confirms a strong agreement between simulated and measured channel impulse responses and that the proposed FSPs produce more robust distance estimates to CFO variations than the *SS* FSP.

INDEX TERMS Asynchronization, carrier frequency offset (CFO), channel frequency response (CFR), channel impulse response (CIR), crystal offset, inverse fast Fourier transform (IFFT), frequency switching pattern (FSP), Internet of Things (IoT), multi-carrier phase difference (MCPD).

I. INTRODUCTION

Emerging wireless technologies are increasingly designed to integrate communication and localization capabilities. This paradigm, known as integrated sensing and communication (ISAC), is particularly relevant for the Internet of Things (IoT), where billions of connected devices are expected to operate autonomously, interact with their surroundings and cooperate seamlessly. By extending the functionality of wireless networks, ISAC enables context-aware IoT applications such as presence detection, real-time positioning, dynamic target tracking, and environment

The associate editor coordinating the review of this manuscript and approving it for publication was Olutayo O. Oyerinde.

© 2025 The Authors. This work is licensed under a Creative Commons Attribution 4.0 License.
For more information, see https://creativecommons.org/licenses/by/4.0/

mapping across smart city, industrial, and consumer domains [1].

Several localization techniques have been investigated in the context of IoT systems, each offering specific advantages but also facing inherent limitations. Received signal strength indicator (RSSI)-based ranging is attractive due to its simplicity and compatibility with low-cost hardware, yet it suffers from poor accuracy and high variability, particularly in multipath-rich indoor environments. Time-of-Flight (ToF) methods provide more reliable distance estimates but require wide bandwidths and fast sampling capabilities, which are generally unavailable on resource-constrained IoT platforms. Ultra-wideband (UWB) technology achieves high precision, but regulatory transmit power restrictions limit its operational range, and its adoption requires specialized hardware not widely supported in consumer-grade IoT devices, making seamless integration into ISAC-enabled IoT networks challenging [2], [3].

An alternative that has gained significant attention is phase-based ranging (PBR), which can deliver accurate distance estimates using narrowband signals [4]. In particular, the multi-carrier phase difference (MCPD) technique exploits phase measurements across several carrier frequencies to achieve decimeter-level accuracy [5]. MCPD is highly attractive for IoT deployments because it is compatible with commodity transceivers, requires low hardware complexity, and exhibits robustness against multipath propagation. These features make it well suited for applications such as indoor localization, asset tracking, and proximity-based services, where cost, energy efficiency, and form factor are critical. Its relevance has increased further with the standardization of channel sounding in Bluetooth Low Energy (BLE), which extends MCPD-based localization capabilities to a wide range of consumer devices [6].

In MCPD ranging, two devices named initiator (INIT) and reflector (REF) exchange signals over a predefined set of carrier frequencies in an alternating transmit and receive mode. By combining the phase measurements collected at both ends, the initial random phase offsets introduced by the local oscillators (LOs) are effectively canceled, leaving only the distance-dependent phase shifts when perfect synchronization is achieved.

In practice, however, deployment on low-cost hardware remains challenging mainly due to the limitations imposed by oscillators instability, carrier frequency offset (CFO) and non-simultaneous phase sampling. Furthermore, the estimated distance error depends not only on oscillator performance but also on the order of carrier frequencies used and the specific distance estimation algorithm. These imperfections introduce additional, non-distance-dependent phase shifts which, if not properly accounted for, can lead to systematic errors in distance estimation.

Such effects are particularly pronounced in low-cost IoT platforms, where typically inexpensive crystal oscillators are used for both radio frequency (RF) generation and for sampling time control. The accuracy and stability of these oscillators, specified in parts per million (ppm), is strongly affected by temperature, humidity, aging, power supply fluctuations, and mechanical vibrations. Manufacturing tolerances further introduce device-to-device variations, while mobility adds additional Doppler-induced CFO. As a result, timing stability and carrier frequency variations directly limit ranging accuracy in realistic IoT deployments. Throughout this work, we use the term *asynchronization* to denote the combined effects of timing misalignment and CFO.

Synchronization and calibration procedures are therefore essential to counteract asynchronization deviations. A common approach is to measure the bias at a known reference distance and subtract it from subsequent estimates. Although effective in controlled settings, calibration is often constrained by the time and cost required, as well as by its sensitivity to environmental conditions, as a single calibration instance rarely guarantees long-term stability. In line with modern zero-touch deployment paradigms, repeated manual calibration is undesirable. The need for repeated calibration can be avoided by implementing methods that effectively mitigate the effects of asynchronization between devices on distance estimation.

Several recent studies have demonstrated that MCPD-based ranging has a strong potential for accurate localization with low-cost hardware, particularly when implemented on widely available technologies such as BLE [7], [8], [9], [10] or IEEE 802.15.4 [4], [11]. However, these works typically either do not propose explicit methods to address the asynchronization problem between devices, or rely on calibration whose temporary adequacy masks the underlying limitations.

In [12], the authors have experimentally demonstrated that CFO introduces an additional phase shift into the phase measurements, adversely affecting the accuracy of the distance measurement. To mitigate this effect, they proposed to estimate the CFO by calculating the slope from multiple phase samples acquired at a single carrier frequency. The integration of MCPD into the BLE standard was proposed in [13], emphasizing that timing asynchronization, CFO, and phase noise significantly affect distance estimation accuracy, especially for slow channel hopping, longer packet lengths, and extended frame spacing. They recommended compensating for crystal offset by measuring the CFO, which is mapped to the crystal offset difference. Studies [14], [15] highlighted that device asynchronization significantly increases distance estimation errors in one-to-many and many-to-many group ranging scenarios due to cumulative measurement delays across transmission slots. Specifically, in [15], a method is proposed for on-the-fly estimation of crystal offsets, in which INIT intentionally changes the timeslot of REFs in two consecutive measurements and relates the resulting variation in distance measurement to the crystal offset. An alternative approach with additional transmissions is presented in [16]. First, the devices measure the phases using the standard INIT

and REF approach and then switch modes to obtain two additional phase measurements and combine all phases to reduce the CFO effect on the distance estimate. However, this method increases power consumption, interference, and the update rate as additional transmissions are required.

Building on these prior studies, our work departs from explicit CFO estimation and compensation procedures and instead focuses on the design of the frequency switching pattern (FSP), which is defined as a structured sequence of carrier frequencies that determines the order in which the carrier frequencies are applied during the MCPD procedure. In conventional MCPD implementations, phase measurements are taken over a sequence of carrier frequencies applied in ascending order with uniform frequency steps within the allocated bandwidth. We refer to this conventional method as the sequential switching (*SS*) FSP. In this paper, we present a novel signal model that explicitly accounts for LO imperfections and analytically demonstrate that the *SS* FSP induces a linear phase trend across the frequency spectrum under asynchronous conditions which results in systematic range estimation errors. To mitigate this effect, we propose a novel approach which rearranges the order of carrier frequencies within the FSP, and introduce a set of novel FSPs specifically designed to eliminate the linear phase trend introduced by the *SS* FSP, thereby reducing the distance estimation error caused by the asynchronization effects. Unlike previous approaches that require explicit CFO or timing offset estimation or demanding additional transmissions our method operates implicitly through the choice of FSP. As a result, it avoids the added computational load, latency, and power consumption associated with explicit compensation schemes. This property makes the proposed solution particularly well suited for low-cost IoT devices, where hardware resources are constrained and environmental conditions can vary rapidly, rendering calibration-based methods ineffective over time. By leveraging FSP design as a lightweight yet powerful tool, our approach enables robust MCPD-based localization in practical IoT and ISAC deployments.

Similar switching-related challenges have been investigated in adjacent domains such as frequency modulated continuous wave (FMCW) radar, channel sounding, and direction-of-arrival (DoA) estimation, where time-division multiplexing is used to switch between antenna elements. For FMCW radar, optimized antenna switching patterns were proposed to suppress motion-induced phase distortions and decouple delay-angle ambiguities [17], [18], [19], [20]. In channel sounding [21], [22], [23], [24], [25], and DoA applications [26], [27], antenna switching patterns were designed to improve the Doppler resolution, minimize the ambiguity of parameter estimation under time-varying conditions, and reduce the bias of DoA estimation caused by CFO. However, to the best of our knowledge, the idea of reordering carrier frequencies in the FSP to suppress systematic errors in MCPD ranging, specifically those arising from device asynchronization, has not been previously explored in the literature. The main contributions of this work are summarized as follows:

- We present a novel signal model for MCPD ranging that explicitly incorporates hardware imperfections of low-cost oscillators and their impact on distance estimation.
- We introduce a new approach to suppress the estimation error of the conventional *SS* FSP under asynchronous conditions by rearranging the carrier frequencies in FSP without requiring explicit CFO or timing offset estimation or additional unnecessary transmissions.
- We design and formulate a set of novel FSPs.
- We provide a comprehensive simulation-based performance evaluation of the proposed FSPs under realistic conditions.
- We validate the practical effectiveness of the proposed FSPs through real-world experiments on low-cost IoT hardware.

The remainder of this paper is organized as follows. Section II introduces the signal model and formalizes the problem. Section III presents the proposed FSPs. In Section IV, we evaluate the performance of the proposed FSPs through simulations and compare them with the conventional *SS* FSP approach. Section V provides an experimental validation. Finally, Section VI summarizes the main findings and outlines possible directions for future research. For clarity, FSPs are represented by indices instead of absolute carrier frequency values, with index 1 corresponding to the lowest frequency and the highest index to the highest frequency in the considered frequency band. For example, the *SS* FSP with 16 carriers is [1, 2, 3, 4, . . . , 15, 16].

II. SIGNAL MODEL AND PROBLEM FORMULATION

We present a free-space propagation model using the transmission and reception scheme described in [28], where the INIT transmits and receives on a given carrier frequency, while the REF receives and then transmits on a frequency offset below the INIT's by the intermediate frequency as shown in Fig 1. This setup ensures consistent transmit and receive frequencies for both devices, enabling cancellation of LO phase offsets inherent to two-way ranging. The corresponding signal sampling times are shown in Fig. 2. We consider the general case where INIT and REF use independent LOs for carrier frequency generation and separate crystal oscillators for timing, which in turn determine the sampling times of the received signal. The frequency errors are modeled as fixed absolute frequency offsets for the carrier generation and fixed relative frequency errors for the timing oscillators, characterized by a ppm parameter. Throughout the paper, it is assumed that the frequency spacing ν between adjacent carrier frequencies is constant over the entire measurement bandwidth.

Considering the i-th carrier frequency in the FSP, where $i \in \{1, \ldots, M\}$ and M is the total number of carrier frequencies used, INIT first transmits an unmodulated continuous wave

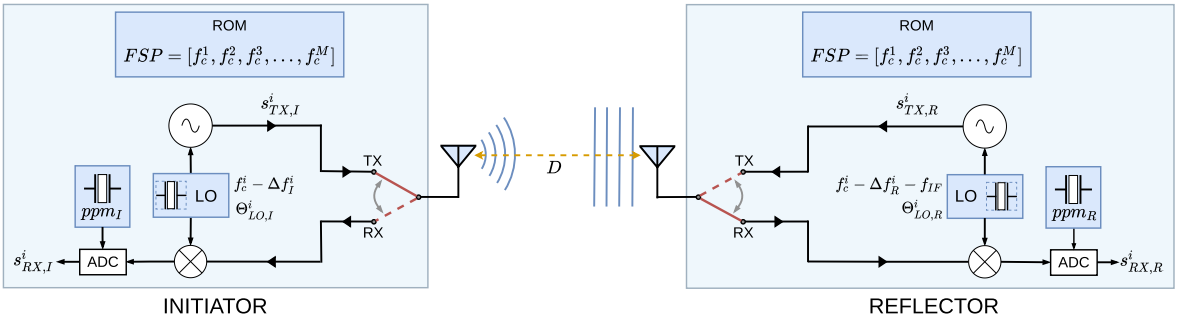


FIGURE 1. System with two transceivers, INIT and REF, which alternately transmit and receive according to a predefined FSP stored in read-only memory (ROM), where i indicates the i-th carrier frequency used in the sequence during the MCPD process. Each transceiver has its own carrier frequency errors caused by the inaccuracies of LO, denoted by Δf_I^i and Δf_R^i, and the inaccuracies of the ADC sampling time, represented by ppm_I and ppm_R, both of which contribute to the observed phase errors.

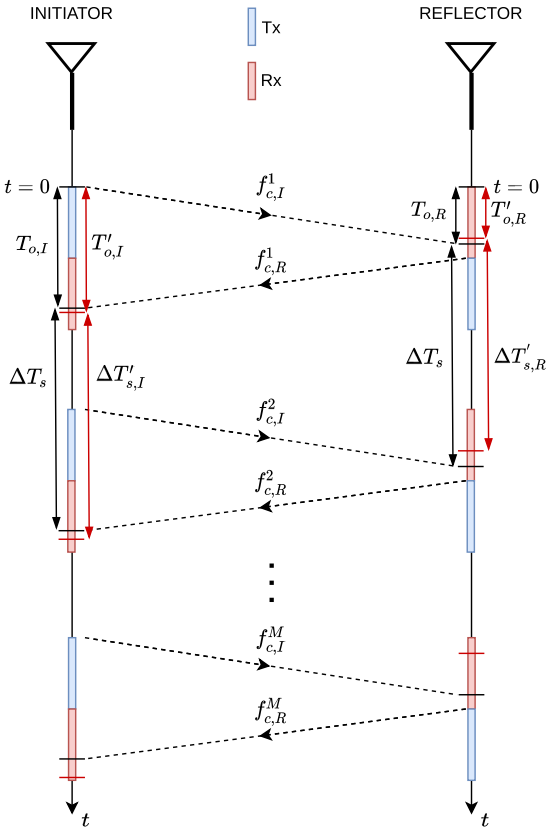


FIGURE 2. Timing diagram showing the sampling instants at INIT and REF for each measurement routine corresponding to a carrier frequency f_c^i in the MCPD process. The signal is sampled after a defined time offset T_o^I and T_o^R from the start of each routine, where ΔT_s denotes the interval between the starts of the routines for successive carriers. Due to clock inaccuracies, these nominal times are affected by drift and the resulting sampling instants are labelled with a prime superscript.

(CW) signal with the frequency $f^i_{c,I} = f^i_c + \Delta f^i_I$, where f^i_c represents the ideal carrier frequency and Δf^i_I denotes the frequency offset resulting from INIT's LO inaccuracies. The signal transmitted by INIT is expressed as

$$s^i_{TX,I}(t) = \Re\{A\ \exp\big(j\left(2\pi f^i_{c,I}\, t + \Theta^i_{LO,I}\right)\big)\}, \tag{1}$$

where A is the amplitude of the transmitted signal, $\Theta^i_{LO,I}$ is the initial phase offset of the INIT LO at the i-th carrier frequency and $\Re\{\cdot\}$ denotes the real part of the complex signal.

The REF receives the delayed version of the transmitted signal from INIT, resulting from the propagation over the distance D

$$s^i_{RX,R}(t) = \Re\{A'\ \exp\big(j\left(2\pi f^i_{c,I}\,(t - D/c) + \Theta^i_{LO,I}\right)\big)\}, \tag{2}$$

where A' is the amplitude of the received signal and c is the speed of light.

The REF down-mixes the received signal using its LO set to $f^i_{c,R} = f^i_c - f_{IF} + \Delta f^i_R$, where Δf^i_R denotes the frequency offset of the REF at carrier i, and the LO is offset below the carrier frequency by the intermediate frequency f_{IF}. Mixing is performed with unity gain and initial LO phase offset $\Theta^i_{LO,R}$. The REF samples the resulting intermediate frequency phase component

$$\begin{aligned}\phi^i_R(t) = {} & 2\pi\left(f_{IF} + \Delta f^i\right) t \\ & - 2\pi\left(f^i_c + \Delta f^i_I\right)\frac{D}{c} \\ & + \Theta^i_{LO,I} \ - \ \Theta^i_{LO,R}.\end{aligned} \tag{3}$$

Here, the first term reflects the phase evolution due to the intermediate frequency and the CFO between INIT and REF, defined as $\Delta f^i = \Delta f^i_I - \Delta f^i_R$, and the second term accounts for the propagation delay.

The REF samples the phase of the down-mixed signal at discrete time instants with a sampling frequency $f'_{s,R}$, starting after a delay of $T'_{o,R}$ from the beginning of each carrier frequency measurement routine. The total time offset of the start of sampling relative to the start of the first frequency in the FSP is given by $(i-1)\Delta T'_{s,R} + T'_{o,R}$, where $\Delta T'_{s,R}$ denotes the time interval between the start of phase sampling on REF on two consecutive carrier frequencies. The resulting sampled

phase at the REF is

$$\begin{aligned}\phi^i_R[n] = {} & 2\pi\left(f_{IF}+\Delta f^i\right)\left((i-1)\Delta T'_{s,R}+T'_{o,R}\right)\\ & +2\pi\left(f_{IF}+\Delta f^i\right)\frac{n}{f'_{s,R}}\\ & -2\pi\left(f^i_c+\Delta f^i_I\right)\frac{D}{c}\\ & +\Theta^i_{LO,I}\ -\ \Theta^i_{LO,R}.\end{aligned}\tag{4}$$

After the REF has sampled the signal, it begins its transmission phase by generating a CW with its own carrier frequency $f^i_{c,R} = f^i_c - f_{IF} + \Delta f^i_R$, with an initial LO phase offset $\Theta^i_{LO,R}$

$$s^i_{TX,R}(t) = \Re\{A\ \exp\left(j\left(2\pi f^i_{c,R}\,t+\Theta^i_{LO,R}\right)\right)\}.\tag{5}$$

This signal then propagates to the INIT, arriving with a delay that corresponds to the distance D. INIT then down-mixes this received signal with its own LO operating at frequency $f^i_{c,I} = f^i_c + \Delta f^i_I$, with an initial phase offset $\Theta^i_{LO,I}$ and a unity gain. The phase component of the resulting down-mixed signal is

$$\begin{aligned}\phi^i_I(t) = {} & 2\pi\left(f_{IF}+\Delta f^i\right)t\\ & -2\pi\left(f^i_c-f_{IF}+\Delta f^i_R\right)\frac{D}{c}\\ & +\Theta^i_{LO,I}\ -\ \Theta^i_{LO,R}.\end{aligned}\tag{6}$$

The INIT samples the phase of the down-mixed signal at discrete time instants with a sampling frequency $f'_{s,I}$, starting after a delay $T'_{o,I}$ from the beginning of each carrier frequency measurement routine. The total time offset of the start of sampling relative to the start of the first frequency in the FSP is given by $(i-1)\Delta T'_{s,I} + T'_{o,I}$, where $\Delta T'_{s,I}$ represents the time interval between the start of phase sampling on INIT on two consecutive carrier frequencies. The resulting sampled phase at the INIT is

$$\begin{aligned}\phi^i_I[n] = {} & 2\pi\left(f_{IF}+\Delta f^i\right)\left((i-1)\Delta T'_{s,I}+T'_{o,I}\right)\\ & +2\pi\left(f_{IF}+\Delta f^i\right)\frac{n}{f'_{s,I}}\\ & +2\pi\left(f^i_c-f_{IF}+\Delta f^i_R\right)\frac{D}{c}\\ & +\Theta^i_{LO,I}\ -\ \Theta^i_{LO,R}.\end{aligned}\tag{7}$$

To eliminate the phase offsets introduced by the LOs, the phase samples acquired at the REF are subtracted from those acquired at the INIT. Taking into account that the sampling instants on both devices are affected by inaccuracies of the crystal oscillators, the time intervals on INIT and REF are expressed as

$\Delta T'_{s,R} = \Delta T_s\,(1+e_R)^{-1}$,
$\Delta T'_{s,I} = \Delta T_s\,(1+e_I)^{-1}$,
$T'_{o,R} = T_{o,R}\,(1+e_R)^{-1}$,
$T'_{o,I} = T_{o,I}\,(1+e_I)^{-1}$,

where the time intervals without the prime superscript represent the ideal, error-free values, and $e_R = ppm_R \cdot 10^{-6}$ and $e_I = ppm_I \cdot 10^{-6}$ are the relative frequency errors of the REF and INIT crystal oscillators, as defined by their respective ppm values ppm_R and ppm_I. The resulting phase difference is

$$\begin{aligned}\phi^i[n] = \phi^i_R[n]\ -\ \phi^i_I[n] = {} & 2\pi\left(f_{IF}+\Delta f^i\right)\cdot\\ & \Bigg[(i-1)\,\Delta T_s\,\frac{e_I-e_R}{1+e_I+e_R+e_I\,e_R}\\ & +\left(T_{o,R}\left(1+e_R\right)^{-1}-\ T_{o,I}\left(1+e_I\right)^{-1}\right)\\ & +\left(\frac{n}{f'_{s,R}}-\frac{n}{f'_{s,I}}\right)\Bigg]\\ & -2\pi\left(2f^i_c+\Delta f^i_I+\Delta f^i_R-f_{IF}\right)\frac{D}{c}.\end{aligned}\tag{8}$$

In the above expression, only the last term corresponds to the desired deterministic phase shift induced by the actual propagation distance, while all other terms arise from timing mismatches and CFO caused by oscillators imperfections, introducing unwanted phase shifts that bias the distance estimation unless properly mitigated. In particular, the first phase term is explicitly dependent on the index i, which represents the position of the corresponding carrier frequency within the FSP. The problem with conventional *SS* FSP is that these additional phase shifts that are dependent on the index i increase linearly with frequency - just as the distance-dependent phase shifts. This correlation leads to ambiguity and introduces systematic bias in the estimated distance. Next, we calculate the absolute error (AE) of the estimated distance using the *SS* FSP to evaluate its effect on the bias of the estimate. Since the gradient of the calculated phase difference across the carrier frequencies is proportional to the distance between the devices, we first calculate the phase difference between the $i+1$-th and i-th carriers of the *SS* FSP

$$\begin{aligned}&\phi^{i+1}[n]-\phi^i[n]\\ &= 2\pi\left(f_{IF}+\Delta f^i\right)\Delta T_s\,\frac{e_I-e_R}{1+e_I+e_R+e_I\,e_R}\\ &\quad +2\pi\left(\Delta f^{i+1}-\Delta f^i\right)\cdot\\ &\quad \Bigg[i\,\Delta T_s\,\frac{e_I-e_R}{1+e_I+e_R+e_I\,e_R}\\ &\quad +\left(T_{o,R}\left(1+e_R\right)^{-1}-\ T_{o,I}\left(1+e_I\right)^{-1}\right)\\ &\quad +\left(\frac{n}{f'_{s,R}}-\frac{n}{f'_{s,I}}\right)\Bigg]\\ &\quad +2\pi\left(-2\cdot\nu-f^{i+1}_I-f^{i+1}_R+f^i_I+f^i_R\right)\frac{D}{c}.\end{aligned}\tag{9}$$

In the context of narrowband technologies such as BLE or IEEE 802.15.4, we assume that the CFO remains approximately constant throughout the operating bandwidth. We therefore set $\Delta f^i \approx \Delta f$ for all i. Under this assumption, the expression for the phase difference between two consecutive carriers is reduced to

$$\phi^{i+1}-\phi^i$$

$$= 2\pi\left(f_{IF} + \Delta f\right)\Delta T_s \frac{e_I - e_R}{1 + e_I + e_R + e_I\, e_R} + 2\pi\left(-2 \cdot \nu\right)\frac{D}{c}. \quad (10)$$

The distance is then estimated from the phase gradient between neighboring carrier frequencies as follows

$$D = \frac{c}{4\pi}\frac{\phi^{i+1} - \phi^i}{\nu}. \quad (11)$$

Finally, the AE of the estimated distance when using the *SS* FSP is given by

$$D_{AE} = \left|\frac{c_0}{2\,\nu}\left(f_{IF} + \Delta f\right)\Delta T_s \frac{e_I - e_R}{1 + e_I + e_R + e_I\, e_R}\right| \approx \left|\frac{c_0}{2\,\nu}\left(f_{IF} + \Delta f\right)\Delta T_s\left(e_I - e_R\right)\right|. \quad (12)$$

As can be seen from the above expression, the AE increases with intermediate frequency f_{IF}, the crystal oscillator ppm differences (COPD) between INIT and REF, expressed as $ppm_I - ppm_R$, the CFO Δf, and the ideal time interval between the start of phase sampling on two consecutive carrier frequencies ΔT_s for INIT and REF, while it decreases with increasing frequency step ν. To evaluate the practical significance of this error, we calculate the AE using parameters f_{IF} =1 MHz, ΔT_s =168 μs, $T_{o,I}$ =88 μs, and $T_{o,R}$ =24 μs, which reflect our hardware capabilities [28], together with COPD = 30 ppm and CFO Δf =10 kHz, which are representative real-world values. The carrier spacing ν corresponds to the use of 16 and 160 carriers within the industrial, scientific, and medical (ISM) band 2405–2480 MHz. The resulting AE is 0.1526 m for M =16 and 1.6176 m for M =160. These results highlight two observations. First, the estimation errors caused by the asynchronization between the devices are substantial even for relatively small M. Second, increasing M, which is generally desirable because a larger number of samples reduces the effects of noise or to obtain a finer resolution in the channel frequency response (CFR), leads to an increase in systematic error. Although a lower intermediate frequency would help reduce AE, it introduces additional challenges, such as the need for more precise low-frequency filtering and a higher susceptibility to relative phase noise, DC offset, and flicker noise - especially for low-cost platforms with constrained analog front-end performance. In the following section, we propose novel FSPs designed to reduce this estimation error without the need for synchronization or calibration procedures.

III. FSP OPTIMIZATION

A major disadvantage of using *SS* FSP is that the additional phase shifts due to asynchronization are strongly correlated with the phase shifts due to propagation distance, leading to a systematic error in distance estimation. Fig. 3(a) illustrates this effect by comparing the ideal phase shifts (under perfect synchronization) with those affected by asynchronization in a single-path scenario, showing how the additional phase contribution alters the slope of the phase shifts profile, which directly corresponds to the propagation distance. To mitigate this bias, we permute the carriers in the FSP so that the i-dependent asynchronization phase shifts $\Delta\Phi$ in (8) are decorrelated from the distance-dependent phase shifts across carrier frequencies. With the permutation of FSP, we therefore manipulate the magnitude of $\Delta\Phi$ for each individual carrier. Note that in Section II, we derived the signal model such that phase shifts due to asynchronization grow by a constant increment $\Delta\Phi$ with each successive carrier in the MCPD procedure, with the first carrier having zero phase shift. Since the magnitude of the estimated channel impulse response (CIR), obtained as the inverse Fourier transform of the CFR, does not change when a common phase offset is added to the phase shifts associated with the carrier frequencies, the phase shifts are centered around zero to facilitate interpretation.

Theoretically, the optimal FSP that minimizes the systematic error due to asynchronization could be found by a brute search over all combinations. However, the number of possible combinations grows factorially, making an exhaustive search computationally infeasible. Instead, we present seven structured approaches for constructing FSP that reduce the asynchronization-induced systematic error.

In the first approach, the FSP is constructed such that the carrier frequencies alternate between the lowest and the highest available carrier frequency, starting with the lowest frequency. We refer to this switching sequence as the *Zigzag* FSP. For example, the *Zigzag* FSP for 16 carriers is: [1, 16, 2, 15, 3, 14, 4, 13, 5, 12, 6, 11, 7, 10, 8, 9]. In contrast to the *SS* FSP, where the additional phase shifts due to asynchronization increase monotonically with frequency, in the *Zigzag* FSP phase shifts increase up to the middle of the frequency band and then decrease symmetrically (see Fig. 3(b)). This symmetry reduces the correlation between phase shifts due to asynchronization and those due to propagation distance. However, the drawback is the appearance of additional sidelobes in the CIR close to the main peak, which can lead to small errors in distance estimation, especially in low signal-to-noise ratio (SNR) environments. Furthermore, if the phase shifts caused by the asynchronization become too large, these sidelobes can exceed the amplitude of the line-of-sight (LOS) component, leading to incorrect distance estimates. This behavior is illustrated in Fig. 4(b), which shows the estimated CIRs affected by the asynchronization together with the ideal CIRs obtained with perfect synchronization in a single-path scenario.

The next two approaches to FSP design were adopted from the literature [19], where the author proposed similar switching patterns to select between eight antenna elements in FMCW systems to allow accurate DoA estimation in the presence of motion. Given the similarity of the underlying problem, we have adapted and generalized

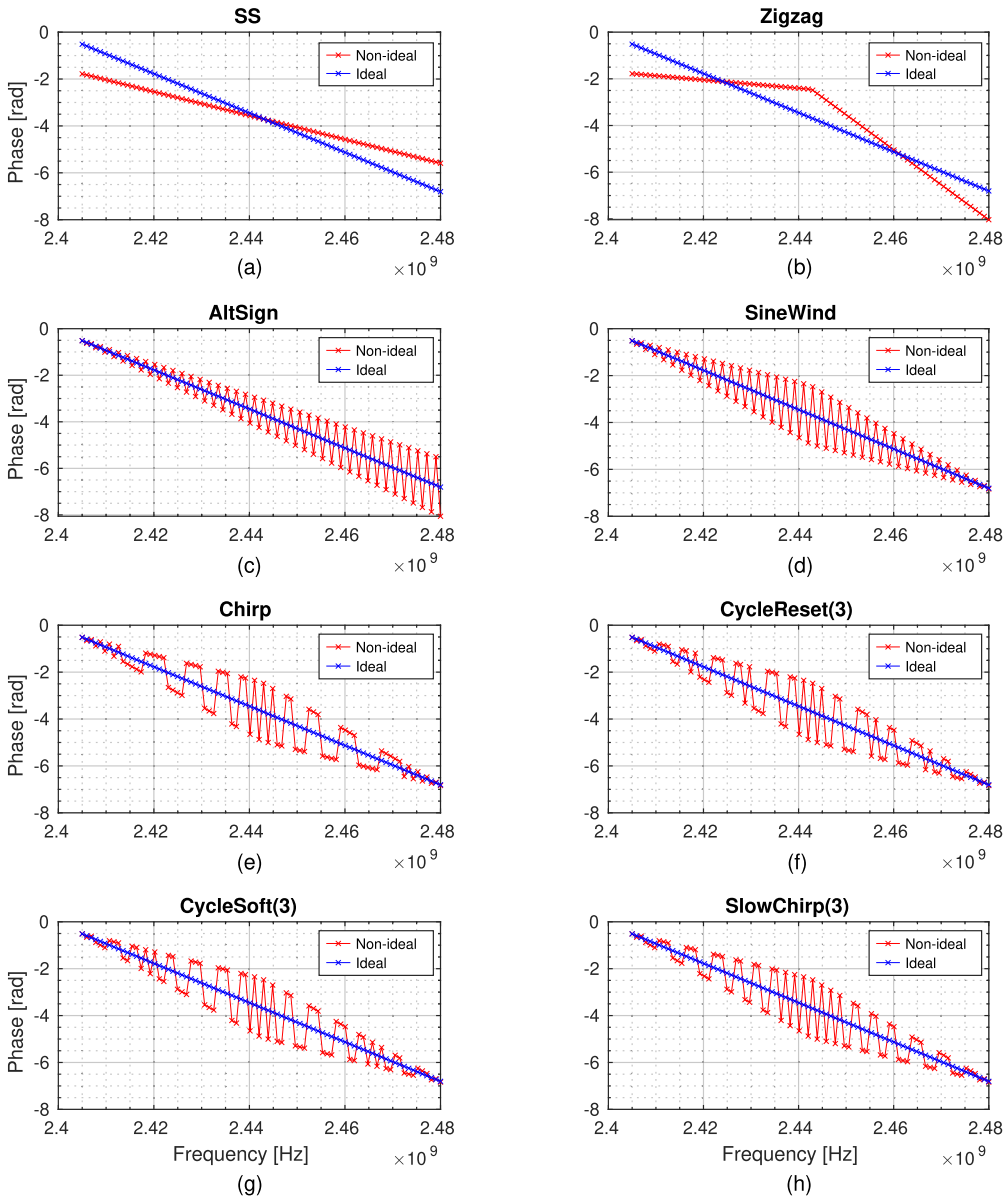


FIGURE 3. **Comparison of the ideal, unwrapped phase profiles (blue), resulting from perfectly synchronized measurements at INIT and REF without frequency or timing errors, and the non-ideal, unwrapped phase profiles (red), containing CFO and sampling time asynchronization effects between INIT and REF, for different FSPs. The simulation uses the same parameters as at the end of Section II, but with $M = 80$ and $D = 2$ m, chosen for clearer visualization.**

these switching strategies for an arbitrary number of carrier frequencies. The first switching sequence, named *AltSign* FSP, produces asynchronization-induced phase shifts that alternate above and below the ideal phase profile, with magnitude increasing toward higher frequencies (see Fig. 3(c)). For 16 carriers, this sequence is [16, 14, 12, 10, 8, 6, 4, 2, 1, 3, 5, 7, 9, 11, 13, 15]. Compared to the *Zigzag* FSP, this pattern produces less prominent sidelobes close to the main peak in the estimated CIR as can be seen in Fig. 4(c). Instead, it introduces a sharp secondary peak halfway across the delay domain from the true peak. Although the CIR is obtained by transforming complex IQ measurements across carrier frequencies from the frequency domain to the time domain, it can also be interpreted as the spectral content of the measured sequence. From this perspective, the peaks in the estimated spectrum correspond to the frequency components in the measured phase-shifts profile across the carrier frequencies. In the case of *AltSign* FSP, the additional phase shifts due to asynchronization oscillate around the ideal phase-shifts profile at the maximum

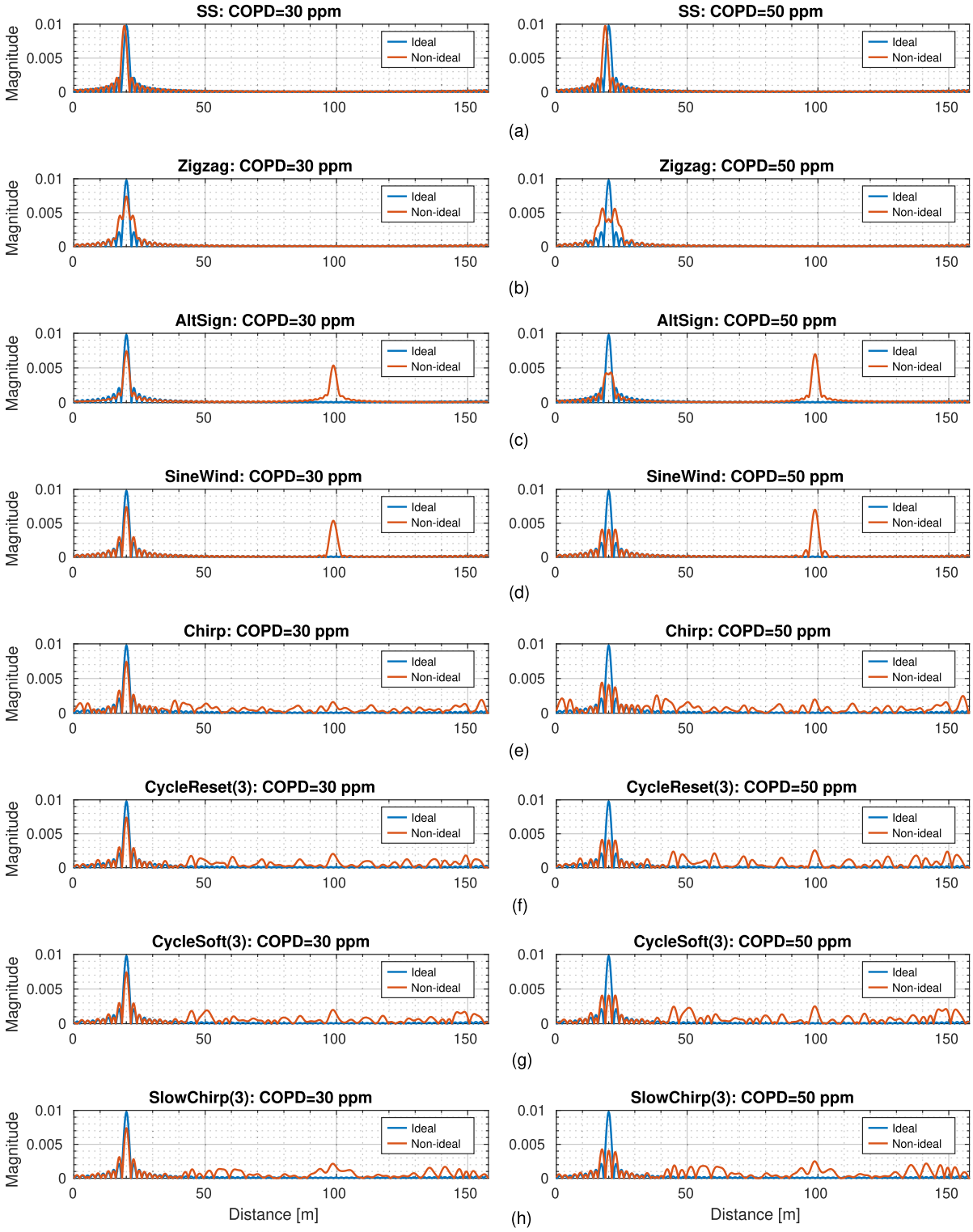


FIGURE 4. Comparison of the ideal CIRs (blue), resulting from perfectly synchronized measurements at INIT and REF without frequency or timing errors, and the non-ideal CIRs (red), which include CFO and sampling time asynchronization effects between INIT and REF, for different FSPs and two COPD values (30 ppm and 50 ppm). The simulation uses the same parameters as at the end of Section II, but with $M = 80$ and $D = 20$ m, chosen for clearer visualization. The non-ideal profiles reveal distinct artifacts whose structure depends on the FSP used.

possible frequency (changing sign at each carrier frequency step), resulting in a strong high-frequency component. This results in a secondary peak that is at a predictable and maximally distant location from the true peak in the CIR. The main disadvantage of this approach is that the amplitude of the secondary peak is relatively high compared to the true peak. With increasing asynchronization between the devices (e.g. due to a larger CFO or COPD), this secondary peak can exceed the LOS component, potentially leading to an incorrect distance estimate. Especially in dense multipath environments or under low-SNR conditions, it becomes increasingly difficult to distinguish ghost peaks from true multipath components. In indoor environments with limited physical dimensions, this peak may be outside the reasonable range of propagation delays, making it easier to identify and filter out as a ghost target.

The second generalized switching pattern from [19] is shown in Fig. 3(d). It follows the same core idea as the *AltSign* FSP - changing the sign of the asynchronization-induced phase shifts at each carrier frequency step relative to the ideal phase-shifts profile - but additionally arranges the carrier frequencies in such a way that the magnitude of the phase shifts gradually decreases to zero towards the edges of the frequency band. This produces a phase shifts profile that resembles a sampled sine function with an applied window function, which has the added benefit of reducing spectral leakage in estimated CIR. We refer to this switching sequence as the *SineWind* FSP. For example, the FSP for 16 carriers is: [8, 10, 6, 12, 4, 14, 2, 16, 1, 15, 3, 13, 5, 11, 7, 9]. The main disadvantage of this FSP is still the amplitude of the secondary peak, which can exceed the amplitude of the true peak in the case of large asynchronization-induced phase shifts, leading to an incorrect distance estimate.

Since the effectiveness of the previously discussed FSPs *AltSign* and *SineWind* is limited by the extent of CFO and COPD between INIT and REF, we introduce four additional FSP variants that are designed to maintain high distance estimation accuracy while improving robustness to higher levels of asynchronization. These FSPs are based on the same core principle: reducing the amplitude of the secondary peak in the CIR by redistributing its energy into multiple path components with lower amplitudes. This is achieved by changing the sign of asynchronization-induced phase shifts relative to the ideal phase-shifts profile less frequent than in the *AltSign* and *SineWind* FSPs, where the sign-change interval (the number of consecutive carrier frequency steps before the phase changes sign) is fixed at one. The problem of designing the FSP can be viewed as assigning a predefined set of phase shifts due to asynchronization, within $\pm(M-1)/2 \cdot \Delta\Phi$ in steps of $\Delta\Phi$, to the available carrier frequencies so that the resulting phase profile attains the desired shape and the corresponding CIR has favorable characteristics as shown in Fig. 5 using the example of *SineWind* FSP. Since the set of phase shifts is finite, the range of achievable CIR shapes is inherently constrained. All four FSP variants begin by assigning the largest positive

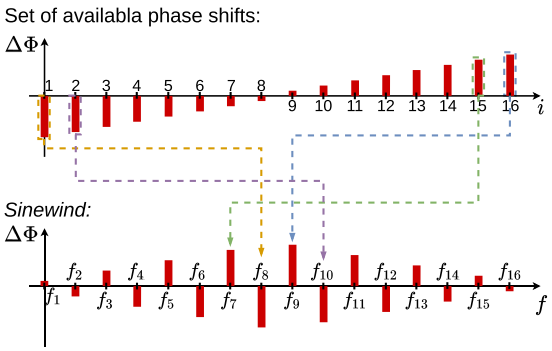


FIGURE 5. **Illustration of the FSP design, showing how the two smallest and two largest asynchronization-induced phase shifts are assigned to the center carrier frequencies. These frequencies are mapped in the FSP by the corresponding index *i* of their assigned phase shifts. The remaining phase shifts are assigned to the other frequencies following the same logic, resulting in the desired phase-shift profile.**

and negative asynchronization-induced phase shifts to the center frequencies of the available frequency band, which corresponds to the positioning of the center frequencies at the end and beginning of the FSP. For an odd number of carriers, these are the center and center-plus-one carriers. We then continue by assigning progressively smaller available phase shifts to the remaining frequencies from the center towards the edges of the frequency band.

In the first FSP variant, unlike the *SineWind* FSP, the sign-change interval is not constant, but starts at one at the band center and increases by one after each sign flip, making the sign flips progressively less frequent toward the band edges, as shown in Fig. 3(e). If the number of carriers remaining towards the edge of the band is less than the number required for the current sign-change interval, we reset the interval to one until the edge. This design choice ensures that the additional path components introduced in the estimated CIR have the highest amplitudes that are as far away from the true peak as possible, minimizing interference with the true path component. The resulting phase shifts profile has fast sign-change rates and high-amplitude phase shifts concentrated in the center of the frequency band, and slower sign-change rates with lower-amplitude phase shifts towards the edges. Due to the similarity of the resulting phase shift profile to a bidirectional chirp signal, we refer to this FSP as *Chirp* FSP. A limitation of the *Chirp* FSP arises when the number of carriers becomes large. In such cases, the sign-change interval can become so large that the resulting additional peaks in the CIR appear too close to the true peak, increasing the risk of interference and peak distortion. To address this problem, the next FSP variants introduces a limit value for the sign-change interval, which is controlled by the user. For example, if the limit is set to 3, the maximum sign-change interval is 3.

The second variant begins similarly to the *Chirp* FSP by gradually increasing the sign-change interval. However, once the specified limit is reached (e.g. 3), the sign-change interval

is reset to 1 before being increased again, as in Fig. 3(f). All other aspects of the design, including the assignment of phase-shift magnitudes and symmetry around the center of the frequency band, remain the same as for the *Chirp* FSP. We refer to this FSP as *CycleReset(n)*, where n is the limit parameter.

The third FSP variant builds on the idea of the *CycleReset(n)* FSP, but replaces the hard reset with a gradual reversal, so that the sign-change interval is not reset to one after reaching the specified limit, but decreases by one until it reaches 1 and then increases again. This produces a smoother alternation pattern, as shown in Fig. 3(g). We refer to this FSP as *CycleSoft(n)*.

In the final FSP variant, the sign-change intervals from 1 to the specified limit n are each repeated the same number of times. Starting from the center of the frequency band, all repetitions of the shortest interval are applied first, then the length of the interval is increased and all its repetitions are applied, continuing in this manner until the limit is reached, as shown in Fig. 3(h). We refer to this sequence as *SlowChirp(n)* FSP.

As illustrated in Fig. 4(e)-(h), the secondary peak observed in the *AltSign* and *SineWind* FSPs is effectively suppressed by each of the four final FSP variants. The corresponding CIRs more closely resemble those of the ideally synchronized case with additive noise with slight differences between them.

In addition to the optimized patterns described above, we investigate FSPs derived from the BLE channel hopping algorithm #1. This method generates a deterministic permutation of carrier indices by repeatedly adding a fixed hop increment h to the current channel index k and taking the result modulo the number of carriers M, i.e. $k \leftarrow (k + h) \bmod M$, until all carriers are visited exactly once. Valid hop increments range from 5 to 16 and must be coprime to 37 (the number of BLE data channels). In our analysis, we only evaluated $h = 8$ and $h = 14$, which yielded the highest accuracy referred to as *BLE #1(8)* and *BLE #1(14)*, respectively. In contrast, BLE algorithm #2 operates in a more randomized manner and may revisit channels before covering the entire set, while algorithm #1 ensures a complete cycle without repetitions, making it directly applicable to MCPD distance measurements. In this work, we use the raw hopping sequence without interference-based channel blacklisting or adaptive channel selection. If this hopping approach is to be generalized for an arbitrary number of carriers, all valid hop increments (coprime to M) would first need to be identified, followed by a selection of the best performing patterns among them.

For completeness, to evaluate the effectiveness of the proposed FSP design approaches, we also include a randomly permuted FSP for comparison. The phase shifts profile and the corresponding CIR of one such random FSP are shown in Fig. 6. We will refer to this FSP as *Random*. The resulting CIR resembles the case of perfectly synchronized devices with additive noise. It is important to note that randomly permuting carrier frequencies can lead to a wide range of performance

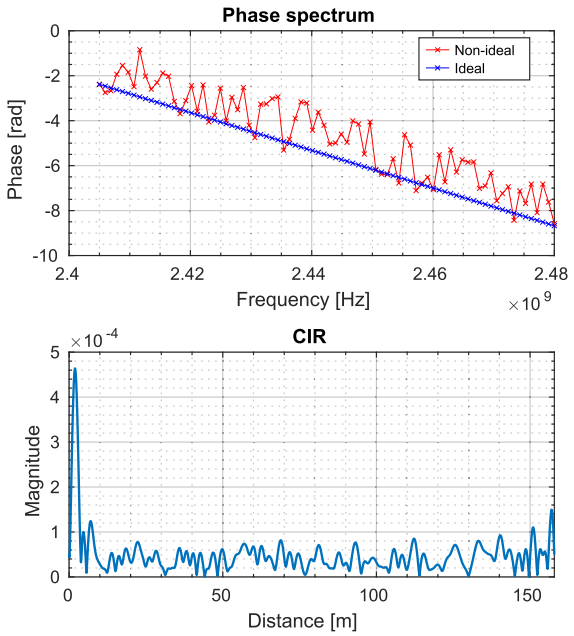


FIGURE 6. Comparison of the ideal, unwrapped phase profile (blue), resulting from perfectly synchronized measurements at INIT and REF without frequency or timing errors, and the non-ideal phase profile (red), containing CFO and sampling time asynchronization effects between INIT and REF, for the *Random* FSP (top). The corresponding CIR (bottom) illustrates the distortion caused by the asynchronization. The simulation assumes single-path scenario and same simulation parameters as at the end of Section II, but with $M = 80$ and $D = 2$ m, chosen for clearer visualization.

outcomes, depending on the specific ordering. Consequently, higher errors in distance estimation can generally be expected compared to the structured FSPs proposed in this work. Nevertheless, random FSPs can be a viable alternative if the goal is spectrum sensing and the exact position of the peaks in the CIR is not critical.

The mechanisms by which a given FSP attenuates the systematic error inherent in the *SS* FSP can be studied rigorously using the inverse discrete Fourier transform (IDFT). Any FSP can be represented by its inverse permutation $\mathbf{P} = [P_1, P_2, \ldots, P_M]$, where the indices of the vector correspond to the ordered carrier frequencies from the lowest ($k = 1$) to the highest ($k = M$) used in MCPD, and each value P_k denotes the position of the corresponding carrier frequency (with index k) within the FSP. Equivalently, P can be interpreted as the additional normalized phase shifts due to asynchronization, expressed as a function of the carrier frequency. For example, under the *AltSign* pattern with M=16 carriers, $\mathbf{P} = [9, 8, 10, 7, 11, 6, 12, 5, 13, 4, 14, 3, 15, 2, 16, 1]$. Multiplying $\mathbf{P}$ by the scalar $2\pi\left(f_{IF} + \Delta f\right)\Delta T_s\left(e_I - e_R\right)$ gives the unnormalized asynchronization-induced phase shifts. By adding the ideal distance-dependent phase ramp, the composite phase spectrum is obtained, which can then be transformed via the IDFT to obtain the CIR. In the example

TABLE 1. Absolute linear regression slopes $|b|$ of P for different FSPs and different number of carriers, where all values are normalized to the *SS* FSP. Lower values of $|b|$ indicate better suppression of the systematic error in the measured distance, with $|b| = 0$ indicating complete cancelation.

FSP	Number of carriers			
	16	37	80	160
SS	1	1	1	1
Zigzag	0.09412	0.04054	0.01875	0.00938
AltSign	0.09412	0.04054	0.01875	0.00938
SineWind	0	0.00213	0	0
Chirp	0.02353	0.00166	0.00056	0.01083
CycleReset(2)	0.02353	0.00261	0	0.00030
CycleReset(3)	0.02353	0.00166	0.00169	0.00016
CycleSoft(2)	0.02353	0.00640	0.00113	0.00002
CycleSoft(3)	0.02353	0.00166	0.00094	0.00082
SlowChirp(2)	0.02353	0.00119	0.00563	0.00396
SlowChirp(3)	0	0.00166	0.00956	0.00422
BLE #1(8)	—	0.00877	—	—
BLE #1(14)	—	0.00877	—	—

of *AltSign*, $\mathbf{P}$ can be expressed analytically as two functions by splitting it into even- and odd-indexed subsequences: one linearly increasing and the other linearly decreasing. The IDFT of each subsequence produces a main peak that is shifted by the same amount, proportional to the slopes of the linear functions, but in opposite directions. The two peaks merge into a single peak when the slopes are low, resulting in a correctly positioned peak. If the slopes diverge strongly, the two peaks separate, resulting in an incorrect distance estimate. A secondary peak occurs at half of the delay domain span because each subsequence has only $M/2$ samples and the pattern repeats. However, due to the different CIR phase responses of the even and odd subsequences, the secondary peaks partially subtract, and the resulting peak is smaller than the main peak.

Although this spectral domain analysis can also be applied to patterns such as *Zigzag* and *SineWind*, the derivation of a closed-form analytical expression for $\mathbf{P}$ becomes increasingly complex for many FSPs. A simpler method that shows how effective FSPs are in attenuating systematic error, but without capturing artifacts induced by the FSP in the estimated CIR, is to fit a straight line to the values of $\mathbf{P}$ using a simple linear regression [29]. The fitted slope b quantifies the degree to which the phase ramp induced by asynchronization deviates from zero. Minimizing $|b|$ therefore minimizes the systematic error. For our problem, the calculation of $|b|$ reduces to the dot product

$$|b| = |\mathbf{w} \cdot \mathbf{P}^{\mathbf{T}}|, \tag{13}$$

where $\mathbf{P}$ has been centered to have zero mean, and $w_k = k - \frac{M+1}{2}$, $k \in \{1, \ldots, M\}$. Table 1 reports the absolute slope metric $|b|$ calculated according to (13) for each FSP and four different number of carriers. All porposed FSPs achieve substantially smaller $|b|$ than the *SS* FSP, with several patterns driving the slope to zero in certain configurations, indicating perfect mitigation of systematic error. Although the BLE frequency hopping patterns listed in Table 1 show performance comparable to some of the

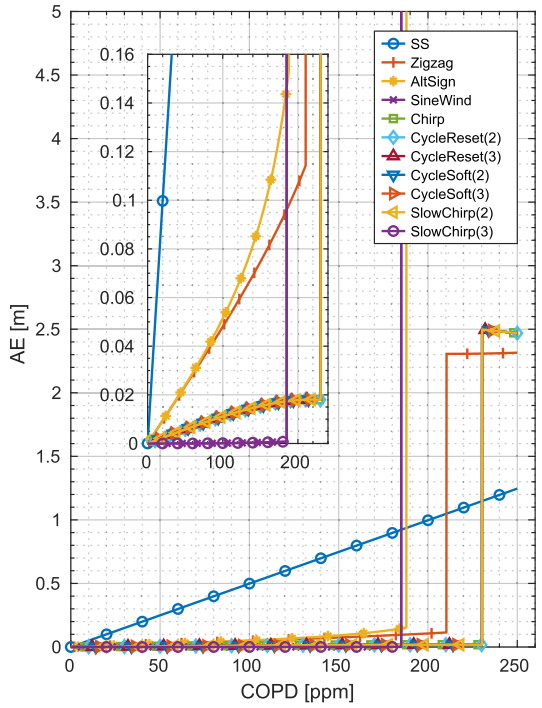


FIGURE 7. AE as a function of COPD for different FSPs using 16 carriers. The COPD bounds of proposed FSPs where AE increases rapidly are clearly visible. The inset shows a zoomed-in view of the lower error region for a better comparison among proposed FSPs.

proposed FSPs, it should be noted that performance varies considerably depending on the hopping value. The mean and standard deviation of $|b|$ over all valid BLE hop values are 0.08041 and 0.09229, respectively, indicating a larger spread in performance compared to optimized patterns.

IV. SIMULATIONS

Simulations in Matlab were performed to evaluate the effects of different levels of asynchronization, noise, and number of carriers on the accuracy of distance estimation. In all cases, a single-path scenario with a distance of 10 m between devices was assumed. The initial phase offsets of the LOs for each carrier frequency were randomly drawn from a uniform distribution, and one IQ sample per carrier frequency was obtained unless otherwise specified. The CIRs were then obtained via an inverse fast Fourier transform (IFFT) of the IQ samples, which included the asynchronization-induced phase shifts, and were zero-padded to 1,048,576 bins. This corresponds to a distance resolution of about about 30 mm in the lowest case when 160 carriers are considered. The estimated distance was determined by identifying the position of the peak with the maximum magnitude in the measured CIR. The following simulation parameters, introduced earlier in the paper, are restated here for clarity: frequency band 2405–2480 MHz, ΔT_s =168 μs, $T_{o,I}$ =88 μs, $T_{o,R}$ =24 μs, and f_{IF} =1 MHz. The remaining parameters are specified later as they depend on the respective analysis.

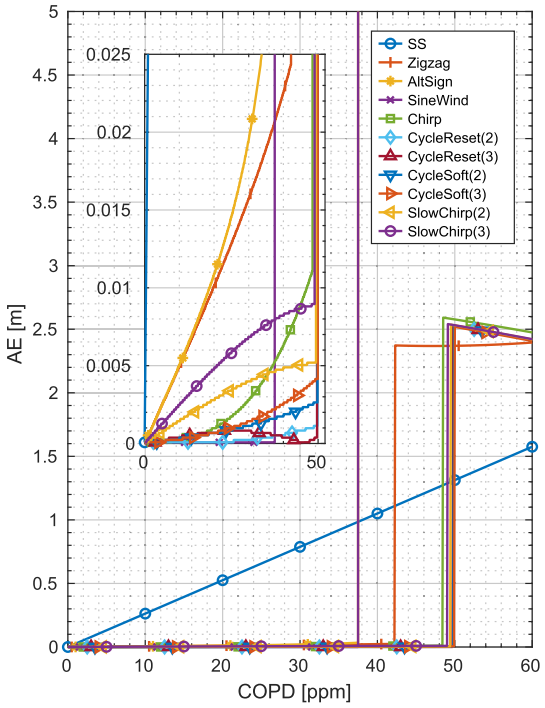


FIGURE 8. AE as a function of COPD for different FSPs using 80 carriers. The COPD bounds of proposed FSPs where AE increases rapidly are clearly visible. The inset shows a zoomed-in view of the lower error region for a better comparison among proposed FSPs.

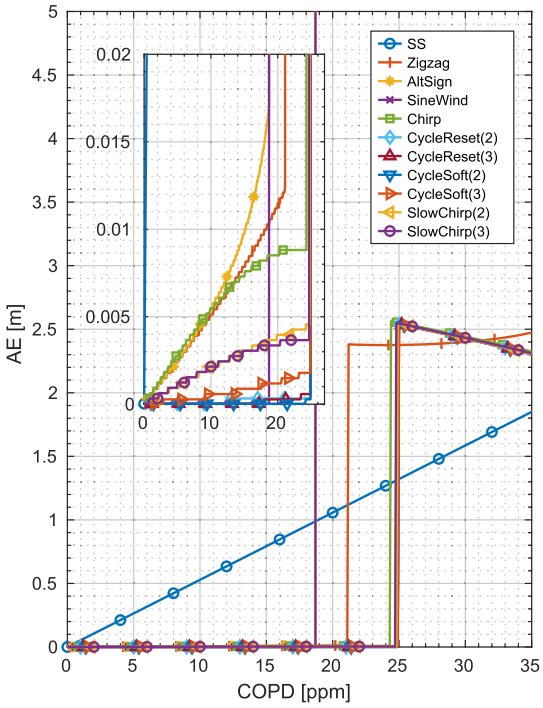


FIGURE 9. AE as a function of COPD for different FSPs using 160 carriers. The COPD bounds of proposed FSPs where AE increases rapidly are clearly visible. The inset shows a zoomed-in view of the lower error region for a better comparison among proposed FSPs.

A. EFFECT OF VARYING COPD ON DISTANCE ESTIMATION

We first performed simulations with a fixed CFO Δf of 10 kHz, while varying the COPD. The AE versus COPD curves for each FSP considered are shown in Fig. 7, 8, and 9, corresponding to the commonly used configurations with 16, 80, and 160 carriers, respectively. As expected according to (12), the AE of the *SS* FSP increases both with COPD and with the number of carriers. For small values of COPD, all proposed FSPs exhibit significantly lower AEs than the *SS* FSP, with AEs generally increasing gradually with increasing COPD. An exception is *CycleReset(3)* with 80 carriers, where the AE first increases and then decreases slightly before increasing again. As COPD continues to increase, each FSP reaches a certain bound, beyond which the AE increases rapidly. This transition reflects the limit of each FSP's ability to mitigate the effect of asynchronization on distance estimation. The higher the number of carriers, the lower the COPD bound at which the proposed FSP shows a significant performance gain over the *SS* FSP. These bounds are jointly influenced by intermediate frequency f_{IF}, CFO, and COPD, all of which contribute to cumulative phase shifts due to asynchronization (12). We therefore refer to these bounds as asynchronization bounds. All proposed FSPs, with the exception of *Zigzag* and *AltSign*, maintain AE values below 2 cm up to their respective bounds on all tested number of carriers, while the AE of the *SS* FSP is no less than 0.922 m at these bounds.

Table 2 summarizes the asynchronization bounds for each proposed FSP, together with the mean value calculated from the AEs corresponding to the COPD values below the respective bound. For comparison with the BLE frequency hopping patterns, the table also includes the results for the configuration with the number of carriers set to 37. The results show that all proposed FSPs, with the exception of *Zigzag* and *AltSign*, exhibit significantly better distance estimation accuracy within their optimal operating ranges compared to *SS* FPS, with the calculated mean values of these FSPs being up to 1.1 cm. The *SineWind* FSP exhibits the lowest AE values below the asynchronization bound due to its minimal spectral leakage, but also has the lowest asynchronization bound and is therefore the most sensitive to asynchronization effects. In contrast, the FSPs *CycleReset(n)*, *CycleSoft(n)*, and *SlowChirp(n)* have the highest bounds, since they introduce more path components with lower amplitudes into the estimated CIR. Among these FSPs, the differences in AEs before reaching the bounds are minimal, on the order of millimeters. Notably, all proposed FSPs generally benefit from a decreasing AE with increasing number of carriers, in contrast to the behavior of the *SS* FSP. The considered BLE frequency hopping patterns achieve mean AE values comparable to the best performing proposed FSPs, but are inherently limited by their relatively low asynchronization bound (81.2 ppm).

TABLE 2. Asynchronization bounds of all proposed FSPs, defined as the COPD values at which AE increases rapidly, together with the mean calculated from AE values corresponding to the COPD values below the respective bound of each FSP. Results are given for 16, 37, 80, and 160 carriers.

FSP	16 carriers		37 carriers		80 carriers		160 carriers	
	bound [ppm]	mean [cm]	bound [ppm]	mean [cm]	bound [ppm]	mean [cm]	bound [ppm]	mean [cm]
Zigzag	210.3	5.3	91.2	2.4	42.2	1.1	21.1	0.6
AltSign	187.9	5.5	81.2	2.5	37.5	1.2	18.7	0.6
SineWind	185.0	0	81.2	0.1	37.5	0	18.7	0
Chirp	230.2	1.1	104.5	0.4	48.4	0.3	24.3	0.6
CycleReset(2)	230.2	1.1	107.4	0.3	49.8	0	24.9	0
CycleReset(3)	230.2	1.1	104.5	0.4	49.7	0	24.9	0
CycleSoft(2)	230.2	1.1	107.9	0.6	49.8	0.1	24.9	0
CycleSoft(3)	230.2	1.1	104.5	0.4	49.9	0.1	24.9	0.1
SlowChirp(2)	230.2	1.1	106.2	0.1	49.4	0.3	24.8	0.2
SlowChirp(3)	185.0	0	104.5	0.4	49.0	0.5	24.7	0.2
BLE #1(8)	—	—	81.2	0.3	—	—	—	—
BLE #1(14)	—	—	81.2	0.2	—	—	—	—

With the specified simulation parameters, the asynchronization bounds for 16 carriers are well above the typical COPD values of low-cost IoT devices (e.g. 30 ppm), indicating robust performance. Increasing to 80 carriers brings the bounds closer to the typical COPD values, and for 160 carriers the bounds are likely to be lower, indicating that asynchronization can cause significant errors unless a robust FSP is used. However, a 16-carrier system results in a limited ambiguity range of $c/(2 \cdot \Delta f)$, which is about 30 m for the considered frequency band and may be insufficient for some applications, so a higher number of carriers is generally preferable.

To evaluate the performance variability of the *Random* FSPs, we performed additional simulations using 100 randomly generated FSP permutations. Particular attention was paid to the case with 160 carrier frequencies, as it exhibits the lowest tolerance to asynchronization effects. AE as a function of COPD is plotted for all 100 *Random* FSP permutations in Fig. 10, where each curve corresponds to a particular individual FSP permutation. The results show that the performance of randomly generated FSPs varies considerably and that the best performing nonrandom FSPs exhibit lower estimation errors. However, some random FSPs approach the accuracy of the best proposed FSPs and, in some cases, even outperform them in terms of the asynchronization bound, as shown in the example of a randomly generated FSP highlighted with a thicker red line in Fig. 10. These findings indicate that deterministic FSPs remain below their performance limit and there is room for further improvement.

Although some random FSPs demonstrate strong performance, their lack of generalizability over a varying number of carriers limits their practical use. Applications that require dynamic carrier adaptation would need to be re-optimized for each case. To develop more broadly applicable design principles, this work focuses on structured, nonrandom FSPs that provide consistent robustness across different configurations.

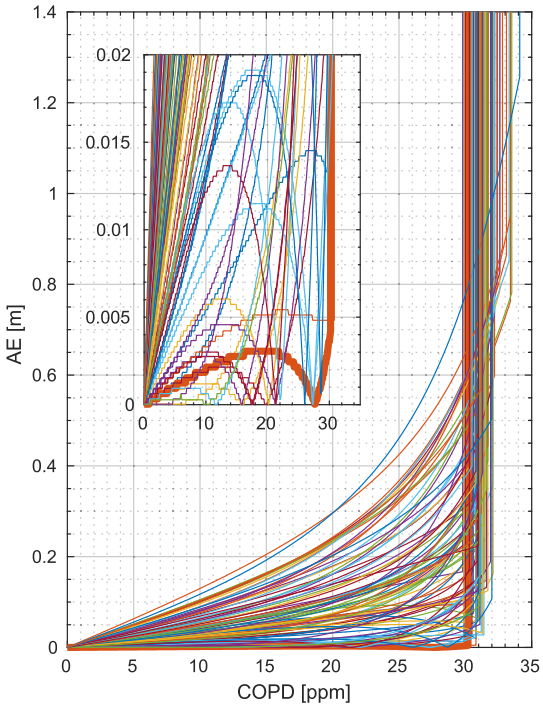


FIGURE 10. AE as a function of COPD for 100 randomly generated FSP permutations using 160 carriers, where each curve corresponds to one FSP. The inset shows a zoomed-in view of the lower error region for a better comparison between FSPs. This illustrates the variability in sensitivity to asynchronization effects for unstructured patterns.

B. EFFECT OF DIFFERENT NUMBER OF CARRIERS ON DISTANCE ESTIMATION

In MCPD ranging, the number of carriers directly affects key performance indicators: with a fixed total bandwidth, it determines the carrier spacing, and thus the maximum unambiguous range, while with a fixed carrier spacing, it determines the total bandwidth, and thus the range resolution. In both cases, there is a trade-off between measurement time and achievable range or resolution, making coarse, faster measurements preferable in power-constrained scenarios, and fine, higher resolution estimates preferable when accuracy is critical. Evaluating how the estimation error of FSPs varies with the number of carriers is therefore essential for applications where the number of carriers is dynamically adjusted, as it helps to identify FSPs that maintain consistently high accuracy. FSPs for

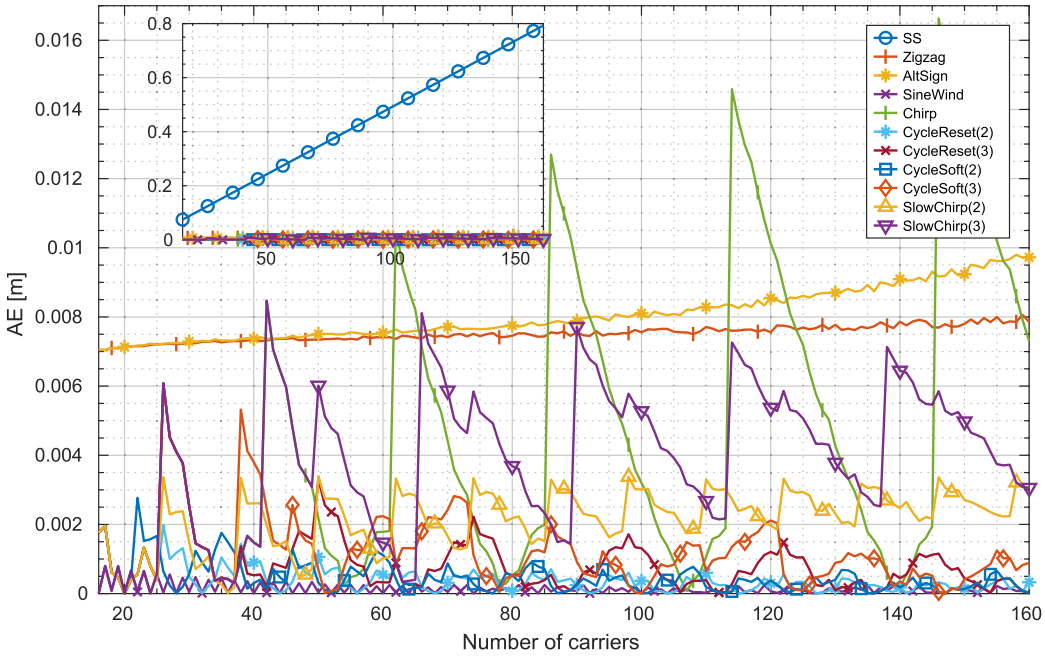


FIGURE 11. AE as a function of the number of carrier frequencies, ranging from 10 to 160, for different FSPs. The inset shows a zoomed-out version of the same plot, allowing a visual comparison of how AE increases with the number of carriers for the *SS* FSP compared to the proposed FSPs.

TABLE 3. Mean value and standard deviation of AEs for the considered FSPs, calculated over the entire range of the number of carriers from 16 to 160.

FSP	Mean [m]	Standard deviation [m]
SS	0.4338	0.2094
Zigzag	0.0075	0.0002
AltSign	0.0081	0.0007
SineWind	0.0001	0.0002
Chirp	0.0046	0.0043
CycleReset(2)	0.0004	0.0004
CycleReset(3)	0.0009	0.0009
CycleSoft(2)	0.0005	0.0005
CycleSoft(3)	0.0012	0.0010
SlowChirp(2)	0.0022	0.0008
SlowChirp(3)	0.0039	0.0021

different numbers of carriers can be precomputed and stored in memory or generated on the fly, with the computation complexity to generate them depending on their structure.

In the following simulation, we have varied the number of carriers in steps of 1 from 16 to 160. The COPD and CFO were set to 15 ppm and 10 kHz, respectively, ensuring operation below the established asynchronization bounds of all FSPs. The results plotted in Fig. 11 show that no single FSP consistently achieves the lowest AE throughout the range of the number of carriers considered. Most FSPs (except *Zigzag* and *AltSign*) show periodic AE fluctuations as a function of the number of carriers. Among them, the *Chirp* FSP shows the strongest sensitivity, with the amplitude of the fluctuation increasing with the number of carriers. This behavior is due to the fact that many FSPs have inherent periodic structures and when the number of carriers is not an integer multiple of the period, the remaining carriers form a residual, non-optimized segment that slightly alters the pattern, resulting in measurable differences in estimation accuracy. Although the AE increases with the number of carriers for some FSPs, it decreases for others. However, all optimized FSPs consistently achieve AEs below 0.017 m over the entire evaluated range, while the AEs for *SS* FSP are significantly higher and increase monotonically with the number of carriers. Table 3 summarizes the mean and standard deviation of AEs for each FSP across all number of carriers. The *SineWind* FSP exhibits the best overall accuracy and the lowest dispersion of the estimates. However, the *CycleReset(2)* and *CycleSoft(2)* FSPs offer almost comparable performance, with mean and standard deviation values only a few millimeters higher.

C. NOISE SENSITIVITY ANALYSIS

The robustness of the proposed FSPs to additive white Gaussian noise, applied to the IQ samples on INIT and REF, is evaluated over a wide range of SNRs, from -10 dB to 60 dB. For each SNR level, 500 Monte Carlo simulations were performed, from which the root mean square error (RMSE) of the distance estimates was calculated. The simulations were performed for two configurations using 16 and 160 carrier frequencies to reflect edge case scenarios. The COPD and CFO were set to 15 ppm and 10 kHz, respectively. For comparison, we also evaluated the conventional *SS* FSP in combination with the estimation and correction of

phase distortions caused by asynchronization, following the approach previously used in the related literature to mitigate the effects of asynchronization on distance estimation. In this method, the timing diagram from Fig. 2 was retained, except that for both INIT and REF, multiple samples were acquired at the first carrier frequency at intervals of 8μs. Specifically, we considered three configurations with 128, 256, and 512 samples at the first frequency. The phase distortions were then estimated from these samples using a 4096-point fast Fourier transform (FFT), refined by quadratic interpolation over three samples around the detected peak, and then used to correct the phase measurements for both INIT and REF prior to distance estimation.

The results presented in Fig. 12 show that with decreasing SNR, all FSPs exhibit a distinct threshold value, below which the RMSE increases sharply. For both numbers of carriers considered, the *SS* FSP consistently shows higher RMSE values than the proposed FSPs for SNR values above the SNR thresholds, which is due to systematic errors caused by asynchronization. A notable difference can be observed in the rate at which the RMSE increases as the SNR decreases. The *SS* FSP shows a more gradual increase, indicating that it is less sensitive to increasing noise compared to the proposed FSPs. Consequently, the performance advantage of the optimized FSPs decreases with decreasing SNR, with the largest improvements seen under high-SNR conditions.

Performance comparison between 160 and 16 carriers reveals that the *SS* FSP exhibits higher RMSE values for 160 carriers, which is due to increased systematic errors. In general, all proposed FSPs demonstrate greater robustness to noise when 160 carriers are used, reflected in the less steep RMSE curves with decreasing SNR and lower SNR thresholds, which is to be expected when a larger number of measurements are acquired. Notably, this trend does not hold for *AltSign* and *SineWind*, where the SNR thresholds do not improve significantly. For 16 carriers, the differences between the proposed FSPs are small and largely negligible, each exhibiting an SNR threshold of about 3 to 4 dB. In contrast, larger performance distinctions emerge with 160 carriers, with *AltSign*, *SineWind*, and *Zigzag* performing worse than the other optimized FSPs, especially under lower SNR conditions. The difference in SNR thresholds between the other optimized FSPs is less than 2 dB.

As expected, the noise immunity of the estimation–correction approach improves with the number of acquired samples. For 16 carriers, the proposed FSPs and the estimation-correction approach show similar performance, with the exception that the latter shows a slightly higher RMSE when 128 samples are acquired. For 160 carriers, the difference in performance is larger, with the proposed FSPs exhibiting greater noise robustness. To match the performance of the best performing FSPs with the estimation-correction approach, even more samples would need to be acquired, increasing measurement time, power consumption, and interference risk. For both numbers of carriers, both approaches converge to approximately zero RMSE at high SNRs.

V. EXPERIMENTAL VALIDATION

The experimental validation aims to demonstrate that asynchronization between devices introduces measurable errors in distance estimation when using the *SS* FSP, and that these errors can be significantly reduced by adopting optimized FSPs. The experiments specifically investigate how the estimated distance varies with different degrees of asynchronization. AE values are not computed, as doing so would require precise knowledge of the true distance, necessitating extensive hardware calibration and reliable reference measurements, both challenging due to unknown delays stemming from RF paths on the printed circuit board (PCB), interconnect media, and environment-dependent calibration factors. Instead, the median distance and standard deviation are reported for varying degrees of asynchronization, reflecting the sensitivity of distance estimation to asynchronization and the dispersion of the measurements. We limited the analysis to two optimized FSPs: *SineWind* and *CycleReset(3)*. These were compared with the *SS* FSP baseline.

A. MEASUREMENT SETUP

We have used low-cost microcontroller platforms with AT86RF215 radio modules, that are compliant with the IEEE 802.15.4 standard [28]. These radios are equipped with an integrated phase measurement unit (PMU) that enables direct access to IQ samples through register-based readout via the serial peripheral interface (SPI) bus [30].

To evaluate the effects of different FSPs on distance estimation at different degrees of asynchronization, we exploited the hardware's ability to fine-tune the CFO. This allowed us to introduce a software-programmed CFO rather than varying the time drift, which would be less controlled and less reliable. Specifically, the frequency offset of the REF device was varied from –39.6728 kHz to 39.6728 kHz from the ideal frequency in steps of 396.728 Hz, with 30 measurements recorded in each setting. During the measurements, it was assumed that the time drift between the devices remained constant. According to (12), a constant non-zero time drift implies that the AE of the distance estimate of *SS* FSP varies proportionally to the CFO. To isolate the effects of asynchronization, we restricted our analysis to a single-path scenario to avoid ambiguities in interpretation that occur in uncontrolled multipath environments where it is difficult to distinguish between errors caused by multipath propagation and those caused by asynchronization. For this reason, the INIT and REF devices were connected via a coaxial cable instead of using antennas for over-the-air measurement.

The INIT device generated a periodic signal using a pulse width modulation (PWM) output on a general-purpose input/output (GPIO) pin with a period of 250 ms. This signal was connected to the second GPIO pin on the INIT device and

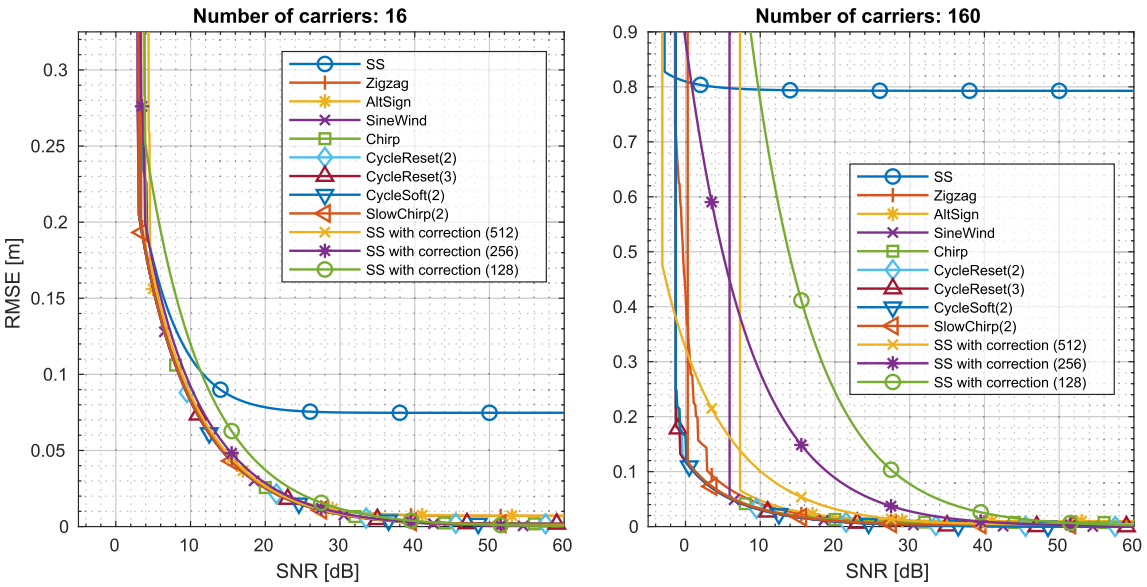


FIGURE 12. RMSE of distance estimation as a function of SNR for different FSPs with 16 and 160 carriers. Curves labeled "SS with correction (*X*)" represent the conventional *SS* FSP combined with an estimation–correction approach for phase distortions caused by asynchronization, where *X* denotes the number of additional samples acquired at the first carrier frequency to perform the estimation.

a corresponding pin on the REF device, both of which were configured to trigger an external interrupt on a rising edge. These interrupts initiated the phase measurement process (PMP) on both devices, switching the carrier frequencies according to the defined FSP. With this setup, the PMP could be triggered almost synchronously on both devices. However, slight differences in interrupt processing led to an initial timing offset on the order of a few microseconds. Although this offset does not directly affect the measurement accuracy, it does influence how long the devices remain in sync before they fall out of sync completely due to clock drift, when one device continues to transmit the CW signal while the other no longer reads the IQ values. Before performing the measurements, we established sufficient synchronization between the devices to reliably complete a PMP sequence with 151 carriers without loss of sync. This was achieved by inserting a carefully calibrated number of NOP assembly instructions between successive measurements on carriers. Since even small timing inconsistencies in PMP execution can significantly affect the results, it was crucial to maintain consistent execution timing for all tested frequency offsets, number of carriers, and FSPs to ensure fair and reliable comparisons. To support this, we chose 16, 76, and 151 for the number of carriers, corresponding to uniform frequency steps of 5 MHz, 1 MHz, and 500 kHz, respectively, within the 2405–2480 MHz band used. These configurations enabled the use of precalculated frequency lookup tables, eliminating the need for dynamic frequency calculations and ensuring a consistent execution time. The IQ samples captured during each PMP at both INIT and REF were transferred via universal asynchronous receiver/transmitter (UART) to a host

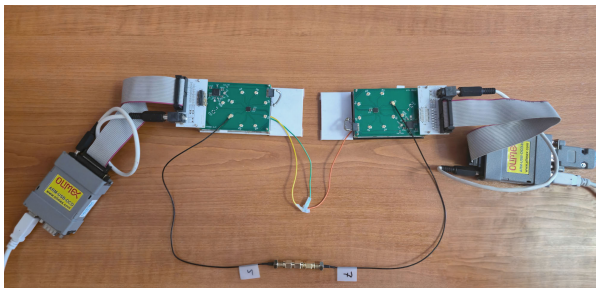


FIGURE 13. Setup of a real-world measurement campaign, showing the INIT and REF connected via an RF cable to ensure a predictable communication channel. Additional connecting cables are used for synchronization to trigger the start of the measurements and connection to a host computer via UART for data acquisition and processing.

computer where they were parsed and processed offline. The estimated distance was determined by identifying the position of the peak with the maximum magnitude in the measured CIR. The measurement setup is shown in Fig. 13.

B. MEASUREMENT RESULTS

The influence of asynchronization between devices and different FSPs on the resulting CIR shape is investigated first. Fig. 14 shows the measured CIRs along with the simulated CIRs without additive noise. The simulation parameters CFO and COPD were adjusted so that the amplitudes of the simulated CIRs match the amplitudes of the measured CIRs.

In the case of the SS FSP, additional peaks appear in the measured CIR that are not present in the simulated

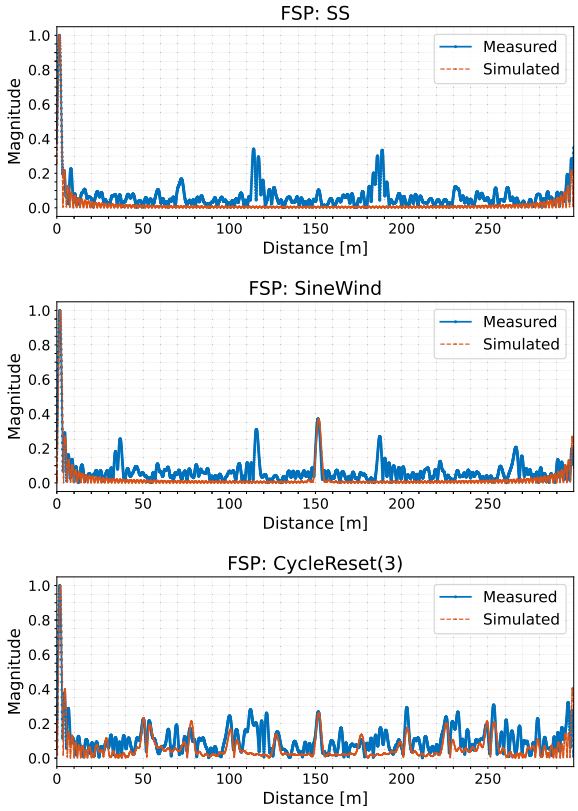


FIGURE 14. Comparison of measured and simulated CIRs for three representative FSPs, showing strong agreement in the positions and shapes of FSP-induced artifacts. Additional peaks in the measured CIRs, which are not present in the simulations, result from phase discontinuities caused by asynchronous register reads. The simulated CIRs are noise-free and are fine-tuned via CFO and COPD to match the measured amplitude values.

CIR. These anomalies are attributed to phase discontinuities caused by asynchronous register reads of IQ values from the PMU, as can be seen in the example of the measured phase spectrum in Fig. 15. Although the appearance of these artifacts varies between measurements, the approximate positions of the additional peaks remain consistent. Similar behavior is observed for the other two FSPs, where additional peaks that are not present in the simulations also appear at similar positions. Disregarding the additional peaks in the measured CIRs caused by asynchronous register-read artifacts, the measured CIRs of the proposed FSPs closely match the simulated ones, with aligned positions and shapes of the main peak and the asynchronization-induced peaks for each FSP, confirming the CIR shape from the simulations.

Next, the effect of varying the frequency offset on the distance estimation for different FSPs is analyzed. The medians of the distance estimates for each software-programmed

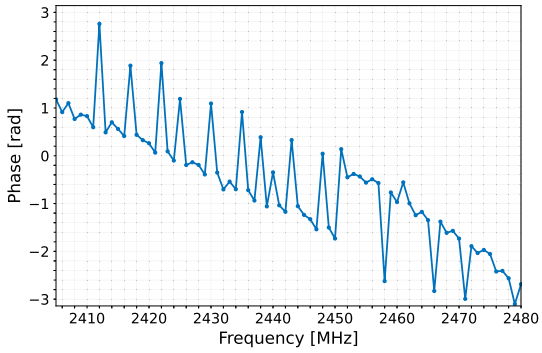


FIGURE 15. Example of measured phase values from a PMP routine showing deviations from the expected linear phase ramp due to abrupt phase jumps caused by asynchronous reading of registers leading to spurious peaks in the measured CIR.

frequency offset and the FSPs considered are shown in Fig. 16(a)-(c). The estimated distances show a clear linear dependence on the frequency offset, with the SS FSP showing the strongest sensitivity compared to the proposed FSPs. This underlines the effectiveness of the proposed FSPs in mitigating distance estimation errors caused by asynchronization. The corresponding slopes of the best-fit lines calculated from the medians for each FSP are presented in Table 4.

As predicted by (12) and confirmed with simulations, the slope for the *SS* FSP increases with the number of carriers. For 16 carriers, the differences in slopes between the FSPs are relatively small, with the *SS* FSP even having a lower slope than *CycleReset(3)*. This indicates that the performance benefit of using optimized FSPs with a small number of carriers is minimal. However, for 76 and 151 carriers, the performance gains of the proposed FSPs become more significant. Among the evaluated FSPs, *SineWind* consistently shows the smallest absolute slope values, indicating greater robustness to frequency offset compared to *CycleReset(3)* across all number of carriers. The residual linear trends observed for the proposed FSPs likely stem from secondary sources of error that were not accounted for in the simplified signal model described in Section II.

The medians of distance estimates are most stable at a frequency offset of about -6 kHz, with variability increasing as the frequency offset deviates from this point. This trend is also reflected in the plots of the calculated standard deviations of the distance estimates for each frequency offset in Fig. 16(d)–(f), where a minimum occurs near -6 kHz and the values increase symmetrically on both sides. This behavior is not explained by the signal model and is caused by asynchronous reads of the IQ values from the PMU register. Although the internal IQ sampling rate is 1 μs, the radio exposes the IQ samples through a register that is only updated with the latest value every 8 μs. Since the radio lacks a synchronization mechanism for reading registers, an initial

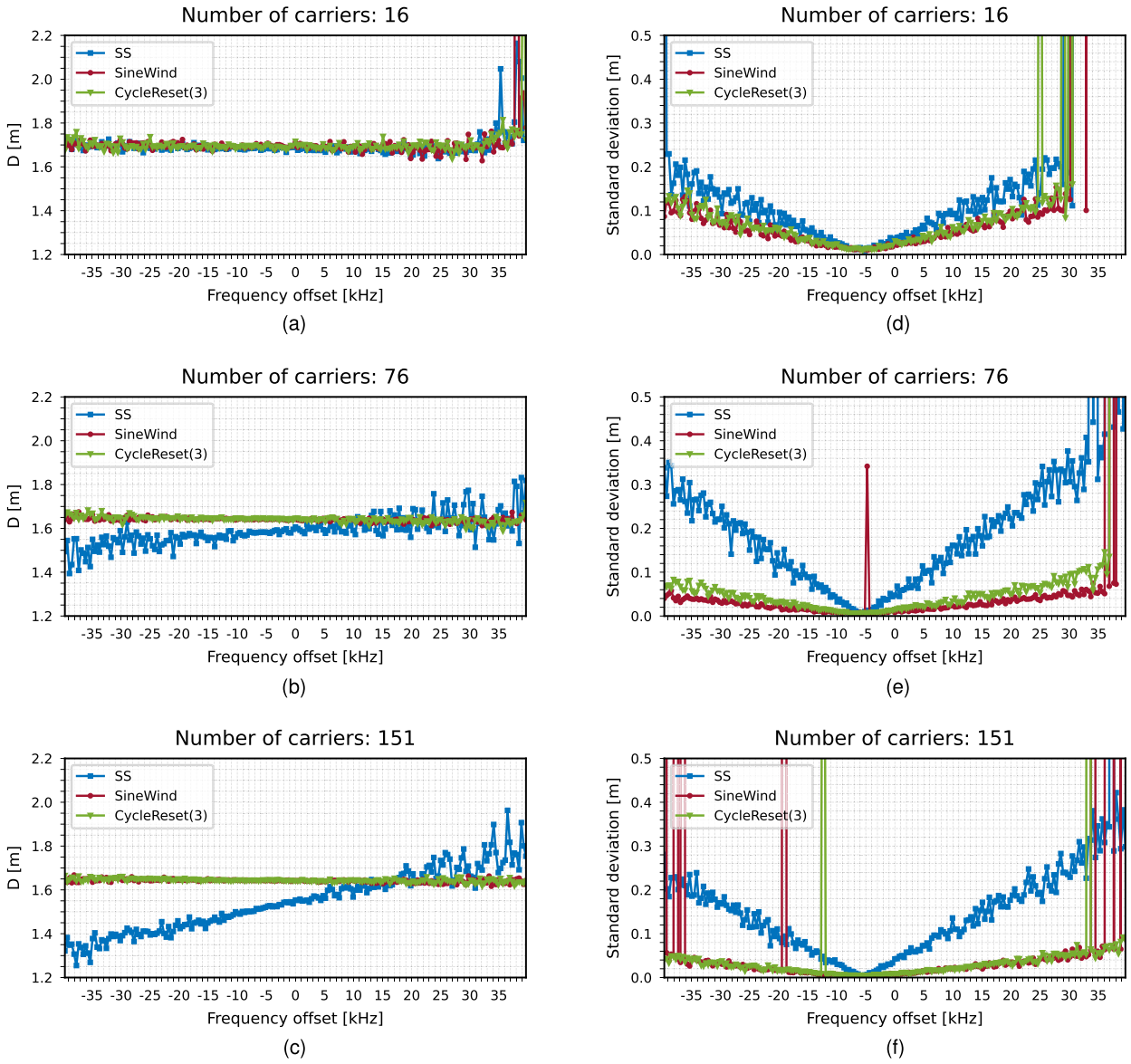


FIGURE 16. Medians ((a)–(c)) and standard deviations ((d)–(f)) of estimated distances as a function of frequency offset, calculated from 30 measurements per frequency offset value, for representative FSPs and number of carriers.

TABLE 4. Slopes of best-fit lines calculated from the medians of the estimated distances over the frequency offset range, together with the average value of standard deviations (Avg of st. devs.) calculated from the standard deviations over the frequency offset range, for representative FSPs and number of carriers.

	16 carriers		76 carriers		151 carriers	
FSP	Slope [m/Hz]	Avg of st. devs. [m]	Slope [m/Hz]	Avg of st. devs. [m]	Slope [m/Hz]	Avg of st. devs. [m]
SS	5.692 e-7	0.100	2.183 e-6	0.178	5.782 e-6	0.144
SineWind	1.162 e-7	0.059	-1.876 e-7	0.030	-1.513 e-7	0.026
CycleReset(3)	6.659 e-7	0.064	-3.308 e-7	0.045	-1.815 e-7	0.038

offset when reading registers or a clock deviation between INIT and REF can result in one device reading an IQ sample that is offset by 8 μs compared to the other device. As already described, this leads to phase jumps in the measured phase spectrum, which manifest themselves as additional peaks in the CIR.

The amplitude of phase jumps depends on the sampling interval and the effective intermediate frequency (including the CFO) and is given by $\Delta\phi = 2\pi(f_{IF} + \Delta f)\,T_s \bmod 2\pi$, where $Ts = 8\mu$s. As the CFO increases, the amplitude of the potential phase jumps also increases, resulting in larger errors in distance estimation. Since phase jumps can occur at different carrier frequencies across measurements, they contribute to a greater spread in the distance estimates. These findings were confirmed by comparing the measured phase jumps with those predicted by the above formula and showed strong agreement between the two. Further supporting this conclusion is that the medians of the distance estimates across frequency offsets show a repeating pattern with a periodicity of $1/(8\ \mu s) = 125$ kHz, which corresponds to the refresh rate of the register. An additional advantage of optimized FSPs is their ability to mitigate this effect, resulting in lower variability and more consistent distance estimates across different frequency offsets compared to the *SS* FSP.

The plots of the calculated standard deviations reveal that the actual CFO between the devices corresponds to the negative of the frequency offset at which the minimum of standard deviations occurs, indicating the point at which the programmed frequency offset effectively cancels the true CFO and minimizes the phase jumps.

VI. CONCLUSION

In this work, we have proposed novel FSPs for MCPD ranging systems to improve the accuracy of distance estimation under asynchronous conditions by suppressing the impact of CFO and timing errors caused by crystal oscillator performance variations due to environmental factors on systematic errors without the need for tight synchronization or additional estimation and correction procedures. We have introduced a new signal model that accounts for the additional phase shifts caused by asynchronization, and we have shown that the standard *SS* FSP accumulates these phase shifts across carriers, leading to large estimation biases.

Motivated by the limitations of the *SS* FSP, we introduced a family of optimized FSPs that rearrange the asynchronization-induced phase shifts across carrier frequencies to prevent the formation of a linear trend in the phase spectrum, thus minimizing the systematic error in distance estimation and shape estimated CIR more favorable. Simulations with different COPD values, noise, and the number of carriers have confirmed that proposed FSPs significantly reduce the estimation error and maintain accuracy up to the asynchronization bounds. Below these bounds, the best performing FSPs achieve errors in the millimeter range, while the *SS* FSP exceeds 1 m. *Random* FSPs can show good performance in some cases, but lacked consistency and scalability over the number of carriers. The effectiveness of the proposed FSPs depends on the number of carriers, with *SineWind* providing the best overall average accuracy and the lowest AE dispersion overall, although no single FSP is optimal across all number of carriers. The performance gain of the proposed FSPs over the *SS* FSP increases with the number of carriers. Noise analysis has shown that optimized FSPs outperform the *SS* FSP under high-SNR conditions in terms of the calculated RMSE, with the performance gain decreasing as the noise increases. Moreover, the robustness of the proposed FSPs to noise increases with the number of carriers. Compared to the estimation-correction approach, the proposed FSPs provide a more efficient means to mitigate asynchronization effects in the presence of noise, achieving higher accuracy while reducing measurement time. Experimental evaluations confirmed that the measured CIR shapes aligned well with the expectations of the simulations and that the distance estimation with the proposed FSPs is more robust to CFO variations than with *SS* FSP.

The proposed FSPs can be readily integrated into any narrowband transceiver with programmable carrier selection that provides baseband access to IQ samples, or into any MCPD ranging system that supports programmable frequency switching. Compared to the conventional *SS* FSP, the only additional processing required when using optimized FSPs is the reordering of the measured IQ samples to align them according to the ascending carrier frequency order before applying the IFFT, which is a negligible computational overhead compared to more complex estimation and correction algorithms used to mitigate asynchronization effects. Although IFFT was used for distance estimation in this work, the proposed FSPs are also suitable for use with other techniques such as linear regression or multiple signal classification (MUSIC). A practical consideration when using optimized FSPs is that a non-monotonic frequency order often increases adjacent frequency spacing compared to *SS* FSP, which can increase the settling times of the phase-locked loop, and thus the overall duration of the measurement. Overall, the proposed FSPs require no hardware modifications and provide a lightweight, low-complexity means of suppressing systematic ranging errors, making them well suited for low-cost IoT systems, especially for deployments in highly fluctuating environmental conditions, where calibration can quickly become outdated and ineffective.

Future work will focus on the development of new FSPs that produce lower sidelobes in the estimated CIR, with the aim of further extending the asynchronization bounds. We also plan to extend the real-world measurement campaign by including a wider range of FSPs and evaluating the performance under different RF propagation conditions.

REFERENCES

[1] J. A. Zhang, M. L. Rahman, K. Wu, X. Huang, Y. J. Guo, S. Chen, and J. Yuan, "Enabling joint communication and radar sensing in mobile networks—A survey," *IEEE Commun. Surveys Tuts.*, vol. 24, no. 1, pp. 306–345, 1st Quart., 2022.

[2] F. Zafari, A. Gkelias, and K. K. Leung, "A survey of indoor localization systems and technologies," *IEEE Commun. Surveys Tuts.*, vol. 21, no. 3, pp. 2568–2599, 3rd Quart., 2019.

[3] P. S. Farahsari, A. Farahzadi, J. Rezazadeh, and A. Bagheri, "A survey on indoor positioning systems for IoT-based applications," *IEEE Internet Things J.*, vol. 9, no. 10, pp. 7680–7699, May 2022.

[4] Y. Schröder and L. Wolf, "InPhase: Phase-based ranging and localization," *ACM Trans. Sensor Netw.*, vol. 18, no. 2, pp. 1–39, Jan. 2022.

[5] Y. Schröder, D. Reimers, and L. Wolf, "Accurate and precise distance estimation from phase-based ranging data," in *Proc. Int. Conf. Indoor Positioning Indoor Navigat. (IPIN)*, Sep. 2018, pp. 1–8.

[6] *Bluetooth Core Specification 6.0*, Bluetooth SIG, Washington, DC, USA, 2024.

[7] M. Nikodem, G. Trajnowicz, G. S. de Blasio, and F. A. Quesada-Arencibia, "Experimental evaluation of multicarrier phase difference localization in Bluetooth low energy," *IEEE Sensors J.*, vol. 25, no. 1, pp. 1548–1560, Jan. 2025.

[8] A. Santra, I. Kravets, N. Kotliar, and A. Pandey, "Enhancing Bluetooth channel sounding performance in complex indoor environments," *IEEE Sensors Lett.*, vol. 8, no. 10, pp. 1–4, Oct. 2024.

[9] S. Cortesi, C. Vogt, and M. Magno, "Comparison between an RSSI- and an MCPD-based BLE indoor localization system," *Computers*, vol. 12, no. 3, p. 59, Mar. 2023.

[10] R. Ayyalasomayajula, D. Vasisht, and D. Bharadia, "BLoc: CSI-based accurate localization for BLE tags," in *Proc. 14th Int. Conf. Emerg. Netw. EXperiments Technol.*, New York, NY, USA, Dec. 2018, pp. 126–138.

[11] M. Gunia, A. Zinke, N. Joram, and F. Ellinger, "Setting up a phase-based positioning system using off-the-shelf components," in *Proc. 14th Workshop Positioning, Navigat. Commun. (WPNC)*, Oct. 2017, pp. 1–6.

[12] M. Pelka, C. Bollmeyer, and H. Hellbrück, "Accurate radio distance estimation by phase measurements with multiple frequencies," in *Proc. Int. Conf. Indoor Positioning Indoor Navigat. (IPIN)*, Oct. 2014, pp. 142–151.

[13] P. Zand, J. Romme, J. Govers, F. Pasveer, and G. Dolmans, "A high-accuracy phase-based ranging solution with Bluetooth low energy (BLE)," in *Proc. IEEE Wireless Commun. Netw. Conf. (WCNC)*, Apr. 2019, pp. 1–8.

[14] P. Zand, A. Duzen, J. Romme, J. Govers, C. Bachmann, and K. Philips, "A high-accuracy concurrent phase-based ranging for large-scale dense BLE network," in *Proc. IEEE 30th Annu. Int. Symp. Pers., Indoor Mobile Radio Commun. (PIMRC)*, Sep. 2019, pp. 1–7.

[15] A. Duzen, "Implementation and evaluation of phase-based group ranging and localization with BLE," Master's thesis, Eindhoven Univ. Technol., Eindhoven, The Netherlands, 2019.

[16] M. Oshiro, S. Otaka, T. Kato, K. Nonin, M. Nishikawa, Y. Nito, H. Ishiwata, and H. Yoshida, "Sub-GHz phase-based ranging system: Implementation and evaluation," in *Proc. IEEE 91st Veh. Technol. Conf. (VTC-Spring)*, Belgium, May 2020, pp. 1–7.

[17] Y. Lin, T. Guo, M. Guo, and Y. Fu, "Motion compensation for SAA FMCW radar based on specific switching scheme," *Appl. Sci.*, vol. 9, no. 17, p. 3441, Aug. 2019.

[18] Y. Lin, K. Yang, M. Guo, and Y. Fu, "Elimination of motion-induced phase based on double-time switching scheme for SAA FMCW radar," *Electronics*, vol. 8, no. 7, p. 786, Jul. 2019.

[19] P. Feil, "Optimizing switching sequence in the case of switched antenna arrays," U.S. Patent 9 035 821, May 19, 2012.

[20] C. Hu, Y. Liu, H. Meng, and X. Wang, "Randomized switched antenna array FMCW radar for automotive applications," *IEEE Trans. Veh. Technol.*, vol. 63, no. 8, pp. 3624–3641, Oct. 2014.

[21] A. Al-Ameri, J. Park, J. M. Sánchez, X. Cai, and F. Tufvesson, "A hybrid antenna switching scheme for dynamic channel sounding," in *Proc. IEEE 97th Veh. Technol. Conf. VTC-Spring)*, Jun. 2023, pp. 1–6.

[22] R. Wang, O. Renaudin, C. U. Bas, S. Sangodoyin, and A. F. Molisch, "On channel sounding with switched arrays in fast time-varying channels," *IEEE Trans. Wireless Commun.*, vol. 18, no. 8, pp. 3843–3855, Aug. 2019.

[23] T. Pedersen, C. Pedersen, X. Yin, B. H. Fleury, R. R. Pedersen, B. Bozinovska, A. Hviid, P. Jourdan, and A. Stucki, "Joint estimation of Doppler frequency and directions in channel sounding using switched Tx and Rx arrays," in *Proc. IEEE Global Telecommun. Conf. (GLOBECOM)*, vol. 4, Nov. 2004, pp. 2354–2360.

[24] T. Pedersen, C. F. Pedersen, X. Yin, and B. H. Fleury, "Optimization of spatiotemporal apertures in channel sounding," *IEEE Trans. Signal Process.*, vol. 56, no. 10, pp. 4810–4824, Oct. 2008.

[25] J. Sanchez, X. Cai, A. Al-Ameri, and F. Tufvesson, "Low-complexity optimization of antenna switching schemes for dynamic channel sounding," *IEEE Trans. Wireless Commun.*, 2025.

[26] A. Simončič, K. Guan, G. Morano, A. Švigelj, A. Hrovat, T. Kocevska, and T. Javornik, "Experimental evaluation of enhanced antenna switching for CFO mitigation in DoA estimation," *IEEE Open J. Antennas Propag.*, vol. 6, pp. 1022–1036, 2025.

[27] P. Avital, G. Chardon, and J. Picheral, "Design of switching sequences for sine parameters estimation on switched antenna arrays," *Signal Process.*, vol. 188, Nov. 2021, Art. no. 108244.

[28] G. Morano, A. Simončič, T. Kocevska, T. Javornik, and A. Hrovat, "Distance- and angle-based hybrid localization integrated in the IEEE 802.15.4 TSCH communication protocol," *Sensors*, vol. 24, no. 12, p. 3925, Jun. 2024.

[29] D. C. Montgomery, E. A. Peck, and G. G. Vining, *Introduction to Linear Regression Analysis*. Hoboken, NJ, USA: Wiley, 2020.

[30] Atmel Corporation. (2016). *AT86RF215 Datasheet*. Accessed: Nov. 14, 2024. [Online]. Available: https://www.microchip.com/en-us/product/at86rf215



ALEŠ SIMONČIČ (Student Member, IEEE) received the B.Sc. and M.Sc. degrees in electrical engineering from the University of Ljubljana, in 2019 and 2022, respectively. He is currently pursuing the Ph.D. degree in information and communication technologies with the Jožef Stefan International Postgraduate School. His master's thesis focused on the estimation of the angle of arrival using BLE technology and antenna arrays.

He is a Young Researcher at the Department of Communication Systems, Jožef Stefan Institute, Ljubljana. His research interests include radio communication systems, particularly protocols, antennas and arrays, direction of arrival estimation methods, embedded systems, and radio environment characterization.



GREGA MORANO (Member, IEEE) received the M.Sc. degree in electrical engineering from the University of Ljubljana, in 2021. He is currently pursuing the Ph.D. degree in information and communication technologies with the Jožef Stefan International Postgraduate School.

He is a Research Assistant at the Department of Communication Systems, Jožef Stefan Institute, Ljubljana. His research interests include the IoT communication protocols, integrated sensing and communication, wireless sensor networks, and wireless experimental testbeds.



ANDREJ HROVAT (Senior Member, IEEE) received the B.Sc. and M.Sc. degrees in electrical engineering from the University of Ljubljana, in 2004 and 2008, respectively, and the Ph.D. degree from the Jožef Stefan International Postgraduate School, in 2011.

He has been with the Department of Communication Systems, Jožef Stefan Institute, since 2004. Currently, he is holding the position of a Senior Research Fellow. He is the author or co-author of more than 120 peer-reviewed journal and conference papers. He works on several projects connected with professional mobile communication systems, 2G–5G, WiFi and the IoT technologies, and satellite and sensor networks, including several COST actions, framework program projects, H2020 projects, European Space Agency (ESA) projects, and numerous national research and application projects. His research and working experience are in telecommunications, focusing on development and performance analysis for fixed and mobile systems, including terrestrial, stratospheric, and satellite systems, and radio-channel modeling for fixed and mobile narrowband and broadband radio communication systems. He serves as a journal editorial board member and a guest editor. He is a TCP member of various international conferences and workshops. He is a reviewer of several international impact-factor journals.



TOMAŽ JAVORNIK (Member, IEEE) received the B.Sc., M.Sc., and Ph.D. degrees in electrical engineering from the University of Ljubljana, Ljubljana, Slovenia, in 1987, 1990, and 1993, respectively.

He is currently a Scientific Counsellor with the Communication Systems Department, Jožef Stefan Institute, Ljubljana, and an Assistant Professor with the Jožef Stefan International Postgraduate School, Ljubljana. He participated in several COST and framework program projects. He has co-authored more than 100 refereed journal and conference papers and several books and book chapters in mobile and wireless communications. He holds two international patents. He serves as a TPC member or a reviewer for several IEEE conferences and journals. His research experience is in telecommunications, focusing on the development and performance analysis of fixed and mobile systems, radio-channel measurements, modeling and simulations, and indoor localization.

Chapter 5

Timing Diagram Design for Robust MCPD Ranging

Publication included in this chapter:

A. Simončič, G. Morano, A. Hrovat, and T. Javornik, "Mitigating Frequency Dependent Carrier Frequency Offset in Multi-carrier Phase Difference Ranging through Timing Diagram Design," *IEEE Access*, pp. 1–1, 2026, ISSN: 2169-3536. DOI: 10.1109/ACCESS.2026.3665049

The derived signal model for MCPD ranging in the previous chapter assumed a constant CFO across carrier frequencies, as is commonly assumed in related signal models for MCPD ranging. In practical radios, RF carrier generation typically relies on a PLL that takes a reference frequency as input and generates an RF carrier frequency that is a carrier-dependent multiple of the reference frequency. This reference is generated by a crystal oscillator whose frequency deviates from nominal and varies with operating conditions, as discussed in previous chapters. Crystal oscillator frequency error is therefore propagated through PLL-based carrier frequency synthesis, and the resulting carrier frequency error scales with the carrier-dependent multiplication factor. As a result, CFO can vary linearly with carrier frequency in PLL-based carrier generation.

For MCPD ranging, a linear CFO trend across carriers does not affect estimation accuracy if both devices exhibit the same trend. However, differences in oscillator performance between devices result in different CFO slopes across carrier frequencies, referred to as CFOSD. In MCPD ranging, under standard TD, CFOSD introduces a linear phase-error trend across carriers, resulting in a systematic distance-estimation bias. The effect of CFOSD on the sampled phase differs fundamentally from the asynchronization effect discussed in the previous chapter, where the phase error at a given carrier frequency depended on the time at which that carrier was used in the MCPD procedure. FSP optimization could therefore influence the phase error associated with a particular carrier by changing the time at which that carrier frequency was used. In contrast, CFOSD-induced phase errors depend on carrier frequency rather than on the time at which the carrier is used. As a result, reordering the carrier frequencies through FSP design is not effective for mitigating CFOSD-induced bias. Mitigation through explicit CFO estimation and correction is also impractical, since CFO would need to be estimated at each carrier frequency, or at least at two carrier frequencies under a linearity assumption, which significantly increases measurement duration and overhead.

The paper included in this chapter presents an efficient approach to mitigate CFOSD-induced bias in MCPD ranging through TD design, suitable for resource-constrained de-

vices, thereby addressing hypothesis **H5**. The paper derives a signal model that incorporates the linear dependence of CFO on carrier frequency and shows how the standard MCPD TD induces estimation bias, thereby providing contribution **SC4.1**. Based on an analysis of the dominant phase terms responsible for CFOSD-induced bias, it proposes two TD modification approaches that reduce the effect of CFOSD on distance estimation without requiring explicit CFO estimation at each carrier or joint parameter estimation, thereby providing contribution **SC4.2**. The temporal differential correction approach (TDCA) suppresses the contribution of CFOSD by acquiring additional phase samples at each carrier at specific time instants and combining them so that the dominant CFOSD-induced phase component is structurally suppressed. The role-switching approach (RSA) modifies the TD by reversing the initiator and reflector roles across carrier frequencies according to a role pattern (RP), while preserving the measurement duration of the standard TD. With a properly designed RP, CFOSD-induced phase terms are decoupled from propagation-induced phase terms. The design goal for the RP is that CFOSD-induced phase errors exhibit no linear trend across carrier frequencies, thereby mitigating distance bias.

The proposed TDs are validated through numerical simulations and experiments, establishing contribution **SC4.3**. The simulation study includes CFOSD sweeps and additive noise at different SNR levels to characterize bias and noise sensitivity in combination with different FSPs. Experimental validation is performed using practical devices, with CFOSD sweeps emulated by applying carrier-dependent CFO across carrier frequencies. The resulting distance estimates obtained with the proposed TDs are compared to those obtained using the standard TD under controlled CFOSD conditions to quantify bias reduction. The results show effective bias reduction by the proposed TDs, further addressing hypothesis **H5**.

IEEE Access
Multidisciplinary ⋮ Rapid Review ⋮ Open Access Journal

Received 23 December 2025, accepted 6 February 2026. Date of publication 00 xxxx 0000, date of current version 00 xxxx 0000.

Digital Object Identifier 10.1109/ACCESS.2026.3665049

Mitigating Frequency Dependent Carrier Frequency Offset in Multi-Carrier Phase Difference Ranging Through Timing Diagram Design

ALEŠ SIMONČIČ, (Student Member, IEEE), GREGA MORANO, (Graduate Student Member, IEEE), ANDREJ HROVAT, (Member, IEEE), AND TOMAŽ JAVORNIK, (Member, IEEE)

Department of Communication Systems, Jožef Stefan Institute, 1000 Ljubljana, Slovenia
Jožef Stefan International Postgraduate School, 1000 Ljubljana, Slovenia

Corresponding author: Aleš Simončič (ales.simoncic@ijs.si)

This work was supported by Slovenian Research and Innovation Agency (ARIS) under Grant J2-4461, Grant P2-0016, and Grant PR-12348.

ABSTRACT Multi-carrier phase difference (MCPD) ranging is promising for low-cost proximity and localization systems, but its performance degrades when devices use inexpensive crystal oscillators. In practice, carrier frequency offset (CFO) can change linearly with carrier frequency, and the difference between the slopes of CFO as a function of carrier frequency, referred to as the carrier frequency offset slope difference (CFOSD), introduces a systematic distance bias. We model MCPD using the standard timing diagram (TD) and derive a closed-form expression for the distance error that reveals a dominant term proportional to both CFOSD and the sampling time offset difference between devices. Two TD design approaches are proposed and validated by simulations with CFOSD sweep and additive noise. The temporal differential correction approach suppresses the effect of CFOSD on distance estimation over a wide CFOSD range and achieves almost zero bias, but at the cost of longer measurement duration, greater sensitivity to timing asynchronization, and a higher required signal-to-noise ratio (SNR). The role switching approach reverses the roles of initiator and reflector across carrier frequencies according to a role pattern, preserves the measurement duration of the standard TD, and reduces CFOSD sensitivity within a method-dependent CFOSD operating range. Experimental results for the standard and role-switching TD designs confirm the signal model, show good agreement between measured and simulated channel impulse responses, and demonstrate that the proposed TD designs substantially reduce distance bias caused by CFOSD while remaining compatible with low-cost implementations.

INDEX TERMS Asynchronization, carrier frequency offset (CFO), channel frequency response (CFR), channel impulse response (CIR), clock drift, crystal oscillator, Internet of Things (IoT), multi-carrier phase difference (MCPD), phase-based ranging (PBR), timing diagram.

I. INTRODUCTION

Integrated sensing and communication (ISAC) aims to unify communication and sensing functionalities within a common hardware platform, allowing each function to benefit from information provided by the other. In bistatic configurations, communication nodes can exploit sensing information extracted from the spatial, spectral, and temporal diversity present in the exchanged signals [1]. Short-range proximity and location information play a central role

The associate editor coordinating the review of this manuscript and approving it for publication was Li Zhang.

© 2026 The Authors. This work is licensed under a Creative Commons Attribution 4.0 License.
For more information, see https://creativecommons.org/licenses/by/4.0/

in many everyday applications, including public transport ticketing, parking, electronic tolling, payment and identification systems, personnel tracking, and physical access control [2]. These applications motivate the development of accurate, low-cost ranging techniques that can be integrated directly into commodity wireless devices. A major challenge in such systems is the lack of synchronization between devices, which can introduce ranging ambiguities and prevent coherent processing of discontinuous measurements [3].

Phase-based ranging (PBR) has gained popularity because it enables decimeter-level accuracy in indoor scenarios [4]. Multi-carrier phase difference (MCPD) extends PBR by acquiring phase measurements across several carrier frequencies using two ranging devices: the initiator (INIT) and the reflector (REF) [5]. This technique provides a larger unambiguous range, reduced multipath sensitivity, and cancellation of random phase-locked loop (PLL)-induced phase offsets across discontinuous transmissions on different frequencies. With low hardware complexity and low energy consumption, MCPD is particularly attractive for low-cost wireless systems.

The imperfections of low-cost crystal oscillators used for both radio frequency (RF) synthesis and timing affect MCPD performance by introducing carrier frequency offset (CFO) and clock drift, which can bias distance estimation. Crystal oscillators are characterized by frequency tolerance and frequency stability, which depend on environmental conditions such as temperature, supply voltage, load capacitance, humidity, pressure, aging, etc. As these conditions vary, the instantaneous frequencies of the crystal oscillators in the two devices involved in ranging can drift differently over time. Although initial calibration between devices can compensate for static biases, environmental changes make such calibration invalid and degrade ranging accuracy. Using higher-grade clock sources would reduce environment-dependent effects on distance estimation but would increase costs. A single highly accurate reference clock, such as one provided by the global navigation satellite system (GNSS), can be distributed wirelessly or via a wired link, but this approach adds complexity, is meaningful only for static anchors in the case of wired clock distribution, and is impractical when only a small number of devices need to be synchronized [3]. These limitations motivate the development of MCPD ranging procedures that are inherently less sensitive to variations in crystal oscillator performance. In particular, we study how to mitigate distance estimation errors in MCPD ranging caused by CFO with a linear dependence on the carrier frequency, which occurs in PLL-based carrier frequency synthesis, where the reference frequency error is multiplied by a carrier-dependent factor, scaling the error proportionally across the carriers. The difference between the slopes of CFO as a function of carrier frequency for the two devices, referred to as the carrier frequency offset slope difference (CFOSD), then produces a systematic distance bias.

Clock and frequency synchronization has been studied extensively in wireless communications [6], [7], ultra-wideband (UWB) ranging [8], and ISAC systems [3]. However, dynamic synchronization aspects in MCPD have received little attention. Previous works address interference mitigation [9], algorithmic improvements [4], [10], [11], or comparisons of localization techniques [12], [13], but do not explicitly model time and frequency misalignment between devices. Asynchronization between devices is typically ignored, mitigated by initial calibration at known distances, or suppressed by assuming high-quality crystal oscillators [14].

The impact of asynchronization on MCPD ranging has been addressed in the following literature. The authors in [15] jointly analyzed timing asynchronization and CFO, proposing to measure the CFO, map it to the underlying crystal offset difference, and correct the phase measurements accordingly. Group-ranging scenarios were examined in [16] and [17], showing that asynchronization has an even stronger impact in multi-device setups. In [17], a technique was proposed in which the INIT shifts the timeslots of REFs in consecutive measurements to estimate crystal offsets. Estimating CFO from multiple phase samples acquired at a single carrier frequency and then correcting the measured phase samples to remove CFO-induced phase shifts was proposed in [18]. While CFO can be estimated during the measurement and compensated for, accurate estimation requires a large number of additional samples [19]. This remains feasible under the assumption that the CFO is constant across the measurement band, since the estimation can be performed at only one frequency. However, when the CFO varies with carrier frequency, this approach becomes impractical, as CFO would have to be estimated separately at each carrier, substantially increasing the measurement duration. Even under the assumption that CFO varies linearly, estimation would need to be performed at least at two carrier frequencies, followed by interpolation or extrapolation.

An approach involving four transmissions per carrier frequency, in which an INIT→REF exchange is followed by a REF→INIT exchange to suppress the impact of a constant CFO in MCPD ranging, was proposed in [20]. We build on this idea and consider timing diagram (TD) optimization with the objective of structurally reducing the effect of CFOSD without requiring explicit CFO estimation at each carrier frequency. While TD optimization for MCPD has received limited attention beyond [20], it has been extensively explored in related time-based ranging systems, particularly in the UWB domain. UWB ranging typically resolves timing offset using the single-sided two-way ranging (SS-TWR) procedure and further suppresses clock drift through the double-sided two-way ranging (DS-TWR) technique [21]. Numerous works have proposed TD refinements to reduce clock-drift-induced bias, often balancing the trade-off between the number of transmissions and estimation accuracy [8], [22], [23], [24], [25], [26]. Additional transmissions have also

been used to obtain extra phase samples that compensate for phase drift due to CFO in UWB system that combine PBR principles, as shown in [22]. In [27], TD parameters have been optimized using Cramer-Rao lower bound (CRLB) analysis, which shows that longer second-response delays reduce estimator variance but simultaneously lower the number of measurements per unit time, thus increasing the overall variance of combined estimates. Sequential time difference of arrival (TDoA) approaches [28] can also avoid explicit timing synchronization between the tag and anchors, but they require at least three anchors with known geometry and remain more sensitive to clock drift than two-way ranging (TWR) procedures.

Among the contributions of this work is a dynamic role-switching scheme within the MCPD procedure to decouple the phase shifts introduced by CFOSD from those caused by signal propagation, thereby reducing the resulting bias in the estimated distance. A conceptually related switching approach was presented in our earlier work [19], where the order of carrier frequencies used in the MCPD procedure was optimized to decouple phase shifts caused by clock-drift differences from those due to propagation, assuming a frequency-independent CFO across the carrier set. This work extends that research by addressing CFOSD, which introduces an additional bias term that frequency order optimization alone cannot remove. Similar switching-related strategies have been explored in adjacent domains such as frequency-modulated continuous wave (FMCW) radar [29], [30], [31], [32], channel sounding [33], [34], [35], [36], [37], and direction-of-arrival (DoA) estimation [38], [39].

The objective of this work is to mitigate the effect of CFOSD on MCPD distance estimation without requiring explicit CFO estimation. We achieve this by modifying the MCPD TD to either structurally cancel CFOSD-induced phase shifts or decouple them from the propagation-induced phase shifts, thereby reducing the resulting bias without extending the measurement duration. The contributions of this paper are:

- Identification and modeling of CFOSD as a previously unaddressed source of systematic bias in MCPD, supported by analytical derivations and measurements.
- Design of TDs that suppress the effect of CFOSD on distance estimation by using temporal-differential correction and dynamic role-switching approaches.
- Evaluation of the effectiveness of the proposed TDs in simulations under noise-free and noisy conditions.
- Experimental validation of TDs based on the dynamic role-switching approach.

The remainder of the paper is organized as follows. Section II presents the signal model and analyzes the CFOSD impact on MCPD distance estimation. The proposed TD optimization approaches are described in Section III. Simulation and experimental evaluations follow in Sections IV and V, respectively. The paper concludes with Section VI.

TABLE 1. List of key acronyms and symbols.

Acronym / Symbol	Description
M	Number of carrier frequencies
i	Carrier frequency index, $i \in \{0, \ldots, M-1\}$
$P[i]$	Vector defining the order in which the carrier frequencies are applied during the MCPD procedure
ν	Carrier spacing
$f_c^{(i)}$	Nominal carrier frequency of the i-th carrier
$f_I^{(i)}, f_R^{(i)}$	Actual carrier frequencies of the i-th carrier generated by INIT and REF
$\Delta f_I^{(i)}, \Delta f_R^{(i)}$	CFOs of INIT and REF of the i-th carrier
$\Delta f^{(i)}$	Effective CFO between devices of the i-th carrier, $\Delta f^{(i)} = \Delta f_I^{(i)} - \Delta f_R^{(i)}$
$\Delta f_{0,I}, \Delta f_{0,R}$	Initial CFO values at $f_c^{(0)}$ for INIT and REF
Δf_0	Difference between initial CFO values, $\Delta f_0 = \Delta f_{0,I} - \Delta f_{0,R}$
$k_{\mathrm{CFO},I}, k_{\mathrm{CFO},R}$	Linear slopes of CFO as a function of carrier frequency for INIT and REF
CFOSD	Carrier frequency offset slope difference, $k_{\mathrm{CFO},I} - k_{\mathrm{CFO},R}$
f_{IF}	Intermediate frequency
ΔT_s	Nominal time difference between the start of two consecutive carrier measurements
$T_{o,R}, T_{o,I}$	Nominal time sampling offsets at REF and INIT after the start of the measurement on each carrier
ΔT_o	Time sampling offset difference, $\Delta T_o = T_{o,R} - T_{o,I}$
e_I, e_R	Relative frequency errors of the timing oscillators at INIT and REF
$\Theta_{\mathrm{LO},I}^{(i)}, \Theta_{\mathrm{LO},R}^{(i)}$	Local oscillator initial phase offsets of the i-th carrier at INIT and REF
$RP[i]$	Role pattern, $RP[i] = 1$ for standard roles and $RP[i] = -1$ for reversed roles

To improve readability, Table 1 summarizes the key acronyms and symbols used in this paper.

II. SIGNAL MODEL AND PROBLEM FORMULATION

Most existing research on MCPD assumes that the CFO of each device is constant across the measurement band. In practice, CFO can be frequency dependent as PLL-based carrier frequency generation is achieved by multiplying the crystal oscillator reference frequency f_{ref} by the carrier-dependent factor $k^{(i)}$ to synthesize the desired carrier frequency $f_c^{(i)} = f_{ref} \cdot k^{(i)}$, where $i \in \{0, \ldots, M-1\}$ is the carrier index and M is the number of carriers used in MCPD. A deviation in the reference oscillator frequency from its nominal value by a multiplicative error e causes the actual reference to be $f'_{ref} = f_{ref}(1+e)$. With uniform carrier spacing ν, the carrier frequency at index i can be expressed in terms of the nominal carrier frequency $f_c^{(0)}$ at $i = 0$ as

$$f_c^{(i)} = f_c^{(0)} + e f_c^{(0)} + (1+e)\, i\, \nu, \tag{1}$$

which shows that the frequency error increases linearly with the carrier index and that the slope of this increase is proportional to the oscillator error e. To examine this effect in practice, we measured the CFO across carrier frequencies for four devices equipped with AT86RF215 radio modules [40].

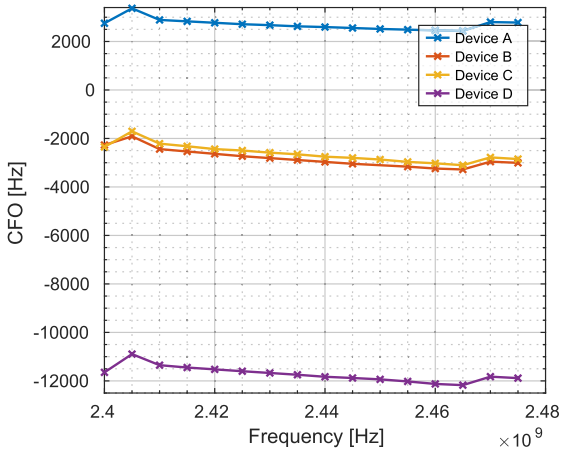


FIGURE 1. Measured CFOs as a function of carrier frequency for four devices equipped with AT86RF215 radio modules, showing a clear linear CFO trend with distinct initial CFO offsets.

TABLE 2. CFO slope values obtained from the measurements in Fig. 1, expressed as the change in CFO per MHz to make the numerical values more interpretable.

	Device A	Device B	Device C	Device D
k_{CFO} $\left[\frac{\text{Hz}}{\text{MHz}}\right]$	-5.46	-13.49	-12.90	-10.79

As shown in Fig. 1, all devices exhibit a clear linear CFO trend with frequency. Table 2 lists the corresponding slopes computed using simple linear regression. The differences between slopes confirm the presence of CFOSD and motivate deriving the signal model to quantify its impact on distance estimation.

We derive a signal model for the standard TD configuration used in MCPD ranging, as shown in Fig. 2(a), which also serves as the basis for the TD optimization in the next section. In the standard TD configuration, REF samples the received signal at a time offset $T_{o,R}$ and INIT at a time offset $T_{o,I}$ after the start of the measurement on each carrier. The time difference between the start of two consecutive carrier measurements is denoted by ΔT_s. The actual sampling instants deviate from the ideally defined times due to the clock drift of each device. Non-ideal sampling times are denoted by a prime superscript and are obtained by scaling the ideal times by the reciprocal of the oscillator frequency error, that is, $(1+e_I)^{-1}$ for INIT and $(1+e_R)^{-1}$ for REF, where e_I and e_R are the dimensionless relative frequency errors of the INIT and REF crystal oscillators, typically specified in parts per million (ppm). The signal model uses separate crystal oscillators for timing and RF carrier generation at INIT and REF, which allows the contributions of clock drift and CFO to the measured phases to be observed independently. The frequency deviations of the crystal oscillators are assumed constant during a single MCPD measurement sequence, and propagation is modeled as free space with REF transmitting and receiving at carrier frequencies that are offset by the intermediate frequency f_{IF}, analogous to the formulation in [19].

The nominal carrier frequency of the i-th carrier is

$$f_c^{(i)} = f_c^{(0)} + i\,\nu.$$

The actual carrier frequencies generated by INIT and REF, affected by crystal-oscillator inaccuracies, are denoted by $f_I^{(i)}$ and $f_R^{(i)}$, respectively. Their corresponding CFO values relative to the nominal carrier,

$$\Delta f_I^{(i)} = f_I^{(i)} - f_c^{(i)}, \qquad \Delta f_R^{(i)} = f_R^{(i)} - f_c^{(i)},$$

represent the individual CFOs of the devices. The effective CFO between INIT and REF on the i-th carrier is defined as

$$\Delta f^{(i)} = \Delta f_I^{(i)} - \Delta f_R^{(i)}.$$

The signal model describing the phase samples acquired at INIT and REF for MCPD with the standard TD configuration, including arbitrary ordering of carrier frequency, was derived in [19]. Considering that one phase sample is acquired per carrier frequency ($n = 0$), the sampled phase at REF for the i-th carrier is

$$\begin{aligned}\phi_{R,0}^{(i)} = {} & 2\pi\left(f_{IF} + \Delta f^{(i)}\right)\left(P[i]\cdot\Delta T'_{s,R} + T'_{o,R}\right) \\ & - 2\pi\left(f_c^{(i)} + \Delta f_I^{(i)}\right)\frac{d}{c} \\ & + \Theta_{LO,I}^{(i)} - \Theta_{LO,R}^{(i)},\end{aligned} \tag{2}$$

where c is the speed of light, d is the distance between the devices, $\Delta T'_{s,R}$ is the non-ideal measurement of the interval ΔT_s at REF due to its own clock drift, $\Theta_{LO,I}^{(i)}$ and $\Theta_{LO,R}^{(i)}$ denote the local oscillator initial phase offsets of the i-th carrier at INIT and REF, and $P[i]$ is the vector that defines the order in which the carrier frequencies are applied during the MCPD procedure [19]. The indices of $P[i]$ correspond to the ordered carrier frequencies from the lowest ($i = 0$) to the highest ($i = M-1$) used in MCPD, and each value P_i specifies when in the sequence the particular carrier frequency with index i is used in the MCPD procedure, with the first position corresponding to value 0. We assume that each carrier frequency is used exactly once in the sequence.

The corresponding phase sampled at INIT for the i-th carrier is

$$\begin{aligned}\phi_{I,0}^{(i)} = {} & 2\pi\left(f_{IF} + \Delta f^{(i)}\right)\left(P[i]\cdot\Delta T'_{s,I} + T'_{o,I}\right) \\ & + 2\pi\left(f_c^{(i)} - f_{IF} + \Delta f_R^{(i)}\right)\frac{d}{c} \\ & + \Theta_{LO,I}^{(i)} - \Theta_{LO,R}^{(i)},\end{aligned} \tag{3}$$

where $\Delta T'_{s,I}$ is the non-ideal measurement of interval ΔT_s at INIT due to its own clock drift.

To cancel the unknown initial phase offsets of the local oscillators, the final phase for the i-th carrier is obtained by subtracting the phase samples acquired at INIT (3) from

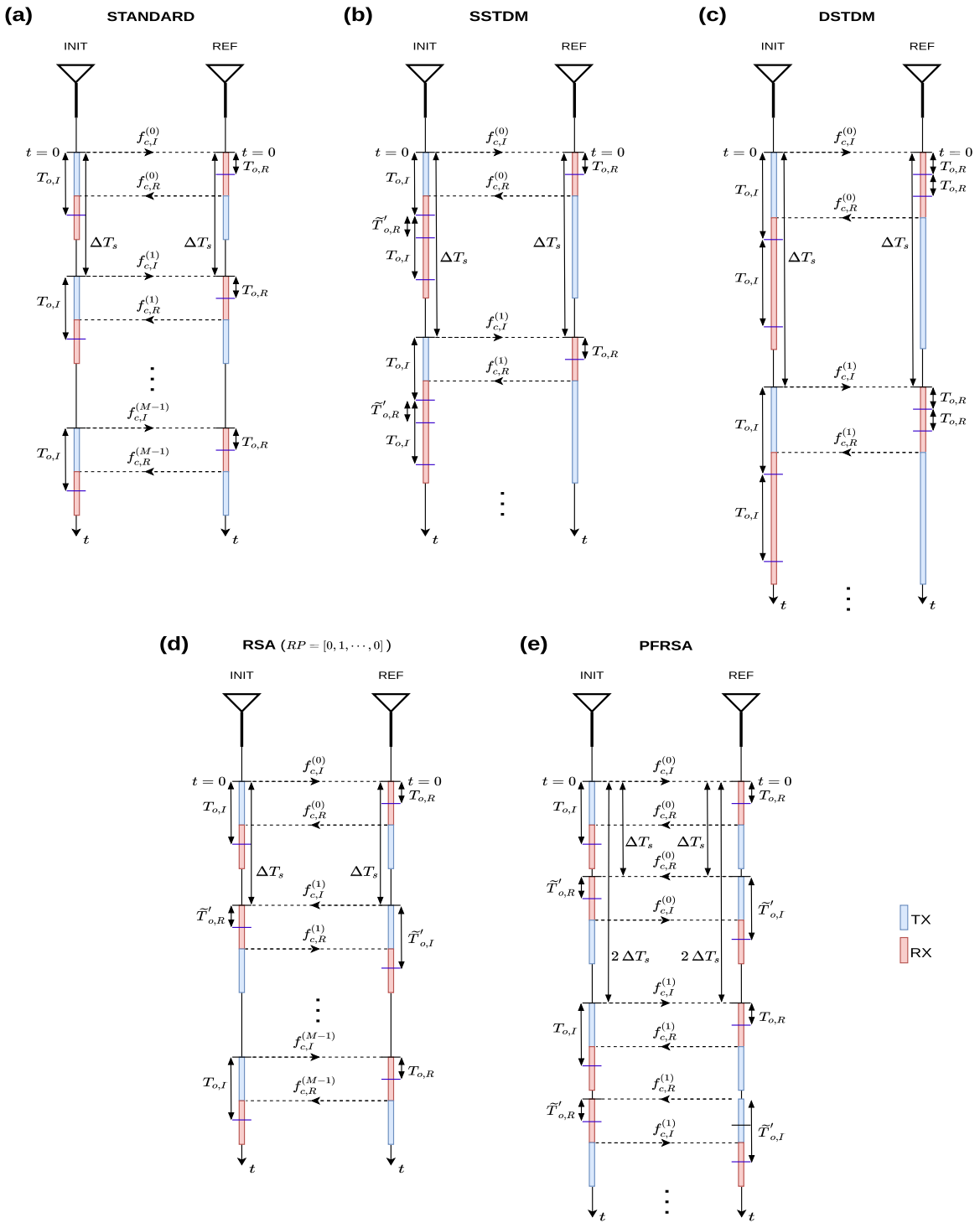


FIGURE 2. TDs for MCPD ranging. (a) Standard TD: INIT and REF sample at fixed offsets on every carrier. (b) SSTDM: INIT acquires additional samples relative to its standard sampling time to suppress the CFOSD-induced phase component. (c) DSTDM: both INIT and REF acquire additional samples, enabling full cancellation of the CFOSD contribution. (d) RSA: a role-switching approach in which INIT and REF alternate roles according to a predefined *RP* vector. (e) PFRSA: on each carrier the measurement is first performed according to the standard TD approach and then repeated with the reversed roles.

REF (2)

$$\phi^{(i)} = \phi^{(i)}_{R,0} - \phi^{(i)}_{I,0} = 2\pi\left(f_{IF} + \Delta f^{(i)}\right)\cdot \left[P[i]\,\Delta T_s\,\frac{e_I - e_R}{1 + e_I + e_R + e_I\,e_R} + \left(T_{o,R}\left(1+e_R\right)^{-1} - T_{o,I}\left(1+e_I\right)^{-1}\right)\right] - 2\pi\left(2f_c^{(i)} + \Delta f_I^{(i)} + \Delta f_R^{(i)} - f_{IF}\right)\frac{d}{c}. \quad (4)$$

The phase $\phi^{(i)}$ contains two bracketed phase terms scaled by $\Delta f^{(i)}$ that are therefore affected by CFOSD. The first phase term captures timing asynchronization caused by clock drift over the measurement procedure and is proportional to the vector $P[i]$ and the relative frequency mismatch between the timing oscillators of INIT and REF, $(e_I - e_R)$. Assuming the CFO is constant across the measured band, this timing asynchronization effect on distance estimation can be efficiently mitigated using the technique in [19], where the frequency switching pattern (FSP), and therefore $P[i]$, is optimized to suppress bias from clock drift differences. Even with frequency-dependent CFO and nonzero CFOSD, the first term contributes negligibly to the CFOSD-induced distance bias. The CFOSD-induced bias is instead dominated by the second phase term in brackets, which depends approximately on the sampling time offset difference between INIT and REF.

To isolate the effect of CFOSD on MCPD distance estimation, we first neglect timing asynchronization by setting $e_I = e_R = 0$. Furthermore, the CFO is modeled as a linear function of the carrier index, and for the i-th carrier it is expressed as

$$\Delta f_I^{(i)} = \Delta f_{0,I} + k_{\mathrm{CFO},I}\; i\; \nu,$$
$$\Delta f_R^{(i)} = \Delta f_{0,R} + k_{\mathrm{CFO},R}\; i\; \nu, \quad (5)$$

where $\Delta f_{0,I}$ and $\Delta f_{0,R}$ denote the initial CFO values at INIT and REF at the beginning of the measured frequency band, and $k_{\mathrm{CFO},I}$ and $k_{\mathrm{CFO},R}$ are their respective CFO slopes with respect to carrier frequency. The CFOSD is equal to $k_{\mathrm{CFO},I} - k_{\mathrm{CFO},R}$.

Expanding the terms $\Delta f^{(i)}$, $f_c^{(i)}$, $\Delta f_I^{(i)}$, and $\Delta f_R^{(i)}$ and substituting the CFO model from (5) into (4), the phase difference for the i-th carrier becomes

$$\phi^{(i)} = 2\pi\left(f_{IF} + \Delta f_0\right)\cdot \Delta T_o + 2\pi\left(k_{\mathrm{CFO},I} - k_{\mathrm{CFO},R}\right)\cdot i \cdot \nu \cdot \Delta T_o - 2\pi\left(2f_c^{(0)} - f_{IF} + \Delta f_{0,I} + \Delta f_{0,R}\right)\frac{d}{c} - 2\pi \cdot i \cdot \left(2 + k_{\mathrm{CFO},I} + k_{\mathrm{CFO},R}\right)\cdot \nu\,\frac{d}{c}, \quad (6)$$

where $\Delta T_o = T_{o,R} - T_{o,I}$ is the sampling time offset difference between devices, and $\Delta f_0 = \Delta f_{0,I} - \Delta f_{0,R}$ denotes the difference between the initial CFO values at the beginning of the measured frequency band of INIT and REF.

The last term in (6) includes the expected linear phase change with carrier index i due to signal propagation. However, the second term, which depends on CFOSD, also exhibits a linear dependence on i. As a result, the CFOSD-induced phase shifts as a function of carrier index i are coupled with the propagation-induced phase shifts, producing a systematic bias in the distance estimate. In MCPD, the distance estimate is obtained from the slope of the measured phase with respect to carrier frequency [2], i.e.,

$$\hat{d} = -\frac{c}{4\pi}\,\frac{\phi^{(i+1)} - \phi^{(i)}}{\nu}. \quad (7)$$

By inserting (6) into (7) and comparing the resulting slope with the ideal CFOSD-free case, the distance bias E introduced by CFOSD is

$$E = \frac{c}{2}\cdot\left(k_{\mathrm{CFO},I} - k_{\mathrm{CFO},R}\right)\cdot \Delta T_o - \frac{1}{2}\left(k_{\mathrm{CFO},I} + k_{\mathrm{CFO},R}\right)\cdot d. \quad (8)$$

The bias expression has two components. The first term depends linearly on the CFOSD and the sampling time offset difference between INIT and REF, ΔT_o. The second term depends on the sum of the CFO slopes and the true distance d. We quantify their relative contributions using example parameters: $k_{\mathrm{CFO},I} = 10\ \frac{\mathrm{Hz}}{\mathrm{MHz}}$, $k_{\mathrm{CFO},R} = 0$, $d = 10$ m, and $\Delta T_o = 120\ \mu$s, which is the approximate sampling time offset difference in our experimental setup. The first term contributes approximately 18 cm of bias, while the second term contributes only about 50 μm, indicating that the second term is negligible, even though it scales with distance. Minimizing CFOSD-induced bias requires the sampling time offset difference ΔT_o to be as small as possible, but in practice, ΔT_o is constrained by hardware capabilities and cannot be made arbitrarily small.

Although the distance estimate can be obtained directly from (7), in practice, a larger set of carrier frequencies is used, and the complex samples acquired at those carriers together form the channel frequency response (CFR). The channel impulse response (CIR) is then obtained by applying the inverse fast Fourier transform (IFFT) to the CFR, and the distance is estimated from the position of the dominant peak in the CIR.

III. TIMING DIAGRAM OPTIMIZATION

This section describes two TD modification approaches that reduce the impact of CFOSD on distance estimation without requiring explicit CFO estimation. The first approach augments standard TD by acquiring additional samples at INIT or at both devices at specific time instants relative to the standard sampling times. These additional samples are combined with those obtained under standard TD using a temporal differential correction approach (TDCA), which suppresses the CFOSD-induced contribution to the overall sampled phase. The second approach dynamically switches the roles of INIT and REF during the MCPD procedure, effectively alternating which device transmits first and which

listens, to decouple CFOSD-induced phase shifts from those caused by propagation. For completeness, a third TD modification proposed in [20] is discussed at the end of this section.

A. TEMPORAL DIFFERENTIAL CORRECTION APPROACH

Two TD optimization methods based on TDCA are proposed. The first is called the *single-sided temporal differential method* (SSTDM) and is illustrated in Fig. 2(b). For the i-th carrier, the phase samples $\phi^{(i)}_{R,0}$ and $\phi^{(i)}_{I,0}$ are acquired at REF and INIT at the same time instants as in the standard TD, that is, at $T'_{o,R}$ and $T'_{o,I}$, respectively. Then, two additional samples are acquired at INIT: the first at $T'_{o,I} + \widetilde{T}_{o,R}$ and the second at $2 \cdot T'_{o,I}$ after the start of the measurement on each carrier. Here, $\widetilde{T}_{o,R}$ denotes the nominal REF sampling offset $T_{o,R}$ as measured on INIT and is therefore affected by INIT's clock drift rather than REF's. In contrast to Section II, where timing asynchronization from clock drift differences was neglected to isolate the CFOSD effect, it is now reintroduced to quantify how the proposed TD designs also affect the timing asynchronization contribution to the distance bias. The phase sample taken at time $T'_{o,I} + \widetilde{T}_{o,R}$ is

$$\begin{aligned}\phi^{(i)}_{I,1} &= 2\pi\left(f_{IF} + \Delta f^{(i)}\right)\left(P[i] \cdot \Delta T'_{s,I} + T'_{o,I} + \widetilde{T}_{o,R}\right) \\ &\quad + 2\pi\left(f^{(i)}_c - f_{IF} + \Delta f^{(i)}_R\right)\frac{d}{c} \\ &\quad + \Theta^{(i)}_{LO,I} - \Theta^{(i)}_{LO,R}. \end{aligned} \tag{9}$$

Similarly, the phase sample taken at time $2 \cdot T'_{o,I}$ is

$$\begin{aligned}\phi^{(i)}_{I,2} &= 2\pi\left(f_{IF} + \Delta f^{(i)}\right)\left(P[i] \cdot \Delta T'_{s,I} + 2\,T'_{o,I}\right) \\ &\quad + 2\pi\left(f^{(i)}_c - f_{IF} + \Delta f^{(i)}_R\right)\frac{d}{c} \\ &\quad + \Theta^{(i)}_{LO,I} - \Theta^{(i)}_{LO,R}. \end{aligned} \tag{10}$$

The final phase sample for the i-th carrier is obtained by combining the four samples according to

$$\begin{aligned}\phi^{(i)} &= \phi^{(i)}_{R,0} - \phi^{(i)}_{I,0} + (\phi^{(i)}_{I,2} - \phi^{(i)}_{I,0}) - (\phi^{(i)}_{I,1} - \phi^{(i)}_{I,0}) \\ &= 2\pi\left(f_{IF} + \Delta f^{(i)}\right)\cdot \\ &\quad \left[P[i]\,\Delta T_s\,\frac{e_I - e_R}{1 + e_I + e_R + e_I\,e_R}\right. \\ &\quad \left. + T_{o,R}\,\frac{e_I - e_R}{1 + e_I + e_R + e_I\,e_R}\right] \\ &\quad - 2\pi\left(2f^{(i)}_c + \Delta f^{(i)}_I + \Delta f^{(i)}_R - f_{IF}\right)\frac{d}{c}. \end{aligned} \tag{11}$$

Compared to the standard TD approach, in which the second phase term in the brackets of (4) introduces the dominant CFOSD-induced distance bias and depends approximately on the sampling time offset difference between INIT and REF, SSTDM reduces this term to a component that depends only on the REF sampling offset $T_{o,R}$, scaled by the relative frequency mismatch between the crystal oscillators used for timing at INIT and REF. This phase component remains because INIT and REF measure the nominal offset $T_{o,R}$ differently due to their respective clock drifts.

The second TDCA-based method, called the *dual-sided temporal differential method* (DSTDM) and shown in Fig. 2(c), builds on SSTDM by eliminating the remaining timing-asynchronization term proportional to $T_{o,R}$. Two additional samples are acquired compared to the standard TD: $\phi^{(i)}_{R,1}$ at REF at time $2{\cdot}T'_{o,R}$ and $\phi^{(i)}_{I,1}$ at INIT at time $2{\cdot}T'_{o,I}$ after the start of the measurement on each carrier. The expressions for the additional phase samples are derived analogously to the SSTDM case. The final phase sample for the i-th carrier is

$$\begin{aligned}\phi^{(i)} &= 2 \cdot \phi^{(i)}_{R,0} - \phi^{(i)}_{R,1} - (2 \cdot \phi^{(i)}_{I,0} - \phi^{(i)}_{I,1}) \\ &= 2\pi\left(f_{IF} + \Delta f^{(i)}\right)P[i]\,\Delta T_s\,\frac{e_I - e_R}{1 + e_I + e_R + e_I\,e_R} \\ &\quad - 2\pi\left(2f^{(i)}_c + \Delta f^{(i)}_I + \Delta f^{(i)}_R - f_{IF}\right)\frac{d}{c}. \end{aligned} \tag{12}$$

Although SSTDM and DSTDM effectively suppress the effect of CFOSD on distance estimation, they do so at the cost of a longer measurement interval, as both operate with a larger ΔT_s than the standard TD, with DSTDM requiring the longest duration. A longer measurement procedure increases the risk of interference, raises energy consumption, reduces the refresh rate of distance measurements, and amplifies the effect of timing asynchronization on distance estimation, as the phase shift associated with the first phase term of (11) and (12) increases with ΔT_s [19]. An increased measurement time can also exceed the channel coherence time T_c, which can be approximated as $T_c \approx 1/(2f_d)$, where f_d is the Doppler frequency shift. For example, in typical indoor environments that involve human motion, Doppler shifts in the 2.4 GHz band are usually below 12 Hz, corresponding to a coherence time of approximately 40 ms [41]. Another drawback of TDCA arises when the required sampling instants are implemented in software, making it difficult to achieve true timing symmetry due to nondeterministic delays such as operating system scheduling, interrupt handling during the measurement procedure, and other software-induced timing variations.

B. ROLE-SWITCHING APPROACH (RSA)

The RSA approach improves on the previously discussed TDCA methods by preserving the same measurement duration as the standard TD approach while reducing the bias caused by CFOSD through dynamic switching of the roles of INIT and REF during the MCPD procedure. In the standard configuration, INIT first transmits the unmodulated continuous wave (CW) and REF samples the phase, after which REF transmits and INIT samples. When the roles are reversed, REF transmits first and INIT performs the initial sampling, followed by INIT transmitting and REF sampling. We define a role pattern vector RP of length M, where each entry corresponds to one of the M ordered carrier frequencies. An entry $RP[i] = -1$ indicates that the roles are reversed for the i-th carrier, while $RP[i] = 1$ indicates that the roles follow

the standard configuration. The general principle of the RSA approach is illustrated in Fig. 2(d).

The effect of reversing roles on the sampled phase is most apparent when timing asynchronization is neglected (i.e., $e_I = e_R = 0$) and only the CFO contribution is considered. Under this assumption, the phase terms in (6) that depend on ΔT_o, change sign when the roles are reversed. Applying the role pattern RP to the MCPD procedure is therefore equivalent to multiplying the ΔT_o-dependent terms by the corresponding entry in RP, which gives

$$\begin{aligned}\phi_{RP}^{(i)} = \; & 2\pi \left(f_{IF} + \Delta f_0\right) \cdot \Delta T_o \cdot RP[i] \\ & + 2\pi \left(k_{\mathrm{CFO},I} - k_{\mathrm{CFO},R}\right) \cdot i \cdot \nu \cdot \Delta T_o \cdot RP[i]. \end{aligned} \tag{13}$$

The design objective for RSA is to determine RP such that $\phi_{RP}^{(i)}$, as a function of the carrier index i, has zero phase slope across carrier frequencies and therefore does not bias the distance estimate. The slope of $\phi_{RP}^{(i)}$ with respect to i is obtained by simple linear regression and is proportional to

$$k \propto \left(\alpha + \tfrac{M-1}{2}\beta\right) \cdot \sum_{i=-\frac{M-1}{2}}^{\frac{M-1}{2}} i \cdot RP[i] \quad + \quad \alpha \cdot \sum_{i=-\frac{M-1}{2}}^{\frac{M-1}{2}} i^2 \cdot RP[i], \tag{14}$$

where the carrier index i has been redefined to be centered around zero, $\alpha = 2\pi \left(f_{IF} + \Delta f_0\right) \cdot \Delta T_o$, and $\beta = 2\pi \left(k_{\mathrm{CFO},I} - k_{\mathrm{CFO},R}\right) \cdot \nu \cdot \Delta T_o$. Setting the slope to zero yields the following two conditions for the RP:

$$\sum_{i=-\frac{M-1}{2}}^{\frac{M-1}{2}} i \cdot RP[i] = 0, \qquad \sum_{i=-\frac{M-1}{2}}^{\frac{M-1}{2}} i^2 \cdot RP[i] = 0. \tag{15}$$

RPs that satisfy both conditions are good candidates, but they do not guarantee unbiased distance estimation when the distance is obtained from the position of the dominant peak in the CIR after applying the IFFT to the CFR. Using an RP with entries that are not all equal introduces phase discontinuities across carriers at each role change, which generate artificial paths in the CIR that can interfere with the line-of-sight (LOS) peak and affect its position. An exhaustive search for an optimal RP is computationally infeasible, as there are 2^M possible patterns. This motivates the use of structured RP designs. In the following, three different methods based on different RP designs are introduced to illustrate how different realizations of RP affect the resulting phase samples and the corresponding CIR, and are analyzed further throughout the paper. All three patterns satisfy the first condition in (15) and have a second sum that is close to zero. Additionally, the artificial peaks they generate have minimal influence on the LOS peak.

All patterns are designed for $M = 76$ carriers spanning the 2405-2480 MHz band, yielding a carrier spacing of $\nu = 1$ MHz. This matches the 1 MHz channel indexing used by the Bluetooth Low Energy (BLE) Channel Sounding feature based on MCPD, reflecting a practically relevant configuration. This configuration is used throughout the paper.

The first RSA method, called *alternating roles every frequency* (AR1), reverses roles every second carrier, corresponding to $RP = [1, -1, 1, -1, \dots]$, with one additional adjustment: the alternating sequence is interrupted at one carrier index above the midpoint of the band and restarted with the negative value of the first element. This break is necessary to ensure that the slope of (14) is close to zero.

The RP of the second method, called *alternating roles every two frequencies* (AR2), consists of repeating blocks of $[1, -1, -1, 1]$. Since a single block satisfies the first condition in (15), the entire RP also satisfies this condition. The switching rate of the role changes is half that of AR1, so phase discontinuities across the frequency band are less frequent, which shifts the positions of the artificial peaks in the computed CIR compared to AR1.

The third method, called the *progressively less-frequent role-switching method* (PLFRSM), is designed to distribute the artificial path components in the CIR over a wider delay range and reduce their peak amplitudes compared to AR1 and AR2. To achieve this, RP uses progressively longer segments of identical values before switching to a different value, resulting in less frequent role changes as the carrier index increases. The pattern starts with the block, which is also used by AR2: $[1, -1, -1, 1]$. The next block doubles the length of the previous block, so the k-th block consists of a run of k consecutive $+1$ elements, followed by $2 \cdot k$ consecutive -1 elements, and then another run of k consecutive $+1$ elements. All blocks satisfy the first condition in (15). Because the total number of carrier frequencies is fixed, the final block may not fit entirely within the available band. In that case, the sequence is truncated at the end of the last block, and the remaining elements of RP are filled using the AR1 pattern.

Examples of simulated phase samples for the proposed methods and standard TD approach, for a fixed CFOSD values of 0 and 10 $\frac{\mathrm{Hz}}{\mathrm{MHz}}$ and different values of Δf_0, are shown in Fig. 3. The distance is set to zero, and timing asynchronization is neglected ($e_I = e_R = 0$) to clearly isolate the biasing effect of CFOSD. The remaining simulation parameters are $T_{o,R} = 105\ \mu$s, $T_{o,I} = 225\ \mu$s, $\Delta T_s = 279.5\ \mu$s, and $f_{IF} = 1$ MHz, which closely match the values used in the experimental validation with the available hardware. Fig. 4 shows the corresponding computed CIR magnitudes for a fixed CFOSD of 10 $\frac{\mathrm{Hz}}{\mathrm{MHz}}$.

The blue curve in all plots in Fig. 3 shows the phase samples for the ideal case when CFOSD $= 0$ and $\Delta f_0 = 0$. Since the distance is zero, the phase shifts due to propagation are equal for all carriers, resulting in a zero phase slope. In the standard TD approach, a nonzero CFOSD produces a linear phase trend across carriers, which is proportional to the bias in the estimated distance. The greater the absolute value of CFOSD, the larger the phase slope and the resulting distance bias.

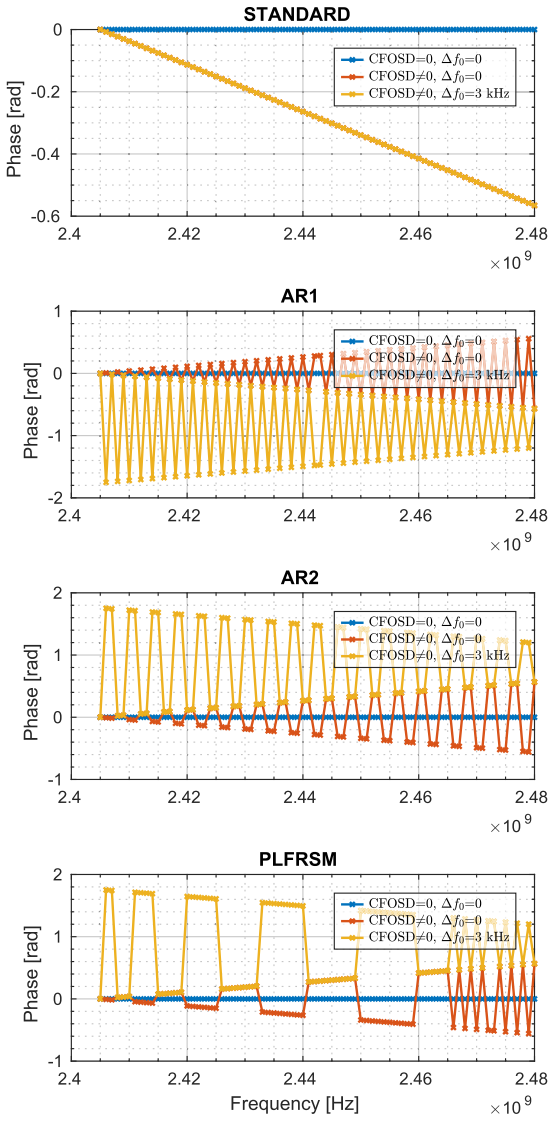


FIGURE 3. Simulated phase samples for the standard TD and the three proposed RSA-based methods. The red and yellow curves for the standard TD overlap.

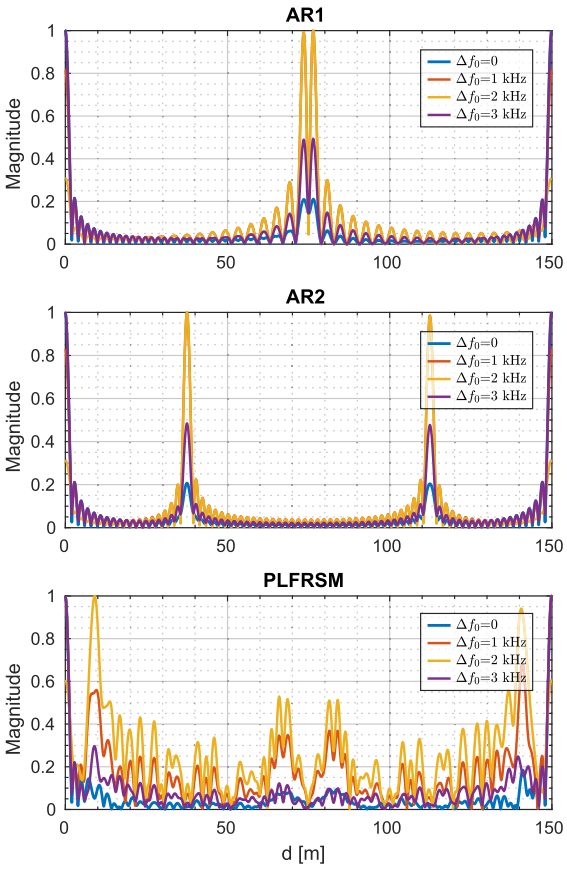


FIGURE 4. Computed CIR magnitudes for the three proposed RSA-based methods for a fixed CFOSD and various values of Δf_0.

The AR1 method for $\Delta f_0 = 0$ and CFOSD $\neq 0$ (red curve) produces phase samples for carriers with standard roles that follow the same phase trend as in the standard TD approach, while samples for carriers with reversed roles follow the same trend but with the opposite sign. As a result, the overall phase slope across carriers is close to zero. A consequence of the alternating roles is the presence of phase jumps at each role switch, as the second phase term in (13) changes sign. For $\Delta f_0 \neq 0$, the phase jumps at each role switch become more pronounced, since the first phase term in (13) also changes sign when the roles are reversed, as shown by the yellow curve. This increases the magnitude of each phase jump by twice the contribution of this phase term, which is independent of i and therefore the same for all carriers when a role switch occurs. The parameters ΔT_o and f_{IF} can be chosen so that their contribution to the overall phase jump is an integer multiple of 2π, ensuring that they do not introduce an additional phase jump, as done in the simulations. In contrast, Δf_0 is not known in advance.

The corresponding CIRs in Fig. 4 show that Δf_0 can have a strong impact on the estimated CIR. Due to the way AR1 defines the *RP*, which determines the carrier indices with role switches and associated phase jumps, the AR1 method generates two closely spaced artificial peaks that appear approximately halfway across the distance domain relative to the LOS peak. The magnitudes of these artificial peaks, as well as the magnitude of the LOS peak, depend on Δf_0. For certain values of Δf_0, the LOS peak becomes smaller than the artificial peaks, which requires a more advanced algorithm for reliable LOS detection and distance estimation.

Similar observations can be made for the AR2 and PLFRSM methods, with phase jumps occurring at positions determined by their respective *RP* patterns. For AR2, the computed CIRs also contain two artificial peaks, but due to the lower role-switching rate, they are located farther apart than in AR1. In the case of PLFRSM, the artificial path components are spread across the entire distance domain.

With a design similar to PLFRSM, the artifacts introduced by the phase jumps can be shaped so that the resulting CIR more closely resembles a noise-like spectrum rather than having a small number of dominant peaks.

To understand the effect of a particular *RP* on the estimated CIR, we examine the complex samples derived from (6). We approximate $2 + k_{\mathrm{CFO},I} + k_{\mathrm{CFO},R} \approx 2$ and omit the phase shift of the third phase term, which does not depend on the carrier index and contributes only to a global phase rotation, and therefore does not influence the CIR magnitude. The complex sample for the i-th carrier can then be written as

$$\begin{aligned} c^{(i)} = A \cdot \exp\big(j\,2\pi\,(f_{IF} + \Delta f_0)\,\Delta T_o \cdot RP[i]\big) \\ \cdot \exp\big(j\,2\pi\,(k_{\mathrm{CFO},I} - k_{\mathrm{CFO},R})\,i\,\nu\,\Delta T_o \cdot RP[i]\big) \\ \cdot \exp\big(-j\,4\pi\,i\,\nu\,d/c\big), \end{aligned} \tag{16}$$

where A is the received signal amplitude. For clarity, we define the three phase components as

$$\begin{aligned} \phi_{\Delta f_0} &= 2\pi\,(f_{IF} + \Delta f_0)\,\Delta T_o \cdot RP[i], \\ \phi_{\mathrm{CFOSD}}[i] &= 2\pi\,(k_{\mathrm{CFO},I} - k_{\mathrm{CFO},R})\,i\,\nu\,\Delta T_o \cdot RP[i], \\ \phi_d[i] &= -4\pi\,i\,\nu\,\frac{d}{c}. \end{aligned} \tag{17}$$

The CIR can be obtained using the Fourier transform property that multiplication in the frequency domain corresponds to circular convolution in the time domain ($\mathcal{F}\{s[t] \circledast h[t]\} = S[i] \cdot H[i]$):

$$\begin{aligned} h[t] = \mathrm{IFFT}\big\{A \cdot \exp\big(j \cdot \phi_d[i]\big)\big\} \\ \circledast \mathrm{IFFT}\big\{\exp\big(j \cdot \phi_{\mathrm{CFOSD}}[i]\big)\big\} \\ \circledast \mathrm{IFFT}\big\{\exp\big(j \cdot \phi_{\Delta f_0}[i]\big)\big\}. \end{aligned} \tag{18}$$

Equation (18) shows that the ideal CIR, represented by $\mathrm{IFFT}\{A \cdot \exp\big(j \cdot \phi_d[i]\big)\}$, is circularly convolved with two additional impulse responses: $\mathrm{IFFT}\{\exp\big(j \cdot \phi_{\mathrm{CFOSD}}[i]\big)\}$ and $\mathrm{IFFT}\{\exp\big(j \cdot \phi_{\Delta f_0}\big)\}$. The first impulse response depends on CFOSD and *RP*, while the second depends on Δf_0 and *RP*. An appropriate choice of *RP* shapes these impulse responses, and their circular convolution with the ideal CIR determines the structure and amplitudes of the artificial peaks introduced by the RSA approach.

1) IMPROVED RSA

The main limitation of the RSA is that distance estimation becomes invalid when the distance is determined from the position of the largest peak in the CIR and when an artificial peak exceeds the LOS peak. This occurs for certain combinations of CFOSD and Δf_0, as shown in Fig. 5, which presents the calculated absolute error (AE) of the estimated distance over CFOSD and Δf_0 sweeps. Yellow regions indicate parameter combinations for which the estimation error is large due to incorrect peak selection.

To address this problem, we introduce improved versions of the RSA-based methods in which the TDs remain unchanged, but the peak search algorithm is enhanced by performing an additional cross-correlation of the acquired CIR with a template CIR. The distance is then estimated from the position of the dominant peak in the resulting cross-correlation function. For each RSA method, a CIR template is generated by simulation for $d = 0$, CFOSD $= 0$, and a suitably chosen value of Δf_0. The template value of Δf_0 is selected by searching over candidates in the range 0-4 kHz with a step of 100 Hz. For each candidate Δf_0, a template CIR is generated. This template is then cross-correlated with a set of CIRs obtained with simulation parameters $d = 0$, Δf_0 swept over the same range as the candidate Δf_0, and CFOSD swept from -10 to 10 $\frac{\mathrm{Hz}}{\mathrm{MHz}}$ with a step of 0.2 $\frac{\mathrm{Hz}}{\mathrm{MHz}}$. For each cross-correlation, the resulting AE is recorded. The optimal template value of Δf_0 is the one that minimizes the accumulated AE over all combinations of Δf_0 and CFOSD. The search range of Δf_0 is limited to 4 kHz because, for the sampling time offset difference ΔT_o considered, the phase shift term $2\pi\,\Delta f_0 \Delta T_o \cdot 2$ wraps around approximately outside this interval, and the pattern then repeats.

The improved versions of AR1, AR2, and PLFRSM are denoted as AR1-XC, AR2-XC, and PLFRSM-XC, respectively. Fig. 5 shows that the peak-search enhancement substantially reduces the occurrence of large AEs compared to basic RSA-based methods, although large AEs still occur for a limited number of parameter combinations in the AR2-XC case. Under such conditions, the maximum search range for the estimated distance can be restricted to values below the first artificial peak, or more advanced LOS detection strategies can be applied. The proposed peak-search improvement is effective because artificial peaks generated by RSA appear at predictable positions relative to the LOS peak. Even when the LOS peak is not the largest in the original CIR, cross-correlation with the template CIR exploits the entire CIR structure, including artificial peaks, and the correlation output is maximized at the delay corresponding to the LOS component.

The main drawback of the improved approach is the additional cross-correlation step, which increases computational load and memory requirements on hardware-constrained devices. However, the cross-correlation can be computed efficiently in the frequency domain as $(h \star g)[t] = \mathrm{IFFT}\{H[k]\,G^*[k]\}$, where $h[t]$ is the measured CIR, $g[t]$ is the template CIR, $H[k]$ and $G[k]$ are their discrete Fourier transforms, and $(\cdot)^*$ denotes complex conjugation. The spectrum $H[k]$ is already available from the phase measurements across carrier frequencies, and $G^*[k]$ can be precomputed and stored in memory. The incremental computational cost is therefore limited to a single element-wise complex multiplication of $H[k]$ and $G^*[k]$. Potential downsides include peak broadening and the appearance of weaker secondary artifacts introduced by the correlation operation.

C. 4-WAY RANGING WITH STANDARD AND REVERSED ROLES

The last TD design approach considered is closely related to the four-way measurement proposed in [20]. On each i-th carrier, INIT and REF first perform the standard

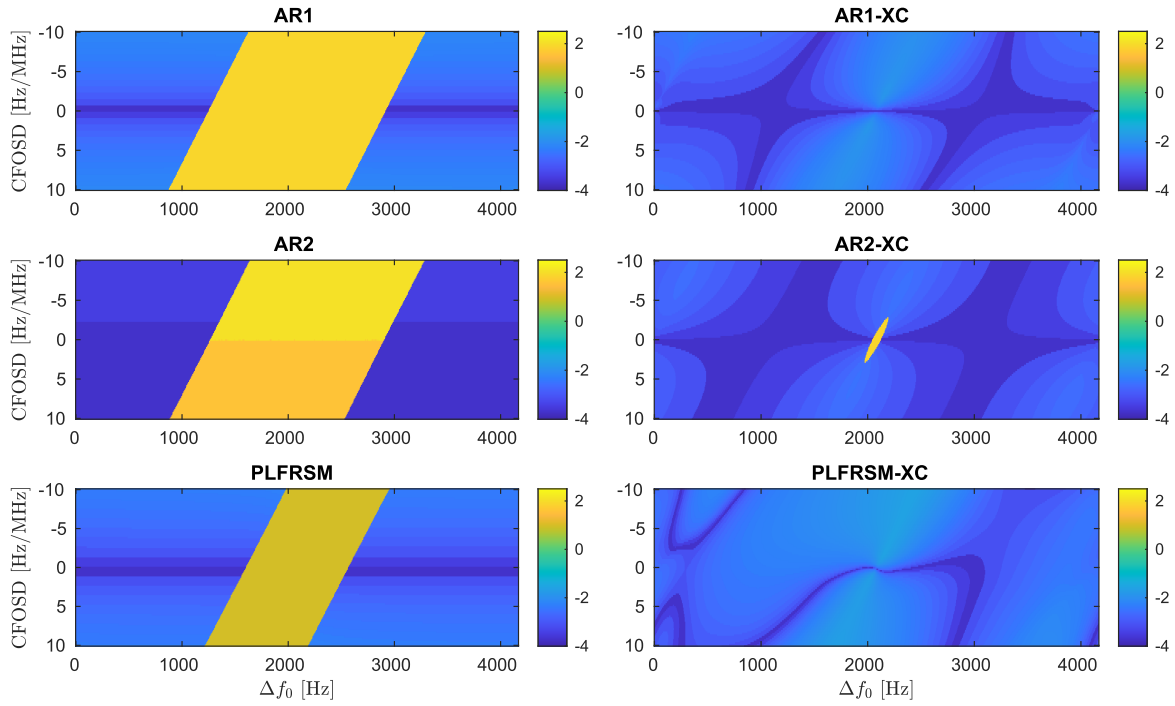


FIGURE 5. AE as a function of CFOSD and Δf_0 for the basic RSA-based methods (left) and the improved versions (right). AE is in logarithmic scale to accommodate the large variation in error magnitude.

two-way exchange, acquiring phase sample $\phi_{R,0}^{(i)}$ at REF and $\phi_{I,0}^{(i)}$ at INIT. The exchange is then repeated on the same carrier with reversed roles, acquiring $\phi_{R,1}^{(i)}$ and $\phi_{I,1}^{(i)}$ at REF and INIT, respectively. We refer to this approach as the *per-frequency role-switching approach* (PFRSA) and is illustrated in Fig. 2(e). For ease of interpretation, we assume that the second exchange starts ΔT_s after the start of the first exchange, and that the measurement on carrier $i+1$ begins $2\cdot\Delta T_s$ after the start of the measurement on carrier i. The final phase for carrier i is obtained by combining the four samples as: $\phi^{(i)} = \phi_{R,0}^{(i)} - \phi_{I,0}^{(i)} + \phi_{R,1}^{(i)} - \phi_{I,1}^{(i)}$ which evaluates to

$$\begin{aligned}\phi^{(i)} = {} & 2\pi\left(f_{IF} + \Delta f^{(i)}\right)\cdot \\ & \left[(4\cdot P[i]+1)\cdot\Delta T_s\,\frac{e_I - e_R}{1+e_I+e_R+e_I\,e_R}\right. \\ & \left. + \left(T_{o,R}+T_{o,I}\right)\frac{e_I - e_R}{1+e_I+e_R+e_I\,e_R}\right] \\ & - 4\pi\left(2f_c^{(i)} + \Delta f_I^{(i)} + \Delta f_R^{(i)} - f_{IF}\right)\frac{d}{c}. \end{aligned} \tag{19}$$

Compared to the standard TD phase in (4), the second bracketed term in PFRSA is reduced to a phase component that depends on the sum of the sampling offsets $T_{o,R}+T_{o,I}$ and is scaled by a small factor determined by the clock-drift mismatch between INIT and REF. With synchronized timing, CFOSD does not affect the measured phases and the distance estimate. The main drawback of PFRSA is its long measurement procedure, which is the longest among the approaches considered and increases the effect of timing asynchronization on distance estimation.

IV. SIMULATIONS

Numerical simulations in Matlab are used to quantify the impact of CFOSD and additive noise on MCPD distance estimation for the TD designs introduced in Section III, compared to the baseline standard TD approach. The simulation setup is defined as follows. The distance is fixed to 10 m and the received complex samples have unit magnitude on all carriers. The CIR is obtained by applying an IFFT with zero padding to 262144 points, which provides a range resolution of approximately 0.572 mm. Other simulation parameters are either specific to each simulation scenario or follow the configuration used in Sections II and III-B: $\Delta T_o = 120\ \mu$s, $\Delta T_s = 279.5\ \mu$s, $f_{IF} = 1$ MHz, $M = 76$, $f_c^{(0)} = 2405$ MHz and $\nu = 1$ MHz.

A. EFFECT OF VARYING CFOSD ON DISTANCE ESTIMATION

The first set of simulations evaluates the effect of CFOSD on the distance estimation error for the considered TD designs without additive noise. CFOSD is varied over $\pm 80\ \frac{\text{Hz}}{\text{MHz}}$ in steps of $0.02\ \frac{\text{Hz}}{\text{MHz}}$.

The simulation Scenario #1 is configured to isolate the impact of CFOSD by neglecting timing asynchronization ($e_I = e_R = 0$), setting $\Delta f_0 = 0$ kHz, and applying the sequential switching (*SS*) FSP, where carrier frequencies during the MCPD procedure are applied in ascending order

TABLE 3. CFOSD limits for RSA-based TD designs, defined as the CFOSD value beyond which the AE exceeds 0.1 m, and the corresponding mean AE within the ±CFOSD limits, for the simulation parameters of Scenario #1 ($e_I = 0$, $e_R = 0$, $\Delta f_0 = 0$ kHz, *SS* FSP) and Scenario #2 ($e_I = 10$ ppm, $e_R = 0$, $\Delta f_0 = 3$ kHz, *CycleReset(3)* FSP).

TD	Scenario #1 lower / upper limit $\left[\frac{\text{Hz}}{\text{MHz}}\right]$	Scenario #1 mean [cm]	Scenario #2 lower / upper limit $\left[\frac{\text{Hz}}{\text{MHz}}\right]$	Scenario #2 mean [cm]
AR1	-33.7 / 33.7	1.63	-1.5 / 44.4	2.14
AR2	-33.4 / 33.4	0.067	-0.4 / 51.4	0.16
PLFRSM	-34.4 / 34.4	1.04	-10.5 / 51.8	1.36
AR1-XC	-52.4 / 52.4	0.53	-49.6 / 41.4	1.89
AR2-XC	-46.0 / 46.0	0.51	-51.7 / 44.7	0.93
PLFRSM-XC	-44.6 / 39.2	0.87	-36.6 / 41.1	4.70

with $P[i] = i$ [19]. The computed AEs are shown in Fig. 6(a). The standard TD approach exhibits a linear increase in AE with increasing absolute CFOSD and has the largest errors among the considered approaches for CFOSD values away from zero. The SSTDM, DSTDM, and PFRSA TD designs maintain zero AE over the entire CFOSD sweep, confirming the wideband behavior of these designs in mitigating the effect of CFOSD on the distance estimate. The RSA-based methods exhibit nonzero AEs and a sharp increase in AE outside a certain CFOSD operating interval specific to each method. We define the CFOSD limits for RSA-based methods as the CFOSD values at which the AE exceeds 0.1 m. Table 3 summarizes the corresponding negative and positive limits, along with the mean AE within those limits. Only AR1 and PLFRSM have mean AEs above 1 cm, while the remaining RSA-based methods remain below 1 cm, with AR2 below 1 mm. Within their respective CFOSD limits, all proposed methods provide substantially improved robustness to CFOSD compared to standard TD. The cross-correlation enhanced variants extend the CFOSD operating interval in which the methods perform efficiently. The limits are symmetric for AR1, AR1-XC, AR2, and PLFRSM, while PLFRSM-XC exhibits asymmetric limits. Overall, RSA-based designs are effective and provide low bias only when the system operates within the CFOSD limits specific to each method.

The simulation Scenario #2 jointly considers CFOSD and timing asynchronization by setting $e_I = 10$ ppm and $e_R = 0$, along with a nonzero $\Delta f_0 = 3$ kHz. Carrier frequencies during the MCPD procedure are applied according to the *CycleReset(3)* FSP, which defines $P[i]$ and mitigates the impact of timing asynchronization on distance estimation [19]. The resulting AEs are shown in Fig. 6(b). In this scenario, the standard TD is biased by CFOSD. SSTDM and DSTDM again achieve the lowest AE over the entire CFOSD range, as the TD designs suppress the CFOSD contribution to overall phase while *CycleReset(3)* reduces the timing asynchronization bias. The PFRSA curve is not visible in Fig. 6(b) because its AEs exceed the plotted range. Large errors occur due to pronounced timing asynchronization effect in PFRSA, which generates large artificial peaks in the CIR specific to the *CycleReset(3)* FSP. The ability of the *CycleReset(3)* FSP to suppress timing asynchronization effects is exceeded when artificial peaks of *CycleReset(3)* induced by timing asynchronization become higher than the LOS peak, resulting in incorrect distance estimation, as observed for PFRSA. For basic RSA-based methods, the CFOSD limits are asymmetric, and the corresponding CFOSD operating interval is shifted due to the nonzero Δf_0. The lower CFOSD limits are particularly restrictive for AR1 and AR2. In contrast, AR1-XC and AR2-XC largely mitigate this effect and retain a wide CFOSD operating interval. In practice, expected CFOSD values are likely well within these limits. Although the mean AEs within the limits increase relative to Scenario #1, they remain below 1 cm for AR2 and AR2-XC. Overall, Scenario #2 highlights the coupled impact of timing asynchronization and CFOSD on distance estimation and illustrates how a more complex FSP, such as *CycleReset(3)*, interacts with the considered TD designs.

B. NOISE SENSITIVITY

The noise robustness of the proposed TD designs is evaluated using Monte Carlo simulations with additive white Gaussian noise (AWGN). Complex AWGN is added independently to each received IQ sample at INIT and REF. The CFOSD is fixed at 10 $\frac{\text{Hz}}{\text{MHz}}$, and Δf_0 is set to 3 kHz. The signal-to-noise ratio (SNR) is varied from -10 dB to 60 dB in steps of 0.1 dB. For each SNR value, 500 Monte Carlo trials are performed, and the root mean square error (RMSE) of the estimated distance is calculated. Timing asynchronization is included by setting $e_I = 10$ ppm and $e_R = 0$.

Fig. 7(a) shows the RMSE as a function of SNR for the considered TD designs when *SS* FSP is used. The *SS* FSP is biased under timing asynchronization, and since the proposed TD designs target CFOSD mitigation rather than timing asynchronization suppression, all approaches exhibit a nonzero bias at high SNR. Consequently, the RMSE curves do not converge to zero. The standard TD achieves the lowest RMSE at high SNR because, for the chosen parameters, the bias contributions from CFOSD and timing asynchronization have opposite signs and partially cancel each other. For the RSA-based methods, the RMSE at high SNR is dominated by timing asynchronization, as the CFOSD-induced bias is effectively suppressed, as shown in Section IV-A. The TDCA-based methods have the largest RMSE values, reflecting their greater sensitivity to timing asynchronization and its associated bias. As the SNR

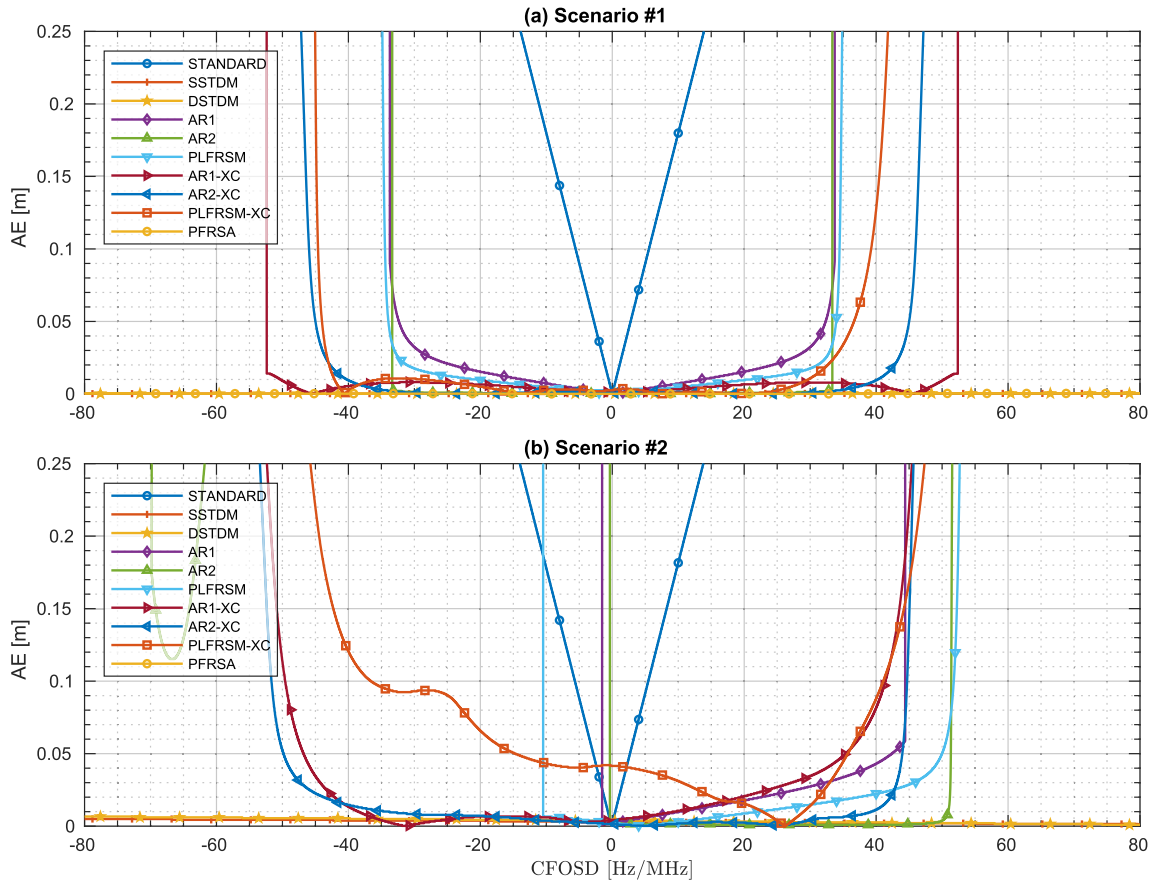


FIGURE 6. AE as a function of CFOSD for the proposed TD designs compared to the standard TD approach in two simulation scenarios: (a) Scenario #1 ($e_I = e_R = 0$, $\Delta f_0 = 0$, and *SS* FSP) and (b) Scenario #2 ($e_I = 10$ ppm, $e_R = 0$, $\Delta f_0 = 3$ kHz, and *CycleReset(3)* FSP).

decreases, all TD designs maintain an approximately constant RMSE down to a method-dependent SNR threshold, below which the RMSE increases sharply as the measurements become dominated by noise and peak selection becomes unreliable. The standard TD has the lowest threshold at approximately -1 dB. The RSA-based methods have higher thresholds, approximately between 1 dB and 4 dB. The highest threshold is observed for DSTDM at just below 7 dB, while SSTDM and PFRSA have thresholds of approximately 3 dB.

The second noise simulation scenario uses the *CycleReset(3)* FSP. The corresponding RMSE results are shown in Fig. 7(b). For all TD designs except the standard TD and PFRSA, the RMSE approaches zero at high SNR, since *CycleReset(3)* mitigates timing asynchronization and the proposed TD designs suppress the remaining CFOSD-induced bias. The standard TD has a nonzero RMSE since it does not suppress the CFOSD-induced bias. PFRSA has the largest RMSE at high SNR due to its strong sensitivity to timing asynchronization, which exceeds the mitigation capability of *CycleReset(3)* FSP and leads to the selection of an artificial peak instead of the LOS peak for distance estimation, as discussed in Section IV-A. Using *CycleReset(3)* FSP results in higher SNR thresholds for all TD designs compared to the *SS* case, consistent with the greater noise sensitivity of *CycleReset(3)* reported in [19]. Moreover, under *CycleReset(3)*, the RMSE of the RSA-based methods increases more rapidly as SNR decreases. This behavior suggests that the increased noise sensitivity is primarily introduced by the FSP selection, whereas the RSA-based TD modification alone remains comparatively less sensitive to noise, as indicated by the flatter RMSE curves obtained with *SS* FSP.

V. EXPERIMENTAL VALIDATION

Experimental validation is performed for standard TD and TD designs based on RSA to confirm the analytical and simulation results on practical hardware. RSA-based TD design methods show strong resilience to CFOSD variations and noise robustness in simulations and, among the proposed approaches, have the shortest measurement duration, making them the most suitable for practical, accurate, robust, and low-power MCPD ranging.

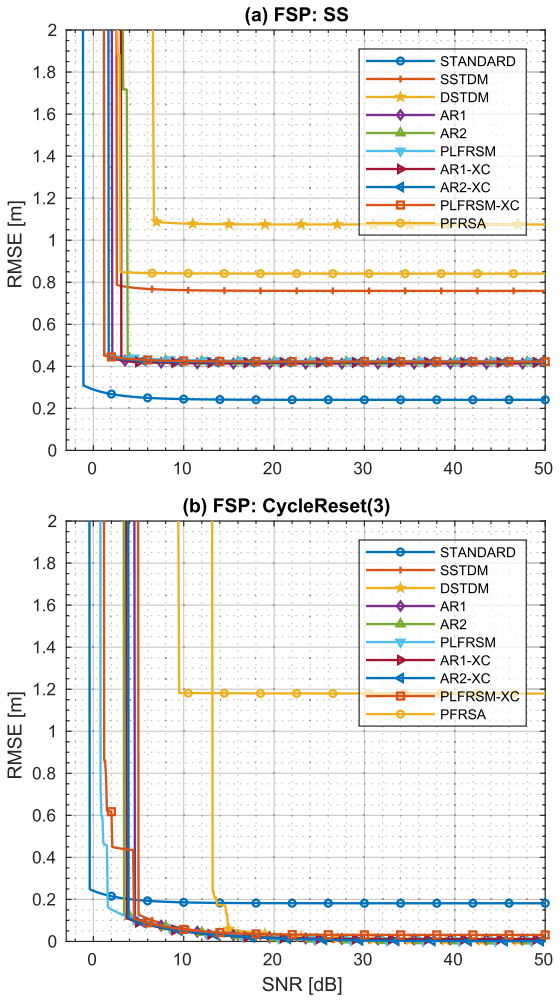


FIGURE 7. RMSE of the estimated distances as a function of SNR for the considered TD designs with fixed CFOSD, fixed Δf_0, and timing asynchronization included, using either the *SS* FSP (a) or the *CycleReset(3)* FSP (b).

The measurements are designed to assess how variations in CFOSD affect changes in the estimated distance. Absolute distance errors are not reported because the estimated propagation delay includes hardware-dependent offsets and other systematic contributions that are not directly observable. Characterizing and compensating for these offsets to achieve absolute accuracy would introduce measurement uncertainty comparable to the targeted resolution and increase sensitivity to environmental changes. Therefore, the analysis focuses on relative changes in the estimated distance as the considered parameters are varied.

Different CFOSD values are achieved by varying the CFO at REF as a function of carrier frequency in software. The smallest available CFO increment with the hardware used is 396.728 Hz, which is too coarse to generate a linear CFO ramp across the carrier frequencies corresponding to the CFOSD range of interest. Instead, a stepped approximation is

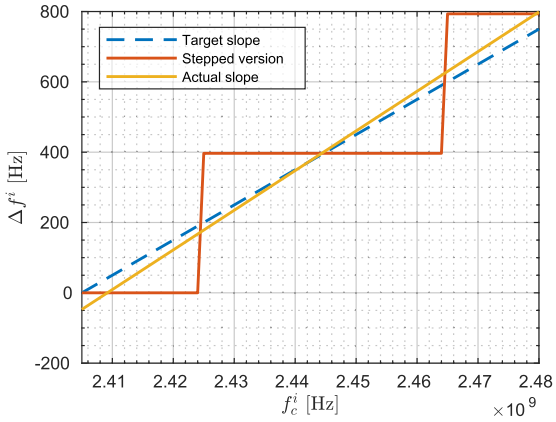


FIGURE 8. Example of CFOSD generation using stepped approximations in the experimental setup, obtained with the minimum CFO step of 396.728 Hz. The blue line shows the intended linear slope, the red line the corresponding stepped approximation, and the yellow line the actual slope estimated by simple linear regression.

used, as illustrated in Fig. 8. A set of target slopes covering the CFOSD sweep from -80 $\frac{\text{Hz}}{\text{MHz}}$ to 80 $\frac{\text{Hz}}{\text{MHz}}$ is first specified, and for each target slope, a stepped CFO profile is constructed to approximate the linear ramp using the available 396.728 Hz step. Linear regression is used to estimate the actual slope of the resulting profile. The difference between the initial CFO values at the beginning of the measured frequency band, Δf_0, is not controlled in software and remains at its default hardware-determined value unless stated otherwise. For each CFOSD configuration, 40 measurements are collected.

A. MEASUREMENT SETUP

INIT and REF are implemented using microcontroller boards equipped with AT86RF215 radio modules compliant with IEEE 802.15.4 [42]. The AT86RF215 integrates a phase measurement unit that provides access to complex IQ samples via register readout over the serial peripheral interface (SPI) bus. Measurements are conducted in a controlled manner by connecting INIT and REF with an RF coaxial cable to isolate the effect of CFOSD on distance estimation, using the same measurement setup as in [19]. Each measurement is initiated by INIT, and a wired triggering signal is provided to REF to ensure a synchronous start of the measurement procedure at both devices.

B. MEASUREMENT RESULTS

First, the CIRs obtained with the experimental setup for the RSA-based TD design methods, without cross-correlation enhancement, are compared with the simulated CIRs in Matlab to evaluate the agreement in peak shapes and locations. Simulated CIRs are generated by setting the distance d so that the LOS peaks align with the measured results and by setting $\Delta f_0 = 5.7$ kHz as an approximate value of the hardware-dependent CFO over the considered frequency band, based on previous measurements with the

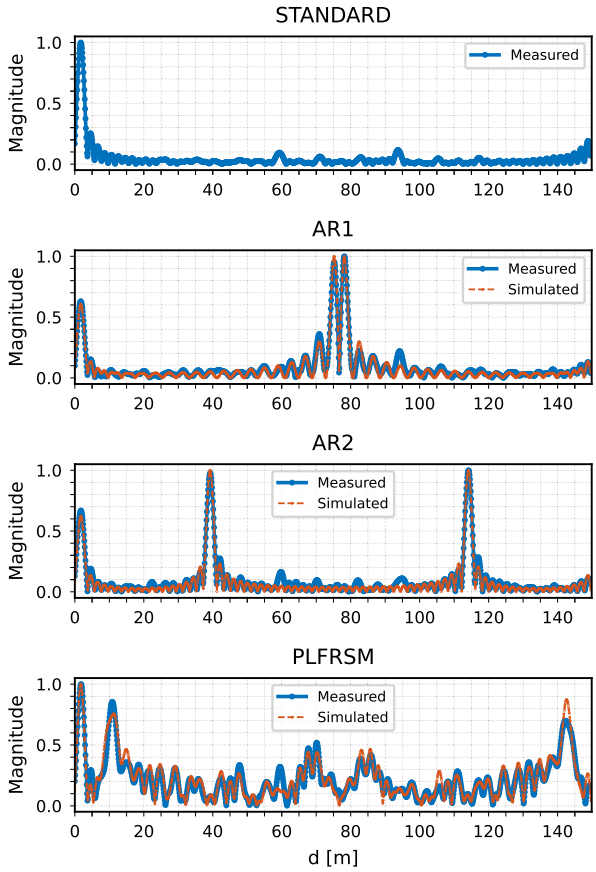


FIGURE 9. Measured and simulated CIRs for the standard TD and the three RSA-based TD designs, without cross-correlation enhancement and with CFOSD in software set to zero.

same devices. Fig. 9 presents the estimated CIRs when no CFOSD is induced in software. The CIR obtained with the standard TD is included for reference and shows a single dominant peak whose position corresponds to the measured distance. The remaining plots show the CIRs for the RSA-based methods, where the blue curves represent the measured CIRs and the red curves represent the simulated CIRs. A close agreement in peak structure and peak locations between the measured and simulated CIRs is observed for all three RSA-based methods, which supports the adopted signal model and simulation framework with the experimental observations.

To evaluate robustness to CFOSD variations, all distance estimates are reported across the induced CFOSD sweep for the standard TD and improved RSA-based methods, selected for their more robust performance. Results are shown in Fig. 10. The estimated distance for the standard TD approach shows a linear dependence on CFOSD, consistent with the distance estimate being proportional to CFOSD. In contrast, the RSA-based methods maintain an approximately constant distance estimate within their CFOSD limits, confirming a strong reduction of CFOSD-induced bias. Beyond the

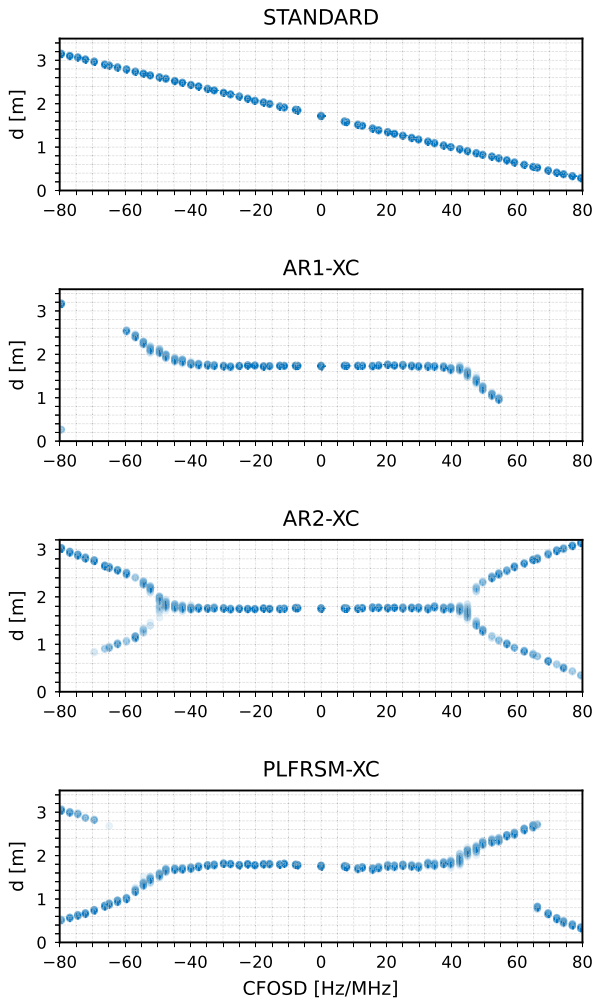


FIGURE 10. Measured distance estimates as a function of CFOSD for the standard TD and selected RSA-based TD designs, showing all 40 measurements for each CFOSD value.

TABLE 4. Slopes of the medians of estimated distances as a function of CFOSD and the standard deviations (Std dev) of the medians within the bounded CFOSD region (±30 $\frac{\text{Hz}}{\text{MHz}}$).

TD	Slope [m·MHz / Hz]	Std dev [m]
Standard	-18.01e-3	0.3425
AR1-XC	170.68e-6	0.0094
AR2-XC	422.99e-6	0.0100
PLFRSM-XC	-1.34e-3	0.0351

CFOSD limits, the dominant LOS peak in the CIR splits into two peaks of comparable magnitude, whose separation increases with the absolute value of CFOSD, explaining the increased spread of the measured values.

The medians and standard deviations of the distance estimates computed for each CFOSD value are shown in Fig. 11. In the median plots, the red line represents a linear regression fitted to the medians within a bounded CFOSD interval of ±30 $\frac{\text{Hz}}{\text{MHz}}$, selected to lie within the

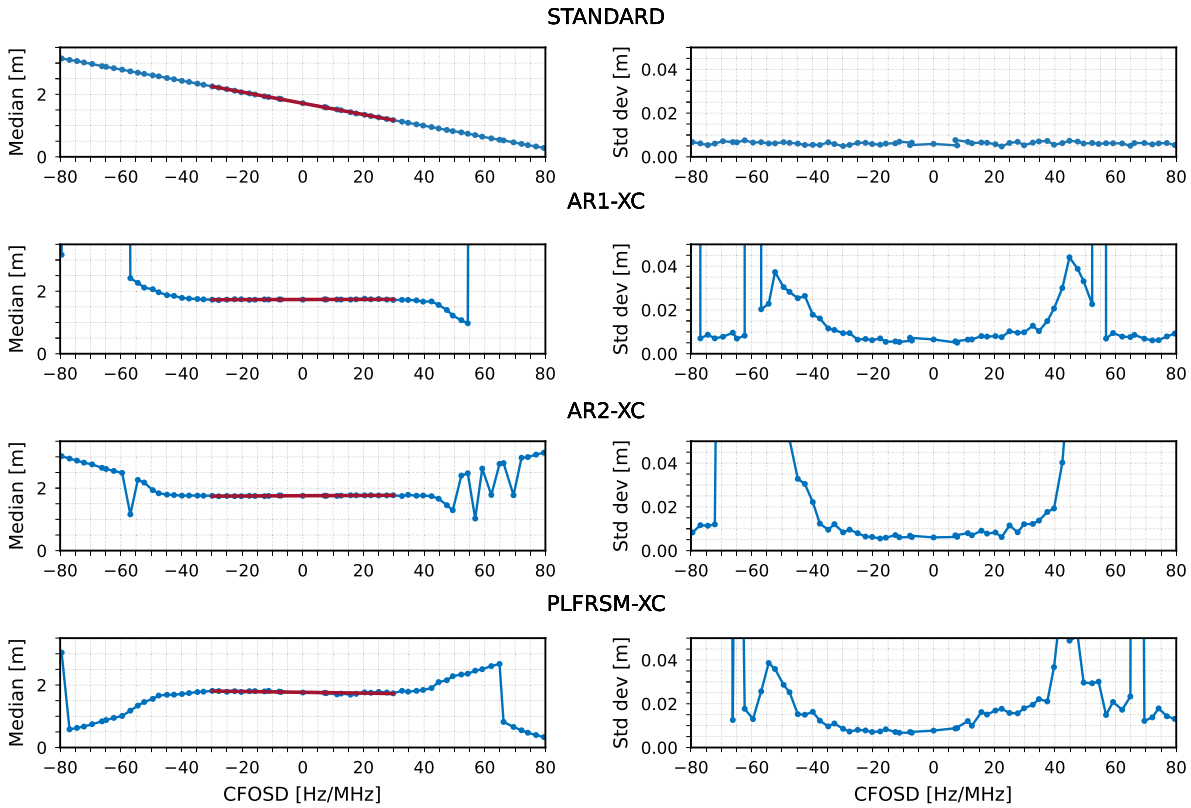


FIGURE 11. Medians (left) and standard deviations (Std dev) (right) of the estimated distance as a function of CFOSD for the standard TD and selected RSA-based TD designs, computed from 40 measurements for each CFOSD configuration. The red curve in the median plots is the fitted line obtained by simple linear regression.

TABLE 5. Qualitative comparison across TD designs. RSA-XC refers to the RSA-based method with cross-correlation-based peak selection. *In basic RSA, estimating distance from the largest peak in the CIR is sensitive to Δf_0, which can cause performance to vary under different operating conditions.

TD	CFOSD bias	Duration	Clock-drift sensitivity	Computation cost and memory footprint	Noise sensitivity	Unambiguous range
Standard	high	short	baseline	low	lowest	$c/(2\,\nu)$
SSTDM	very low	medium	high	low	medium	$c/(2\,\nu)$
DSTDM	very low	long	higher	low	medium	$c/(2\,\nu)$
RSA	variable*	short	baseline	low	low	$c/(2\,\nu)$
RSA-XC	low	short	baseline	medium	low	$c/(2\,\nu)$
PFRSA	very low	medium	highest	low	medium	$c/(4\,\nu)$

CFOSD limits of the RSA-based methods. The resulting slopes of the fitted lines, reported in Table 4, show that all RSA-based methods outperform standard TD, with AR1-XC achieving the smallest slope, followed by AR2-XC and PLFRSM-XC. A pronounced performance gap is observed between PLFRSM-XC and the other two RSA-based methods. The slope obtained for the standard TD matches the prediction of (8), which also evaluates to $-18{\cdot}10^{-3}\ \frac{\text{m·MHz}}{\text{Hz}}$ for $\Delta T_o = 120\ \mu$s. Table 4 further reports the standard deviation of the computed median distances within the bounded CFOSD interval, quantifying the spread of the median estimate under CFOSD variation. The values obtained are approximately 1 cm for AR1-XC and AR2-XC and 3.5 cm for PLFRSM-XC, which remains roughly one order of magnitude lower than for the standard TD.

The computed standard deviations for each CFOSD value show that, for small absolute values of CFOSD, the RSA-based methods have a spread of distance estimates comparable to the standard TD, indicating no increased sensitivity to measurement noise. As the CFOSD limits are approached, the standard deviation increases because the LOS peak begins to split into two peaks of similar magnitude, and for repeated measurements, the distance estimate alternates between the corresponding delays.

To evaluate the robustness of the selected TD designs to variations in Δf_0 and to quantify the benefit of cross-correlation enhancement for LOS detection in RSA-based methods, additional measurements were performed in which Δf_0 was swept from 0 to 3967 Hz in steps of 396.728 Hz alongside CFOSD. For each CFOSD and

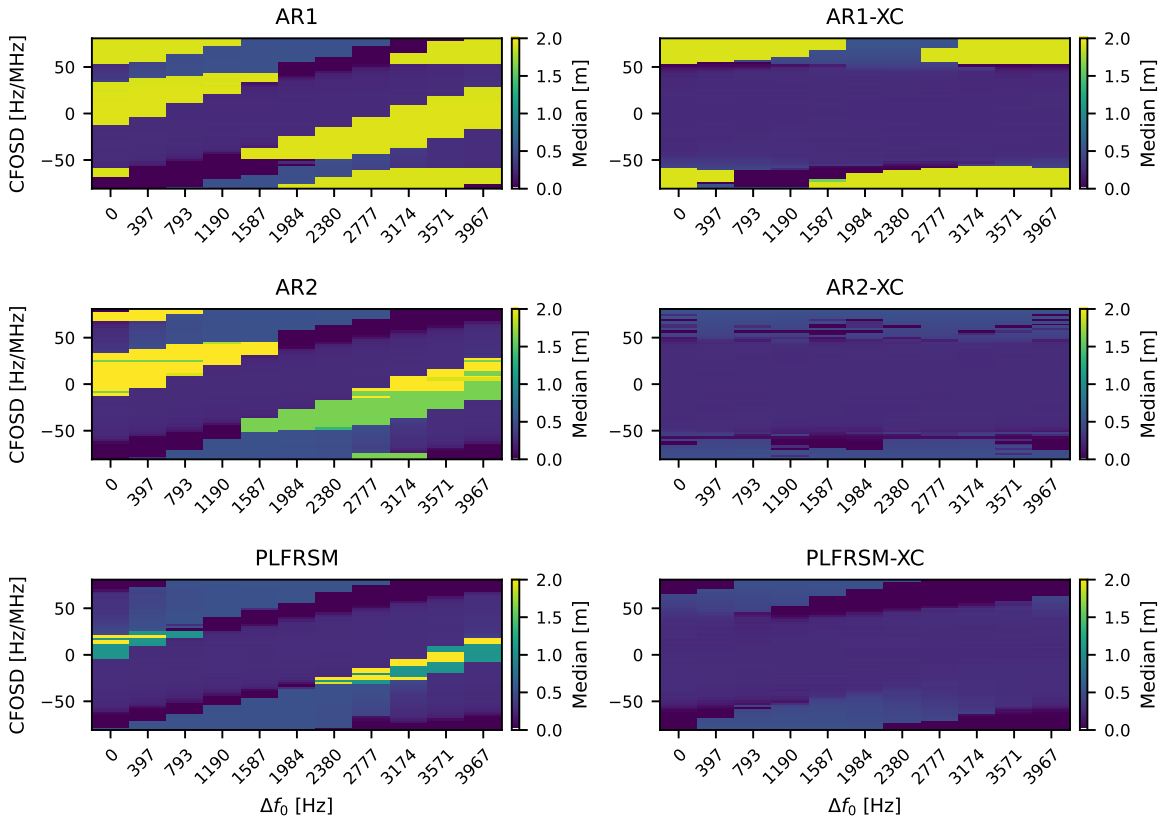


FIGURE 12. Median estimated distance as a function of CFOSD and Δf_0 for the three considered RSA-based TD designs without (left) and with (right) cross-correlation enhancement. The estimated distance is shown on a logarithmic color scale to accommodate the large variation in magnitude.

Δf_0 pair, 10 measurements were collected, and the median distance was computed, as shown in Fig. 12. The left-hand plots correspond to the basic RSA-based methods without cross-correlation enhancement. For certain combinations of CFOSD and Δf_0, large errors occur because an artificial peak is selected instead of the LOS peak, a behavior observed for all three methods. The right-hand plots show the corresponding cross-correlation enhanced variants. Within approximately $\pm 50\ \frac{\text{Hz}}{\text{MHz}}$, the uniform color indicates that the estimated distance remains constant and LOS detection is reliable. The measured results are consistent with the simulation results in Section III-B, with a horizontal shift attributed to the additional CFO contributed by the hardware, which is added to the software-controlled CFO.

VI. DISCUSSION AND CONCLUSION

This paper demonstrates that CFOSD is pronounced in devices equipped with low-cost crystal oscillators with loose tolerances and stability, and that CFOSD introduces a systematic bias in MCPD distance estimation using the standard TD. Based on a signal model for the standard TD, a closed-form expression for the distance error is derived, revealing a dominant bias term determined by CFOSD and the sampling time offset difference ΔT_o.

To mitigate CFOSD-induced bias, two TD design approaches are proposed. Simulation results with CFOSD sweep and additive noise show that TDCA-based methods suppress CFOSD-induced terms over a wide CFOSD range and achieve nearly zero bias, at the cost of longer measurement duration, increased sensitivity to timing asynchronization, and higher SNR requirements. In contrast, RSA-based methods reverse the roles of INIT and REF across carrier frequencies according to a role pattern *RP*, preserve the measurement duration of the standard TD, reduce CFOSD sensitivity within a CFOSD operating range, and require only a modest increase in SNR requirements compared to the standard TD. A cross-correlation peak-search enhancement further improves LOS selection for RSA-based methods and extends the effective CFOSD operating range.

Experimental validation is performed with standard TD and RSA-based TD design methods. Different CFOSD values are generated by applying frequency-varying CFO at REF in software. The measured CIRs closely match the simulated results in both peak structure and peak locations. Results from the CFOSD sweep confirm the linear dependence of the estimated distance on CFOSD for standard TD, while the proposed methods, particularly AR1-XC, AR2-XC, and PLFRSM-XC, maintain an approximately constant distance estimate within their optimal operating ranges.

Table 5 provides a qualitative comparison of the TD designs considered, based on analytical and simulation results. A longer measurement duration increases energy consumption and the probability of interference, reduces the refresh rate of distance updates and the data throughput available for transmission, and imposes a stricter coherence time requirement, which can limit performance under mobility or fast channel variation.

Although the signal model and validation consider a single-path channel, the expected behavior in a multipath channel follows directly from the given signal model. The asynchronization-induced phase term is common to all path components at a given carrier because it is generated by the transceiver oscillators rather than by propagation. Consequently, (16) can be extended to a multipath channel scenario by replacing the single exponential describing the propagation phase shift with a sum of complex path contributions over all path components at that carrier, while the asynchronization-induced terms remain unchanged. From the CFR-to-CIR relationship (18), it follows that the asynchronization-induced artificial peaks in the CIR are present for each path component. A detailed analysis is left for future work.

The choice of an optimal *RP* for RSA depends on the application. The *RP*s proposed in this paper primarily illustrate how different designs affect the CIR and how distance estimation is influenced by CFOSD. Future work will investigate *RP* designs that are more robust to CFOSD and Δf_0 variations, and will study the joint optimization of *RP* and FSP to improve robustness to both CFOSD and timing asynchronization.

REFERENCES

[1] K. Wu, J. Pegoraro, F. Meneghello, J. A. Zhang, J. O. Lacruz, J. Widmer, F. Restuccia, M. Rossi, X. Huang, D. Zhang, G. Caire, and Y. J. Guo, "Sensing in bistatic ISAC systems with clock asynchronism: A signal processing perspective," *IEEE Signal Process. Mag.*, vol. 41, no. 5, pp. 31–43, Sep. 2024.

[2] H. Ólafsdóttir, A. Ranganathan, and S. Capkun, "On the security of carrier phase-based ranging," in *Cryptographic Hardware and Embedded Systems—CHES 2017*, vol. 10529, W. Fischer and N. Homma, Eds., Cham, Switzerland: Springer, Aug. 2017, pp. 490–509.

[3] J. A. Zhang, K. Wu, X. Huang, Y. J. Guo, D. Zhang, and R. W. Heath Jr., "Integration of radar sensing into communications with asynchronous transceivers," *IEEE Commun. Mag.*, vol. 60, no. 11, pp. 106–112, Nov. 2022.

[4] Z. Bin Tariq, J. P. Van Marter, A. G. Dabak, N. Al-Dhahir, and M. Torlak, "Reduced complexity deep learning approach for Bluetooth ranging in multipath environments," *IEEE Sensors J.*, vol. 24, no. 19, pp. 31431–31441, Oct. 2024.

[5] W. Kluge and E. Sachse, "Circuit and method for distance measurement between two nodes of a radio network," U.S. Patent 20 110 006 942 A1, Jan. 2011. [Online]. Available: https://patents.google.com/patent/US20110006942A1/en

[6] K. Balakrishnan, R. Dhanalakshmi, B. B. Sinha, and R. Gopalakrishnan, "Clock synchronization in industrial Internet of Things and potential works in precision time protocol: Review, challenges and future directions," *Int. J. Cognit. Comput. Eng.*, vol. 4, pp. 205–219, Jun. 2023.

[7] A. A. Nasir, S. Durrani, H. Mehrpouyan, S. D. Blostein, and R. A. Kennedy, "Timing and carrier synchronization in wireless communication systems: A survey and classification of research in the last 5 years," *EURASIP J. Wireless Commun. Netw.*, vol. 2016, no. 1, p. 180, Dec. 2016.

[8] M. Pelka, D. Amann, M. Cimdins, and H. Hellbriick, "Evaluation of time-based ranging methods: Does the choice matter?" in *Proc. 14th Workshop Positioning, Navigat. Commun. (WPNC)*, Oct. 2017, pp. 1–6.

[9] I. Kravets, N. Kotliar, O. Karpin, and A. Luchechko, "BLE phase-based ranging: Accuracy and capability under strong Wi-Fi interference," *Int. J. Electron. Telecommun.*, vol. 71, no. 3, pp. 1–7, 2025, doi: 10.24425/ijet.2025.153626.

[10] A. Santra, I. Kravets, N. Kotliar, and A. Pandey, "Enhancing Bluetooth channel sounding performance in complex indoor environments," *IEEE Sensors Lett.*, vol. 8, no. 10, pp. 1–4, Oct. 2024.

[11] Y. Schröder and L. Wolf, "InPhase: Phase-based ranging and localization," *ACM Trans. Sensor Netw.*, vol. 18, no. 2, pp. 1–39, Jan. 2022.

[12] M. Nikodem, G. Trajnowicz, G. S. de Blasio, and F. A. Quesada-Arencibia, "Experimental evaluation of multicarrier phase difference localization in Bluetooth low energy," *IEEE Sensors J.*, vol. 25, no. 1, pp. 1548–1560, Jan. 2025.

[13] S. Cortesi, C. Vogt, and M. Magno, "Comparison between an RSSI- and an MCPD-based BLE indoor localization system," *Computers*, vol. 12, no. 3, p. 59, Mar. 2023.

[14] M. Gunia, A. Zinke, N. Joram, and F. Ellinger, "Setting up a phase-based positioning system using off-the-shelf components," in *Proc. 14th Workshop Positioning, Navigat. Commun. (WPNC)*, Oct. 2017, pp. 1–6.

[15] P. Zand, J. Romme, J. Govers, F. Pasveer, and G. Dolmans, "A high-accuracy phase-based ranging solution with Bluetooth low energy (BLE)," in *Proc. IEEE Wireless Commun. Netw. Conf. (WCNC)*, Apr. 2019, pp. 1–8.

[16] P. Zand, A. Duzen, J. Romme, J. Govers, C. Bachmann, and K. Philips, "A high-accuracy concurrent phase-based ranging for large-scale dense BLE network," in *Proc. IEEE 30th Annu. Int. Symp. Pers., Indoor Mobile Radio Commun. (PIMRC)*, Sep. 2019, pp. 1–7.

[17] A. Duzen, "Implementation and evaluation of phase-based group ranging and localization with BLE," M.S. thesis, Dept. Elect. Eng., Electron. Syst. Res. Group, Eindhoven Univ. Technol., Eindhoven, The Netherlands, Aug. 2019.

[18] M. Pelka, C. Bollmeyer, and H. Hellbruck, "Accurate radio distance estimation by phase measurements with multiple frequencies," in *Proc. Int. Conf. Indoor Positioning Indoor Navigat. (IPIN)*, Oct. 2014, pp. 142–151.

[19] A. Simončič, G. Morano, A. Hrovat, and T. Javornik, "Optimizing frequency switching pattern to reduce asynchronization effect in MCPD ranging systems," *IEEE Access*, vol. 13, pp. 169791–169811, 2025.

[20] M. Oshiro, S. Otaka, T. Kato, K. Nonin, M. Nishikawa, Y. Nito, H. Ishiwata, and H. Yoshida, "Sub-GHz phase-based ranging system: Implementation and evaluation," in *Proc. IEEE 91st Veh. Technol. Conf. (VTC-Spring)*, Belgium, May 2020, pp. 1–7.

[21] *IEEE Standard for Low-Rate Wireless Networks—Amendment 1: Enhanced Ultra Wideband (UWB) Physical Layers (PHYs) and Associated Ranging Techniques*, IEEE Standard Std 802.15.4z-2020, Aug. 2020, pp. 1–174.

[22] J. Ma, F. Zhang, B. Jin, C. Su, S. Li, Z. Wang, and J. Ni, "Push the limit of highly accurate ranging on commercial UWB devices," *Proc. ACM Interact., Mobile, Wearable Ubiquitous Technol.*, vol. 8, no. 2, pp. 1–27, May 2024.

[23] D. Neirynck, E. Luk, and M. McLaughlin, "An alternative double-sided two-way ranging method," in *Proc. 13th Workshop Positioning, Navigat. Commun. (WPNC)*, Oct. 2016, pp. 1–4.

[24] M. Kwak and J. Chong, "A new double two-way ranging algorithm for ranging system," in *Proc. 2nd IEEE InternationalConference Netw. Infrastructure Digit. Content*, Sep. 2010, pp. 470–473.

[25] Y. Jiang and V. C. M. Leung, "An asymmetric double sided two-way ranging for crystal offset," in *Proc. Int. Symp. Signals, Syst. Electron.*, Jul. 2007, pp. 525–528.

[26] J. X. Lee, Z. Lin, and F. C. P. Shin, "Symmetric double side two way ranging with unequal reply time," in *Proc. IEEE 66th Veh. Technol. Conf.*, Sep. 2007, pp. 1980–1983.

[27] M. A. Shalaby, C. C. Cossette, J. R. Forbes, and J. Le Ny, "Reducing two-way ranging variance by signal-timing optimization," *IEEE Trans. Aerosp. Electron. Syst.*, vol. 60, no. 3, pp. 3718–3724, Jun. 2024.

[28] M. Pelka and H. Hellbruck, "S-TDoA-sequential time difference of arrival—A scalable and synchronization free approach forl positioning," in *Proc. IEEE Wireless Commun. Netw. Conf.*, Apr. 2016, pp. 1–6.

[29] Y. Lin, T. Guo, M. Guo, and Y. Fu, "Motion compensation for SAA FMCW radar based on specific switching scheme," *Appl. Sci.*, vol. 9, no. 17, p. 3441, Aug. 2019.

[30] Y. Lin, K. Yang, M. Guo, and Y. Fu, "Elimination of motion-induced phase based on double-time switching scheme for SAA FMCW radar," *Electronics*, vol. 8, no. 7, p. 786, Jul. 2019.
[31] P. Feil, "Optimizing switching sequence in the case of switched antenna arrays," U.S. Patent 20 120 182 174 A1, Jul. 2012. Accessed: Feb. 16, 2026. [Online]. Available: https://patents.google.com/patent/US20120182174A1/en
[32] C. Hu, Y. Liu, H. Meng, and X. Wang, "Randomized switched antenna array FMCW radar for automotive applications," *IEEE Trans. Veh. Technol.*, vol. 63, no. 8, pp. 3624–3641, Oct. 2014.
[33] A. Al-Ameri, J. Park, J. Sanchez, X. Cai, and F. Tufvesson, "A hybrid antenna switching scheme for dynamic channel sounding," in *Proc. IEEE 97th Veh. Technol. Conf. (VTC-Spring)*, Jun. 2023, pp. 1–6.
[34] R. Wang, O. Renaudin, C. U. Bas, S. Sangodoyin, and A. F. Molisch, "On channel sounding with switched arrays in fast time-varying channels," *IEEE Trans. Wireless Commun.*, vol. 18, no. 8, pp. 3843–3855, Aug. 2019.
[35] T. Pedersen, C. Pedersen, X. Yin, B. H. Fleury, R. R. Pedersen, B. Bozinovska, A. Hviid, P. Jourdan, and A. Stucki, "Joint estimation of Doppler frequency and directions in channel sounding using switched Tx and Rx arrays," in *Proc. IEEE Global Telecommun. Conf.*, vol. 4, Nov. 2004, pp. 2354–2360.
[36] T. Pedersen, C. Pedersen, X. Yin, and B. H. Fleury, "Optimization of spatiotemporal apertures in channel sounding," *IEEE Trans. Signal Process.*, vol. 56, no. 10, pp. 4810–4824, Oct. 2008.
[37] J. Sanchez, X. Cai, A. Al-Ameri, and F. Tufvesson, "Low-complexity optimization of antenna switching schemes for dynamic channel sounding," *IEEE Trans. Wireless Commun.*, vol. 25, pp. 7729–7743, 2026.
[38] A. Simončič, K. Guan, G. Morano, A. Švigelj, A. Hrovat, T. Kocevska, and T. Javornik, "Experimental evaluation of enhanced antenna switching for CFO mitigation in DoA estimation," *IEEE Open J. Antennas Propag.*, vol. 6, pp. 1022–1036, 2025.
[39] P. Avital, G. Chardon, and J. Picheral, "Design of switching sequences for sine parameters estimation on switched antenna arrays," *Signal Process.*, vol. 188, Nov. 2021, Art. no. 108244.
[40] Atmel Corporation. (2016). *AT86RF215 Datasheet*. Accessed: Oct. 15, 2025. [Online]. Available: https://www.microchip.com/en-us/product/at86rf215
[41] Y. Xie, Z. Li, and M. Li, "Precise power delay profiling with commodity Wi-Fi," *IEEE Trans. Mobile Comput.*, vol. 18, no. 6, pp. 1342–1355, Jun. 2019.
[42] G. Morano, A. Simončič, T. Kocevska, T. Javornik, and A. Hrovat, "Distance- and angle-based hybrid localization integrated in the IEEE 802.15.4 TSCH communication protocol," *Sensors*, vol. 24, no. 12, p. 3925, Jun. 2024.



ALEŠ SIMONČIČ (Student Member, IEEE) received the B.Sc. and M.Sc. degrees in electrical engineering from the University of Ljubljana, in 2019 and 2022, respectively. He is currently pursuing the Ph.D. degree in information and communication technologies with the Jožef Stefan International Postgraduate School.

He is currently a Young Researcher with the Department of Communication Systems, Jožef Stefan Institute, Ljubljana. His master's thesis focused on the estimation of the angle of arrival using BLE technology and antenna arrays. His research interests include radio communication systems, particularly protocols, antennas and arrays, direction of arrival estimation methods, embedded systems, and radio environment characterization.



GREGA MORANO (Graduate Student Member, IEEE) received the M.Sc. degree in electrical engineering from the University of Ljubljana, in 2021. He is currently pursuing the Ph.D. degree in information and communication technologies with the Jožef Stefan International Postgraduate School.

He is currently a Research Assistant with the Department of Communication Systems, Jožef Stefan Institute, Ljubljana. His research interests include the IoT communication protocols, wireless localization, integrated sensing and communication, embedded systems, wireless sensor networks, and wireless experimental testbeds.



ANDREJ HROVAT (Member, IEEE) received the B.Sc. and M.Sc. degrees in electrical engineering from the University of Ljubljana, in 2004 and 2008, and the Ph.D. degree from the Jožef Stefan International Postgraduate School, in 2011.

Since 2004, he has been with the Department of Communication Systems, Jožef Stefan Institute. He is currently holding the position of a Senior Research Fellow. He works on several projects connected with professional mobile communication systems, 2G-5G, WiFi and the IoT technologies, satellite and sensor networks, including several COST actions, Framework Program projects, H2020 Projects, European Space Agency (ESA) Projects, and numerous national research and application projects. He is the author or co-author of more than 120 peer-reviewed journal and conference papers. His research and working experience are in telecommunications, focusing on development and performance analysis for fixed and mobile systems, including terrestrial, stratospheric, and satellite systems, and radio-channel modeling for fixed and mobile narrowband and broadband radio communication systems. He is a TCP member for various international conferences and workshops. He serves as a journal editorial board member and the guest editor. He is a reviewer for several international impact-factor journals.



TOMAŽ JAVORNIK (Member, IEEE) received the B.Sc., M.Sc., and Ph.D. degrees in electrical engineering from the University of Ljubljana, Ljubljana, Slovenia, in 1987, 1990, and 1993, respectively.

He is currently a Scientific Counsellor with the Communication Systems Department, Jožef Stefan Institute, Ljubljana, and an Assistant Professor with the Jožef Stefan International Postgraduate School, Ljubljana. He participated in several COST and Framework Programme Projects. He has co-authored more than 100 refereed journal and conference papers and several books and book chapters in mobile and wireless communications. He holds two international patents. His research experience interests include telecommunications, focusing on the development and performance analysis of fixed and mobile systems, radio-channel measurements, modeling and simulations, and indoor localization. He serves as a TPC member or a reviewer for several IEEE conferences and journals.

Chapter 6

Conclusions and Future Work

This dissertation investigated the measurement stage of localization using phase-based approaches implemented on low-cost radios subject to hardware non-idealities that introduce phase errors and systematic estimation bias. The work focused on two phase-based measurement approaches for localization-relevant spatial quantities: (1) DoA estimation with SAA and single-RF-chain architectures, and (2) distance estimation with MCPD ranging. These approaches were chosen because they enable accurate direction and distance estimation in indoor environments, can operate with simple, low-cost transceiver architectures, and can be integrated into widely deployed communication devices. This supports scalable localization systems and aligns with ISAC concepts based on shared hardware and signals. Since both approaches rely on measured phase, the dissertation examined the dominant hardware-related impairments that distort phase measurements and bias the estimated sensing parameters.

6.1 Summary of the Dissertation, Addressed Hypotheses, and Scientific Contributions

The first part of the dissertation addressed DoA estimation with single-RF-chain architectures, where an SAA is required to obtain spatial samples for direction finding. Specifically, the work in Chapter 2 examined phase errors introduced by the RF implementation of the SAA. Hypothesis **H1** concerned the achievable DoA accuracy of a practical SAA. The included paper supports **SC1** by presenting a complete SAA design workflow, including array geometry selection, simulation-driven optimization of array parameters, switching network design, high-frequency RF routing, antenna selection and tuning, and analysis of radiation-pattern distortions caused by the proximity of antenna elements to the array edge and to adjacent elements. Throughout the design process, emphasis was placed on minimizing phase distortions across switched antenna elements and RF paths so that the resulting SAA achieves accurate DoA estimation without requiring calibration after fabrication. **SC1** was further supported by experimental validation. Outdoor experiments confirmed that the designed SAA achieves sub-degree DoA accuracy, consistent with hypothesis **H1**. Indoor validation showed that estimation performance depends on the frequency channel and that some BLE channels can exhibit increased error under strong multipath. The results also showed that combining DoA estimates across multiple channels can improve robustness to multipath. However, measurement scenarios designed to exhibit strong multipath propagation resulted in errors slightly above one degree, indicating that severe multipath remains challenging to fully mitigate through channel diversity alone.

Next, asynchronization-induced bias in DoA estimation with single-RF-chain architectures was analyzed, particularly the influence of CFO on direction estimates resulting from non-ideal crystal oscillators. The papers included in Chapter 3 addressed hypothesis **H2** and supported contribution **SC2.1** by formulating the systematic bias mechanism under sequential geometric sampling of antenna elements in the presence of CFO and by showing how the induced phase errors can correlate with DoA-dependent phase terms. The stated hypothesis **H3** and contribution **SC2.2** were addressed by proposing an efficient asynchronization-mitigation approach based on ASP optimization, which does not require explicit estimation and correction of phase errors or joint parameter estimation, making it suitable for resource-constrained devices. Two ASP design methods for ULA and UCA configurations were proposed and evaluated through numerical simulations across CFO and noise levels, as well as through experimental validation, supporting **SC2.3** and **SC2.4**. The results showed that the proposed approach mitigates bias within the identified CFO operating bounds specific to each ASP. Extending the CFO operating range was proposed through an initial coarse CFO estimation and correction step.

Since DoA estimation benefits from frequency diversity to improve robustness in multipath-rich environments, the dissertation then transitioned to phase-based distance estimation using the MCPD method, which inherently uses multiple carrier frequencies and naturally complements DoA estimation with frequency diversity or serves as a standalone source of localization-relevant spatial information. Because MCPD ranging is also based on carrier-phase measurements, the dissertation further examined how asynchronization between devices affects the measured phase and, consequently, distance estimation. A signal model that accounts for asynchronization between devices was derived in Chapter 4, showing that the SFO difference between devices alters the sampling times at the initiator and reflector. It was shown that under the conventional SSW FSP, this induces a linear phase-error trend across carrier frequencies that correlates with the distance-induced phase shifts and biases the distance estimate, thereby supporting hypothesis **H2** and contribution **SC3.1**. The work further showed that the choice of FSP determines how asynchronization-induced phase errors are mapped onto carrier frequencies, meaning that the per-carrier phase-error magnitude can be influenced through FSP design. Based on this observation, the work proposed optimizing the FSP so that the resulting phase-error pattern across carrier frequencies exhibits an approximately zero linear trend and thereby mitigating distance-estimation bias, addressing hypothesis **H4** and supporting **SC3.2**. Compared to estimation and correction of phase errors or joint parameter estimation approaches, the proposed approach provides a lightweight mitigation strategy suitable for resource-constrained devices. A set of structured FSPs was developed to realize this principle, supporting **SC3.3**. Changing the FSP reshapes the phase-error profile across carrier frequencies, so each FSP affects the estimated CIR in a distinct way and can introduce artificial peaks whose magnitude and position depend on both the asynchronization level and the selected FSP. If an artificial peak exceeds the true propagation peak and the distance-estimation algorithm searches only for the largest peak, an estimation error occurs. This behavior defines FSP-dependent asynchronization bounds within which a given FSP performs optimally. The proposed FSPs were evaluated through numerical simulations across SFO mismatch conditions, different numbers of carriers, and SNR values, as well as through experimental validation, supporting **SC3.4**. The results demonstrate robust performance within the FSP-dependent asynchronization bounds and reduced systematic bias relative to the SSW FSP.

Another source of distance-estimation bias in MCPD ranging is the linear dependence of CFO on carrier frequency resulting from PLL-based RF carrier generation with crystal oscillator reference error. In Chapter 5, a signal model for MCPD ranging with the

standard TD was derived, accounting for the linear dependence of CFO on carrier frequency. The analysis showed that differences in CFO slopes between devices, denoted as CFOSD, introduce a linear phase-error trend across carriers that biases MCPD distance estimates, addressing hypothesis **H5** and supporting contribution **SC4.1**. This bias cannot be mitigated by carrier reordering through FSP optimization. Based on the analysis of the dominant phase terms responsible for CFOSD-induced bias, two TD design approaches for bias mitigation suitable for resource-constrained devices were proposed, further addressing hypothesis **H5** and supporting **SC4.2**. In the TDCA, additional phase samples are acquired at the initiator or at both devices and combined to structurally suppress the dominant CFOSD-induced phase component. In contrast, the RSA modifies the TD by reversing the initiator and reflector roles across carrier frequencies according to a RP. With a properly designed RP, CFOSD-induced phase terms are decoupled from propagation-induced phase terms. The proposed TDs were evaluated through numerical simulations across different CFOSD values and noise conditions, including combinations with different FSPs, and through experimental validation using a controlled CFOSD sweep, supporting **SC4.3**. The results showed improved robustness of the proposed TDs to CFOSD compared with the standard TD in both simulations and experimental validation. The evaluation also highlighted approach-specific trade-offs. Although TDCA can achieve high accuracy over a broader range of CFOSD values, its longer measurement routine increases sensitivity to timing asynchronization and interference, and reduces practical suitability due to higher energy consumption and a lower refresh rate. In contrast, RSA preserves the measurement duration of the standard TD but can be more susceptible to induced artificial peaks in the estimated CIR because changing the RP reshapes the phase-error profile across carriers. The magnitude of these artificial peaks depends strongly on the difference in the initial CFO values at the lowest carrier frequency. To improve the robustness of LoS peak detection under unfavorable conditions, a refined peak-search procedure was proposed for more reliable distance estimation.

6.2 Future Work

The results presented in the dissertation motivate several directions for future work to further strengthen both the theoretical understanding and practical applicability of considered phase-based direction- and distance-estimation approaches.

Improved MCPD ranging. Future work on MCPD ranging should address tighter integration with practical protocol constraints. Applying the proposed asynchronization mitigation approaches to emerging BLE channel sounding procedures introduces additional constraints, such as dynamic carrier selection and the omission of carriers with low SNR. In such scenarios, switching patterns and timing designs should adapt to variable carrier availability while preserving bias mitigation properties.

MCPD ranging would also benefit from a Cramér–Rao lower bound analysis to quantify the best achievable accuracy under realistic noise assumptions. Such an analysis could guide the selection of key parameters, including the number of samples per carrier, the number of carriers, and the total spanned bandwidth, and would clarify trade-offs among noise sensitivity, measurement duration, and estimation variance.

TD optimization based on role switching can be further improved. Sensitivity to the initial CFO values at the start of the measurement band could be reduced by acquiring multiple samples at the first carrier, estimating the associated phase jumps, and applying a correction to subsequent carriers.

Extensions to cooperative and group-ranging scenarios are also of practical interest for localization systems. In group ranging with multiple devices, some protocols reduce

airtime by allowing multiple receivers to listen simultaneously and then scheduling individual reflector responses [67]. In such settings, the delay between reception and response depends on the response order and can become large, increasing the sensitivity to timing asynchronization. The next research step is to investigate whether scheduling strategies, conceptually analogous to FSP optimization, can reduce systematic timing-induced bias through the design of reflector-response order.

Extended evaluation in realistic environments and at system level. The proposed mitigation approaches for phase error induced by asynchronization in single-RF-chain DoA estimation and MCPD ranging were evaluated under controlled single-path scenarios to isolate the effect of asynchronization. A broader study in realistic and dynamic environments remains important. This includes extending the analytical models beyond single-path assumptions to multipath channels and evaluating estimator performance when the LoS component is not dominant. Another research direction is system-level evaluation, where multiple DoA estimates, multiple distance estimates, or joint DoA and distance estimates are fused to localize targets in space, and end-to-end localization accuracy is quantified under representative deployment conditions.

Joint optimization across design dimensions. Joint optimization across design dimensions is another promising direction. In single-RF-chain DoA estimation, ASP design can be co-optimized with estimator selection and practical constraints such as switching time and the number of acquired samples. A deeper analysis of the pseudospectrum under different ASPs is also needed, with the goal of translating this analysis into practical design guidelines. In MCPD ranging, the dissertation analyzed timing asynchronization and frequency-dependent CFO as separate effects to clarify their individual influence on distance estimation and the corresponding mitigation approaches. In practical systems, both effects are present simultaneously, so joint optimization of FSP and TD is expected to further improve robustness and reduce sensitivity to combined impairments.

Suppression of artificial spectral peaks. Switching-based mitigation methods for asynchronization in DoA estimation with ASP and in MCPD ranging with FSP and TD introduce artificial peaks in the computed spectra used for DoA or distance estimation. Future work could investigate methods for suppressing these artificial peaks in the estimated spectra. One possible approach is to design complementary switching methods so that their artificial peaks appear at different positions in the estimated spectrum, and then combine the resulting spectra so that stable peaks correspond to physical propagation components, while shifted peaks can be identified as artifacts and suppressed.

Secure phase-based localization. Secure localization is an important research direction. DoA estimation and MCPD ranging should remain reliable under adversarial conditions, including spoofing, replay, meaconing, jamming, and coordinated interference. Future work could investigate threat models specific to phase-based sensing, develop lightweight consistency checks, and explore protocol-level defenses that reduce the feasibility of structured attacks without significantly increasing overhead.

References

[1] A. Bensky, *Wireless Positioning Technologies and Applications* (GNSS Technology and Applications Series). Boston: Artech house, 2008, ISBN: 978-1-59693-130-5.

[2] A. Abraha and B. Wang, "A Survey on Scalable Wireless Indoor Localization: Techniques, Approaches and Directions," *Wireless Personal Communications*, vol. 136, pp. 1–42, Jun. 27, 2024. DOI: 10.1007/s11277-024-11300-2.

[3] L.-P. Tian, L.-Q. Chen, Z.-M. Xu, and Z. (Chen, "A Localization and Tracking System Using Single WiFi Link," *Remote Sensing*, vol. 15, no. 9, p. 2461, Jan. 2023, ISSN: 2072-4292. DOI: 10.3390/rs15092461.

[4] T. Savic, X. Vilajosana, and T. Watteyne, "Constrained Localization: A Survey," *IEEE Access*, vol. 10, pp. 1–1, May 2, 2022. DOI: 10.1109/ACCESS.2022.3171859.

[5] Y. Cui, F. Liu, X. Jing, and J. Mu, "Integrating Sensing and Communications for Ubiquitous IoT: Applications, Trends, and Challenges," *IEEE Network*, vol. 35, no. 5, pp. 158–167, Sep. 2021, ISSN: 1558-156X. DOI: 10.1109/MNET.010.2100152.

[6] L. Zhang and H. Wang, "Device-Free Tracking via Joint Velocity and AOA Estimation With Commodity WiFi," *IEEE Sensors Journal*, vol. 19, no. 22, pp. 10 662–10 673, Nov. 2019, ISSN: 1558-1748. DOI: 10.1109/JSEN.2019.2929580.

[7] D. Vasisht, S. Kumar, and D. Katabi, "Decimeter-level localization with a single WiFi access point," in *Proceedings of the 13th Usenix Conference on Networked Systems Design and Implementation*, ser. NSDI'16, USA: USENIX Association, Mar. 16, 2016, pp. 165–178, ISBN: 978-1-931971-29-4.

[8] F. Zafari, A. Gkelias, and K. K. Leung, "A Survey of Indoor Localization Systems and Technologies," *IEEE Communications Surveys & Tutorials*, vol. 21, no. 3, pp. 2568–2599, 2019, ISSN: 1553-877X. DOI: 10.1109/COMST.2019.2911558.

[9] A. Sesyuk, S. Ioannou, and M. Raspopoulos, "A Survey of 3D Indoor Localization Systems and Technologies," *Sensors*, vol. 22, p. 9380, Dec. 1, 2022. DOI: 10.3390/s22239380.

[10] H. Liu, H. Darabi, P. Banerjee, and J. Liu, "Survey of Wireless Indoor Positioning Techniques and Systems," *IEEE Transactions on Systems, Man, and Cybernetics, Part C (Applications and Reviews)*, vol. 37, no. 6, pp. 1067–1080, Nov. 2007, ISSN: 1558-2442. DOI: 10.1109/TSMCC.2007.905750.

[11] P. Yadav and S. C. Sharma, "Unveiling the Cutting Edge: A Comprehensive Survey of Localization Techniques in WSN, Leveraging Optimization and Machine Learning Approaches," *Wireless Personal Communications*, vol. 132, no. 4, pp. 2293–2362, Oct. 1, 2023, ISSN: 1572-834X. DOI: 10.1007/s11277-023-10630-x.

[12] Y. Gu, A. Lo, and I. Niemegeers, "A survey of indoor positioning systems for wireless personal networks," *IEEE Communications Surveys & Tutorials*, vol. 11, no. 1, pp. 13–32, 2009, ISSN: 1553-877X. DOI: 10.1109/SURV.2009.090103.

[13] S. Pandey and P. Agrawal, "A survey on localization techniques for wireless networks," *Journal of the Chinese Institute of Engineers*, vol. 29, no. 7, pp. 1125–1148, Oct. 1, 2006, ISSN: 0253-3839. DOI: 10.1080/02533839.2006.9671216.

[14] S. Kuutti, S. Fallah, K. Katsaros, M. Dianati, F. Mccullough, and A. Mouzakitis, "A Survey of the State-of-the-Art Localization Techniques and Their Potentials for Autonomous Vehicle Applications," *IEEE Internet of Things Journal*, vol. 5, no. 2, pp. 829–846, Apr. 2018, ISSN: 2327-4662. DOI: 10.1109/JIOT.2018.2812300.

[15] S. He and S.-H. G. Chan, "Wi-Fi Fingerprint-Based Indoor Positioning: Recent Advances and Comparisons," *IEEE Communications Surveys & Tutorials*, vol. 18, no. 1, pp. 466–490, 2016, ISSN: 1553-877X. DOI: 10.1109/COMST.2015.2464084.

[16] G. Morano, A. Simončič, T. Kocevska, T. Javornik, and A. Hrovat, "Distance- and Angle-Based Hybrid Localization Integrated in the IEEE 802.15.4 TSCH Communication Protocol," *Sensors*, vol. 24, no. 12, p. 3925, Jan. 2024, ISSN: 1424-8220. DOI: 10.3390/s24123925.

[17] F. Wen and C. Liang, "Fine-Grained Indoor Localization Using Single Access Point With Multiple Antennas," *IEEE Sensors Journal*, vol. 15, no. 3, pp. 1538–1544, Mar. 2015, ISSN: 1558-1748. DOI: 10.1109/JSEN.2014.2364121.

[18] K. Qian, C. Wu, Y. Zhang, G. Zhang, Z. Yang, and Y. Liu, "Widar2.0: Passive Human Tracking with a Single Wi-Fi Link," in *Proceedings of the 16th Annual International Conference on Mobile Systems, Applications, and Services*, ser. MobiSys '18, New York, NY, USA: Association for Computing Machinery, Jun. 10, 2018, pp. 350–361, ISBN: 978-1-4503-5720-3. DOI: 10.1145/3210240.3210314.

[19] S. M. Lanzisera and K. Pister, "RF Ranging for Location Awareness," EECS Department, University of California, Berkeley, May 2009. [Online]. Available: http://www2.eecs.berkeley.edu/Pubs/TechRpts/2009/EECS-2009-69.html.

[20] R. C. Shit et al., "Ubiquitous Localization (UbiLoc): A Survey and Taxonomy on Device Free Localization for Smart World," *IEEE Communications Surveys & Tutorials*, vol. 21, no. 4, pp. 3532–3564, Win. 2019, ISSN: 1553-877X, 2373-745X. DOI: 10.1109/COMST.2019.2915923.

[21] J. Xiao, Z. Zhou, Y. Yi, and L. M. Ni, "A Survey on Wireless Indoor Localization from the Device Perspective," *ACM Computing Surveys*, vol. 49, no. 2, pp. 1–31, Jun. 30, 2017, ISSN: 0360-0300, 1557-7341. DOI: 10.1145/2933232.

[22] G. Deak, K. Curran, and J. Condell, "A survey of active and passive indoor localisation systems," *Computer Communications*, vol. 35, no. 16, pp. 1939–1954, Sep. 2012, ISSN: 01403664. DOI: 10.1016/j.comcom.2012.06.004.

[23] G. K. J. Fischer et al., "A Systematic Survey and Comparative Analysis of Angular-Based Indoor Localization and Positioning Technologies," *IEEE Communications Surveys & Tutorials*, vol. 28, pp. 3830–3869, 2026, ISSN: 1553-877X. DOI: 10.1109/COMST.2025.3567765.

[24] J. A. Zhang et al., "Enabling Joint Communication and Radar Sensing in Mobile Networks—A Survey," *IEEE Communications Surveys & Tutorials*, vol. 24, no. 1, pp. 306–345, 2022, ISSN: 1553-877X. DOI: 10.1109/COMST.2021.3122519.

[25] Z. Wei et al., "Integrated Sensing and Communication Signals Toward 5G-A and 6G: A Survey," *IEEE Internet of Things Journal*, vol. 10, no. 13, pp. 11 068–11 092, Jul. 2023, ISSN: 2327-4662. DOI: 10.1109/JIOT.2023.3235618.

[26] N. González-Prelcic et al., "The Integrated Sensing and Communication Revolution for 6G: Vision, Techniques, and Applications," *Proceedings of the IEEE*, vol. 112, no. 7, pp. 676–723, Jul. 2024, ISSN: 1558-2256. DOI: 10.1109/JPROC.2024.3397609.

[27] X. Zhu et al., "Enabling Intelligent Connectivity: A Survey of Secure ISAC in 6G Networks," *IEEE Communications Surveys & Tutorials*, vol. 27, no. 2, pp. 748–781, Apr. 2025, ISSN: 1553-877X. DOI: 10.1109/COMST.2024.3432871.

[28] T. Wild, V. Braun, and H. Viswanathan, "Joint Design of Communication and Sensing for Beyond 5G and 6G Systems," *IEEE Access*, vol. 9, pp. 30 845–30 857, 2021, ISSN: 2169-3536. DOI: 10.1109/ACCESS.2021.3059488.

[29] W. Zhou, R. Zhang, G. Chen, and W. Wu, "Integrated Sensing and Communication Waveform Design: A Survey," *IEEE Open Journal of the Communications Society*, vol. 3, pp. 1930–1949, 2022, ISSN: 2644-125X. DOI: 10.1109/OJCOMS.2022.3215683.

[30] Y. Xie, Z. Li, and M. Li, "Precise Power Delay Profiling with Commodity Wi-Fi," *IEEE Transactions on Mobile Computing*, vol. 18, no. 6, pp. 1342–1355, Jun. 2019, ISSN: 1558-0660. DOI: 10.1109/TMC.2018.2860991.

[31] J. P. Van Marter, M. Ben-Shachar, Y. Alpert, A. G. Dabak, N. Al-Dhahir, and M. Torlak, "A Multichannel Approach and Testbed for Centimeter-Level WiFi Ranging," *IEEE Journal of Indoor and Seamless Positioning and Navigation*, vol. 2, pp. 76–91, 2024, ISSN: 2832-7322. DOI: 10.1109/JISPIN.2024.3366850.

[32] Bluetooth SIG, Inc., "Bluetooth core specification, version 6.2," Bluetooth SIG, Inc., Nov. 2025. Accessed: Jan. 12, 2026. [Online]. Available: https://www.bluetooth.com/wp-content/uploads/Files/Specification/HTML/Core-62/out/en/index-en.html.

[33] "IEEE Standard for Information Technology – Telecommunications and Information Exchange Between Systems Local and Metropolitan Area Networks – Specific Requirements - Part 11: Wireless LAN Medium Access Control (MAC) and Physical Layer (PHY) Specifications - Amendment 4: Enhancements for Wireless LAN Sensing," *IEEE Std 802.11bf-2025 (Amendment to IEEE 802.11-2024, as amended by IEEE 802.11bh-2024, IEEE 802.11be-2024, and IEEE 802.11bk-2025)*, pp. 1–228, Sep. 2025. DOI: 10.1109/IEEESTD.2025.11184214.

[34] R. Du et al., "An Overview on IEEE 802.11bf: WLAN Sensing," *IEEE Communications Surveys & Tutorials*, vol. 27, no. 1, pp. 184–217, Feb. 2025, ISSN: 1553-877X. DOI: 10.1109/COMST.2024.3408899.

[35] F. Meneghello, C. Chen, C. Cordeiro, and F. Restuccia, "Toward Integrated Sensing and Communications in IEEE 802.11bf Wi-Fi Networks," *IEEE Communications Magazine*, vol. 61, no. 7, pp. 128–133, Jul. 2023, ISSN: 1558-1896. DOI: 10.1109/MCOM.001.2200806.

[36] Z. Chen, G. Gokeda, and Y. Yu, *Introduction to Direction-of-arrival Estimation*. Artech House, 2010, 193 pp., ISBN: 978-1-59693-089-6. Google Books: IsZQmAEACAAJ.

[37] D. Zhang, J.-d. Zhang, C. Cui, W. Wu, and D.-g. Fang, "Single RF Channel Digital Beamforming Array Antenna Based on Compressed Sensing for Large-Scale Antenna Applications," *IEEE Access*, vol. 6, pp. 4340–4351, 2018, ISSN: 2169-3536. DOI: 10.1109/ACCESS.2018.2800399.

[38] Z. Ying, K. Zhao, E. Bengtsson, H. Tataria, and F. Tufvesson, "Design of Switched Antenna Arrays for a 28 GHz Propagation Channel Sounder," in *2020 IEEE International Symposium on Antennas and Propagation and North American Radio Science Meeting*, Jul. 2020, pp. 55–56. DOI: 10.1109/IEEECONF35879.2020.9329997.

[39] O. Crisafulli et al., "Performance Analysis of BLE-5.1 Angle of Arrival Estimation Using Embedded Radiation Patterns on a 3 × 3 Uniform Rectangular Array," *IEEE Access*, vol. 12, pp. 42 572–42 584, 2024, ISSN: 2169-3536. DOI: 10.1109/ACCESS.2024.3379011.

[40] A. Florio, G. Avitabile, and G. Coviello, "A Linear Technique for Artifacts Correction and Compensation in Phase Interferometric Angle of Arrival Estimation," *Sensors*, vol. 22, no. 4, p. 1427, Jan. 2022, ISSN: 1424-8220. DOI: 10.3390/s22041427.

[41] Sesma Santos, Victor and Egorov, Victor, *Improved accuracy for indoor positioning with bluetooth 5.1: From theory to measurements*, 2020.

[42] F. A. Toasa, L. Tello-Oquendo, C. R. Peñafiel-Ojeda, and G. Cuzco, "Experimental Demonstration for Indoor Localization Based on AoA of Bluetooth 5.1 Using Software Defined Radio," in *2021 IEEE 18th Annual Consumer Communications & Networking Conference (CCNC)*, Jan. 2021, pp. 1–4. DOI: 10.1109/CCNC49032.2021.9369638.

[43] Z. Li, Z. Tian, Z. Wang, and Z. Zhang, "Multipath-Assisted Indoor Localization Using a Single Receiver," *IEEE Sensors Journal*, vol. 21, no. 1, pp. 692–705, Jan. 2021, ISSN: 1558-1748. DOI: 10.1109/JSEN.2020.3012786.

[44] Z. Bin Tariq, J. P. Van Marter, A. G. Dabak, N. Al-Dhahir, and M. Torlak, "Reduced Complexity Deep Learning Approach for Bluetooth Ranging in Multipath Environments," *IEEE Sensors Journal*, vol. 24, no. 19, pp. 31 431–31 441, Oct. 2024, ISSN: 1558-1748. DOI: 10.1109/JSEN.2024.3441596.

[45] Y. Schröder, D. Reimers, and L. Wolf, "Accurate and Precise Distance Estimation from Phase-Based Ranging Data," in *2018 International Conference on Indoor Positioning and Indoor Navigation (IPIN)*, Sep. 2018, pp. 1–8. DOI: 10.1109/IPIN.2018.8533871.

[46] W. Kluge and E. Sachse, "Circuit and method for distance measurement between two nodes of a radio network," U.S. Patent 20110006942A1, Jan. 13, 2011. Accessed: Apr. 29, 2025. [Online]. Available: https://patents.google.com/patent/US20110006942A1/en.

[47] M. Nikodem, G. Trajnowicz, G. Salvatore de Blasio, and F. Alexis Quesada-Arencibia, "Experimental Evaluation of Multicarrier Phase Difference Localization in Bluetooth Low Energy," *IEEE Sensors Journal*, vol. 25, no. 1, pp. 1548–1560, Jan. 2025, ISSN: 1558-1748. DOI: 10.1109/JSEN.2024.3495030.

[48] S. N. Shoudha, J. P. Van Marter, S. Helwa, A. G. Dabak, M. Torlak, and N. Al-Dhahir, "Reduced-Complexity Decimeter-Level Bluetooth Ranging in Multipath Environments," *IEEE Access*, vol. 10, pp. 38 335–38 350, 2022, ISSN: 2169-3536. DOI: 10.1109/ACCESS.2022.3165653.

[49] A. Santra, I. Kravets, N. Kotliar, and A. Pandey, "Enhancing Bluetooth Channel Sounding Performance in Complex Indoor Environments," *IEEE Sensors Letters*, vol. 8, no. 10, pp. 1–4, Oct. 2024, ISSN: 2475-1472. DOI: 10.1109/LSENS.2024.3456002.

[50] J. Mazur, "High-Resolution Phase-Based Ranging Using Inverse Fourier Transform in an Iterative Bayesian Approach," *Sensors*, vol. 24, no. 20, p. 6758, 20 Jan. 2024, ISSN: 1424-8220. DOI: 10.3390/s24206758.

[51] M.-I. Stanciu, J. Brillant, C. Rey, and K. Waheed, "Accurate Distance Measurement Using Narrowband Systems," in *2021 IEEE International Midwest Symposium on Circuits and Systems (MWSCAS)*, Aug. 2021, pp. 937–940. DOI: 10.1109/MWSCAS47672.2021.9531873.

[52] Y. Schröder, D. Reimers, and L. Wolf, "Accurate and Precise Distance Estimation from Phase-Based Ranging Data," in *2018 International Conference on Indoor Positioning and Indoor Navigation (IPIN)*, Sep. 2018, pp. 1–8. DOI: 10.1109/IPIN.2018.8533871.

[53] J. P. Van Marter, A. G. Dabak, N. Al-Dhahir, and M. Torlak, "Support Vector Regression for Bluetooth Ranging in Multipath Environments," *IEEE Internet of Things Journal*, vol. 10, no. 13, pp. 11 533–11 546, Jul. 2023, ISSN: 2327-4662. DOI: 10.1109/JIOT.2023.3244743.

[54] P. Boer, J. Romme, J. Govers, and G. Dolmans, "Performance of High-Accuracy Phase-Based Ranging in Multipath Environments," in *2020 IEEE 91st Vehicular Technology Conference (VTC2020-Spring)*, May 2020, pp. 1–5. DOI: 10.1109/VTC2020-Spring48590.2020.9128721.

[55] M. Oshiro et al., "Sub-GHz Phase-Based Ranging System: Implementation and Evaluation," in *2020 IEEE 91st Vehicular Technology Conference (VTC2020-Spring)*, Antwerp, Belgium: IEEE, May 2020, pp. 1–7, ISBN: 978-1-7281-5207-3. DOI: 10.1109/VTC2020-Spring48590.2020.9128575.

[56] H. Ólafsdóttir, A. Ranganathan, and S. Capkun. "On the Security of Carrier Phase-based Ranging." arXiv: 1610.06077 [cs], Accessed: Feb. 1, 2023. [Online]. Available: http://arxiv.org/abs/1610.06077, pre-published.

[57] Y. Xie, Z. Li, and M. Li, "Precise Power Delay Profiling with Commodity Wi-Fi," *IEEE Transactions on Mobile Computing*, vol. 18, no. 6, pp. 1342–1355, Jun. 2019, ISSN: 1558-0660. DOI: 10.1109/TMC.2018.2860991.

[58] J. Vig, "Introduction to Quartz Frequency Standards. Revision," *NASA STI/Recon Technical Report N*, vol. 93, p. 15 330, Sep. 30, 1992.

[59] F. Walls and J. Gagnepain, "Environmental sensitivities of quartz oscillators," *IEEE transactions on ultrasonics, ferroelectrics, and frequency control*, vol. 39, pp. 241–9, Feb. 1, 1992. DOI: 10.1109/58.139120.

[60] Vectron International, "Environmental influences on quartz oscillator short term stability," Vectron International (Microchip Technology Inc.), White Paper. Accessed: Jan. 14, 2026. [Online]. Available: https://ww1.microchip.com/downloads/aemDocuments/documents/VOP/ApplicationNotes/ApplicationNotes/Environmental+Influences+on+Quartz+Oscillator+Short+Term+Stability.pdf.

[61] S. Cloudt, "Bluetooth Low Energy Direction Finding on Embedded Hardware by Mitigating Carrier Frequency Offset and Multipath Fading," Mar. 22, 2021.

[62] G. Morano, A. Simončič, T. Kocevska, T. Javornik, and A. Hrovat, "Angle of Arrival Estimation Using IEEE 802.15.4 TSCH Protocol," in *2023 IEEE 34th Annual International Symposium on Personal, Indoor and Mobile Radio Communications (PIMRC)*, Sep. 2023, pp. 1–7. DOI: 10.1109/PIMRC56721.2023.10293886.

[63] L. Yao, "Bluetooth Direction Finding," M.S. thesis, Delft University of Technology, 2018. Accessed: Jan. 11, 2024. [Online]. Available: https://repository.tudelft.nl/islandora/object/uuid%3Ac07eb3a2-a303-4690-ac3e-e96f0064afcd.

[64] M. Pelka, C. Bollmeyer, and H. Hellbrück, "Accurate radio distance estimation by phase measurements with multiple frequencies," in *2014 International Conference on Indoor Positioning and Indoor Navigation (IPIN)*, Oct. 2014, pp. 142–151. DOI: 10.1109/IPIN.2014.7275478.

[65] A. Duzen, "Implementation and Evaluation of Phase-Based Group Ranging and Localization with BLE," M.S. thesis, Eindhoven University of Technology, 31.8.2019, 2019.

[66] P. Zand, J. Romme, J. Govers, F. Pasveer, and G. Dolmans, "A high-accuracy phase-based ranging solution with Bluetooth Low Energy (BLE)," in *2019 IEEE Wireless Communications and Networking Conference (WCNC)*, Apr. 2019, pp. 1–8. DOI: 10.1109/WCNC.2019.8885791.

[67] P. Zand, A. Duzen, J. Romme, J. Govers, C. Bachmann, and K. Philips, "A high-accuracy concurrent phase-based ranging for large-scale dense BLE network," in *2019 IEEE 30th Annual International Symposium on Personal, Indoor and Mobile Radio Communications (PIMRC)*, Sep. 2019, pp. 1–7. DOI: 10.1109/PIMRC.2019.8904093.

[68] J. Cheng, K. Guan, and F. Quitin, "Direction-of-Arrival Estimation With Virtual Antenna Array: Observability Analysis, Local Oscillator Frequency Offset Compensation, and Experimental Results," *IEEE Transactions on Instrumentation and Measurement*, vol. 70, pp. 1–13, 2021, ISSN: 1557-9662. DOI: 10.1109/TIM.2021.3088434.

[69] X. Qiu, B. Wang, J. Wang, and Y. Shen, "AOA-Based BLE Localization with Carrier Frequency Offset Mitigation," in *2020 IEEE International Conference on Communications Workshops (ICC Workshops)*, Jun. 2020, pp. 1–5. DOI: 10.1109/ICCWorkshops49005.2020.9145137.

[70] F. Quitin, V. Govindaraj, X. Zhong, and W. P. Tay, "Virtual Multi-Antenna Array for Estimating the Angle-of-Arrival of a RF Transmitter," in *2016 IEEE 84th Vehicular Technology Conference (VTC-Fall)*, Sep. 2016, pp. 1–5. DOI: 10.1109/VTCFall.2016.7881965.

[71] C.-C. Shen and W. Jhang, "Joint CFO and DOA Estimation Based on MVDR Criterion in Interleaved OFDMA/SDMA Uplink," *IEICE Transactions on Fundamentals of Electronics, Communications and Computer Sciences*, vol. E107.A, no. 7, pp. 1066–1070, Jul. 1, 2024, ISSN: 0916-8508, 1745-1337. DOI: 10.1587/transfun.2023EAL2064.

[72] A. Simončič, T. Javornik, A. Sešek, and A. Hrovat, "Direction of arrival estimation for BLE: Antenna array design and evaluation," *AEU - International Journal of Electronics and Communications*, vol. 168, p. 154 722, Aug. 1, 2023, ISSN: 1434-8411. DOI: 10.1016/j.aeue.2023.154722.

[73] A. Simončič, G. Morano, A. Švigelj, A. Hrovat, and T. Javornik, "Optimizing Switching Pattern to Reduce CFO Effects in Single RF Chain Direction Finding Systems," in *2024 7th International Balkan Conference on Communications and Networking (BalkanCom)*, Jun. 2024, pp. 113–118. DOI: 10.1109/BalkanCom61808.2024.10557208.

[74] A. Simončič et al., "Experimental Evaluation of Enhanced Antenna Switching for CFO Mitigation in DoA Estimation," *IEEE Open Journal of Antennas and Propagation*, vol. 6, no. 4, pp. 1022–1036, Aug. 2025, ISSN: 2637-6431. DOI: 10.1109/OJAP.2025.3558671.

[75] A. Simončič, G. Morano, A. Hrovat, and T. Javornik, "Optimizing Frequency Switching Pattern to Reduce Asynchronization Effect in MCPD Ranging Systems," *IEEE Access*, vol. 13, pp. 169 791–169 811, 2025, ISSN: 2169-3536. DOI: 10.1109/ACCESS.2025.3614753.

[76] A. Simončič, G. Morano, A. Hrovat, and T. Javornik, "Mitigating Frequency Dependent Carrier Frequency Offset in Multi-carrier Phase Difference Ranging through Timing Diagram Design," *IEEE Access*, pp. 1–1, 2026, ISSN: 2169-3536. DOI: 10.1109/ACCESS.2026.3665049.

Bibliography

Publications Related to the Thesis

Journal Articles

A. Simončič, T. Javornik, A. Sešek, and A. Hrovat, "Direction of arrival estimation for BLE: Antenna array design and evaluation," *AEU - International Journal of Electronics and Communications*, vol. 168, p. 154 722, Aug. 1, 2023, ISSN: 1434-8411. DOI: 10.1016/j.aeue.2023.154722.

A. Simončič et al., "Experimental Evaluation of Enhanced Antenna Switching for CFO Mitigation in DoA Estimation," *IEEE Open Journal of Antennas and Propagation*, vol. 6, no. 4, pp. 1022–1036, Aug. 2025, ISSN: 2637-6431. DOI: 10.1109/OJAP.2025.3558671.

A. Simončič, G. Morano, A. Hrovat, and T. Javornik, "Optimizing Frequency Switching Pattern to Reduce Asynchronization Effect in MCPD Ranging Systems," *IEEE Access*, vol. 13, pp. 169 791–169 811, 2025, ISSN: 2169-3536. DOI: 10.1109/ACCESS.2025.3614753.

A. Simončič, G. Morano, A. Hrovat, and T. Javornik, "Mitigating Frequency Dependent Carrier Frequency Offset in Multi-carrier Phase Difference Ranging through Timing Diagram Design," *IEEE Access*, pp. 1–1, 2026, ISSN: 2169-3536. DOI: 10.1109/ACCESS.2026.3665049.

Conference Paper

A. Simončič, G. Morano, A. Švigelj, A. Hrovat, and T. Javornik, "Optimizing Switching Pattern to Reduce CFO Effects in Single RF Chain Direction Finding Systems," in *2024 7th International Balkan Conference on Communications and Networking (BalkanCom)*, Jun. 2024, pp. 113–118. DOI: 10.1109/BalkanCom61808.2024.10557208.

Technical Documents

A. Simončič, T. Javornik, and A. Hrovat, "Uniform circular antenna array for direction of arrival estimation," in *COST INTERACT 4th MC and 4th Technical Meeting*, Dubrovnik, Croatia, Jan. 23, 2023.

A. Simončič, A. Hrovat, and T. Javornik, "Enhancing DoA accuracy in single RF chain systems through CFO-aware switching pattern," in *COST INTERACT 7th MC and 7th Technical Meeting*, Lisbon, Portugal, Jan. 22, 2024.

A. Simončič et al., "Performance evaluation of CFO-resilient switching patterns for accurate DoA estimation," in *COST INTEERACT 8th MC and 8th Technical Meeting*, Helsinki, Finland, Jun. 17, 2024.

Other Publications

Journal Articles

A. Simončič, M. Mohorčič, M. Mohorčič, and A. Hrovat, "Non-Intrusive Privacy-Preserving Approach for Presence Monitoring Based on WiFi Probe Requests," *Sensors*, vol. 23, no. 5, p. 2588, 5 Jan. 2023, ISSN: 1424-8220. DOI: 10.3390/s23052588.

A. Hrovat, A. Simončič, T. Kocevska, G. Morano, A. Švigelj, and T. Javornik, "Integrated Communications and Sensing in Terahertz Band: A Propagation Channel Perspective," *Journal of Communications Software and Systems*, vol. 20, no. 1, pp. 23–37, Jan. 30, 2024, ISSN: 1846-6079. DOI: 10.24138/jcomss-2023-0174.

G. Morano, A. Simončič, T. Kocevska, T. Javornik, and A. Hrovat, "Distance- and Angle-Based Hybrid Localization Integrated in the IEEE 802.15.4 TSCH Communication Protocol," *Sensors*, vol. 24, no. 12, p. 3925, 12 Jan. 2024, ISSN: 1424-8220. DOI: 10.3390/s24123925.

G. Morano, T. Javornik, A. Simončič, A. Švigelj, and A. Hrovat, "Interference Mitigation in One-Way Channel Reconstruction for Robust Phase-Based Ranging," *IEEE Access*, vol. 14, pp. 939–955, 2026, ISSN: 2169-3536. DOI: 10.1109/ACCESS.2025.3649293.

Conference Papers

A. Simončič, A. Hrovat, G. Morano, T. Kocevska, and T. Javornik, "Near-field Beam Steering with Planar Antenna Array," in *2024 7th International Balkan Conference on Communications and Networking (BalkanCom)*, Jun. 2024, pp. 31–36. DOI: 10.1109/BalkanCom61808.2024.10557212.

A. Simončič, G. Morano, M. Mohorčič, T. Kocevska, M. Mohorčič, and A. Hrovat, "Validation of solution for people tracking and counting using WiFi network messages," in *Joint European Conference on Networks and Communications & 6G Summit (EuCNC/6G Summit)*, Antwerp, Belgium, 2024, pp 69 (1–4).

T. Kocevska et al., "UWB Channel Impulse Response Alignment Techniques for Accurate Indoor Radio Sensing," in *2024 International Conference on Software, Telecommunications and Computer Networks (SoftCOM)*, Sep. 2024, pp. 1–6. DOI: 10.23919/SoftCOM62040.2024.10721882.

T. Mlakar, A. Hrovat, A. Simončič, T. Javornik, and G. Morano, "Ocenjevanje oddaljenosti med napravami s pomočjo faze signala in algoritma MUSIC," in *Proceedings of the 33rd International Electrotechnical and Computer Science Conference (ERK)*, A. Žemva and A. Trost, Eds., ser. ISSN 2591-0442, Slovenska sekcija IEEE and Fakulteta za elektrotehniko, Sep. 26, 2024, pp. 61–65. [Online]. Available: https://erk.fe.uni-lj.si/2024/papers/mlakar(ocenjevanje_oddaljenosti).pdf.

G. Morano, A. Simončič, T. Kocevska, T. Javornik, and A. Hrovat, "Angle of Arrival Estimation Using IEEE 802.15.4 TSCH Protocol," in *2023 IEEE 34th Annual International Symposium on Personal, Indoor and Mobile Radio Communications (PIMRC)*, Sep. 2023, pp. 1–7. DOI: 10.1109/PIMRC56721.2023.10293886.

G. Morano, A. Simončič, A. Hrovat, and T. Javornik, "Integrated sensing and communication in TSCH networks," in *26th Seminar on Radio Communications SRK 2024*, T. Mlinar and B. Batagelj, Eds., Založba Fakultete za elektrotehniko, Univerza v Ljubljani, 2024, str. 86–87, ISBN: 978-961-243-461-8. [Online]. Available: https://srk.fe.uni-lj.si/zborniki/ZBORNIK%20SRK2024.pdf.

M. Murko et al., "Experimental Validation of UWB CIR Estimation with VNA Measurements in Indoor Scenario," in *2024 7th International Balkan Conference on Communications and Networking (BalkanCom)*, Jun. 2024, pp. 158–162. DOI: 10.1109/BalkanCom61808.2024.10557168.

P. Nimac et al., "Spremljanje hitrosti in načina gibanja uporabnika multimedijske storitve z visokofrekvenčnimi radijskimi signali," in *Proceedings of the 29rd International Electrotechnical and Computer Science Conference ERK 2021*, Slovenska sekcija IEEE and Fakulteta za elektrotehniko, 2020, pp. 78–81. [Online]. Available: https://www.dlib.si/stream/URN:NBN:SI:doc-64WGZ2UC/e32e6f83-9afb-4657-90ee-5e379433d2d5/PDF.

A. Simončič, T. Javornik, K. Bregar, and A. Hrovat, "Merilni sistem za merjenje impulznega odziva radijskega kanala s tehnologijo UWB," in *Proceedings of the 30rd International Electrotechnical and Computer Science Conference ERK 2021*, A. Žemva and A. Trost, Eds., ser. ISSN 2591-0442, Slovenska sekcija IEEE and Fakulteta za elektrotehniko, Sep. 20, 2021, pp. 43–47. [Online]. Available: https://erk.fe.uni-lj.si/2021/erk21.pdf.

Technical Documents

G. Morano, A. Simončič, T. Kocevska, T. Javornik, and A. Hrovat, "Angle of Arrival Estimation Using IEEE 802.15.4 TSCH Protocol," in *COST INTERACT 6th MC and 6th Technical Meeting*, Poznań, Poland, Sep. 11, 2023.

G. Morano, A. Simončič, T. Javornik, and A. Hrovat, "Single access point localization in TSCH network," in *COST INTERACT 7th MC and 7th Technical Meeting*, Lisbon, Portugal, Jan. 22, 2024.

M. Murko et al., "Evaluation of cost-effective UWB technology for accurate indoor CIR measurements," in *COST INTERACT 8th MC and 8th Technical Meeting*, Helsinki, Finland, Jun. 17, 2024.

Datasets

T. Kocevska, A. Simončič, G. Morano, T. Javornik, and A. Hrovat, *Channel Measurements from Sitarjevec Mine for Propagation Modelling in a Cave Environment*, Zenodo, Jul. 24, 2024. DOI: 10.5281/zenodo.12804477.

M. Mohorčič, A. Simončič, M. Mohorčič, and A. Hrovat, *Dataset of IEEE 802.11 probe requests from an uncontrolled urban environment*, Zenodo, Jan. 6, 2023. DOI: 10.5281/zenodo.7509280.

G. Morano, A. Simončič, T. Javornik, and A. Hrovat, *Phase Measurements for AoA Estimation in IEEE 802.15.4 TSCH-based Networks*, Zenodo, Oct. 29, 2025. DOI: 10.5281/zenodo.17476028.

G. Morano, A. Simončič, T. Javornik, and A. Hrovat, *Distance and Angle Measurements for Hybrid Localization in IEEE 802.15.4 TSCH Networks*, Zenodo, Oct. 30, 2025. DOI: 10.5281/zenodo.17481601.

A. Simončič, M. Mohorčič, M. Mohorčič, and A. Hrovat, *Labeled dataset of IEEE 802.11 probe requests*, Zenodo, Jan. 4, 2023. DOI: 10.5281/zenodo.7503594.

Biography

Aleš Simončič (born 23. 06. 1997, Ljubljana) received his B.Sc. degree from the Faculty of Electrical Engineering, University of Ljubljana, in 2019 and enrolled in the M.Sc. program in Electronics the same year, where he developed an interest in wireless communications. During his master's studies, he worked on the interdisciplinary project *Motion and movement tracking of multimedia service users with super high frequency radio signals*, obtained an amateur radio license, and joined the Jožef Stefan Institute (JSI), E6-Department of Communication Systems, as a student researcher under the mentorship of Prof. Dr. Tomaž Javornik. His work focused primarily on ultra-wideband (UWB) technology and radio channel measurements.

In 2022, he completed his M.Sc. degree with a thesis titled *Angle-of-Arrival Estimation Using BLE Technology and an Antenna Array*, supervised by Assoc. Prof. Dr. Aleksander Sešek and Assoc. Prof. Dr. Andrej Hrovat.

That same year, he enrolled in the doctoral program in Communication and Information Technologies at the Jožef Stefan International Postgraduate School and began working as a Young Researcher at JSI, E6-Department of Communication Systems. His research includes UWB channel measurements, device counting using Wi-Fi–enabled devices, near-field propagation of large antenna arrays, and improvements to localization techniques such as Angle-of-Arrival (AoA) and phase-based ranging (PBR) under asynchronous conditions.

His PhD research has been presented at national (ERK, SRK) and international (BalkanCom, EuCNC) conferences and published in several journal papers. He has worked on national (P2-0016, J2-4461) and European projects (RESILOC, UP-SCALE, KreATIVE). He participated in the CONFRONT Wi-Fi device counting challenge, achieving second place. He has attended several international training schools on integrated sensing and communications, antenna design, analysis and design of antenna arrays and reflect arrays, and channel modeling. He regularly participates in COST INTERACT meetings and workshops and presents the department's work to visitors on open days at the Jožef Stefan Institute and to students in primary and secondary schools.